

**Functionalized 2D Nano Materials for Selective Separation and
Related Interfacial Interaction Mechanisms**

by

Wenjiahao Hu

A thesis submitted in partial fulfillment of the requirements for the degree of

Doctor of Philosophy

in

Chemical Engineering

Department of Chemical and Materials Engineering
University of Alberta

© Wenjiahao Hu, 2020

Abstract

The functionalized 2D nanomaterials have attracted increasing attention due to their promising selective interfacial separation performance, including oil-water separation, desalination, ion extraction, wastewater treatment and ionic sieving. To help understand the separation performance or transport phenomena within the nanopores or channels formed by the functionalized 2D materials, the surface properties and interaction mechanisms between transport species and these nanomaterials have been investigated. In this study, the 2D materials, such as graphene oxide (GO), molybdenum disulfide (MoS_2) and Nb_2CT_x MXene, were modified and assembled as the composite or crosslinked materials for selective separation. Some chemical or physical methods such as hydrothermal synthesis, centrifugation, ultrasonication, vacuum filtration and spin coating were used to exfoliate the 2D materials and prepare surface-modified 2D nanosheets.

The separation performance of the above-mentioned materials was evaluated by using several complementary experimental techniques. The atomic force microscopy (AFM), transmission electron microscopy (TEM), scanning electron microscope (SEM), X-ray powder diffraction (XRD), X-ray photoelectron spectroscopy (XPS), zeta potential and size distribution, contact angle measurement and Fourier-transform

infrared spectroscopy (FTIR) were applied to characterize the synthesized functionalized 2D materials in terms of surface structure, heterogeneity, electrochemical properties and hydrophobicity. The ion rejection and permeation properties were studied by using inductively coupled plasma mass spectrometry (ICP-MS), while dye concentration was detected by using ultraviolet-visible (UV-Vis) spectroscopy. The transport behavior of ion selective separation within the functionalized 2D nanosheet channels is highly dependent on the interaction between transported ions and surface functional groups of the 2D nanosheets.

In this work, a series of 2D nanosheet materials such as graphene oxide (GO), molybdenum disulfide (MoS_2) and Nb_2CT_x MXene incorporated with guest materials have been synthesized as functionalized materials (e.g., membrane, and hydrogel) in order to achieve highly selective separation performance. The resulted LA/F/rGO hydrogel owns selective permeation of oil or water flow depending on the pre-soaking condition. The intriguing bouncing performance of the LA/F/rGO hydrogel suggests that it has significant potential application as new oil fence material.

Another surface modified 2D-based material TAMoS₂ (tannic acid-modified, water-stabilized MoS₂ (MoSe₂) nanosheets) has been successfully synthesized through a two-stage, L-ascorbic acid (LA)-assisted exfoliation method with a high yield of 90%

$\pm 5\%$. The as-prepared vacuum-filtered membranes from the resultant TAMoS₂ nanosheets shows fast water flux around 32 L m⁻² h⁻¹ (LMH) and >97% rejection of various cations under osmosis pressure static diffusion mode. In addition, under vacuum-driven filtration conditions, such a hybrid membrane demonstrates ultrafast water flux of 15,000 \pm 100 L/(m²h.bar) and 99.87 \pm 0.1% rejection of various model organic dyes, e.g., basic blue, toluidine blue and rhodamine 6g. The superior performance of TA-modified MoS₂ membranes demonstrates their significant potential for practical applications in water desalination, purification and ion/dye separation.

Furthermore, sodium alginate modified Nb₂CTx Mxene (NbSA) nanosheets have been successfully synthesized through one-step ultrasonication method. The NbSA nanosheet membrane with a thickness of 5 μ m shows ultrahigh rejection rates (>95%) towards multiple cations while maintaining high water flux of 1.7-2.2 LMH under forward osmosis process. In terms of vacuum filtration, the NbSA nanosheet membrane demonstrates ultrahigh rejection rates (~100%) towards multiple target dyes including basic blue, toluidine blue and rhodamine 6g while possesses high water flux of ~2200 LMHB.

This work provides novel and instructive methods to fabricate 2D nanosheet-based materials (e.g., hydrogel and membrane) with high separation performance

toward oil/water mixture, multiple ions and dyes at the nanoscale. The built-up concepts of designing 2D nanosheet membrane provide constructive strategies for surface modification of 2D nanosheets. The selective separation results for oil/water mixture or ion-water exchange process as demonstrated in this work provide valuable and quantitative information for analyzing and understanding the nanoscale transport phenomena between wanted and unwanted species within the membrane matrix.

Preface

This thesis is presented in manuscript-based format. Chapters 3, 4 and 5 have been published, submitted, or under preparation for submission as described below.

Chapter 3 has been published in the *Chemical Engineering Journal*: W Hu, P Zhang, X Liu, B Yan, L Xiang, J Zhang, L Gong, J Huang, K Cui, L Zhu, H Zeng*

An Amphiphobic Graphene-based Hydrogel as Oil-Water Separator and Oil Fence Material

DOI: 10.1016/j.cej.2018.07.147

Chapter 4 has been published in the *Journal of Colloid and Interface Science*: W Hu, X Cui*, L Xiang, L Gong, L Zhang, M Gao, W Wang, J Zhang, F Liu, B Yan*, H Zeng*

Tannic Acid Modified MoS₂ Nanosheet Membranes with Superior Water Flux and Ion/Dye Rejection

DOI: 10.1016/j.jcis.2019.10.068

Chapter 5 has been published in the *Journal of Colloid and Interface Science*: W Hu, L Xie, H Zeng*

Novel Sodium Alginate-Assisted MXene Nanosheets for Ultrahigh Rejection of Multiple Cations and Dyes

DOI: 10.1016/j.jcis.2020.02.028

Chapters 1, 2, and 6 are originally written by Wenjihao Hu, and have never been published before.

Acknowledgements

Four years ago, a handsome custom officer told me nicely “Welcome to Canada”, which initiates my impressive story for my PhD study. The whole process is filled with happiness, surprise, enrichment and sometimes with a little bit exhaustion. Approximately four years have passed for my PhD study, it is still my great honor to claim that I have experienced one of the greatest periods in my life, which I would never forget. At the near end of this journey, it is almost difficult to say goodbye to my student life. The PhD training taught me a lot on how to become a strong person while facing with difficulties in the past or the future steps of my career.

I would like to express my sincere gratitude to a lot of friends since this thesis would not have been completed without the help or support from them. Their kind words, behaviors, thoughtful insights inspired me a lot, which brought me enough confidence on facing with the difficulties during my PhD study.

Firstly, I would like to give my sincere respect and gratitude to my supervisor, Prof. Hongbo Zeng. He is the best supervisor so far that I have met in my life with immeasurable encouragement, guidance and support for my study. I would never forget the most pleasant sound in the world when it is required to purchase some expensive lab supplies – “go ahead and buy it”; I would never forget those timely calls from him when you got lost from your research – “move on, I believe you”; I would never forget the discussions and encouragements in his office – “nice work and keep going”. It was Dr. Zeng who guided me into the field of colloid interfacial sciences and how it related to my original membrane area. Those advices and guidance from him would deeply affect the rest of my research life.

Secondly, I would like to thank my father, Yuehua Hu, my mother, Yufang Liu.

Thank you all for the selfless help and immeasurable support. You always tell me to take care of myself, though I even not spent a whole spring festival with you during my four-year PhD study.

Thirdly, I would like to thank all the group members for their kind help and discussions on my experiment difficulties and daily troubles. Thanks to Dr. Bin Yan, Dr. Linbo Han and Dr. Xiaokong Liu, I would never forget the struggle time that we spent together every night. Many thanks to my friends, Peibin Zhang, Yaqian Zhang, Chao Qi, Bo Liu and Hongbiao Tao who helped me during my stay in Edmonton.

In addition, I would like to deliver my sincere gratitude to Chinese Scholarship Council for their strong financial support to cover my four-year PhD study living expense. Many thanks to Natural Sciences and Engineering Research Council of Canada (NSERC), Canada Foundation for Innovation and the Canada Research Chairs Program (Dr. Hongbo Zeng) for lab support.

Once again, thanks to all the people that I mentioned above or those I have met during my PhD study. Wish you all the best!

Table of Contents

| | |
|--|------|
| Abstract..... | ii |
| Preface..... | vi |
| Acknowledgements..... | vii |
| Table of Contents | ix |
| List of Figures | xiii |
| List of Abbreviations..... | xxi |
| Chapter 1 Introduction and Literature Review | 1 |
| 1.1 Introduction | 1 |
| 1.1.1 Wastewater source | 3 |
| 1.1.2 Methodologies on wastewater treatment..... | 3 |
| 1.1.3 Reusable water resources | 4 |
| 1.1.4 Remaining challenges on wastewater treatment | 5 |
| 1.1.5 2D Materials on wastewater treatment..... | 6 |
| 1.1.6 Exfoliation and reorganization of 2D nanosheets | 7 |
| 1.1.7 Surface termination | 7 |
| 1.1.8 2D material-based hydrogel | 8 |
| 1.1.9 2D material-based membrane..... | 9 |
| 1.2 Objectives | 10 |
| 1.3 Structure of the thesis | 11 |
| 1.4 References | 13 |
| Chapter 2 Experimental techniques | 23 |
| 2.1 Scanning electron microscope (SEM) | 23 |
| 2.2 Atomic force microscope (AFM) | 25 |
| 2.3 Transmission electron microscopy (TEM) | 27 |
| 2.4 X-ray diffraction (XRD)..... | 28 |
| 2.5 Ultraviolet-visible (UV-vis) spectroscopy | 29 |
| 2.6 Fourier-transform infrared (FTIR) spectroscopy..... | 30 |
| 2.7 X-ray photoelectron spectroscopy (XPS)..... | 31 |
| 2.8 Zeta potential and size measurement..... | 32 |
| 2.9 Contact angle measurement..... | 33 |
| 2.10 Inductively coupled plasma mass spectrometry (ICP-MS) | 34 |
| 2.11 Forward osmosis | 35 |
| 2.12 Vacuum filtration | 36 |

| | |
|--|----|
| 2.13 Hydrothermal synthesis | 36 |
| 2.14 Surface force apparatus (SFA)..... | 37 |
| 2.15 Centrifugation..... | 38 |
| 2.16 Ultrasonication..... | 39 |
| 2.17 Spin coating..... | 39 |
| 2.18 References | 39 |
| Chapter 3 An Amphiphobic Graphene-Based Hydrogel as Oil-Water Separator and Oil Fence Material | 49 |
| 3.1 Introduction | 49 |
| 3.2 Experimental Section..... | 51 |
| 3.3 Results and Discussion | 55 |
| 3.3.1 Synthesis of 3D Fluorinated rGO nanosheets (F/rGO) Macrostructure Precursor | 55 |
| 3.3.2 Synthesis and Characterization of 3D LA/F/rGO..... | 55 |
| 3.3.3 Oil Adsorption Behaviors of LA/F/rGO hydrogel and Regeneration by Thermal Treatment..... | 61 |
| 3.3.4 Oil-Water Separation and Bouncing Activity of LA/F/rGO hydrogel | 64 |
| 3.4 Conclusions | 68 |
| 3.5 References | 70 |
| Chapter 4 Tannic Acid Modified MoS ₂ Nanosheet Membranes with Superior Water Flux and Ion/Dye Rejection..... | 78 |
| 4.1 Introduction | 78 |
| 4.2 Materials and Methods | 80 |
| 4.2.1 Two-stage Exfoliation Method..... | 80 |
| 4.2.2 Preparation of MoS ₂ -based Membranes..... | 81 |
| 4.2.3 Membrane Testing Condition..... | 82 |
| 4.2.4 Osmotic Pressure..... | 82 |
| 4.2.5 Water Transport | 83 |
| 4.2.6 Ion Transport | 83 |
| 4.2.7 Surface Force Measurement..... | 83 |
| 4.2.8 Yield Calculation | 84 |
| 4.2.9 Sample Characterization | 85 |
| 4.3 Results and Discussion | 85 |
| 4.3.1 Synthesis and Characterization of TAMoS ₂ (TAMoSe ₂) Nanosheets | 85 |

| | |
|--|-----|
| 4.3.2 High water flux and high ion rejection rates for MoS ₂ membranes with TA modification under osmosis pressure | 92 |
| 4.3.3 Effect of TA Molecules on Water Flux..... | 96 |
| 4.3.4 Ultrahigh water flux and dye rejection rate for MoS ₂ membranes with TA modification in vacuum-driven conditions..... | 98 |
| 4.4 Conclusions | 100 |
| 4.5 References | 101 |
| Chapter 5 Novel Sodium Alginate-Assisted MXene Nanosheets for Ultrahigh Rejection of Multiple Cations and Dyes | 106 |
| 5.1 Introduction | 106 |
| 5.2 Materials and Methods | 108 |
| 5.2.1 Synthesis of Nb ₂ CTx MXene nanosheets | 108 |
| 5.2.2 Delamination of Nb ₂ CTx MXene nanosheets..... | 110 |
| 5.2.3 Synthesis of NbSA nanosheets..... | 110 |
| 5.2.4 Characterization | 111 |
| 5.2.5 Preparation of NbSA Membranes | 111 |
| 5.2.6 NbSA Nanosheet Membrane testing condition..... | 112 |
| 5.2.7 Osmotic pressure..... | 112 |
| 5.2.8 Water transport rate | 113 |
| 5.2.9 Water transport rate (vacuum filtration)..... | 113 |
| 5.2.10 Ion transport rate | 113 |
| 5.2.11 Ion rejection rate..... | 114 |
| 5.2.12 Dye rejection rate | 114 |
| 5.3 Results and Discussion | 115 |
| 5.3.1 Synthesis of Nb ₂ CTx Mxene and NbSA nanosheets..... | 115 |
| 5.3.2 Characterization of NbSA nanosheets..... | 117 |
| 5.3.3 Synthesis and characterization of NbSA membrane | 119 |
| 5.3.4 Ion rejection performance through osmosis process | 120 |
| 5.3.5 Vacuum filtration process towards multiple dyes | 125 |
| 5.3.6 Li ⁺ /Mg ²⁺ selective separation after long-term stability..... | 127 |
| 5.4 Conclusion..... | 128 |
| 5.5 References | 130 |
| Chapter 6 Conclusions and Future Work | 164 |
| 6.1 Major conclusions..... | 164 |
| 6.2 Original contributions..... | 166 |
| 6.3 Suggestions for future work | 168 |

| | |
|--------------------|-----|
| Bibliography | 154 |
| Appendix..... | 196 |

List of Figures

| | | |
|------------|--|----|
| Figure 1.1 | Schematic global water distribution. Data from Shiklomanov and Rodda, 2003. Freshwater has a global volume of 35.2 million cubic kilometres (km ³). | 2 |
| Figure 2.1 | Typical core components of a scanning electron microscope (SEM) configuration. Figure is addapeted from reference with Elsevier permission liscence (No.4660410235374). | 23 |
| Figure 2.2 | Typical core components of an atomic force microscope (AFM). | 25 |
| Figure 2.3 | Typical core components of a transmission electron microscope (TEM) configuration. Figure is addapeted from reference with Elsevier permission liscence (No. 4660440530381). | 27 |
| Figure 2.4 | The simplified schematic illustration of a generic X-ray scattering measurement. | 28 |
| Figure 2.5 | Typical core components of ultraviolet-visible (UV-vis) spectroscopy. | 29 |
| Figure 2.6 | Typical core components of Fourier-transform infrared (FTIR) spectroscopy. | 30 |

| | | |
|-------------|---|----|
| Figure 2.7 | Typical core components of X-ray photoelectron spectroscopy (XPS). | 31 |
| Figure 2.8 | Typical core components for the instrumentation of DLS. Figure is addapeted from reference with ScienceDirect permission liscence (No. 4661451205919). | 32 |
| Figure 2.9 | Schematic diagram of contact angle. | 33 |
| Figure 2.10 | Schematic diagram of membrane process including forward osmosis and reverse osmosis process..... | 35 |
| Figure 2.11 | (a) Cross section view of the SFA 2000 main body through the center of the apparatus, (b) top view of the main stage and the bottom disk holder. ¹ Figure is addapeted from reference with IOP Science permission liscence (No. 4661720952113). | 37 |
| Figure 3.1 | Illustration of the formation process for LA/F/rGO hydrogel. The hydrothermalreaction time was set as 6 h and the reduction process was set as 1 h. | 56 |
| Figure 3.2 | SEM images of LA/F/rGO hydrogel before (a1-c1) and after (a2-c2) burning treatment. AFM images for single fluorographene nanosheets under different reaction times (d-6h, e-24h) and the associated height profiles. | 57 |

| | | |
|------------|--|----|
| Figure 3.3 | TEM image of pure graphene (a, b) and PF grafted graphene (d, e) and high-resolution Fast Fourier Transform (FFT) image of graphene hydrogel (c, f). | 59 |
| Figure 3.4 | Elemental mapping for LA/F/rGO hydrogel. | 60 |
| Figure 3.5 | (a) Fourier transform infrared (FTIR) spectra of GO and LA/F/rGO. (b) X-ray diffraction (XRD) patterns of rGO and LA/F/rGO hydrogel. | 60 |
| Figure 3.6 | Photographs on burning oil-saturated LA/F/rGO hydrogel for 0 s to 50 s (a1-a6) and 5-minute selective adsorption process of toluene on water surface in a petri dish (b1-b3), 1-minute selective adsorption of hexadecane on water surface in a 20-ml glass bottle (c1-c3) and recyclability through fire burning treatment on the flame of a fire lighter (Turboflame Ranger Windproof Lighter). | 62 |
| Figure 3.7 | Weight gain of the LA/F/rGO hydrogel during adsorption of various organic solvents. | 64 |
| Figure 3.8 | Oil-water mixture separation process using (a) LA/F/rGO hydrogel pre-treated/pre-soaked with water to permit water flow for separation of oil, and (b) LA/F/rGO hydrogel pre-treated/pre-soaked with oil to permit oil flow for separation of water..... | 65 |

| | | |
|------------|---|----|
| Figure 3.9 | (a) Bouncing behavior to oil droplet of LA/F/rGO hydrogel underwater (also see video in Supporting Information). (b) Schematic for oil droplet interacting with the hydrogel surface and the possible interaction mechanism for the bouncing phenomenon. | 66 |
| Figure 4.1 | Schematic illustration of the exfoliation process for TAMoS ₂ (TAMoSe ₂) nanosheets (a); HRTEM image of TAMoS ₂ nanosheets demonstrating the microstructure of TA-modified MoS ₂ nanosheets (b); FFT pattern (c) obtained from the highlighted region in red in (b); reverse FFT-filtered atomic resolution image showing the atom arrangements in (002) plane of MoS ₂ nanosheets (d); enlarged HRTEM image (e); high-resolution XPS patterns of C 1s and O1s (f), HAADF-STEM image and STEM-EDX mapping of TAMoS ₂ nanosheets (elements C and O) illustrating the attachment of TA molecules onto the surface of MoS ₂ nanosheets (g). | 88 |
| Figure 4.2 | XRD spectra for TAMoS ₂ , LAMoS ₂ and MoS ₂ | 91 |

Figure 4.3 (a) Membrane thickness standard line versus loading amount for bare-MoS₂ membranes, TAMoS₂ membranes, and a hybrid membrane with 1 wt% TAMoS₂; (b) Top view SEM image of a 40- μ m-thick TAMoS₂ membrane with an inset image of a freestanding 40- μ m-thick TAMoS₂ membrane (upper) and an inset image of a flexible 5- μ m-thick TAMoS₂ membrane on a support (lower).92

Figure 4.4 Comparison of 5- μ m-thick hybrid membrane with 1% TAMoS₂, TAMoS₂ membrane and MoS₂ membrane in terms of rejection rate (%) (a); cation permeation rate (b) and water flux (c). Feed side is DI water and 0.25M cationic solution as the draw side under room temperature and pressure, the stabilized time is set as 360 min. Inductive Coupled Plasma Emission Spectrometer was used to obtain the cation concentrations in solutions.95

Figure 4.5 The synergistic effect to achieve the ultrafast water flux of $\sim 15,000$ L/(m²h.bar) at 1% weight percentage of TAMoS₂ nanosheets (a); AFM force measurement of a water droplet to TAMoS₂ membrane surface (b) (based on experimental setup shown in Figure S4.10); AFM force profile of a water droplet interacting with a bare MoS₂ membrane surface (c); schematic illustration showing the structure to achieve the synergistic effect (d).
97

Figure 4.6 Water flux and rejection rates for 5 μ m-thick 1% TAMoS₂ hybrid membrane, TAMoS₂ membrane and MoS₂ membrane on basic blue, toluidine blue and rhodamine 6g (c) under vacuum filtration ~ 0.7 bar. The abbreviation LMHB represents L/(m²h.bar).
99

Figure 5.1 Schematic illustration for the synthesis process of Nb₂CT_x MXene nanosheets and NbSA nanosheets: (A) hydrofluoric acid (40 wt% concentration) etching process for the removal of Al from Nb₂AlC powders and the delamination process by using DMSO solution as polar solvent followed by washing and ultrasonication steps. (B) Ultrasonication process for the synthesis of NbSA nanosheets by using sodium alginate (1 mg/ml concentration).....121

Figure 5.2 (A) High resolution TEM image of NbSA nanosheets (the inserted image on the right is written by a brush pen with MXene ink), (1)

amorphous structure; (2) lattice structure with a lattice spacing of 1.1038 nm; (B) atomic force microscopy (AFM) height profile of NbSA nanosheets coated on silica surface with the value of ~3 nm.122

Figure 5.3 Characterization of NbSA nanosheets. (A) X-ray diffraction (XRD) analysis for Nb₂CT_x-SA (NbSA) nanosheets; Nb₂CT_x nanosheets and Nb₂AlC powders as compared to JCPDS #: 30-0033 (Nb₂AlC) card; (B and C) X-ray photoelectron spectroscopy (XPS) analysis for Nb₂CT_x – SA nanosheets (B) C1s and (C) O1s.....124

Figure 5.4 (A) Schematic illustration for synthesizing NbSA nanosheet (as shown on the right enlarged FE-SEM image) membrane through filtration method on polyvinylidene fluoride (PVDF) filter substrate (~0.7 bar) (B) Schematic image for the NbSA nanosheet membrane including cross view image and top view image.125

Figure 5.5 (A) Forward osmosis process results for Nb₂CT_x nanosheet membrane including the rejection rate/permeation rate for multiple cations; (B) Forward osmosis process results for NbSA nanosheet membrane. The feed side is DI water and the draw side is 0.25 M salt solution; both sides are under magnetic stirring at 100 rpm to avoid concentration gradient.126

Figure 5.6 Stability test of the membrane for rejection rate versus permeation rate of multiple cations (A) K⁺; (B) Na⁺; (C) Li⁺; (D) Ca²⁺; (E) Mg²⁺.

The process is forward osmosis with DI water as feed side and 0.25 M salt solution as draw side. The magnetic stir bars with 100 rpm speed are added at both sides to avoid concentration gradient.129

Figure 5.7 (A) Water flux and rejection rate toward target dyes (basic blue, toluidine blue and rhodamine 6g); (B) UV standard concentration line for rhodamine 6g; (C) UV standard concentration line for basic blue; (D) UV standard concentration line for toluidine blue. The vacuum is ~0.7 bar and the dye concentration are 100 ppm.....131

Figure 5.8 Declines in water flux with Basic blue dye solution (100 ppm) from filtration up to 2000 s.133

List of Abbreviations

| | |
|--------|--|
| AFM | Atomic force microscopy |
| ATR | Attenuated total reflection |
| APTES | (3-Aminopropyl) triethoxysilane |
| CVD | Chemical vapor deposition |
| CA | Contact angle |
| DA | Dopamine |
| DLS | Dynamic light scattering |
| DLVO | Derjaguin-Landau-Verwey-Overbeek |
| DMSO | Dimethylsulfoxide |
| DMT | Derhaguin-Muller-Toporov |
| DOPA | <i>L</i> -3,4-dihydroxyphenylalanine |
| EDL | Electrostatic double-layer |
| EDX | Energy dispersive X-ray spectroscopy |
| FO | Forward osmosis |
| FTIR | Fourier transform infrared spectroscopy |
| GA | Gallic acid |
| HF | Hydrofluoric acid |
| ICP-MS | Inductively coupled plasma mass spectrometry |
| LA | L-ascorbic acid |
| LbL | Layer-by-layer |
| LERO | Low energy reverse osmosis |
| LPRO | Low pressure reverse osmosis |
| MCE | Mixed cellulose ester |
| NF | Nanofiltration |
| O/W | Oil-in-water |
| PAA | Polyacrylamide |
| PF | 1H,1H,2H,2H-perfluorodecanethiol |
| PTFE | Polytetrafluoroethylene |

| | |
|--------|--|
| PVA | Polyvinyl alcohol |
| PVDF | Polyvinylidene fluoride |
| RAFT | Reversible addition-fragmentation chain transfer |
| RO | Reverse osmosis |
| rGO | Reduced graphene oxide |
| SA | Sodium alginate |
| SEM | Scanning electron microscope |
| SFA | Surface forces apparatus |
| TEM | Transmission electron microscope |
| TIMS | Thermal ionization mass spectrometry |
| TMDC | Transition metal dichalcogenides |
| UV-vis | Ultraviolet-visible (uv-vis) spectroscopy |
| vDW | Van der waals |
| W/A | Water-in-air |
| XPS | X-ray photoelectron spectroscopy |
| XRD | X-ray diffraction |

Chapter 1 Introduction and Literature Review

1.1 Introduction

Energy and resources are the major concerns all over the world, which attracted tremendous attention from many researchers.²⁻⁴ Energy provides strong power to accelerate the advances of human society, while resources guarantee the living of humans. On one hand, both energy and resources are urgently needed in the daily life cycle.^{3, 5} On the other hand, the storage of energy and resources is limited on earth. Thus, the efficient utilization of both energy and resources is considered a tough task worldwidely. The utilization of resources consists of two aspects: generation and recycle, while recovery as well as production are the two aspects for resources.^{3, 4, 6} In terms of the efficient generation and production for energy and resources, massive techniques have been springing out since first industrial revolution back in 18th century.^{2, 5, 7} However, not until 1987, the brand-new theory “sustainable development” was proposed, which was the actual starting point of recovery and recycle for energy and resources.^{6, 8} Numerous technologies and journal papers have sprung up since then; nonetheless, there are many remaining difficulties on facing the challenge for the recovery and recycle of energy and resources globally.^{4, 9}

In this thesis, the recyclability and sustainable development of water resource has been investigated intensively. In general, water resource exists everywhere in the daily life of humans: in the air, above the earth surface, below the ground and in the oceans.^{6,}

⁹ However, only 2.5% of the above-mentioned water resources are drinkable, most of

which exist in glaciers or ice caps (~70% of usable water resources) as shown in **Figure 1.1**.^{2, 5, 10} The major source for water supply on earth is the ground water with small percentage of fresh water in air and above ground.^{2, 6, 11} On one hand, the water consumption is increasing dramatically due to human activities – namely urbanization, growth in population, high quality living standards and pollution.^{7, 9, 10} On the other hand, the existing technologies for water recycling could not meet the requirement on tackling the water shortage issue.⁸ The water recycling process contains two aspects: recover useful materials from wastewater and reuse of water, which has already been explored but far from safe, reliable, and cost-effective technologies to reuse effluent materials from wastewater and recycle water.^{10, 11} The aim for this thesis is to make contribution to such technologies for wastewater treatment.

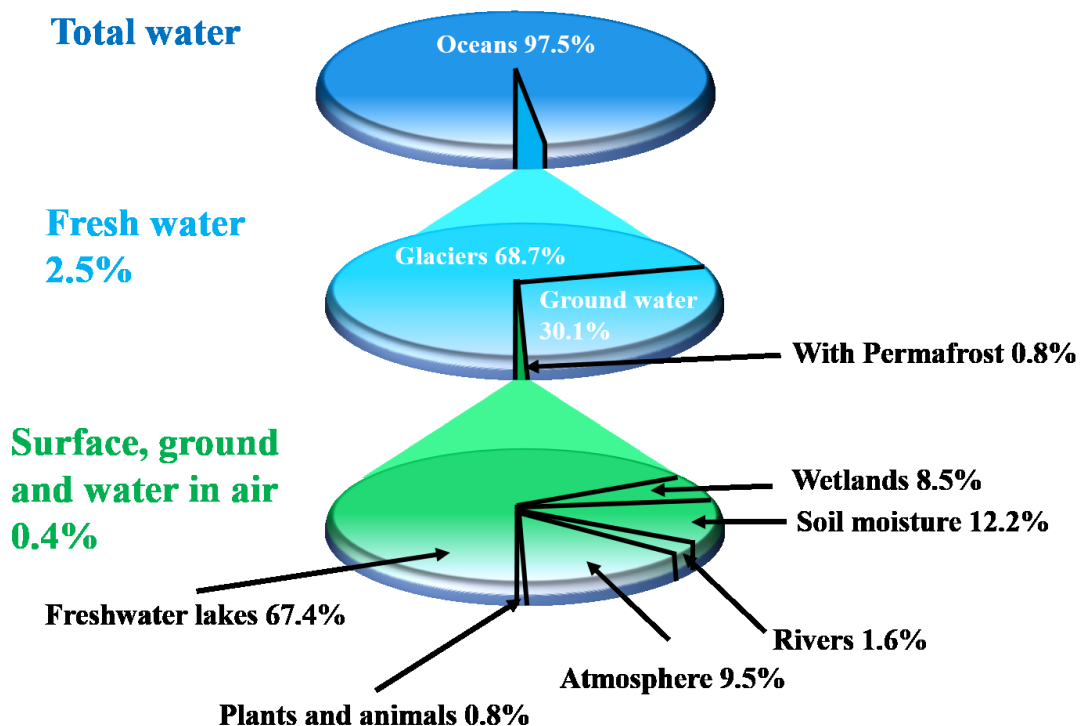


Figure 1.1. Schematic of global water distribution. Data from Shiklomanov and Rodda, 2003. Freshwater has a global volume of 35.2 million cubic kilometres (km³).¹²

1.1.1 Wastewater source

In order to build up cost-effective technologies for wastewater treatment, the wastewater sources are required to be determined. There are three types of wastewater or sewage as classified by contamination composition including domestic (normally from daily life such as bathroom sinks, laundry machines etc.), industrial (originally from manufacturing or chemical processes) and storm (water from run-off, energy generation plants agricultural facilities or car garages).¹³⁻¹⁶ Domestic type is estimated to be 99.9 percent of wastewater by weight, while the rest types own less than 0.1 percent of wastewater by weight.^{13, 17, 18} In general, the composition of the wastewater consists of organic materials (biochemical oxygen demand or BOD), suspended solids, plant nutrients (compounds of nitrogen and phosphorus) and microbes.^{13, 19, 20}

1.1.2 Methodologies on wastewater treatment

The wastewater treatment and disposal are classified into primary treatment, secondary treatment and tertiary treatment.^{21, 22} Around 60 percent of total suspended solids and about 35 percent of BOD would be removed in the primary treatment, while 85 percent of both suspended solids and BOD were removed from secondary treatment.^{23, 24} Normally, most of the large sized suspended solids and BOD are removed from secondary effluent.²² The tertiary treatment is a further polishing process most likely using granular media filters, much like the filters for purifying drinking water.^{22, 23} The cost for tertiary treatment would be more expensive as compared to primary and secondary treatment. The above-mentioned primary, secondary and tertiary

treatments were time and land consuming. In order to improve the treatment efficiencies, new treatment methods have been developed including membrane technology, ballasted flocculation reactor and integrated fixed-film activated sludge (IFAS) process.^{21, 23, 24} The membrane technologies are more effective for tertiary treatment meanwhile less land area is required.

1.1.3 Reusable water resources

With the dramatically increasing amount of population, reused wastewater is gradually becoming valuable in cities or towns since water supplies are limited.^{22, 25} The effective reuse of wastewater can reduce discharges of effluent. Normally, there are two types of wastewater reuse: direct and indirect.²⁶ The direct reuse of water is a treatment of wastewater by using some types of water system without premixing with other effluent, while indirect reuse of water involves the mixing of other wastewater effluent.^{21, 23, 26} The quality level for the reusable water becomes more critical, which depends on the intended use of the water. Some intentions such as drinking water may require additional treatment in order to achieve high quality standard of recyclable water, e.g., filtration, adsorption, forward/reverse osmosis etc.^{27, 28} Apart from the reused wastewater, seawater desalination could be treated as an optimal solution for tackling with water scarcity.^{27, 29} Normally, the seawater desalination process is conducted by reverse osmosis to mitigate the environmental impacts of the high salinity brine. However, due to the membrane design limitations, e.g., flux, mechanical property and fouling issue, the reverse osmosis (RO) process is operating at a low pressure (LP)

or a low energy (LE), which is generally called “LPRO” or “LERO” process.^{23, 25, 30} Though either LPRO or LERO was energy friendly, the low-pressure condition would limit the water permeability and membrane fouling susceptibility.^{23, 28, 30} Therefore, a well designed, energy efficient membranes are remaining urgently needed for desalination and separation from brine or reusable water source due to the increasing demand for fresh water.

1.1.4 Remaining challenges on wastewater treatment

In general, current challenges on wastewater treatment are relevant to meeting the increased water quality standards and are difficult to tackle with the limitation of energy conservation, carbon footprint reduction and space expansion.^{31, 32} The challenges are most likely to exist in tertiary wastewater treatment including the improvement of treatment efficiencies without additional space.³¹ The most commonly used treatment on obtaining reusable water resources for either reusable wastewater treatment or desalination is membrane technology.^{31, 33-35} As a considerable natural treatment method, membrane technology has been considered to have promising potential as an improved tertiary wastewater treatment method to face the energy and electricity consuming challenges for its simplicity, cost-effectiveness, reliability, space and friendly environment.^{32, 33} However, fouling and flux enhancement are the major challenges in membrane technology, which limits its wide application.³³ Therefore, a well-designed energy efficient membrane is urgently needed to face the coming water shortage issue.

1.1.5 2D Materials on wastewater treatment

The pressure driven membrane technologies include ultrafiltration, nanofiltration and reverse osmosis have been investigated as a promising solution for mass production of potable water.³⁶⁻³⁹ However, the demerits on those processes including energy consumption, efficient selectivity and economic investment have limited the industrialization.^{36, 40, 41} Therefore, advanced membrane-assisted technologies are urgently needed to face the challenge on water crisis.⁴² The 2D nanoporous materials have been alternatives for wastewater treatment and desalination owing to their large surface area and excellent mechanical strength.^{37, 39, 43} Recent progress on 2D nanoporous materials including graphene, graphene oxide, graphyne, molybdenum disulfide (MoS₂), tungsten chalcogenides (WS₂) and MXene are highlighted.^{38,43,44} The 2D composite materials could generate enormous potential for wastewater treatment and desalination through surface modification by changing the structure, hydrophilic nature, mechanical strength and antifouling properties.^{38,40,45} Subsequently, the newly developed 2D materials have been investigated for their applications and performance evaluation in wastewater treatment and desalination applications though only limited types of 2D materials have been investigated.^{36,44} Thus, it is an imperative field, which requires more attention for further advancing these materials on industrial scale in the near future.

1.1.6 Exfoliation and reorganization of 2D nanosheets

The study of two-dimensional (2D) materials has been attracting much attention

since the first discovery of graphene.^{46, 47} The preparation methodologies including mechanical exfoliation, chemical vapor deposition (CVD), liquid-phase ultrasonication and electrochemical exfoliation are significant to fabricate energy and cost effective 2D materials.^{48, 49} Comparatively, liquid-phase exfoliation is cost-effective, efficient and versatile for the massive production of large quantities of two-dimensional (2D) nanosheets in a range of polar solvents.⁵⁰ Besides, those polar solvents could be various types of stabilizers, including surfactants or amphiphiles and polymers, which could effectively break the weak van der Waals forces among inter layers of the composite 2D materials.^{46, 49, 51} The resultant liquid-suspended single-layer or few-layer 2D nanosheets suspension among different polar solvents have been investigated and characterized in detail and used for a wide range of applications including wastewater treatment.^{46, 51, 52} The liquid-phase assisted ultrasonication methods are convenient, controllable and have been reported to be a suitable method for industrial mass production.

1.1.7 Surface termination

There are large numbers of transition metal carbides and nitrides 2D materials (TMDCs) that have shown promising applications such as electromagnetic interference shielding, energy storage and wastewater treatment.⁵³⁻⁵⁶ The TMDCs such as MXenes have strong optical absorption capability and tunable surface chemistry through their metallic nature.⁵³ The physical properties of those TMDCs are strongly dependent on the surface terminations during the synthetic or liquid-phase assisted exfoliation

process.^{54, 57} Those liquids were mostly polar solvents and the polar molecules from the solvents were normally able to attach onto the 2D nanosheet surface during the exfoliation process since the binding energy between the polar molecules and 2D nanosheets was higher than the dissociation energy of polar molecules in water.^{53, 54, 58} The resulted liquid suspension is surface terminated 2D nanosheets or functionalized 2D nanosheets.

1.1.8 2D material-based hydrogel

The 2D material-based hydrogel could be formed through self-aggregation of functionalized 2D nanosheets such as graphene oxide nanosheets hydrothermal process or crosslinking of functionalized 2D nanosheets.⁵⁹⁻⁶¹ Various kinds of applications have been illustrated by using 2D material-based hydrogel, such as adsorption, energy storage, oil/water separation and wastewater treatment due to the large specific area and rapid responsiveness towards external circumstances.^{59, 62, 63} Nevertheless, there are many problems that limit the scale-up production of those hydrogels in industrial applications such as poor mechanical properties due to the weak physical interactions among 2D nanosheets.^{59, 62, 64} In addition, the complicated composition of industrial wastewater would limit the adsorption behavior of the hydrogel under multiple external circumstances.^{59, 65} Therefore, the 2D material-based hydrogel would require further modification on tackling with the harsh environmental conditions.^{64, 66, 67} The self-assembled functionalized 2D nanosheets were one of the optimal choices with an introduction of functional groups into 2D material-based hydrogel with enhanced

properties including mechanical strength, adsorption capacity and antifouling, which was investigated in this thesis.

1.1.9 2D material-based membrane

The unique structure of 2D material-based membranes including thin, laminar and mixed matrix types have led to a superior separation performance (i.e. high-water permeability and selectivity).⁶⁸⁻⁷⁰ The unique structure and surface modifiable properties make 2D material-based membrane a promising potential in various kinds of applications, such as energy storage, oil/water separation and wastewater treatment.^{68, 71, 72} It has been a decade that membrane materials have not been significantly improved since the commercial driving force is weak due to the fouling issue on facing the harsh environmental conditions and long-time stability for maintaining continuous high permeation rate.^{68, 70, 73} Current status has illustrated that various 2D nanosheet-based membranes including thin film, laminar as well as mixed matrix types have superior separation performance with regular and ordinary pore sizes, controllable interlayer distances or surface functional groups as compared with conventional polymer membranes.^{68, 74, 75} However, despite significant progresses in 2D nanosheet-based membranes, there are challenges that required to be addressed to meet the industry inquiries such as mass production of 2D nanosheets, controllable surface modification, scale-up processability and comprehensive separation mechanisms.^{69, 74, 76, 77} In this thesis, some intriguing materials were developed as well as detailed discussions in relate to the separation and selectivity mechanisms for the membrane materials have

been addressed for contributing the next generation of membranes.

1.2 Objectives

Despite much progress has been made over the past few decades, the superior separation performance and clear interfacial mechanisms for functionalized 2D materials remain challenges including synthesis of 2D nanosheets, surface modification, scale-up processability and separation mechanisms. The overall objective of this thesis is developing a suitable functionalized 2D materials, conducting superior separation and selectivity performance, and comprehensively understanding the interfacial separation science in the field of wastewater treatment. The detailed objectives are as follows.

- (1) Developing 2D material-based hydrogel using surface termination to achieve enhanced mechanical property and superior selectivity and separation performance.
- (2) Developing 2D material-based membrane using surface termination to achieve enhanced water permeation and superior rejection rate towards target contaminants including cations and organic dyes.
- (3) Developing 2D material-based membrane using surface termination to achieve selectivity performance toward multiple ions at either low or high concentration.
- (4) Investigating the surface interaction among cations on each modified individual 2D nanosheet inside the laminar composite membrane channels,

which will provide nanoscopic insights into the permeation/rejection mechanisms.

1.3 Structure of the thesis

Chapter 1 reviews relevant literature on water shortage and some current methods on wastewater treatment and desalination. Current progress on 2D materials and 2D-based materials including remaining challenges are reviewed. The objectives of this thesis are listed.

Chapter 2 describes the experiment techniques used in this study and relevant listed fundamentals.

Chapter 3 demonstrates a facile, novel, environmental-friendly and economical method for synthesizing the fluorographene nanosheets through Michael's Addition reaction and fabricating amphiphobic LA/F/rGO hydrogel. The selectivity and bouncing activity results of the hydrogel are presented and discussed.

Chapter 4 presents a novel method for preparing tannic acid (TA)-modified MoS₂ (or MoSe₂) nanosheets with a high yield production and have demonstrated the superior performance of water flux and rejection of cations/organic dyes on the as-prepared membranes based on the TA-modified MoS₂ (MoS₂) nanosheets. A hybrid membrane is designed and shows a fast water flux and high rejection of cations including K⁺, Na⁺, Li⁺, Ca²⁺, and Mg²⁺ under static diffusion mode. When tested under vacuum-driven filtration condition, this hybrid membrane demonstrates ultrafast water flux as well as high rejection towards multiple model organic dyes, e.g., basic blue, toluidine blue and

rhodamine 6g.

Chapter 5 demonstrates a novel, facile and scalable sodium alginate (SA)-assisted surface termination method to fabricate SA-modified Nb₂CTx MXene (NbSA) nanosheets. The NbSA film with a thickness of 5 μm shows >99% rejection towards various cations under forward osmosis process and a fast water flux of 2,200 ± 100 L m⁻² h⁻¹ bar⁻¹ (LMHB) with almost 100% rejection rate towards multiple dyes under vacuum-driven filtration mode. A selective separation performance on Li⁺/Mg²⁺ mixture solution under forward osmosis process was observed for the NbSA film.

Chapter 6 provides the major conclusions as well as original contributions for this thesis. The future plans and suggestions are provided.

1.4 References

1. Israelachvili, J.; Min, Y.; Akbulut, M.; Alig, A.; Carver, G.; Greene, W.; Kristiansen, K.; Meyer, E.; Pesika, N.; Rosenberg, K.; Zeng, H., Recent advances in the surface forces apparatus (SFA) technique. *Reports on Progress in Physics* **2010**, *73* (3), 036601.
2. Salgot, M.; Priestley, G. K.; Folch, M., Golf Course Irrigation with Reclaimed Water in the Mediterranean: A Risk Management Matter. *Water* **2012**, *4* (2), 389-429.
3. Bick, A.; Gillerman, L.; Manor, Y.; Oron, G., Economic Assessment of an Integrated Membrane System for Secondary Effluent Polishing for Unrestricted Reuse. *Water* **2012**, *4* (1), 219-236.
4. Bertone, E.; Stewart, R. A., Framework for Enhancing the Supply-Demand Balance of a Tri-Supply Urban Water Scheme in Australia. *Water* **2011**, *3* (4), 976-987.
5. Lazarova, V.; Sturny, V.; Sang, G. T., Relevance and Benefits of Urban Water Reuse in Tourist Areas. *Water* **2012**, *4* (1), 107-122.
6. Kapellakis, I. E.; Paranychianakis, N. V.; Tsagarakis, K. P.; Angelakis, A. N., Treatment of Olive Mill Wastewater with Constructed Wetlands. *Water* **2012**, *4* (1), 260-271.
7. Liang, X.; Dijk, M. P. v., Optimal Level of Groundwater Charge to Promote Rainwater Usage for Irrigation in Rural Beijing. *Water* **2011**, *3* (4), 1077-1091.
8. Voudouris, K., Artificial Recharge via Boreholes Using Treated Wastewater: Possibilities and Prospects. *Water* **2011**, *3* (4), 964-975.
9. Kalavrouziotis, I. K.; Arambatzis, C.; Kalfountzos, D.; Varnavas, S. P., Wastewater Reuse Planning in Agriculture: The Case of Aitolokarnania, Western Greece. *Water*

2011, 3 (4), 988-1004.

10. Schacht, K.; Gönster, S.; Jüschke, E.; Chen, Y.; Tarchitzky, J.; Al-Bakri, J.; Al-Karablieh, E.; Marschner, B., Evaluation of Soil Sensitivity towards the Irrigation with Treated Wastewater in the Jordan River Region. *Water* **2011**, 3 (4), 1092-1111.

11. Apostolidis, N.; Hertle, C.; Young, R., Water Recycling in Australia. *Water* **2011**, 3 (3), 869-881.

12. Rodda, S. a., Global Hydrology and Water Resources. *Water Resources* **2003**.

13. Hepbasli, A.; Biyik, E.; Ekren, O.; Gunerhan, H.; Araz, M., A key review of wastewater source heat pump (WWSHP) systems. *Energy Conversion and Management* **2014**, 88, 700-722.

14. Repert, D. A.; Barber, L. B.; Hess, K. M.; Keefe, S. H.; Kent, D. B.; LeBlanc, D. R.; Smith, R. L., Long-Term Natural Attenuation of Carbon and Nitrogen within a Groundwater Plume after Removal of the Treated Wastewater Source. *Environmental Science & Technology* **2006**, 40 (4), 1154-1162.

15. Larsen*, T. A.; Alder, A. C.; Eggen, R. I. L.; Maurer, M.; Lienert, J., Source Separation: Will We See a Paradigm Shift in Wastewater Handling? *Environmental Science & Technology* **2009**, 43 (16), 6121-6125.

16. Murphy, F.; Ewins, C.; Carbonnier, F.; Quinn, B., Wastewater Treatment Works (WwTW) as a Source of Microplastics in the Aquatic Environment. *Environmental Science & Technology* **2016**, 50 (11), 5800-5808.

17. Culha, O.; Gunerhan, H.; Biyik, E.; Ekren, O.; Hepbasli, A., Heat exchanger applications in wastewater source heat pumps for buildings: A key review. *Energy and*

Buildings **2015**, *104*, 215-232.

18. Almeida, M. C.; Butler, D.; Friedler, E., At-source domestic wastewater quality.

Urban Water **1999**, *1* (1), 49-55.

19. Hartmann, A.; Alder, A. C.; Koller, T.; Widmer, R. M., Identification of fluoroquinolone antibiotics as the main source of umuC genotoxicity in native hospital wastewater. **1998**, *17* (3), 377-382.

20. Chao, S.; Yiqiang, J.; Yang, Y.; Shiming, D., Experimental performance evaluation of a novel dry-expansion evaporator with defouling function in a wastewater source heat pump. *Applied Energy* **2012**, *95*, 202-209.

21. Rodman, K. E.; Cervania, A. A.; Budig-Markin, V.; Schermesser, C. F.; Rogers, O. W.; Martinez, J. M.; King, J.; Hassett, P.; Burns, J.; Gonzales, M. S.; Folkerts, A.; Duin, P.; Virgil, A. S.; Aldrete, M.; Lagasca, A.; Infanzon-Marin, A.; Aitchison, J. R.; White, D.; Boutros, B. C.; Ortega, S.; Davis, B.; Tran, V. N.; Achilli, A., Coastal California Wastewater Effluent as a Resource for Seawater Desalination Brine Commingling. **2018**, *10* (3), 322.

22. Gatta, G.; Gagliardi, A.; Disciglio, G.; Lonigro, A.; Francavilla, M.; Tarantino, E.; Giuliani, M. M., Irrigation with Treated Municipal Wastewater on Artichoke Crop: Assessment of Soil and Yield Heavy Metal Content and Human Risk. **2018**, *10* (3), 255.

23. Schmid, S.; Bogner, F. X., What Germany's University Beginners Think about Water Reuse. **2018**, *10* (6), 731.

24. Colla, V.; Matino, I.; Branca, T. A.; Fornai, B.; Romaniello, L.; Rosito, F., Efficient Use of Water Resources in the Steel Industry. **2017**, *9* (11), 874.

25. Park, H.-G.; Kwon, Y.-N., Long-Term Stability of Low-Pressure Reverse Osmosis (RO) Membrane Operation—A Pilot Scale Study. **2018**, *10* (2), 93.
26. Hong, P.-Y.; Julian, T. R.; Pype, M.-L.; Jiang, S. C.; Nelson, K. L.; Graham, D.; Pruden, A.; Manaia, C. M., Reusing Treated Wastewater: Consideration of the Safety Aspects Associated with Antibiotic-Resistant Bacteria and Antibiotic Resistance Genes. **2018**, *10* (3), 244.
27. Manheim, D. C.; Jiang, S. C., Investigation of Algal Biotoxin Removal during SWRO Desalination through a Materials Flow Analysis. **2017**, *9* (10), 730.
28. Jumat, M. R.; Hasan, N. A.; Subramanian, P.; Heberling, C.; Colwell, R. R.; Hong, P.-Y., Membrane Bioreactor-Based Wastewater Treatment Plant in Saudi Arabia: Reduction of Viral Diversity, Load, and Infectious Capacity. **2017**, *9* (7), 534.
29. Kurihara, M.; Takeuchi, H., SWRO-PRO System in “Mega-ton Water System” for Energy Reduction and Low Environmental Impact. **2018**, *10* (1), 48.
30. Caldera, U.; Bogdanov, D.; Afanasyeva, S.; Breyer, C., Role of Seawater Desalination in the Management of an Integrated Water and 100% Renewable Energy Based Power Sector in Saudi Arabia. **2018**, *10* (1), 3.
31. Fletcher, T. D.; Deletic, A.; Mitchell, V. G.; Hatt, B. E., Reuse of Urban Runoff in Australia: A Review of Recent Advances and Remaining Challenges. **2008**, *37* (5_Supplement), S-116-S-127.
32. Gao, H.; Scherson, Y. D.; Wells, G. F., Towards energy neutral wastewater treatment: methodology and state of the art. *Environmental Science: Processes & Impacts* **2014**, *16* (6), 1223-1246.

33. Dinar, A.; Hogarth, M., Game Theory and Water Resources: Critical Review of its Contributions, Progress and Remaining Challenges. *Foundations and Trends® in Microeconomics* **2015**, *11* (1–2), 1-139.
34. Li, W.-W.; Yu, H.-Q., From wastewater to bioenergy and biochemicals via two-stage bioconversion processes: A future paradigm. *Biotechnology Advances* **2011**, *29* (6), 972-982.
35. Ali, M.; Okabe, S., Anammox-based technologies for nitrogen removal: Advances in process start-up and remaining issues. *Chemosphere* **2015**, *141*, 144-153.
36. Zhang, C.; Jiang, Y.; Li, Y.; Hu, Z.; Zhou, L.; Zhou, M., Three-dimensional electrochemical process for wastewater treatment: A general review. *Chemical Engineering Journal* **2013**, *228*, 455-467.
37. Huang, X.; Wang, R.; Jiao, T.; Zou, G.; Zhan, F.; Yin, J.; Zhang, L.; Zhou, J.; Peng, Q., Facile Preparation of Hierarchical AgNP-Loaded MXene/Fe₃O₄/Polymer Nanocomposites by Electrospinning with Enhanced Catalytic Performance for Wastewater Treatment. *ACS Omega* **2019**, *4* (1), 1897-1906.
38. Chandra, D.; Das, S. K.; Bhaumik, A., A fluorophore grafted 2D-hexagonal mesoporous organosilica: Excellent ion-exchanger for the removal of heavy metal ions from wastewater. *Microporous and Mesoporous Materials* **2010**, *128* (1), 34-40.
39. Dervin, S.; Dionysiou, D. D.; Pillai, S. C., 2D nanostructures for water purification: graphene and beyond. *Nanoscale* **2016**, *8* (33), 15115-15131.
40. Zhang, S.; Lian, G.; Si, H.; Wang, J.; Zhang, X.; Wang, Q.; Cui, D., Ultrathin BN nanosheets with zigzag edge: one-step chemical synthesis, applications in wastewater

treatment and preparation of highly thermal-conductive BN–polymer composites.

Journal of Materials Chemistry A **2013**, *1* (16), 5105-5112.

41. Li, R.; Zhang, L.; Shi, L.; Wang, P., MXene Ti₃C₂: An Effective 2D Light-to-Heat Conversion Material. *ACS Nano* **2017**, *11* (4), 3752-3759.

42. He, P.; Tang, X.; Chen, L.; Xie, P.; He, L.; Zhou, H.; Zhang, D.; Fan, T., Patterned Carbon Nitride–Based Hybrid Aerogel Membranes via 3D Printing for Broadband Solar Wastewater Remediation. **2018**, *28* (29), 1801121.

43. Kyzas, G. Z.; Deliyanni, E. A.; Matis, K. A., Graphene oxide and its application as an adsorbent for wastewater treatment. **2014**, *89* (2), 196-205.

44. Mousset, E.; Wang, Z.; Hammaker, J.; Lefebvre, O., Physico-chemical properties of pristine graphene and its performance as electrode material for electro-Fenton treatment of wastewater. *Electrochimica Acta* **2016**, *214*, 217-230.

45. Tatarova, E.; Bundaleska, N.; Sarrette, J. P.; Ferreira, C. M., Plasmas for environmental issues: from hydrogen production to 2D materials assembly. *Plasma Sources Science and Technology* **2014**, *23* (6), 063002.

46. Coleman, J. N.; Lotya, M.; O'Neill, A.; Bergin, S. D.; King, P. J.; Khan, U.; Young, K.; Gaucher, A.; De, S.; Smith, R. J.; Shvets, I. V.; Arora, S. K.; Stanton, G.; Kim, H.-Y.; Lee, K.; Kim, G. T.; Duesberg, G. S.; Hallam, T.; Boland, J. J.; Wang, J. J.; Donegan, J. F.; Grunlan, J. C.; Moriarty, G.; Shmeliov, A.; Nicholls, R. J.; Perkins, J. M.; Grievson, E. M.; Theuwissen, K.; McComb, D. W.; Nellist, P. D.; Nicolosi, V., Two-Dimensional Nanosheets Produced by Liquid Exfoliation of Layered Materials. **2011**, *331* (6017), 568-571.

47. Grayfer, E. D.; Kozlova, M. N.; Fedorov, V. E., Colloidal 2D nanosheets of MoS₂ and other transition metal dichalcogenides through liquid-phase exfoliation. *Advances in Colloid and Interface Science* **2017**, *245*, 40-61.
48. Osada, M.; Sasaki, T., Exfoliated oxide nanosheets: new solution to nanoelectronics. *Journal of Materials Chemistry* **2009**, *19* (17), 2503-2511.
49. Kim, I. Y.; Jo, Y. K.; Lee, J. M.; Wang, L.; Hwang, S.-J., Unique Advantages of Exfoliated 2D Nanosheets for Tailoring the Functionalities of Nanocomposites. *The Journal of Physical Chemistry Letters* **2014**, *5* (23), 4149-4161.
50. Lin, Q.; Li, L.; Liang, S.; Liu, M.; Bi, J.; Wu, L., Efficient synthesis of monolayer carbon nitride 2D nanosheet with tunable concentration and enhanced visible-light photocatalytic activities. *Applied Catalysis B: Environmental* **2015**, *163*, 135-142.
51. Fukuda, K.; Akatsuka, K.; Ebina, Y.; Ma, R.; Takada, K.; Nakai, I.; Sasaki, T., Exfoliated Nanosheet Crystallite of Cesium Tungstate with 2D Pyrochlore Structure: Synthesis, Characterization, and Photochromic Properties. *ACS Nano* **2008**, *2* (8), 1689-1695.
52. Nicolosi, V.; Chhowalla, M.; Kanatzidis, M. G.; Strano, M. S.; Coleman, J. N., Liquid Exfoliation of Layered Materials. **2013**, *340* (6139), 1226419.
53. Druce, J.; Téllez, H.; Burriel, M.; Sharp, M. D.; Fawcett, L. J.; Cook, S. N.; McPhail, D. S.; Ishihara, T.; Brongersma, H. H.; Kilner, J. A., Surface termination and subsurface restructuring of perovskite-based solid oxide electrode materials. *Energy & Environmental Science* **2014**, *7* (11), 3593-3599.
54. Pietsch, G. J.; Higashi, G. S.; Chabal, Y. J., Chemomechanical polishing of silicon:

- Surface termination and mechanism of removal. **1994**, *64* (23), 3115-3117.
55. Chambers, S. A.; Joyce, S. A., Surface termination, composition and reconstruction of Fe₃O₄(001) and γ -Fe₂O₃(001). *Surface Science* **1999**, *420* (2), 111-122.
56. Sun, S.; Sun, Y.; Liu, Z.; Lee, D.-I.; Peterson, S.; Pianetta, P., Surface termination and roughness of Ge(100) cleaned by HF and HCl solutions. **2006**, *88* (2), 021903.
57. Tryk, D. A.; Tsunozaki, K.; Rao, T. N.; Fujishima, A., Relationships between surface character and electrochemical processes on diamond electrodes: dual roles of surface termination and near-surface hydrogen. *Diamond and Related Materials* **2001**, *10* (9), 1804-1809.
58. Yagi, I.; Tsukagoshi, K.; Aoyagi, Y., Modification of the electric conduction at the pentacene / SiO₂ interface by surface termination of SiO₂. **2005**, *86* (10), 103502.
59. Song, H. S.; Kwon, O. S.; Kim, J.-H.; Conde, J.; Artzi, N., 3D hydrogel scaffold doped with 2D graphene materials for biosensors and bioelectronics. *Biosensors and Bioelectronics* **2017**, *89*, 187-200.
60. Xu, Y.; Lin, Z.; Huang, X.; Liu, Y.; Huang, Y.; Duan, X., Flexible Solid-State Supercapacitors Based on Three-Dimensional Graphene Hydrogel Films. *ACS Nano* **2013**, *7* (5), 4042-4049.
61. Xu, Y.; Lin, Z.; Huang, X.; Wang, Y.; Huang, Y.; Duan, X., Functionalized Graphene Hydrogel-Based High-Performance Supercapacitors. **2013**, *25* (40), 5779-5784.
62. Lutolf, M. P.; Gilbert, P. M.; Blau, H. M., Designing materials to direct stem-cell fate. *Nature* **2009**, *462* (7272), 433-441.

63. Han, D.; Yan, L., Supramolecular Hydrogel of Chitosan in the Presence of Graphene Oxide Nanosheets as 2D Cross-Linkers. *ACS Sustainable Chemistry & Engineering* **2014**, *2* (2), 296-300.
64. Benoit, D. S. W.; Schwartz, M. P.; Durney, A. R.; Anseth, K. S., Small functional groups for controlled differentiation of hydrogel-encapsulated human mesenchymal stem cells. *Nature Materials* **2008**, *7* (10), 816-823.
65. Servant, A.; Leon, V.; Jasim, D.; Methven, L.; Limousin, P.; Fernandez-Pacheco, E. V.; Prato, M.; Kostarelos, K., Graphene-Based Electroresponsive Scaffolds as Polymeric Implants for On-Demand Drug Delivery. **2014**, *3* (8), 1334-1343.
66. Guo, W.; Cheng, C.; Wu, Y.; Jiang, Y.; Gao, J.; Li, D.; Jiang, L., Bio-Inspired Two-Dimensional Nanofluidic Generators Based on a Layered Graphene Hydrogel Membrane. **2013**, *25* (42), 6064-6068.
67. Ke, Q.; Wang, J., Graphene-based materials for supercapacitor electrodes – A review. *Journal of Materiomics* **2016**, *2* (1), 37-54.
68. Liu, G.; Jin, W.; Xu, N., Two-Dimensional-Material Membranes: A New Family of High-Performance Separation Membranes. **2016**, *55* (43), 13384-13397.
69. Ji, J.; Kang, Q.; Zhou, Y.; Feng, Y.; Chen, X.; Yuan, J.; Guo, W.; Wei, Y.; Jiang, L., Osmotic Power Generation with Positively and Negatively Charged 2D Nanofluidic Membrane Pairs. **2017**, *27* (2), 1603623.
70. Dong, Y.; Wu, Z.-S.; Ren, W.; Cheng, H.-M.; Bao, X., Graphene: a promising 2D material for electrochemical energy storage. *Science Bulletin* **2017**, *62* (10), 724-740.
71. Fathizadeh, M.; Xu, W. L.; Zhou, F.; Yoon, Y.; Yu, M., Graphene Oxide: A Novel

2-Dimensional Material in Membrane Separation for Water Purification. **2017**, *4* (5), 1600918.

72. Wang, Z.; Mi, B., Environmental Applications of 2D Molybdenum Disulfide (MoS₂) Nanosheets. *Environmental Science & Technology* **2017**, *51* (15), 8229-8244.

73. Kim, W.-g.; Nair, S., Membranes from nanoporous 1D and 2D materials: A review of opportunities, developments, and challenges. *Chemical Engineering Science* **2013**, *104*, 908-924.

74. Shao, J.; Xie, H.; Wang, H.; Zhou, W.; Luo, Q.; Yu, X.-F.; Chu, P. K., 2D Material-Based Nanofibrous Membrane for Photothermal Cancer Therapy. *ACS Applied Materials & Interfaces* **2018**, *10* (1), 1155-1163.

75. Zhu, X.; Tian, C.; Do-Thanh, C.-L.; Dai, S., Two-Dimensional Materials as Prospective Scaffolds for Mixed-Matrix Membrane-Based CO₂ Separation. **2017**, *10* (17), 3304-3316.

76. Liu, G.; Jin, W.; Xu, N., Graphene-based membranes. *Chemical Society Reviews* **2015**, *44* (15), 5016-5030.

77. Zhao, Y.; Xie, Y.; Liu, Z.; Wang, X.; Chai, Y.; Yan, F., Two-Dimensional Material Membranes: An Emerging Platform for Controllable Mass Transport Applications. **2014**, *10* (22), 4521-4542.

Chapter 2 Experimental techniques

In this chapter, the experiment techniques used in this research will be presented briefly. The techniques include scanning electronic microscopy (SEM), atomic force microscopy (AFM), transmission electron microscopy (TEM), X-ray diffraction (XRD), ultraviolet-visible (UV-vis) spectroscopy, X-ray photoelectron spectroscopy (XPS), zeta potential and size measurement, contact angle measurement, inductively coupled plasma mass spectrometry (ICP-MS), forward osmosis (FO), vacuum filtration, hydrothermal synthesis, surface forces apparatus (SFA), centrifugation, ultrasonication and spin coating.

2.1 Scanning electron microscopy (SEM)

The scanning electron microscopy (SEM) is a typical technique for characterizing synthesized materials. The core components of SEM are electron source – electron beam generator; Anode and condenser lenses – beam energy adaptor; objective lens – beam alignment; detector and sample stage as shown in Figure 2.1.¹ The electron source owns an acceleration voltage range of 1 – 30 kV as indicated in the user manual of the field emission scanning electron microscope (FESEM, Zeiss, low vacuum 10⁻⁵ Pa) used in this thesis. Both secondary electron (SE) detector and back scattered electron (BSE) detector were used in this thesis for receiving the signals for displaying the morphology of the synthesized material including shape and thickness.^{2, 3} The energy-dispersive X-ray spectroscopy (EDX) spot spectrum (X-ray generated by electron transitions within atoms in the sample) generated by FESEM enables quantitative

analysis of material composition of the sample by counting the number of X-rays reaching the detector with different energies.^{2, 4} The FESEM provides direct observation and analysis for the structure, surface morphology and components of the synthesized 2D based functionalized materials, which is one of the most frequently used technique in this thesis.

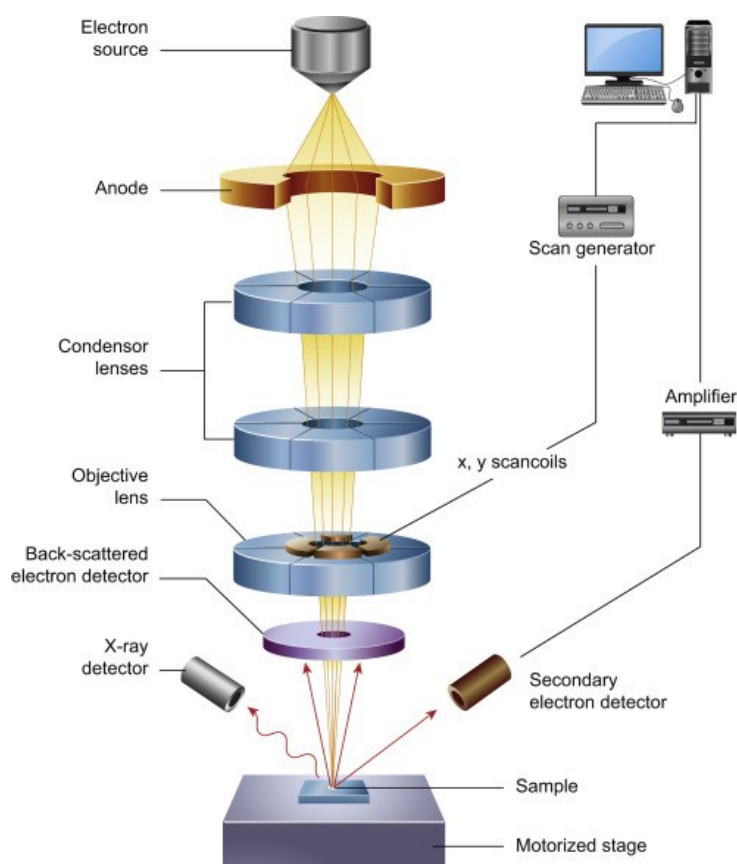


Figure 2.1. Typical core components of a scanning electron microscope (SEM) configuration.¹ Figure is addapeted from reference with Elsevier permission liscence (No. 4660410235374).

2.2 Atomic force microscope (AFM)

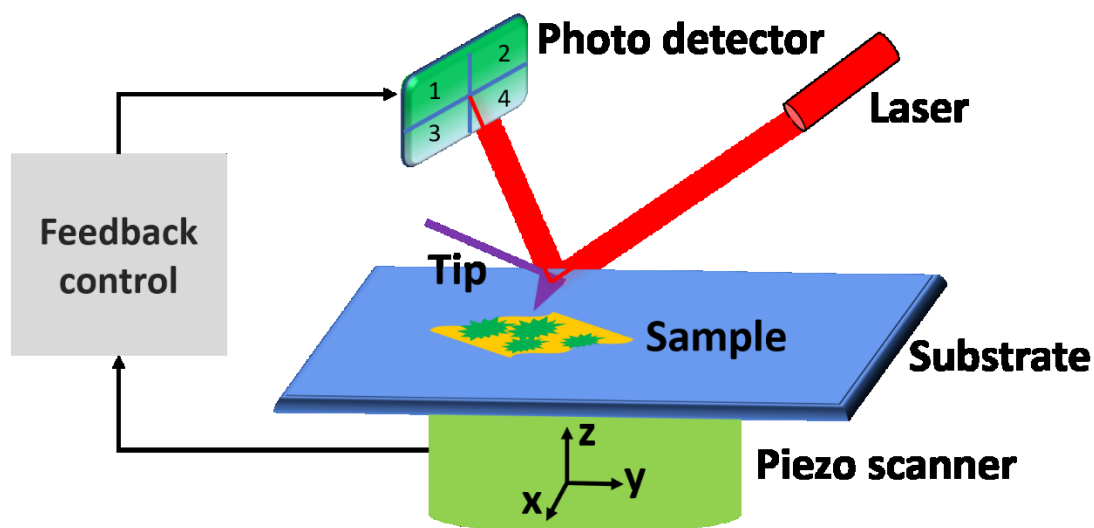


Figure 2.2. Typical core components of an atomic force microscope (AFM).

The atomic force microscope (AFM) is another powerful technique that could characterize the surface morphology and hydrophilicity, thickness and size of the synthesized 2D based functionalized materials. The core components of an AFM are illustrated in **Figure 2.2**, which contains a photo detector, a laser, a tip, a sample, a substrate, a piezo scanner and an internal feedback control. The principle of AFM is recording the precise movements of the tip from the oscillation signal created by a piezo transducer.^{5,6} The tip interacts directly with the prepared sample and the motion of the tip is measured with the assistance of a laser beam and quadrant displacement sensor (feedback control).^{7,8} In general, the AFM contains two functions: imaging and force measurement, both of which are measuring the signal changes from the piezo scanner between the tip and the sample surface under feedback control. The surface morphology, thickness and size of the synthesized 2D based functionalized nanosheets could be characterized by using the imaging function of AFM.^{9,10} The resulted height profile

would provide direct evidence for the thickness and size of the materials. In order to get high resolution height profile, the sample surface should be as flat as possible.

In terms of surface hydrophilicity of the synthesized 2D based functionalized nanosheets, the force measurement function of the AFM was used. In this thesis, the tip was modified with hydroxyl or carboxyl functional groups interacting with prepared sample surface under multiple conditions (e.g. concentration, pH, etc.). The force measurement function of AFM provides more detailed evidences to support the proposed mechanism behind the macroscopic experimental data.

2.3 Transmission electron microscopy (TEM)

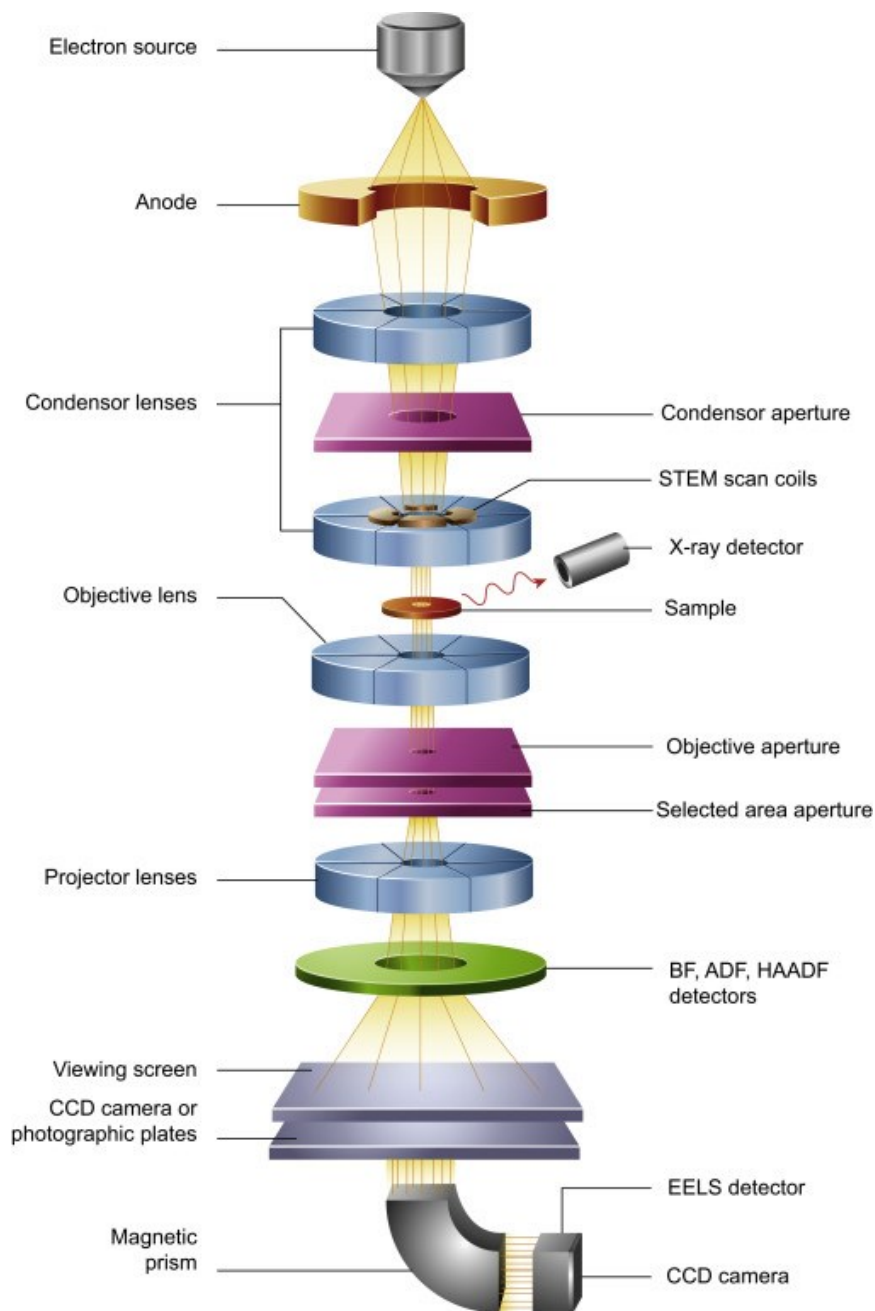


Figure 2.3. Typical core components of a transmission electron microscope (TEM) configuration.¹ Figure is adapted from reference with Elsevier permission license (No. 4660440530381).

The transmission electron microscopy (TEM) is a typical technique for characterizing the crystal structure of synthesized materials in terms of physical and

chemical sciences.^{11, 12} The core components of a TEM are shown in **Figure 2.3**. In general, the TEM consists of an electron source, condenser lenses, objective lens, projective lenses, a viewing screen, and a detector.^{11, 13, 14} A beam generated from the electron source would transmit through all the above-mentioned components and the prepared sample to generate an image.^{12, 13} The detection limit of TEM was less than 100 nm for the as prepared sample thickness. The TEM is able to image at a significantly higher resolution at a molecular level than light microscopes in terms of crystal structure and amorphous structure.^{12, 15}

2.4 X-ray diffraction (XRD)

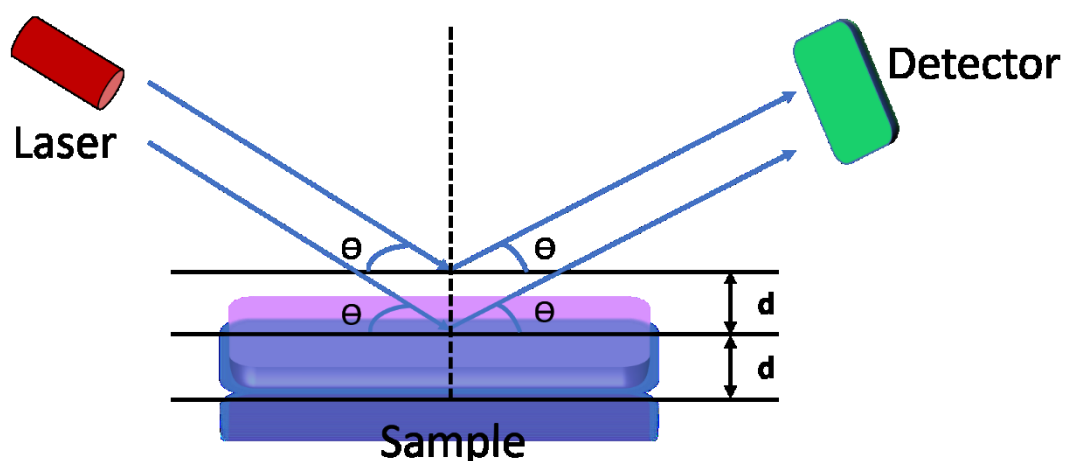


Figure 2.4. The simplified schematic illustration of a generic X-ray diffraction measurement.¹⁶

The X-ray diffraction (XRD) was employed for analyzing the crystal structure of the synthesized 2D materials at atomic or molecular level.^{16, 17} In this study, a Rigaku XRD with Cu X-rays on the order of 0.154 nm was used to produce a diffraction pattern, which works best for crystalline materials and may be able to investigate non-

crystalline materials.¹⁸ The information from the X-ray scattering pattern provides the internal structure with a length scale range from 0.1 to 100 nm.¹⁷ The scattering intensity for the X-ray beams directly towards the sample was measured as a function of outgoing direction. The well-known Bragg's Law could describe the constructive interference as shown below:^{18, 19}

$$n \lambda = 2 d \sin \theta \quad 2.1$$

λ : The wavelength of the X-ray beam, in this study, the value is 0.154 nm

d: Separated distance

θ : Half of the scattering angle

2.5 Ultraviolet-visible (UV-Vis) spectroscopy

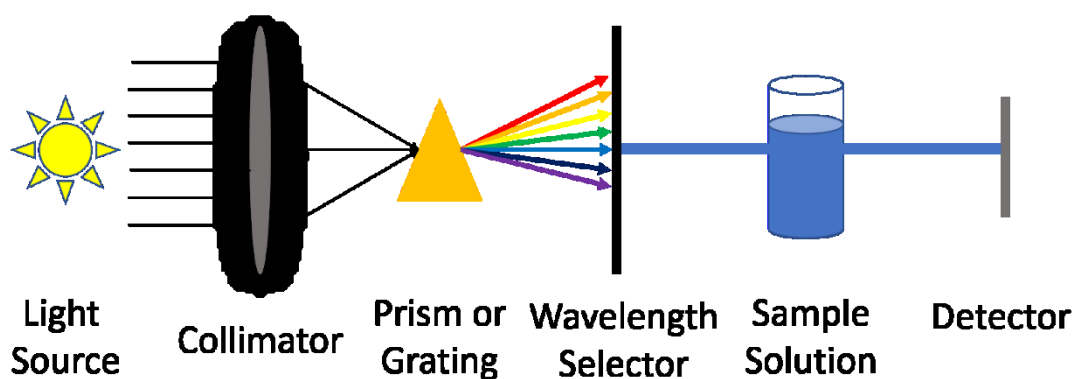


Figure 2.5. Typical core components of ultraviolet-visible (UV-Vis) spectroscopy.²⁰

In this thesis, some dye separation experiments by using 2D based functionalized materials for wastewater treatment were conducted. An Evolution 300 UV-Vis spectrophotometer (Thermo Fisher Scientific) was used to characterize the absorption peaks from target dyes (e.g., methylene blue; rhodamine 6g; basic blue, etc.) In order to estimate the separation performance of the 2D based functionalized materials,

concentration difference of the target dyes before and after separation should be characterized. In general, the UV-Vis spectroscopy reflects the absorption capability in a long range of lights from the target pollutants whose electrons transit from the ground state to the excited state.^{21,22} Typically, the absorption intensity versus the concentration gradient has a linear relationship named as concentration gradient standard line. The concentration difference could then be measured based on the concentration gradient standard line. The concentration of contaminants (dyes) in wastewater were examined by UV-Vis analysis.

2.6 Fourier-transform infrared (FTIR) spectroscopy

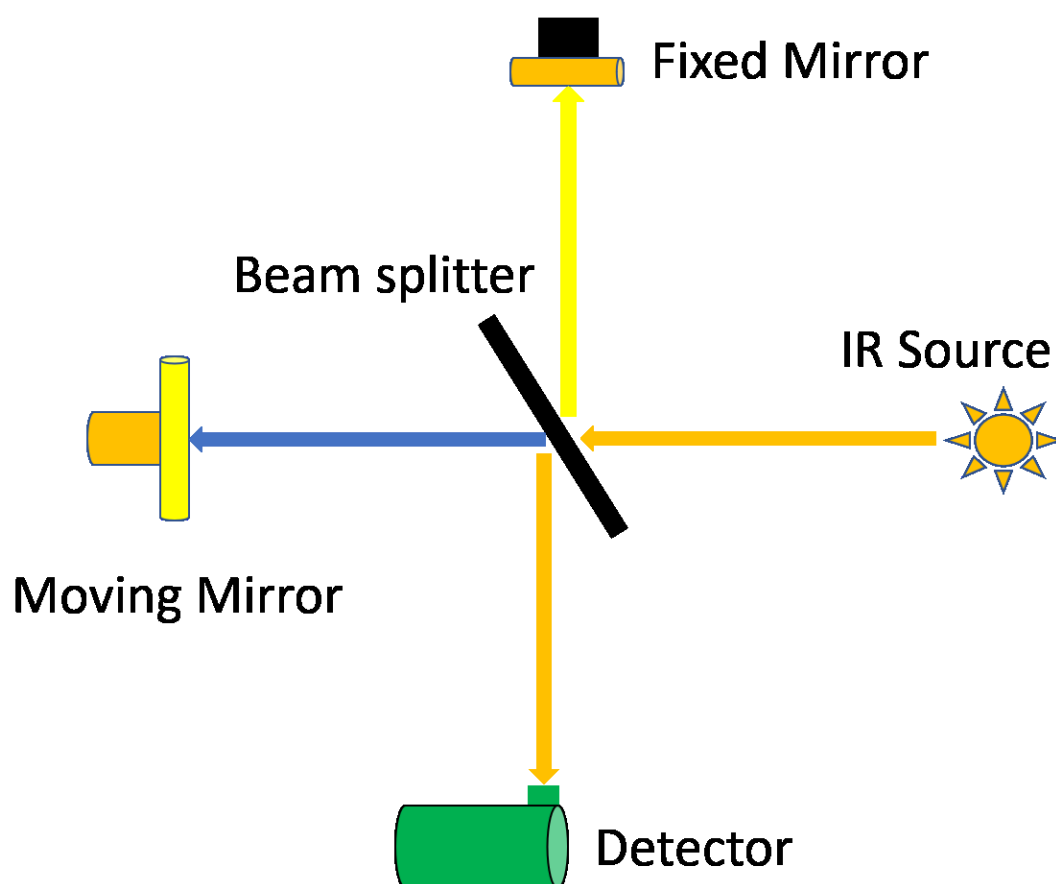


Figure 2.6. Typical core components of Fourier-transform infrared (FTIR) spectroscopy.²³

The FTIR spectrometer was used to identify the functional groups for the synthesized materials. The existence of specific functional groups in solid, liquid or gas samples could have a wide range of spectral emissions at a time.^{24, 25} The FTIR spectrometer was used to obtain the infrared spectrum of the absorption for the signal simultaneously wavelength range from 10 cm^{-1} to 12800 cm^{-1} .²³ The Thermo Nicolet 8700 FTIR Spectrometer was used in this thesis and the core components are shown in **Figure 2.6**.

2.7 X-ray photoelectron spectroscopy (XPS)

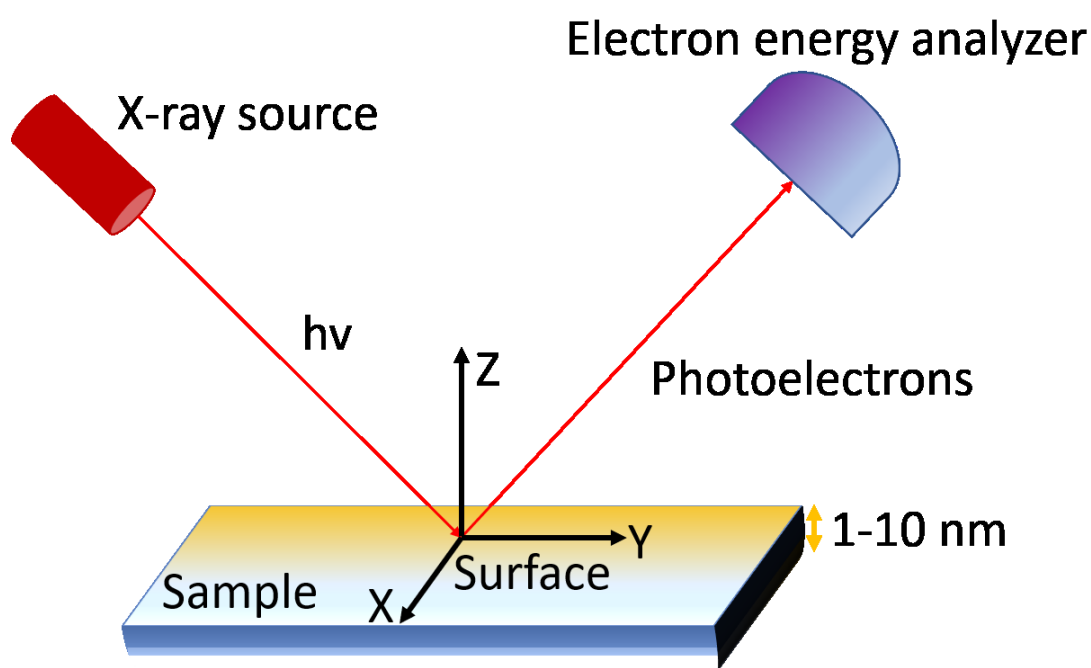


Figure 2.7. Typical core components of X-ray photoelectron spectroscopy (XPS).²⁶

The elemental composition for the synthesized materials could be characterized by XPS. The core components of XPS are X-ray source, electron analyzer and sample as shown in **Figure 2.7**. The X-ray beam at a given energy is used to irradiate a sample at the surface depth around 10 nm .^{27, 28} The irradiated surface would emit

photoelectrons to the electron energy analyzer. The electron energy analyzer analyzes the binding energy for different sample component irradiated by X-ray source.²⁶ The binding energy could be analyzed theoretically by equation:^{29, 30}

$$E_{\text{binding}} = E_{\text{photon}} - (E_{\text{kinetic}} + E_{\phi}) \quad 2.2$$

E_{photon} : The X-ray photon energy

E_{kinetic} : The photoelectrons kinetic energy

E_{ϕ} : The solid effects correction

The binding energy difference represents the unique format for each component of the synthesized 2D based functional materials, which helps analyzing the structure. A Kratos Axis Ultra spectrometer was used in this thesis.

2.8 Zeta potential and size measurement

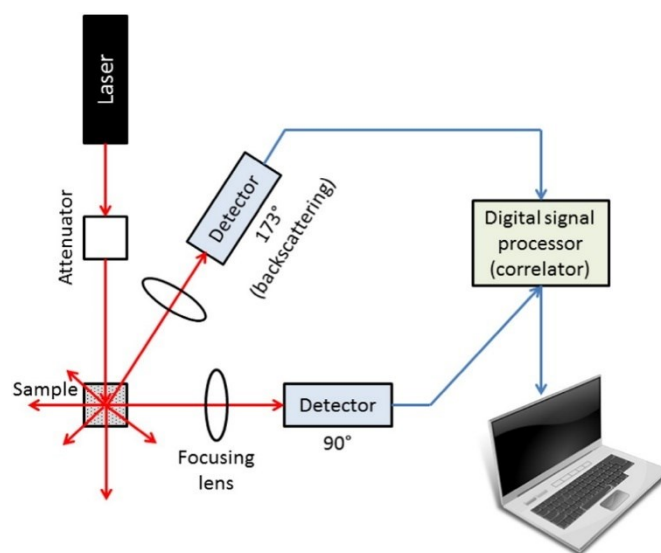


Figure 2.8. Typical core components for the instrumentation of dynamic light scattering (DLS).³¹ Figure is adapted from reference with ScienceDirect permission license (No. 4661451205919).

Zeta potential is the potential difference between a particle surface and the bulk fluid. A charged particle in an aqueous solution would be surrounded by a decreasing concentration gradient of opposite charged ions.^{31, 32} The concentrated ions near the particle surface is called surface charge including stern layer and slipping plane with the decrease of charged ions concentration. The zeta potential value indicates the electrostatic interaction behavior between a particle surface and the bulk fluid and the stability among colloidal particles under aqueous solution environment. The Malvern Nanosizer Nano ZSP has been used in this thesis and the core components are illustrated in **Figure 2.8**.^{31, 33} In addition, the Malvern Nanosizer Nano ZSP equipment could measure the size of the colloidal particles through dynamic light scattering (DLS) characterization.

2.9 Contact angle measurement

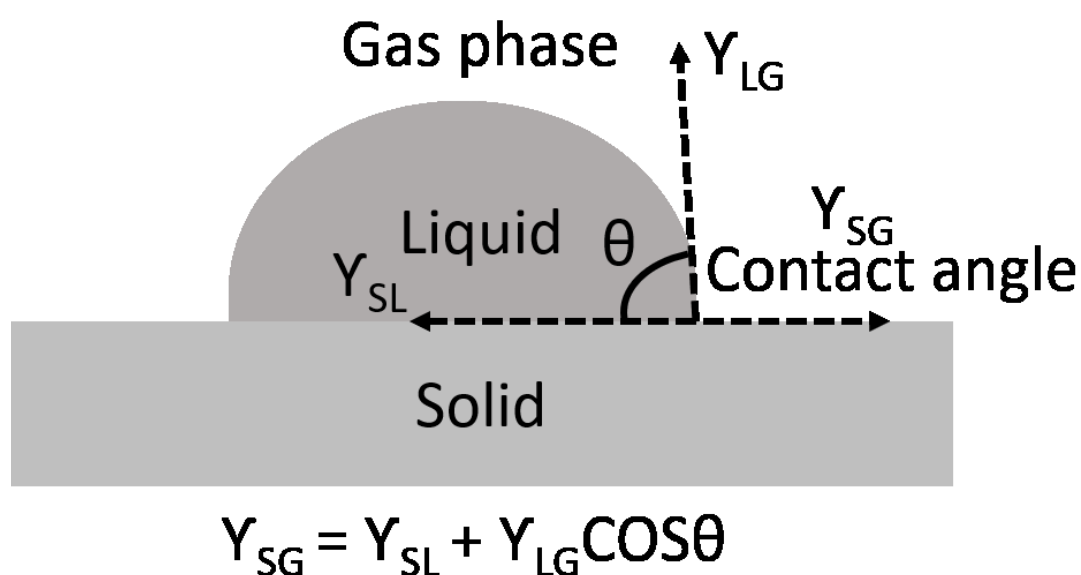


Figure 2.9. Schematic diagram of contact angle.^{34, 35}

In terms of wastewater treatment, hydrophobicity or hydrophilicity of the synthesized surface is of great significance. Contact angle could provide direct measurement of surface wettability of the synthesized functional 2D based materials wherever the intensity of the contact between liquid and solid substrates could be checked.^{35, 36} Either water-in-air (W/A) or oil-in-water (O/W) contact angles on different sample surfaces are measured through the image of a sessile drop on solid surface at the points of intersection (three-phase contact points).^{34, 36} The Young's equation could describe the relationship among the three phases:³⁵

$$Y_{SG} = Y_{SL} + Y_{LG}\cos\theta \quad 2.3$$

Contact angle: θ

Liquid surface tension in air: Y_{LG}

Interfacial tension between material surface and liquid: Y_{SL}

Surface tension of the solid: Y_{SG}

2.10 Inductively coupled plasma mass spectrometry (ICP-MS)

Inductively coupled plasma mass spectrometry (ICP-MS) was used to analyze the metals such as K^+ , Na^+ , Li^+ , Ca^{2+} , Mg^{2+} and several non-metals ions in aqueous samples. The ICP-MS has a greater speed, accuracy, and sensitivity as compared to other mass spectrometry (e.g., thermal ionization mass spectrometry (TIMS), etc.) with the existence of energized plasma by inductively heated gas.³⁷

2.11 Forward osmosis (FO)

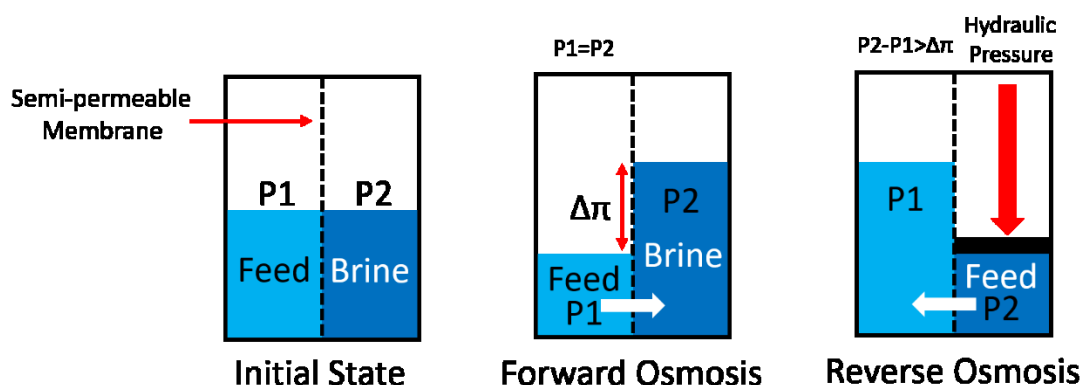


Figure 2.10. Schematic diagram of membrane process including forward osmosis and reverse osmosis process.^{38, 39}

Forward osmosis (FO) and reverse osmosis (RO) have been investigated and widely applied on sea water desalination over the past decade. In general, FO is a separation or diffusion process in between feed side and high concentration draw side, while an additional hydraulic pressure is added for RO process. The most significant aspect for both processes is the semi-permeable membrane design in order to achieve energy efficient and effective separation.⁴⁰ The consideration for semi-permeable membrane design includes structure parameters of the membrane, solute flux selectivity, permeability-selectivity tradeoff and fouling reversibility. The membrane fouling issue is reversible for FO process, however irreversible for RO process, though RO process has better performance in water permeation.^{41, 42} In this thesis, the membrane properties, fouling reversibility, water flux, solute rejection and fundamental analysis for FO process were investigated. An ideal FO membrane contains three significant aspects: high water flux, complete rejection rate towards solutes and robust mechanical property. Those aspects are critical for the support and active layer of the membrane. Therefore,

the design goals for this thesis were (1) to minimize the influence of the support layer and increase water flux and (2) maximize the selectivity between solute and water of the active layer to reduce loss of the draw solution through surface termination methodology.

2.12 Vacuum filtration

The vacuum filtration device consists of a disposable filter funnel and a disposable filtrate receptacle. Both funnel and receptacle are connected to a vacuum source through a connecting passage to the vacuum pump.⁴³ In this thesis, the vacuum filtration method was used to synthesize the functionalized membrane as well as conduct the separational performance for the synthesized membrane (e.g., waste dye separation).

2.13 Hydrothermal synthesis

Hydrothermal synthesis is defined to be a method for synthesizing materials in hot water under high pressure.^{44, 45} The hydrothermal process could create crystalline phases and the materials can be grown at high temperature and pressure.⁴⁶ It is accessible for mass production of good-quality materials through hydrothermal process, though the size is not controllable and impossible to observe the growth for the materials inside the autoclave.⁴⁷ In this study, hydrothermal process was used to synthesize the GO hydrogel as mentioned in Chapter 3.

2.14 Surface force apparatus (SFA)

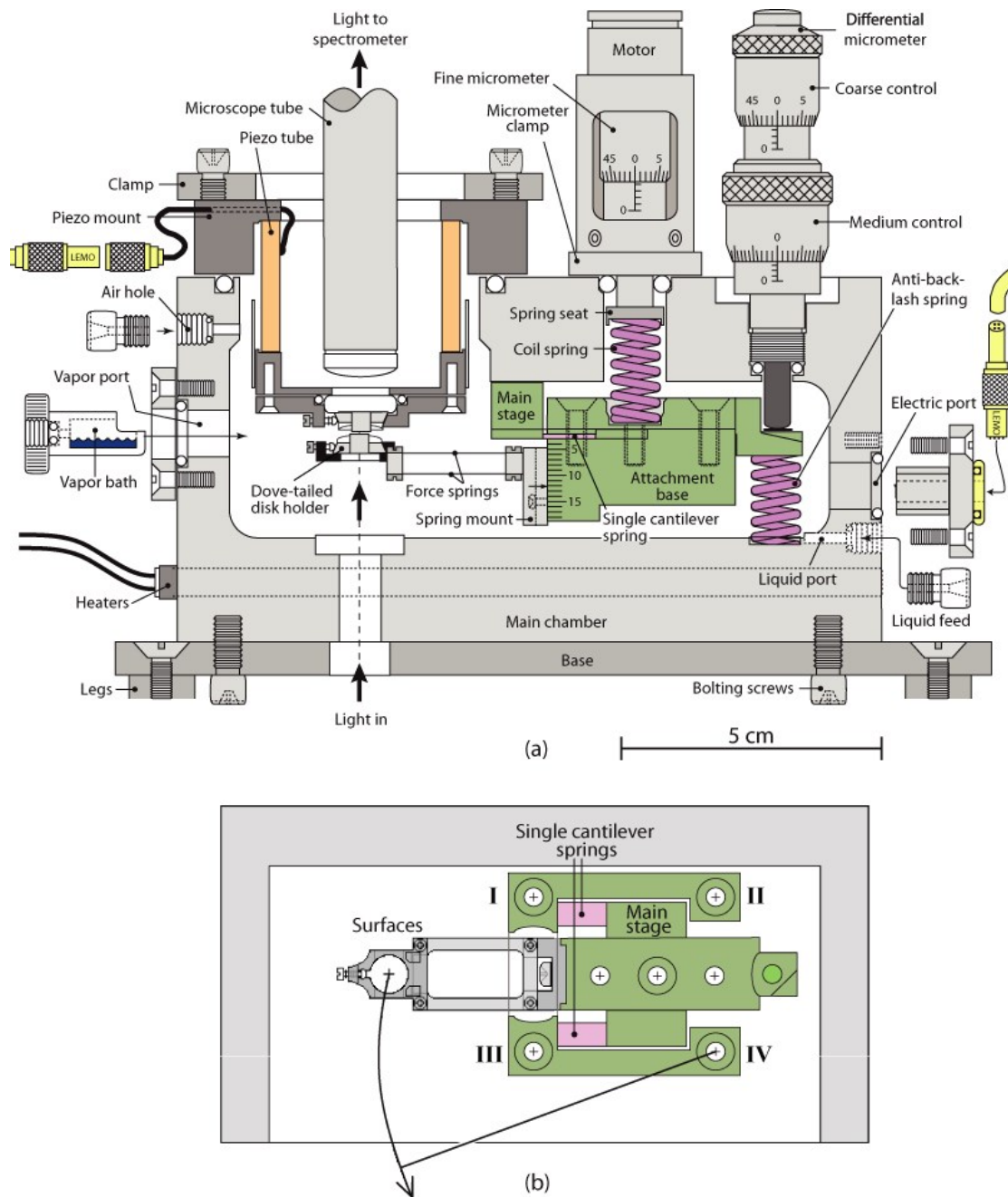


Figure 2.11. (a) Cross section view of the SFA 2000 main body through the center of the apparatus, (b) top view of the main stage and the bottom disk holder.⁴⁸ Figure is adapted from reference with IOP Science permission liscence (No. 4661720952113).

The surface force apparatus (SFA) is used to measure the interaction forces

between two confined surfaces as they are brought together and retracted under motor control.^{49, 50} The surface is held by a spring with known constant, and the deflection of the spring is used to calculate the interaction force. The calculation is based primarily on Hooke's law, $F = kx$, where F is the force being exerted, k is the spring constant and x is the displacement of the spring.⁵¹

The force between two contact surfaces is calculated by using^{52, 53}

$$\Delta F(x) = k(\Delta x_{\text{applied}} - \Delta x_{\text{measured}}) \quad 2.4$$

$\Delta x_{\text{applied}}$ is the change by the micrometer that could be read on the set up and

$\Delta x_{\text{measured}}$ is the displacement by interferometry.

In 1960s at Cambridge University, SFA was developed by D. Tabor, R.H.S. Winterton.^{51, 52} By the mid-1970s, J.N. Israelachvili first introduced this design to aqueous environment, while at the Australian National University and later at University of California Santa Barbara, the technique was further advanced for friction and electro-chemical surface studies.^{52, 53}

In this study, SFA was used to measure the surface forces between functionalized 2D nanosheets and interaction behavior under multiple concentrations of salt solution.

2.15 Centrifugation

The centrifugation is used for the separation of particles from a solution according to the mass or density differences between the medium and the particles under multiple motor speeds.⁵⁴⁻⁵⁶ In this thesis, water was used as the only solvent for both washing and separation processes. The washing step includes the removal of acid and other

solute from the synthesized 2D material suspension. The centrifugation separation process was to find different sizes of the synthesized 2D nanosheets according to their gravity.

2.16 Ultrasonication

The ultrasonication process is a well-established mechanical technology for disintegration of solutes.^{57, 58} The ultrasound waves could initiate powerful hydromechanical shear forces and some reactive radicals (H and OH).^{59, 60} The mechanical shear forces as well as the reactive radicals would contribute to the overcome Van der Waals forces among the stacked 2D nanosheets synthesized in this work resulting a well dispersed suspension.^{61, 62}

2.17 Spin coating

Spin coating is used to deposit uniform thin films onto flat substrates with continued angular speed of spinning.^{63, 64} The thickness of the film is controlled by the deposition time and solution concentration.^{65, 66} Some characterizations are strictly required flatter surface, such as AFM, SFA, etc. In this work, spin coating was used to fabricate the uniform 2D nanosheets film with disired roughness as prepared for characterizations.

2.18 References

1. Inkson, B. J., 2 - Scanning electron microscopy (SEM) and transmission electron microscopy (TEM) for materials characterization. In *Materials Characterization Using Nondestructive Evaluation (NDE) Methods*, Hübschen, G.; Altpeter, I.; Tschuncky, R.; Herrmann, H.-G., Eds. Woodhead Publishing: 2016; pp 17-43.
2. Denk, W.; Horstmann, H., Serial Block-Face Scanning Electron Microscopy to Reconstruct Three-Dimensional Tissue Nanostructure. *PLOS Biology* **2004**, 2 (11), e329.
3. Venables, J. A.; Harland, C. J., Electron back-scattering patterns—A new technique for obtaining crystallographic information in the scanning electron microscope. *The Philosophical Magazine: A Journal of Theoretical Experimental and Applied Physics* **1973**, 27 (5), 1193-1200.
4. Nation, J. L., A New Method Using Hexamethyldisilazane for Preparation of Soft Insect Tissues for Scanning Electron Microscopy. *Stain Technology* **1983**, 58 (6), 347-351.
5. Cleveland, J. P.; Anczykowski, B.; Schmid, A. E.; Elings, V. B., Energy dissipation in tapping-mode atomic force microscopy. *Applied Physics Letters* **1998**, 72 (20), 2613-2615.
6. Fang, H. H. P.; Chan, K.-Y.; Xu, L.-C., Quantification of bacterial adhesion forces using atomic force microscopy (AFM). *Journal of Microbiological Methods* **2000**, 40 (1), 89-97.
7. Meyer, G.; Amer, N. M., Novel optical approach to atomic force microscopy.

Applied Physics Letters **1988**, 53 (12), 1045-1047.

8. Lou, S.-T.; Ouyang, Z.-Q.; Zhang, Y.; Li, X.-J.; Hu, J.; Li, M.-Q.; Yang, F.-J., Nanobubbles on solid surface imaged by atomic force microscopy. *Journal of Vacuum Science & Technology B: Microelectronics and Nanometer Structures Processing, Measurement, and Phenomena* **2000**, 18 (5), 2573-2575.

9. Zhong, Q.; Inniss, D.; Kjoller, K.; Elings, V. B., Fractured polymer/silica fiber surface studied by tapping mode atomic force microscopy. *Surface Science Letters* **1993**, 290 (1), L688-L692.

10. Stipp, S. L. S.; Eggleston, C. M.; Nielsen, B. S., Calcite surface structure observed at microtopographic and molecular scales with atomic force microscopy (AFM). *Geochimica et Cosmochimica Acta* **1994**, 58 (14), 3023-3033.

11. Brooke, B. D.; Kloke, G.; Hunt, R. H.; Koekemoer, L. L.; Tem, E. A.; Taylor, M. E.; Small, G.; Hemingway, J.; Coetzee, M., Bioassay and biochemical analyses of insecticide resistance in southern African *Anopheles funestus* (Diptera: Culicidae). *Bulletin of Entomological Research* **2007**, 91 (4), 265-272.

12. Sun, K.-t.; Lin, Y.-c.; Yu, C.-j., A study on learning effect among different learning styles in a Web-based lab of science for elementary school students. *Computers & Education* **2008**, 50 (4), 1411-1422.

13. Torpo, L.; Marlo, M.; Staab, T. E. M.; Nieminen, R. M., Comprehensiveab initiostudy of properties of monovacancies and antisites in 4H-SiC. *Journal of Physics: Condensed Matter* **2001**, 13 (28), 6203-6231.

14. Verhagen, T. E. M.; Hendriks, D. J.; Bancsi, L. F. J. M. M.; Mol, B. W. J.;

- Broekmans, F. J. M., The accuracy of multivariate models predicting ovarian reserve and pregnancy after in vitro fertilization: a meta-analysis. *Human Reproduction Update* **2008**, *14* (2), 95-100.
15. Steenweg, M. E.; Ghezzi, D.; Haack, T.; Abbink, T. E. M.; Martinelli, D.; van Berkel, C. G. M.; Bley, A.; Diogo, L.; Grillo, E.; Te Water Naudé, J.; Strom, T. M.; Bertini, E.; Prokisch, H.; van der Knaap, M. S.; Zeviani, M., Leukoencephalopathy with thalamus and brainstem involvement and high lactate 'LTBL' caused by EARS2 mutations. *Brain* **2012**, *135* (5), 1387-1394.
16. Hatchard, T. D.; Dahn, J. R., In Situ XRD and Electrochemical Study of the Reaction of Lithium with Amorphous Silicon. *Journal of The Electrochemical Society* **2004**, *151* (6), A838-A842.
17. Drits, V.; Środoń, J.; Eberl, D. D., XRD Measurement of Mean Crystallite Thickness of Illite and Illite/Smectite: Reappraisal of the Kubler Index and the Scherrer Equation. *Clays and Clay Minerals* **1997**, *45* (3), 461-475.
18. Kontoyannis, C. G.; Vagenas, N. V., Calcium carbonate phase analysis using XRD and FT-Raman spectroscopy. *Analyst* **2000**, *125* (2), 251-255.
19. Borchert, H.; Shevchenko, E. V.; Robert, A.; Mekis, I.; Kornowski, A.; Grübel, G.; Weller, H., Determination of Nanocrystal Sizes: A Comparison of TEM, SAXS, and XRD Studies of Highly Monodisperse CoPt₃ Particles. *Langmuir* **2005**, *21* (5), 1931-1936.
20. Haiss, W.; Thanh, N. T. K.; Aveyard, J.; Fernig, D. G., Determination of Size and Concentration of Gold Nanoparticles from UV-Vis Spectra. *Analytical Chemistry* **2007**,

79 (11), 4215-4221.

21. Lichtenthaler, H. K.; Buschmann, C., Chlorophylls and Carotenoids: Measurement and Characterization by UV-VIS Spectroscopy. *Current Protocols in Food Analytical Chemistry* **2001**, *1* (1), F4.3.1-F4.3.8.

22. Meier, H.; Stalmach, U.; Kolshorn, H., Effective conjugation length and UV/vis spectra of oligomers. *Acta Polymerica* **1997**, *48* (9), 379-384.

23. REHMAN, I.; BONFIELD, W., Characterization of hydroxyapatite and carbonated apatite by photo acoustic FTIR spectroscopy. *Journal of Materials Science: Materials in Medicine* **1997**, *8* (1), 1-4.

24. Byler, D. M.; Susi, H., Examination of the secondary structure of proteins by deconvolved FTIR spectra. *Biopolymers* **1986**, *25* (3), 469-487.

25. Chen, G.; Liu, S.; Chen, S.; Qi, Z., FTIR Spectra, Thermal Properties, and Dispersibility of a Polystyrene/Montmorillonite Nanocomposite. *Macromolecular Chemistry and Physics* **2001**, *202* (7), 1189-1193.

26. Fujii, T.; de Groot, F. M. F.; Sawatzky, G. A.; Voogt, F. C.; Hibma, T.; Okada, K., In situ XPS analysis of various iron oxide films grown by NO_2 -assisted molecular-beam epitaxy. *Physical Review B* **1999**, *59* (4), 3195-3202.

27. Okpalugo, T. I. T.; Papakonstantinou, P.; Murphy, H.; McLaughlin, J.; Brown, N. M. D., High resolution XPS characterization of chemical functionalised MWCNTs and SWCNTs. *Carbon* **2005**, *43* (1), 153-161.

28. Grosvenor, A. P.; Biesinger, M. C.; Smart, R. S. C.; McIntyre, N. S., New interpretations of XPS spectra of nickel metal and oxides. *Surface Science* **2006**, *600*

(9), 1771-1779.

29. Grosvenor, A. P.; Kobe, B. A.; Biesinger, M. C.; McIntyre, N. S., Investigation of multiplet splitting of Fe 2p XPS spectra and bonding in iron compounds. *Surface and Interface Analysis* **2004**, *36* (12), 1564-1574.

30. Dupin, J.-C.; Gonbeau, D.; Vinatier, P.; Levasseur, A., Systematic XPS studies of metal oxides, hydroxides and peroxides. *Physical Chemistry Chemical Physics* **2000**, *2* (6), 1319-1324.

31. Bhattacharjee, S., DLS and zeta potential – What they are and what they are not? *Journal of Controlled Release* **2016**, *235*, 337-351.

32. Kirby, B. J.; Hasselbrink Jr., E. F., Zeta potential of microfluidic substrates: 1. Theory, experimental techniques, and effects on separations. *ELECTROPHORESIS* **2004**, *25* (2), 187-202.

33. Clogston, J. D.; Patri, A. K., Zeta Potential Measurement. In *Characterization of Nanoparticles Intended for Drug Delivery*, McNeil, S. E., Ed. Humana Press: Totowa, NJ, 2011; pp 63-70.

34. Zisman, W. A., Relation of the Equilibrium Contact Angle to Liquid and Solid Constitution. In *Contact Angle, Wettability, and Adhesion*, AMERICAN CHEMICAL SOCIETY: 1964; Vol. 43, pp 1-51.

35. Yuan, Y.; Lee, T. R., Contact Angle and Wetting Properties. In *Surface Science Techniques*, Bracco, G.; Holst, B., Eds. Springer Berlin Heidelberg: Berlin, Heidelberg, 2013; pp 3-34.

36. Wenzel, R. N., Surface Roughness and Contact Angle. *The Journal of Physical and*

Colloid Chemistry **1949**, 53 (9), 1466-1467.

37. Liu, Y.; Hu, Z.; Zong, K.; Gao, C.; Gao, S.; Xu, J.; Chen, H., Reappraisal and refinement of zircon U-Pb isotope and trace element analyses by LA-ICP-MS. *Chinese Science Bulletin* **2010**, 55 (15), 1535-1546.

38. Lee, S.; Boo, C.; Elimelech, M.; Hong, S., Comparison of fouling behavior in forward osmosis (FO) and reverse osmosis (RO). *Journal of Membrane Science* **2010**, 365 (1), 34-39.

39. Chung, T.-S.; Zhang, S.; Wang, K. Y.; Su, J.; Ling, M. M., Forward osmosis processes: Yesterday, today and tomorrow. *Desalination* **2012**, 287, 78-81.

40. Cath, T. Y.; Childress, A. E.; Elimelech, M., Forward osmosis: Principles, applications, and recent developments. *Journal of Membrane Science* **2006**, 281 (1), 70-87.

41. Shaffer, D. L.; Werber, J. R.; Jaramillo, H.; Lin, S.; Elimelech, M., Forward osmosis: Where are we now? *Desalination* **2015**, 356, 271-284.

42. Zhao, S.; Zou, L.; Tang, C. Y.; Mulcahy, D., Recent developments in forward osmosis: Opportunities and challenges. *Journal of Membrane Science* **2012**, 396, 1-21.

43. Zhang, S.; Li, Y.; Pan, N., Graphene based supercapacitor fabricated by vacuum filtration deposition. *Journal of Power Sources* **2012**, 206, 476-482.

44. Yoshimura, M.; Suda, H.; Okamoto, K.; Ioku, K. J. J. o. M. S., Hydrothermal synthesis of biocompatible whiskers. **1994**, 29 (13), 3399-3402.

45. Komarneni, S.; Roy, R.; Li, Q. H., Microwave-hydrothermal synthesis of ceramic powders. *Materials Research Bulletin* **1992**, 27 (12), 1393-1405.

46. Feng, S.; Xu, R., New Materials in Hydrothermal Synthesis. *Accounts of Chemical Research* **2001**, *34* (3), 239-247.
47. SIBSON, R. H.; MOORE, J. M. M.; RANKIN, A. H., Seismic pumping—a hydrothermal fluid transport mechanism. **1975**, *131* (6), 653-659.
48. Israelachvili, J.; Min, Y.; Akbulut, M.; Alig, A.; Carver, G.; Greene, W.; Kristiansen, K.; Meyer, E.; Pesika, N.; Rosenberg, K.; Zeng, H., Recent advances in the surface forces apparatus (SFA) technique. *Reports on Progress in Physics* **2010**, *73* (3), 036601.
49. Sridhar, I.; Johnson, K. L.; Fleck, N. A., Adhesion mechanics of the surface force apparatus. *Journal of Physics D: Applied Physics* **1997**, *30* (12), 1710-1719.
50. Crassous, J.; Charlaix, E.; Loubet, J. L., Capillary Condensation between High-Energy Surfaces. An Experimental Study with a Surface Force Apparatus. *Europhysics Letters (EPL)* **1994**, *28* (1), 37-42.
51. Stewart, A. M.; Christenson, H. K., Use of magnetic forces to control distance in a surface force apparatus. *Measurement Science and Technology* **1990**, *1* (12), 1301-1303.
52. Kumacheva, E., Interfacial friction measurement in surface force apparatus. *Progress in Surface Science* **1998**, *58* (2), 75-120.
53. Bec, S.; Tonck, A.; Georges, J. M.; Georges, E.; Loubet, J. L., Improvements in the indentation method with a surface force apparatus. *Philosophical Magazine A* **1996**, *74* (5), 1061-1072.
54. Timonen, T.; Saksela, E., Isolation of human NK cells by density gradient centrifugation. *Journal of Immunological Methods* **1980**, *36* (3), 285-291.
55. Murphy, J. R., Influence of temperature and method of centrifugation on the

- separation of erythrocytes. *The Journal of Laboratory and Clinical Medicine* **1973**, *82* (2), 334-341.
56. Brakke, M. K., Zonal separations by density-gradient centrifugation. *Archives of Biochemistry and Biophysics* **1953**, *45* (2), 275-290.
57. Chen, W.; Yu, H.; Liu, Y.; Chen, P.; Zhang, M.; Hai, Y., Individualization of cellulose nanofibers from wood using high-intensity ultrasonication combined with chemical pretreatments. *Carbohydrate Polymers* **2011**, *83* (4), 1804-1811.
58. Zhang, D.; Fu, H.; Shi, L.; Pan, C.; Li, Q.; Chu, Y.; Yu, W., Synthesis of CeO₂ Nanorods via Ultrasonication Assisted by Polyethylene Glycol. *Inorganic Chemistry* **2007**, *46* (7), 2446-2451.
59. Singh, A. K.; Fernando, S. D.; Hernandez, R., Base-Catalyzed Fast Transesterification of Soybean Oil Using Ultrasonication. *Energy & Fuels* **2007**, *21* (2), 1161-1164.
60. Zhang, L.-J.; Cheng, L.-M.; Xu, N.; Zhao, N.-M.; Li, C.-G.; Yuan, J.; Jia, S.-R., Efficient Transformation of Tobacco by Ultrasonication. *Bio/Technology* **1991**, *9* (10), 996-997.
61. Landfester, K.; Eisenblätter, J.; Rothe, R. J. J. R., Preparation of polymerizable miniemulsions by ultrasonication. **2004**, *1* (1), 65-68.
62. Imai, M.; Ikari, K.; Suzuki, I., High-performance hydrolysis of cellulose using mixed cellulase species and ultrasonication pretreatment. *Biochemical Engineering Journal* **2004**, *17* (2), 79-83.
63. Scriven, L. E., Physics and Applications of DIP Coating and Spin Coating. *MRS*

Proceedings **1988**, *121*, 717.

64. Flack, W. W.; Soong, D. S.; Bell, A. T.; Hess, D. W., A mathematical model for spin coating of polymer resists. **1984**, *56* (4), 1199-1206.

65. Lawrence, C. J., The mechanics of spin coating of polymer films. **1988**, *31* (10), 2786-2795.

66. Bornside, D. E.; Macosko, C. W.; Scriven, L. E., Spin coating: One-dimensional model. **1989**, *66* (11), 5185-5193.

Chapter 3 An Amphiphobic Graphene-Based Hydrogel as Oil-Water Separator and Oil Fence Material

3.1 Introduction

Hydrogels based on graphene materials, especially reduced graphene oxide (rGO), have attracted increasing attention in oil-water separation due to its high surface area and flexibility in assembling of the nanosheets.¹⁻⁴ The abundant nanopores within the hydrogels formed via crosslinking or modifying the graphene nanosheets, provide high volume of adsorption and allow efficient fluid filtration.⁵⁻⁹ The adsorption performance and functionalities of the hydrogels can be readily tuned by introducing desirable functional groups or polymers onto the graphene nanosheets.¹⁰⁻¹³ To achieve environmental-friendly and highly efficient separation of oil and water, many studies have been reported on the fabrication of graphene-based materials of varying super hydrophobicity, super hydrophilicity, super oleophobicity, or super oleophilicity.¹⁴⁻¹⁷ However, limited work has been reported on the synthesis of partially amphiphilic or amphiphobic materials and their applications. Fluoride, as an amphiphobic element, has been introduced in fluorographene as one type of graphene derivatives for oil-water separation, which has been investigated for its low surface energy, strong amphiphobic, high thermal stability, and large energy band gap.¹⁸⁻²⁰ Currently, fluorographene has been widely used in surface protection coating, lubrication coating and amphiphobic coating with various engineering applications.^{19, 21-23}

The conventional approaches for fabrication of fluorographene include chemical

reaction methods and physical exfoliation methods, which are not cost-effective and not suitable for practical applications due to some major disadvantages such as harsh reaction process and requirement of complex facilities.^{19, 21, 22, 24-27} Introduction of fluorinating agents and fluorochemical vapor reactions are the most commonly used chemical reaction methods. The fluorination reaction generally uses fluorinating agent BrF_3 , which is highly poisonous, contaminative, flammable and dangerous.²⁸⁻³¹ In fluorochemical vapor reactions, a highly purified F_2 vapor is commonly used in a sealed polytetrafluoroethylene (PTFE) container at high temperature. To enhance the fluorination efficiency, a combination of the above two traditional methods has been proposed by using a relatively weak fluorinating agent ClF_3 at room temperature followed by thermal expansion at high temperature.³²⁻³⁵ However, this combination could result in a low yield production of single graphene nanosheets, but thermally expanded fluorinated graphite instead. Previous study also reported the fabrication of single layer fluorinated graphene nanosheet through hydrothermal process and showed that the reaction efficiency and ratio of F to C could be significantly influenced by temperature and reaction time.³⁶⁻⁴⁰ Despite the much effort devoted to the production of fluorinated graphene nanosheets, several critical issues including high poisonousness, severe pollution of environment, high cost and harsh reaction conditions, still remain unsolved for the fluorinating chemical reaction process.^{23, 41, 42}

The physical exfoliation methods to fabricate fluorographene include liquid exfoliation and mechanical exfoliation. Mechanical exfoliation approach could destroy the structure of the graphene nanosheets, leading to relatively small nanosheet size.⁴³⁻

⁴⁶ In contrast, the liquid exfoliation process has the potential for large-scale production with more flexibility. However, it is reported that the side products as the impurities in the liquid solution are difficult to be removed, some of which could even lead to defluorination.⁴⁷⁻⁴⁹ The selection of the liquid medium plays a critical role in the exfoliation process and is still under investigation.

In this work, we report a new, facile and cost-effective method for fabricating fluorinated graphene nanosheets and fluorographene hydrogel, based on the interactions of rGO containing carbonyl groups and 1H,1H,2H,2H-perfluorodecanethiol (PF) in the presence of L-ascorbic acid. The new fabrication process developed shows distinct advantages in terms of mild and environmental-friendly reaction conditions and high production efficiency with no side products. The as-prepared hydrogel shows intriguing performances in bouncing oil droplets underwater, excellent adsorption capacity of various oils and organic solvents. The as-prepared graphene-based hydrogel materials show significant application potential as efficient adsorbents in wastewater treatment, filters for oil-water separation and underwater oil repellent agent for preventing leaking oil from spreading.

3.2 Experimental Section

3.2.1 Materials

Natural graphite (Alfa Aesar, median 7-10 micron, 99% metals basis); Sodium nitrate (shawinigan, the McArthur Chemical Co. LTD); Sulfuric acid (Fisher Scientific

Canada, 95 to 98 w/w %); KMnO_4 (Sigma Aldrich ACS reagent >99%); HCl (Sigma Aldrich, 36.5-38% ACS grade); 1H,1H,2H,2H-Perfluorodecanethiol (Sigma Aldrich 97%); L-Ascorbic acid (Fisher Scientific Canada, F.W. 176.13); Ethanol (Fisher Scientific Canada, 70% v/v).

Graphene Oxide (GO) Synthesis and Purification: GO was prepared by oxidation of natural graphite through modified Hummer's method⁷. The obtained GO dispersion would be dialyzed to get an ultra-purified GO dispersion.

3.2.2 Synthesis of F/rGO Precursor

F/rGO precursor was prepared by mixing the GO dispersion (10 mL, 5 mg mL^{-1}) with desired amount of 1H,1H,2H,2H-Perfluorodecanethiol solution (mass ratio 10:1) and then underthrough a relatively low temperature solvothermal process at 50°C for 24 h. The F/rGO precursor was then washed by ethanol and stored in ethanol solution at 50°C .

3.2.3 Synthesis of LA/F/rGO hydrogel

LA/F/rGO hydrogel was obtained by a fast reduction process using the F/rGO precursor dispersion and L-ascorbic acid via solvothermal process. Briefly, 20 ml F/rGO precursor was first experienced solvothermal process under 90°C for 3 h. The L-ascorbic Acid was then added to the dispersion and the reduction reaction process was continued for another 96 h. The final product would be obtained after lyophilizing procedure. The LA/F/rGO hydrogel product was stored in ethanol solution at 50°C .

3.2.4 Material Characterizations

A Fourier transform infrared (FTIR) spectrometer was used to characterize the material chemistry (e.g., functional groups) (Thermo Scientific Nicolet, iS50 FT-IR). The material structure was characterized using a field-emission scanning electron microscope (FESEM on a working distance of 7.5 mm, 15 kV for different magnification) and transmission electron microscopy (TEM, JEOL JEM-ARM200C S/TEM, beam voltage: 200kV). The crystal structure was recorded by X-ray diffraction (XRD) using a Rigaku Ultima IV XRD with high intensity Cu Ka radiation at a 2⁰/min scanning speed and 2 theta scanning axis. The X-ray sources was 40 kV and 44mA. X-ray photoelectron spectroscopy (XPS) measurement was conducted using a Kratos AXIS 165 XPS.

3.2.5 Oil Adsorption Experiments

The LA/F/rGO hydrogel was put in various organic solvents or oils for approximately 1 minute and then taken out. Then it was placed on a filter paper for removing the surface residue solvents and weighted. The adsorption capacity (Q) % (or weight gain) was caculated according to the following equation:

$$Q = \frac{W_f}{W_i} \times 100 \quad 3.1$$

where W_f (g) and W_i (g) are the final and initial weight of the LA/F/rGO hydrogel during oil adsorption process, respectively.

3.2.6 Oil Bouncing Experiment

The LA/F/rGO hydrogel was first placed on the water surface (which was partially pre-soaked in water at 50⁰ C) for 15 minutes. A U-shape needle was applied to produce the oil droplets (i.e., hexadecane mixed with red dye) under water for injection. The generated oil drop would rise due to the low density and buoyance force underwater, moving toward the floated hydrogel. A video camera was used to monitor the whole interaction process.

3.2.7 Oil-Water Separation

The synthesized LA/F/rGO hydrogel was applied to test its capability in separating oil and water from their mixture. In a typical experiment, LA/F/rGO hydrogel was first placed in a syringe (2 cm in diameter and 13 cm in length) shown in **Figure 3.7**. The hydrogel was then pre-treated (or pre-soaked) with water or oil. The pre-treatment using water was achieved by pushing 10 ml DI water through the LA/F/rGO hydrogel under a mild external pressure (i.e., by the syringe piston), which was repeated for three times. The hydrogel pre-soaked with water was then applied to separate toluene and water by flowing a mixture of water and toluene (marked with red dye). The oil pre-soaking process was achieved by immersing the LA/F/rGO hydrogel in a glass via filled with chloroform which was soaked at 50⁰C for 24 h. The hydrogel pre-soaked with oil was then used for the oil-water separation test, in which a mixture of methylene blue marked water solution and chloroform was used as the model oil-water system.

3.3 Results and Discussion

3.3.1 Synthesis of 3D Fluorinated rGO nanosheets (F/rGO) Macrostructure

Precursor

The F/rGO precursor was prepared by a facile one-step low temperature solvothermal process at 50 °C for 24h in the presence of 1H,1H,2H,2H-perfluorodecanethiol (PF) in ethanol. The strong activity of thiol group in PF would facilitate the grafting of polymer chains onto the GO nanosheets via Michael's Addition reaction, during which the graphene oxide sheets started getting partially reduced. The GO dispersion mixed with PF showed brown color, which turned into black color after the partial reduction of GO and Michael's Addition reaction process at 50 °C. The resulted black suspension would be used as F/rGO precursor for further hydrothermal treatment.

3.3.2 Synthesis and Characterization of 3D LA/F/rGO

The F/rGO precursor was first treated under a solvothermal process at 90 °C for 6 hours, partially reducing the GO nanosheets to initiate the formation of porous hydrogel. A strong reducing agent, L-ascorbic acid (LA), was introduced into the mixture and the reaction was continued for another 12 hours, and the hydrogel would then be formed, facilitated by the π - π interaction of the rGO-rGO nanosheets. The LA/F/rGO hydrogel would then experience a lyophilization process and a uniform crosslinked structure could be formed. The LA/F/rGO hydrogel was stored in ethanol solution at 50 °C. In

order to preserve the surface structure of the hydrogel, the hydrogel would then experience critical point drying procedure. The illustration figure is shown in **Figure 3.1**.

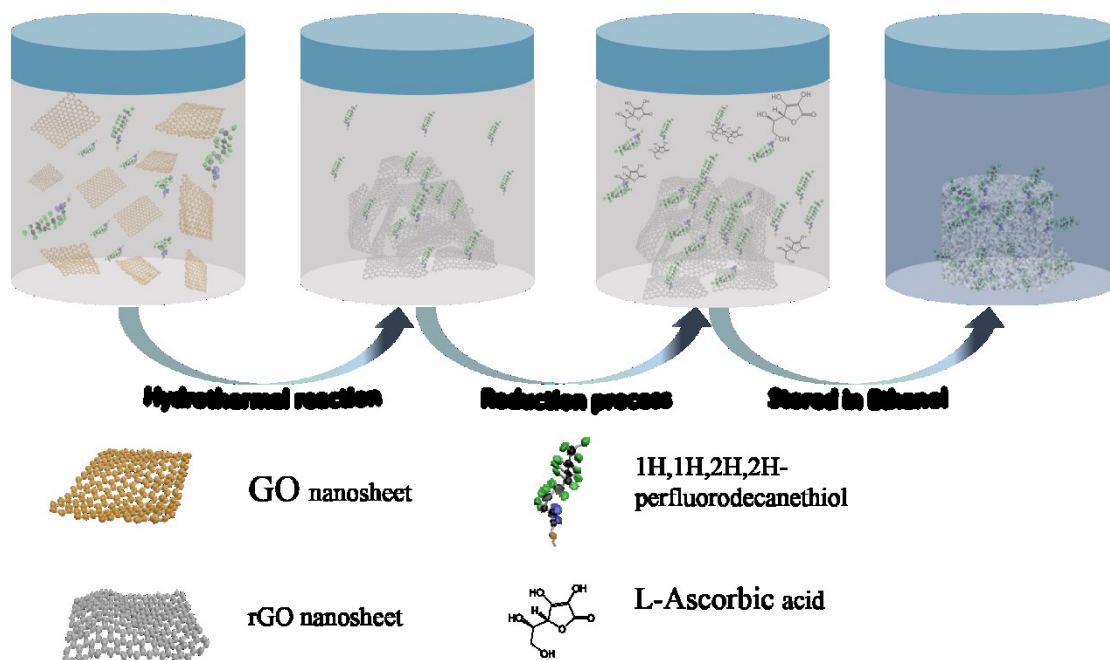


Figure 3.1. Illustration of the formation process for LA/F/rGO hydrogel. The hydrothermal reaction time was set as 6 h and the reduction process was set as 1 h.

The typical size of the synthesized cylinder-shape LA/F/rGO hydrogel was 10 mm in diameter and 15 mm in height, limited by the size of the glass bottle container used, and the dry hydrogel density was as low as 19 mg/cm^3 suggesting a highly porous structure to be used as an adsorbent. As shown in **Figure S3.1**, it was found that the reaction time, GO concentration and mass ratio of GO and PF could influence the size of the final product. With increasing the reaction time, the more complete reaction and more condensed hydrogel could be achieved.

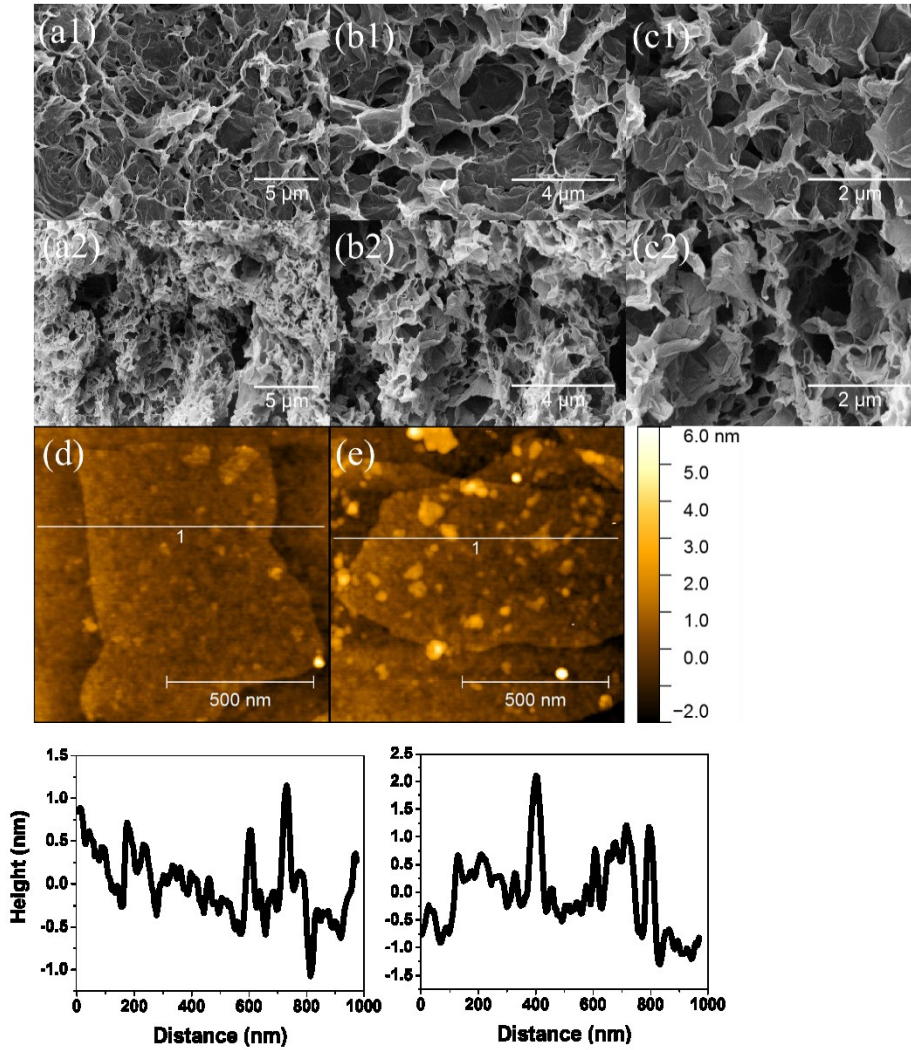


Figure 3.2. SEM images of LA/F/rGO hydrogel before (a1-c1) and after (a2-c2) burning treatment. AFM images for single fluorographene nanosheets under different reaction times (d-6h, e-24h) and the associated height profiles.

The morphology of the LA/F/rGO hydrogel was characterized by scanning electron microscopy (SEM). **Figure 3.2** (a1-c1) shows the typical SEM images of the LA/F/rGO hydrogel, revealing its porous and crosslinking structure. As indicated in **Figure 3.2** (a1-c1), the pore diameters in LA/F/rGO hydrogel are around several micrometers. Burning treatment was used to regenerate the hydrogel materials after oil adsorption and to test its thermal stability (as further discussed in Section 2.3). **Figure**

3.2 (a2-c2) show the typical SEM images of the LA/F/rGO hydrogel after burning treatment on the flame of fire lighter (Turboflame Ranger Windproof Lighter), and no obvious structure change could be observed. **Figure 3.2d-3.2e** show the topographic AFM images for single fluorographene nanosheets and the aggregates on the nanosheet surface under different reaction times (**d-6h, e-24h**) and the associated height profile, suggesting that with increasing the reaction time, more PF chains could be grafted to the graphene nanosheets.

The AFM height profile (**Figure 3.2d**) demonstrates the thickness of single layer graphene nanosheet after 6 h reduction process is around 0.34 nm in the pristine area of graphene nanosheet, consist with theoretical thickness value (i.e., 0.334 nm) of single layer graphene nanosheet, and small aggregates are present on the nanosheets surface.⁵⁰ The high-resolution topographic AFM image (**Figure 3.2e**) shows that more aggregates are deposited on the graphene nanosheets after 24 h reduction process. The corresponding height images have clearly demonstrated the successful grafting of PF chains on the graphene nanosheets, which increases with increasing the reaction time.

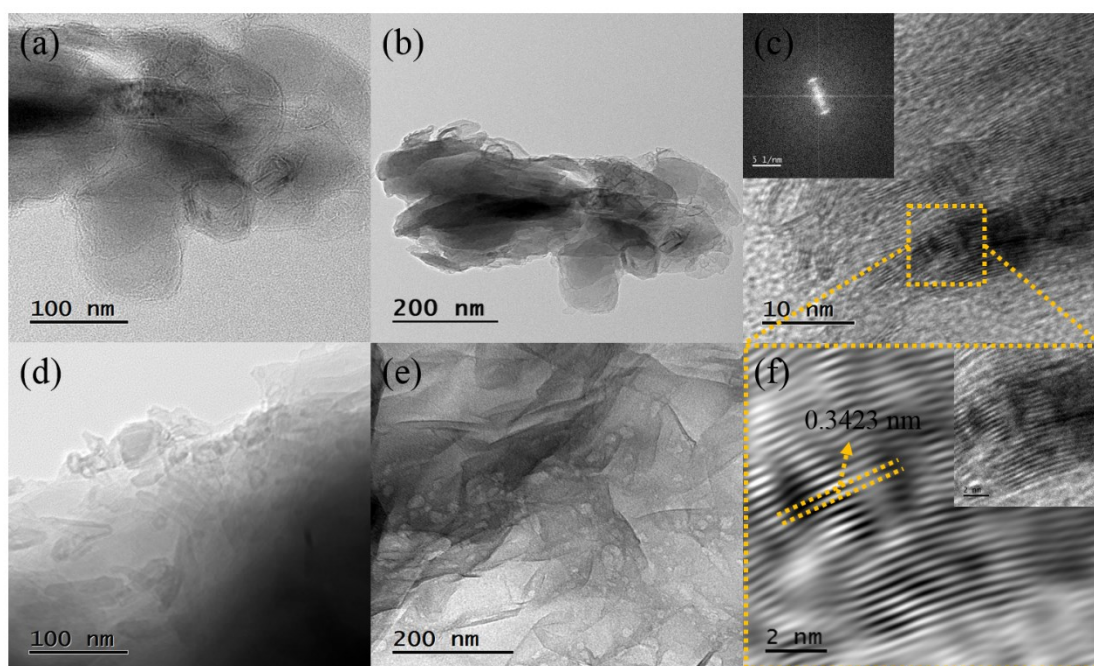


Figure 3.3. TEM image of pure graphene (a, b) and PF grafted graphene (d, e) and high-resolution Fast Fourier Transform (FFT) image of graphene hydrogel (c, f).

The high resolution TEM images of pure graphene and PF modified rGO nanosheets are presented in **Figure 3.3 (a, b)** and **Figure 3.3 (d, e)**, respectively. **Figure 3.3f** shows that the TEM image of layered graphene hydrogel has a typical nanosheet thickness ~ 0.34 nm. The PF grafted nanosheets were further characterized by field-emission scanning electron microscopy with energy dispersive X-ray spectroscopy (FESEM-EDX) as shown in **Figure 3.4** and **Figure S3.2**. The EDX spectrum (~ 1.2 Cps/eV for F and ~ 0.7 Cps/eV for S) and elemental mapping in **Figure 3.4** and **Figure S3.2** clearly demonstrate the successful grafting of PF on graphene nanosheets.

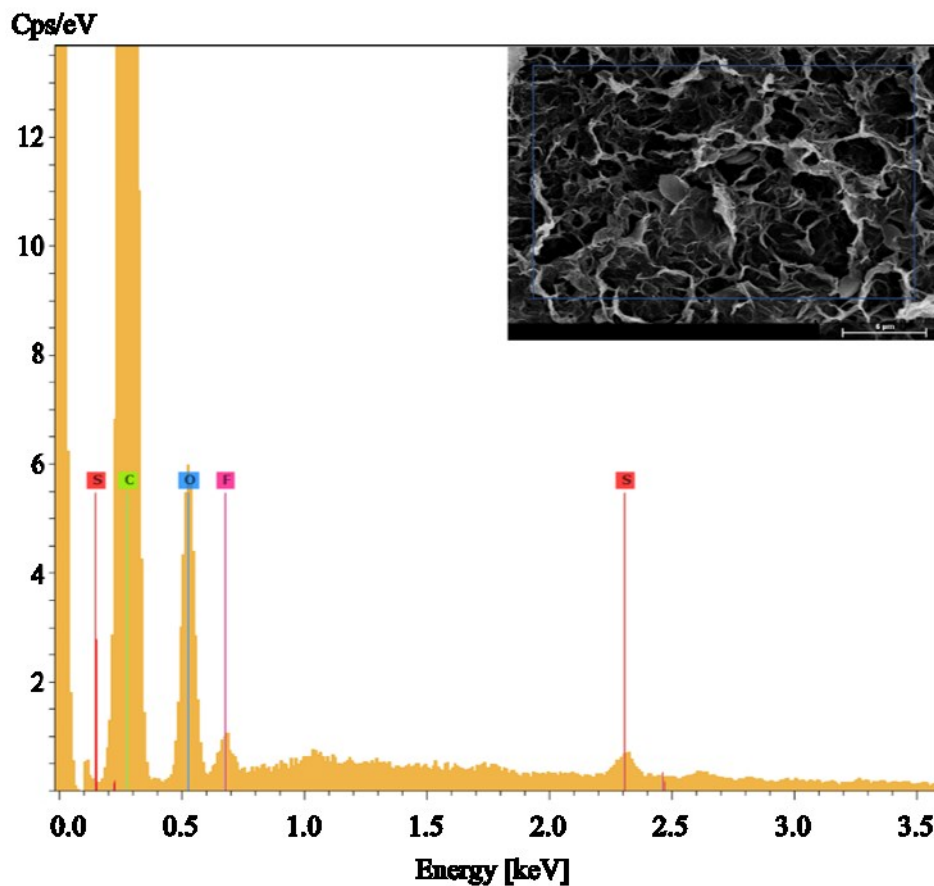


Figure 3.4. Elemental mapping for LA/F/rGO hydrogel.

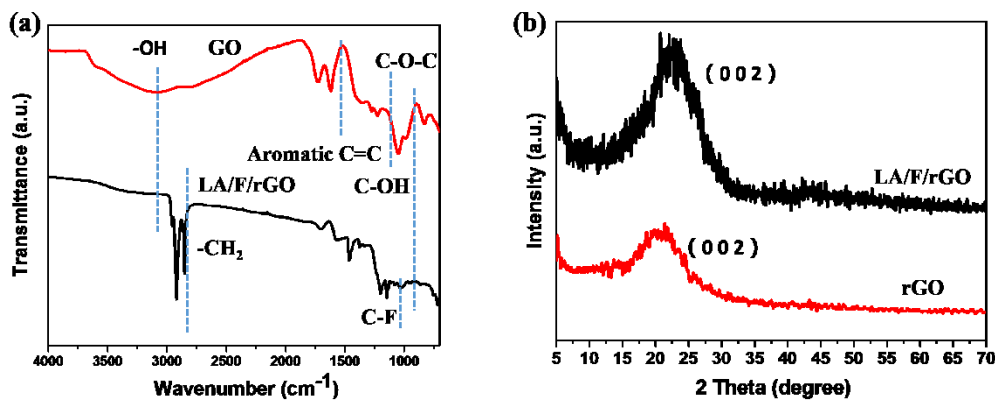


Figure 3.5. (a) Fourier transform infrared (FTIR) spectra of GO and LA/F/rGO. (b) X-ray diffraction (XRD) patterns of rGO and LA/F/rGO hydrogel.

Figure 3.5a represents the Fourier transform infrared (FTIR) spectra of LA/F/rGO and GO nanosheets. The FTIR spectrum of GO shows absorption peaks at around 3300 cm^{-1} (O-H stretching vibration), 2900 cm^{-1} (-CH₂ stretching vibration), 1630 cm^{-1}

(C=C), 1400 cm^{-1} (C-OH stretching vibration) and 1050 cm^{-1} (C-O-C stretching vibration), respectively. However, the stretching vibration is different for the LA/F/rGO spectrum, which shows that only 3300 cm^{-1} (O-H stretching vibration), more peaks at 2900 cm^{-1} ($-\text{CH}_2$ stretching vibration), and 1000 to 1350 cm^{-1} (C-F multi-stretching vibration) suggest the successful modification of PF polymer on the rGO nanosheets. It is also evident from the absence of C=C peak in the FTIR spectrum of LA/F/rGO (**Figure 3.5a**) that the grafting of PF polymer to rGO was achieved through Michael's Addition reaction. The FTIR results indicate that GO nanosheets were partially reduced during the solvothermal process. **Figure 3.5b** represents the X-ray diffraction (XRD) patterns of LA/F/rGO and rGO. GO is widely known to have a diffraction peak at around 9.8° , corresponding to the (002) diffraction peak. After the hydrothermal reaction, the peak shifts to 23.0° , indicating that the GO nanosheets were partially reduced.

3.3.3 Oil Adsorption Behaviors of LA/F/rGO hydrogel and Regeneration by Thermal Treatment.

One advantage of the novel LA/F/rGO hydrogel was that it was oleophobic yet comparatively more hydrophobic for adsorption of oils and organic solvents from oil-water mixtures, with potential application in oil-spill recovery. The photographs in **Figure 3.6 (a1-a6)** show the burning process of oil-saturated LA/F/rGO over increased time period (from 0 to 50 s) for recycling, and the shape of the LA/F/rGO hydrogel remained well even after burning on the flame of a fire lighter (Turboflame Ranger

Windproof Lighter). The photographs in **Figure 3.6 (b1-b3)** demonstrated the 5-minute selective adsorption process for toluene on water surface. **Figure 3.6 (c1-c3)** showed the selective adsorption process for hexadecane on the water surface in a 20-ml glass bottle. **Figures 3.6 (b1-b3)** and **(c1-c3)** clearly show that the as-prepared LA/F/rGO hydrogel can readily and efficiently remove the organic solvents from water (as further discussed in **Figure 3.7**). The unchangeable structure from **Figure 3.6** and FESEM image from **Figure 3.2** after thermal treatment, together with the cyclic performance shown in **Figure S3.4**, demonstrated a promising excellent thermal stability in practical application.

As shown in **Figure 3.7**, the LA/F/rGO hydrogel possesses an outstanding adsorption capacity (~ 2-10 times higher than reported literature) of various oils or organic solvents (up to 20 times of the hydrogel weight), including aromatic compounds (e.g., toluene, divinylbenzene) and hydrocarbons (e.g., hexadecane, 1-bromohexadecane.), which are common pollutants in nature environment.⁵¹ **Figure S3.3** shows the XPS spectra for C, O, S, F elements at 163.9, 285, 532, and 689 eV attributed to S2p, C1s, O1s and CF2 before and after continuous burning. As further demonstrated in **Figure S3.4**, after five adsorption cycles of various organic solvents (i.e., ethanol, acetone, methanol and diethyl ether), the adsorption volume or adsorption capacity of the LA/F/rGO hydrogel was not significantly changed. The XPS spectra and the recycling tests clearly demonstrate the good thermal stability of the LA/F/rGO hydrogel and its excellent regeneration capability as a promising adsorbent for oils.

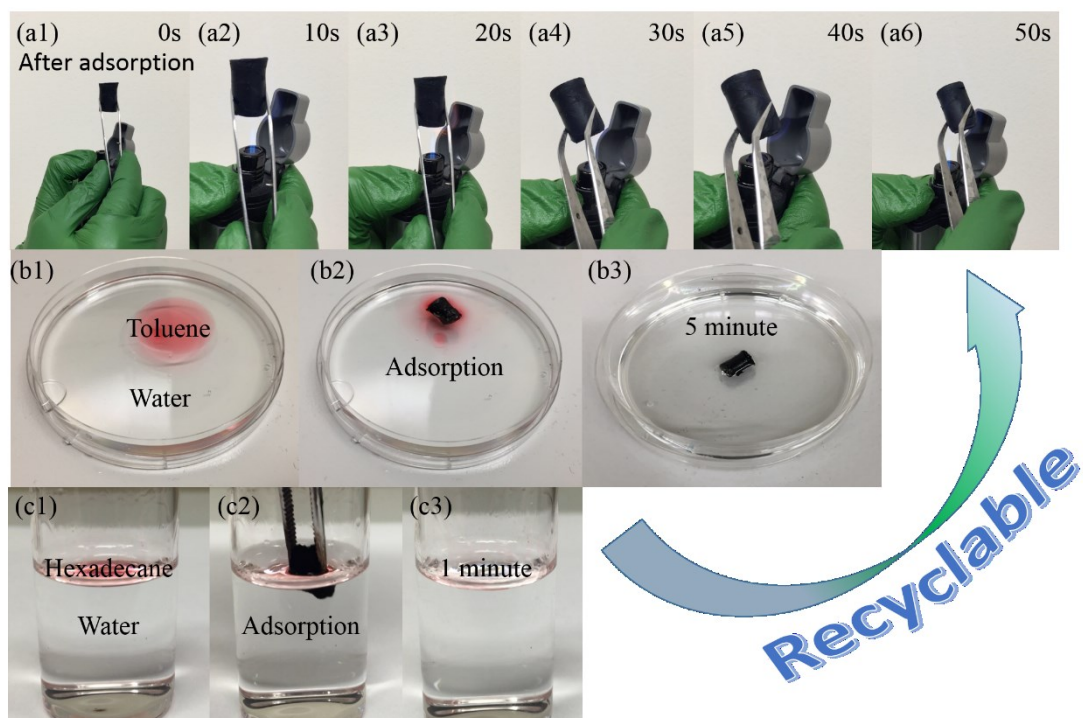


Figure 3.6. Photographs on burning oil-saturated LA/F/rGO hydrogel for 0 s to 50 s (a1-a6) and 5-minute selective adsorption process of toluene on water surface in a petri dish (b1-b3), 1-minute selective adsorption of hexadecane on water surface in a 20-ml glass bottle (c1-c3) and recyclability through fire burning treatment on the flame of a fire lighter (Turboflame Ranger Windproof Lighter).

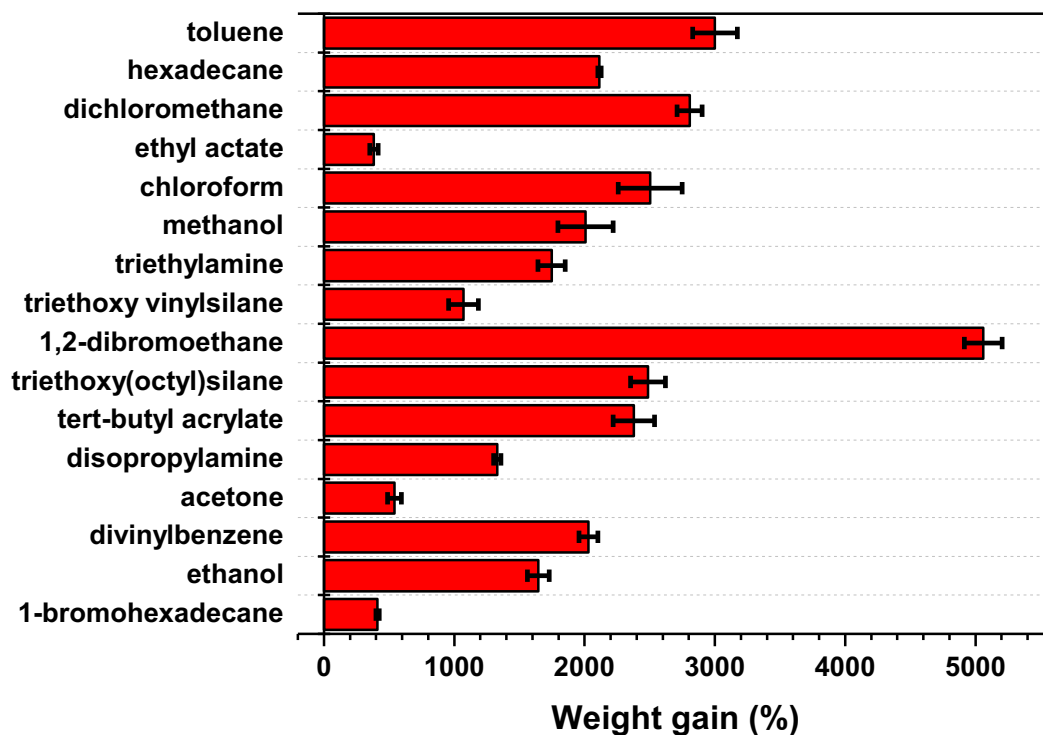


Figure 3.7. Weight gain of the LA/F/rGO hydrogel during adsorption of various organic solvents.

3.3.4 Oil-Water Separation and Bouncing Activity of LA/F/rGO hydrogel

The new LA/F/rGO hydrogel also possesses excellent performance in oil-water separation. Due to the amphiphobic surface properties of the as-prepared LA/F/rGO hydrogel material, it would allow selective filtration/separation of oil or water depending on the pre-soaking treatment.

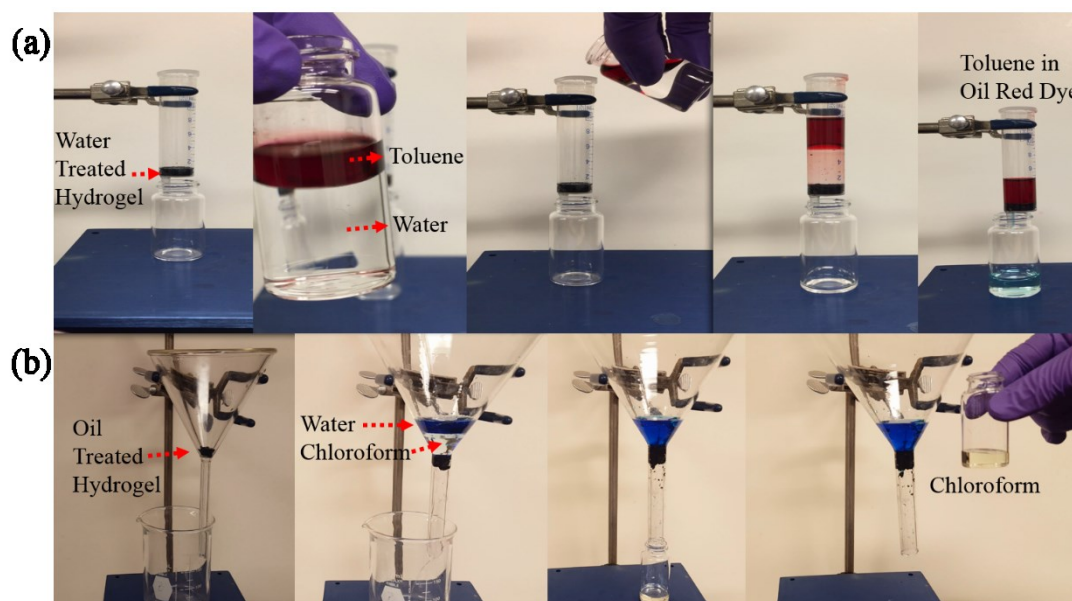


Figure 3.8. Oil-water mixture separation process using (a) LA/F/rGO hydrogel pre-treated/pre-soaked with water to permit water flow for separation of oil, and (b) LA/F/rGO hydrogel pre-treated/pre-soaked with oil to permit oil flow for separation of water.

Figure 3.8a shows that after the hydrogel was pretreated (or pre-soaked) with water, it would allow the aqueous solutions to pass through while inhibit the flow of oil (toluene as a model oil), achieving the successful separation of oil-water by gravity. The water pre-soaking process was achieved by pushing 10 ml DI water through the LA/F/rGO hydrogel filter (shown in **Figure 3.8a**) under a mild external pressure (i.e., by the syringe piston) which was repeated for three times. The FESEM images of the LA/F/rGO hydrogel demonstrated the layered porous structure of the as-prepared hydrogel, which provides the space for water molecules to be stored and form a water zone layer during the water pre-soaking process. Such water zone layers developed during the water pre-soaking process facilitate the flow of aqueous media but effectively inhibit the flow of oil media during oil-water separation process.

In contrast, **Figure 3.8b** shows that after the LA/F/rGO hydrogel was pretreated (or pre-soaked) with oil, it would allow the oil media to pass through under gravity while inhibit the flow of aqueous solutions, demonstrated as an effective water separator. The oil pre-soaking process was achieved by immersing the LA/F/rGO hydrogel in a glass vial filled with chloroform which was soaked at 50 °C for 24 h. The oil treated hydrogel was then used for the oil-water separation test as shown in **Figure 3.8b**, in which methylene blue treated water solution mixed with chloroform was used the model oil-water separation system.

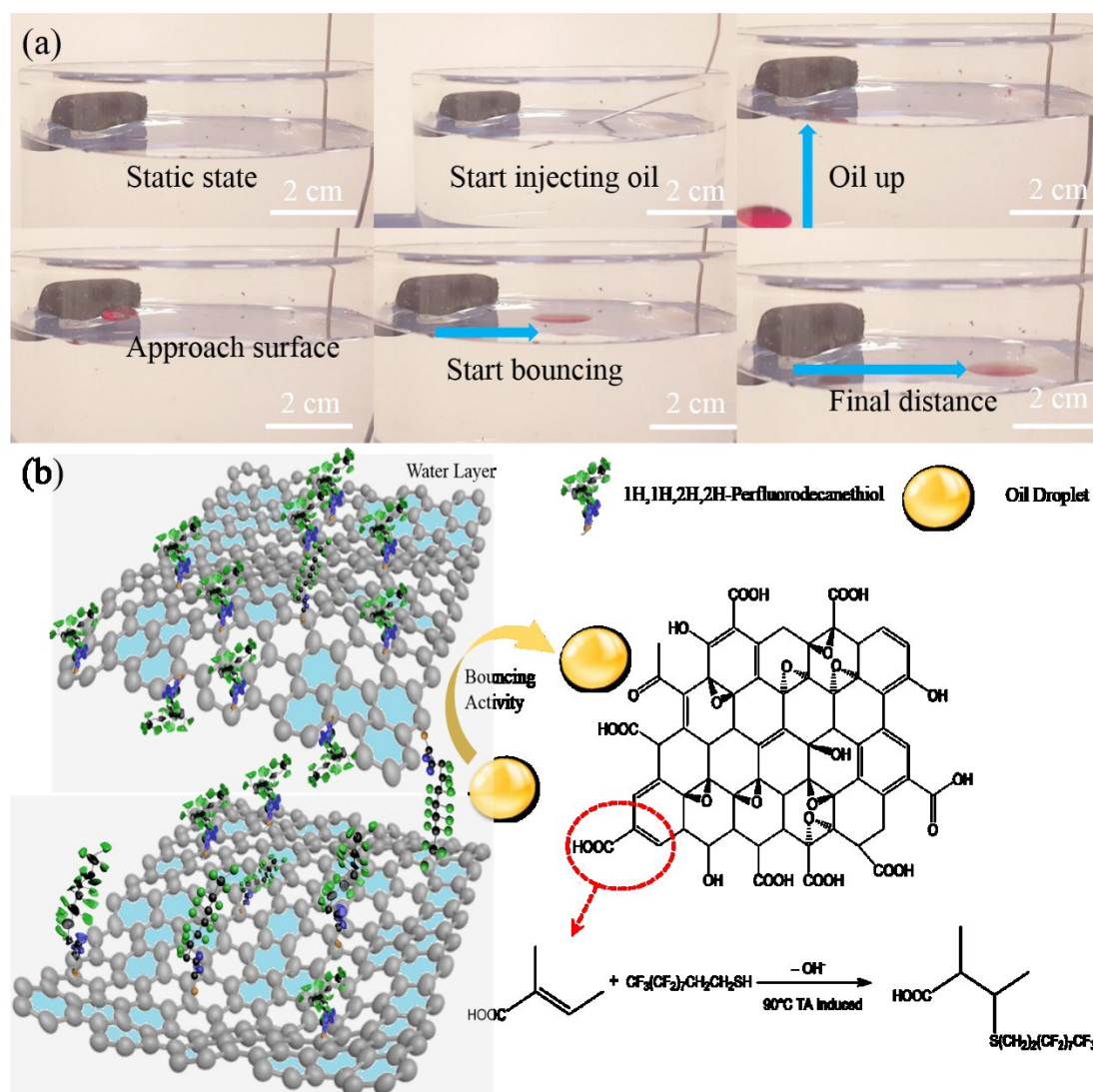


Figure 3.9. (a) Bouncing behavior to oil droplet of LA/F/rGO hydrogel underwater (also see video in Supporting Information). (b) Schematic for oil droplet interacting with the hydrogel surface and the possible interaction mechanism for the bouncing phenomenon.

The lyophilized LA/F/rGO hydrogel shows intriguing bouncing behaviors to oil droplets, as shown in **Figure 3.9**. To demonstrate its bouncing behaviors to oil droplets, the pre-soaked (described in experiment session) LA/F/rGO hydrogel was first placed on the water surface after which, the light oil droplets would be introduced under the hydrogel and float up towards the hydrogel surface due to buoyancy force. It was interesting to notice that after a short period of stacking, the droplet would be bounced away from the hydrogel surface, typically over several centimeters (e.g., ~5 cm) (**Figure 3.9a**). This intriguing bouncing behaviors is highly related to the amphiphobic nature of the LA/F/rGO hydrogel surfaces, mainly due to the fluorinated functional groups and rough surface structures of the hydrogel, as confirmed by the contact angle measurement shown in **Figure S3.5**. The contact angle for water on the hydrogel in air was 125.1° and for toluene in air was 115.3° . In contrast, the contact angle for oil on the hydrogel surface under water increased to 121.5° for toluene in water and 155.6° for hexadecane in water. The unique porous structures of the as prepared hydrogel allows a certain amount of surrounding water molecules stored to form a water zone around certain areas of the hydrogel surfaces. When the rising oil droplet driven by buoyancy approached and reached the vicinity of the hydrogel surfaces, various surface interactions would play a role, such as electrical double layer interaction, van der Waals forces, hydrophobic interaction, and hydration interaction. These surface interactions

would act together with the hydrodynamic interaction on the oil droplet. The overall surface interactions between the oil droplet and the LA/F/rGO hydrogel underwater would be repulsive, which repelled and bounced the oil droplet away from the hydrogel surfaces (as illustrated in **Figure 3.9b**). Such an intriguing oil bouncing behavior of the as-prepared LA/F/rGO hydrogel demonstrates its important application potential in inhibiting the leaking/spreading of spilled oil.

3.4 Conclusions

In summary, this work reports a facile, novel, environmental-friendly and economical method for synthesizing the fluorographene nanosheets through Michael's Addition reaction and –fabricating amphiphobic LA/F/rGO hydrogel. The obtained LA/F/rGO hydrogel has a low density of ~19 mg/ml, good thermal stability and a considerable adsorption capacity (up to 20 times its original weight) towards various organic solvents, demonstrated as a promising material for efficient adsorbents in waste water treatment. The as-prepared LA/F/rGO hydrogel shows intriguing spontaneous repellent to oil droplets underwater, viz., the oil droplets could be bounced away from the hydrogel material underwater. The selective permeation of oil or water flow depending on the pre-soaking condition makes the LA/F/rGO hydrogel a new membrane or filtration material for oil/water separation. The intriguing bouncing performance of the LA/F/rGO hydrogel suggests that it has significant potential application as new oil fence material. Our results provide new insights into the development of novel and effective approaches on tackling oil leakage in ocean and oil-

water separation in related industrial processes, with useful implications for fabrication of new fluoride graphene nanosheet based multifunctional materials with a wide range of engineering and environmental applications.

3.5 References

1. Chi, K.; Zhang, Z.; Xi, J.; Huang, Y.; Xiao, F.; Wang, S.; Liu, Y., Freestanding Graphene Paper Supported Three-Dimensional Porous Graphene–Polyaniline Nanocomposite Synthesized by Inkjet Printing and in Flexible All-Solid-State Supercapacitor. *ACS Applied Materials & Interfaces* **2014**, *6* (18), 16312-16319.
2. Chronopoulos, D. D.; Bakandritsos, A.; Lazar, P.; Pykal, M.; Čépe, K.; Zbořil, R.; Otyepka, M., High-Yield Alkylation and Arylation of Graphene via Grignard Reaction with Fluorographene. *Chemistry of Materials* **2017**, *29* (3), 926-930.
3. Das, S.; Irin, F.; Ma, L.; Bhattacharia, S. K.; Hedden, R. C.; Green, M. J., Rheology and Morphology of Pristine Graphene/Polyacrylamide Gels. *ACS Applied Materials & Interfaces* **2013**, *5* (17), 8633-8640.
4. Díaz-Blancas, V.; Ocampo-Pérez, R.; Leyva-Ramos, R.; Alonso-Dávila, P. A.; Moral-Rodríguez, A. I., 3D modeling of the overall adsorption rate of metronidazole on granular activated carbon at low and high concentrations in aqueous solution. *Chemical Engineering Journal* **2018**, *349*, 82-91.
5. Fu, Y.; Wang, J.; Liu, Q.; Zeng, H., Water-dispersible magnetic nanoparticle–graphene oxide composites for selenium removal. *Carbon* **2014**, *77*, 710-721.
6. Geim, A. K.; Novoselov, K. S., The rise of graphene. *Nature Materials* **2007**, *6*, 183.
7. González-Domínguez, J. M.; Martín, C.; Durá, Ó. J.; Merino, S.; Vázquez, E., Smart Hybrid Graphene Hydrogels: A Study of the Different Responses to Mechanical Stretching Stimulus. *ACS Applied Materials & Interfaces* **2018**, *10* (2), 1987-1995.

8. Haibin, S.; Can, F.; Yanli, G.; Pengfei, G.; Chunlei, W.; Wenchao, Y.; Qishang, W.; Chongwu, Z.; Junya, W.; Junqi, X., Electrical property of macroscopic graphene composite fibers prepared by chemical vapor deposition. *Nanotechnology* **2018**, *29* (30), 305601.
9. Han, H.; Zongbin, Z.; Wubo, W.; Yury, G.; Jieshan, Q., Ultralight and Highly Compressible Graphene Aerogels. *Advanced Materials* **2013**, *25* (15), 2219-2223.
10. Lee, H.; Lee, B. P.; Messersmith, P. B., A reversible wet/dry adhesive inspired by mussels and geckos. *Nature* **2007**, *448*, 338.
11. Li, J.; Xie, J.; Gao, L.; Li, C. M., Au Nanoparticles–3D Graphene Hydrogel Nanocomposite To Boost Synergistically in Situ Detection Sensitivity toward Cell-Released Nitric Oxide. *ACS Applied Materials & Interfaces* **2015**, *7* (4), 2726-2734.
12. Liang, P.; Wang, F.; Hu, Z.-A., Controlled synthesis of ordered sandwich CuCo₂O₄/reduced graphene oxide composites via layer-by-layer heteroassembly for high-performance supercapacitors. *Chemical Engineering Journal* **2018**, *350*, 627-636.
13. Liu, X.; Miller, A. L.; Park, S.; Waletzki, B. E.; Zhou, Z.; Terzic, A.; Lu, L., Functionalized Carbon Nanotube and Graphene Oxide Embedded Electrically Conductive Hydrogel Synergistically Stimulates Nerve Cell Differentiation. *ACS Applied Materials & Interfaces* **2017**, *9* (17), 14677-14690.
14. Meng, X.; Lu, L.; Sun, C., Green Synthesis of Three-Dimensional MnO₂/Graphene Hydrogel Composites as a High-Performance Electrode Material for Supercapacitors. *ACS Applied Materials & Interfaces* **2018**, *10* (19), 16474-16481.
15. Mingyang, J.; Nan, J.; Jian, C.; Junqi, S., Near-Infrared Light-Driven, Highly

Efficient Bilayer Actuators Based on Polydopamine-Modified Reduced Graphene Oxide. *Advanced Functional Materials* **2014**, *24* (34), 5412-5419.

16. Wang, Q.; Zhang, X.; Huang, L.; Zhang, Z.; Dong, S., One-Pot Synthesis of Fe₃O₄ Nanoparticle Loaded 3D Porous Graphene Nanocomposites with Enhanced Nanozyme Activity for Glucose Detection. *ACS Applied Materials & Interfaces* **2017**, *9* (8), 7465-7471.

17. Xu, Y.; Sheng, K.; Li, C.; Shi, G., Self-Assembled Graphene Hydrogel via a One-Step Hydrothermal Process. *ACS Nano* **2010**, *4* (7), 4324-4330.

18. Ho, K.-I.; Huang, C.-H.; Liao, J.-H.; Zhang, W.; Li, L.-J.; Lai, C.-S.; Su, C.-Y., Fluorinated Graphene as High Performance Dielectric Materials and the Applications for Graphene Nanoelectronics. *Scientific Reports* **2014**, *4*, 5893.

19. Jeon, K.-J.; Lee, Z.; Pollak, E.; Moreschini, L.; Bostwick, A.; Park, C.-M.; Mendelsberg, R.; Radmilovic, V.; Kosteckii, R.; Richardson, T. J.; Rotenberg, E., Fluorographene: A Wide Bandgap Semiconductor with Ultraviolet Luminescence. *ACS Nano* **2011**, *5* (2), 1042-1046.

20. R., N. R.; Wencai, R.; Rashid, J.; Ibtisam, R.; G., K. V.; Liam, B.; Peter, B.; Fredrik, S.; S., M. A.; Shengjun, Y.; I., K. M.; Hui-Ming, C.; Wlodek, S.; G., B. L.; V., O. A.; V., G. I.; N., G. A.; S., N. K.; K., G. A., Fluorographene: A Two-Dimensional Counterpart of Teflon. *Small* **2010**, *6* (24), 2877-2884.

21. Im, K.; Nguyen, D. N.; Kim, S.; Kong, H. J.; Kim, Y.; Park, C. S.; Kwon, O. S.; Yoon, H., Graphene-Embedded Hydrogel Nanofibers for Detection and Removal of Aqueous-Phase Dyes. *ACS Applied Materials & Interfaces* **2017**, *9* (12), 10768-10776.

22. Wang, X.; Dai, Y.; Gao, J.; Huang, J.; Li, B.; Fan, C.; Yang, J.; Liu, X., High-Yield Production of Highly Fluorinated Graphene by Direct Heating Fluorination of Graphene-oxide. *ACS Applied Materials & Interfaces* **2013**, *5* (17), 8294-8299.
23. Chronopoulos, D. D.; Bakandritsos, A.; Pykal, M.; Zbořil, R.; Otyepka, M., Chemistry, properties, and applications of fluorographene. *Applied Materials Today* **2017**, *9*, 60-70.
24. Ajao, V.; Bruning, H.; Rijnaarts, H.; Temmink, H., Natural flocculants from fresh and saline wastewater: Comparative properties and flocculation performances. *Chemical Engineering Journal* **2018**, *349*, 622-632.
25. Chen, C.; Li, F.; Zhang, Y.; Wang, B.; Fan, Y.; Wang, X.; Sun, R., Compressive, ultralight and fire-resistant lignin-modified graphene aerogels as recyclable absorbents for oil and organic solvents. *Chemical Engineering Journal* **2018**, *350*, 173-180.
26. Konwar, A.; Kalita, S.; Kotoky, J.; Chowdhury, D., Chitosan–Iron Oxide Coated Graphene Oxide Nanocomposite Hydrogel: A Robust and Soft Antimicrobial Biofilm. *ACS Applied Materials & Interfaces* **2016**, *8* (32), 20625-20634.
27. Lu, Z.; Yu, J.; Zeng, H.; Liu, Q., Polyamine-modified magnetic graphene oxide nanocomposite for enhanced selenium removal. *Separation and Purification Technology* **2017**, *183*, 249-257.
28. Shi, M.; Kan, Q.; Sha, Z.; Kang, G., The Edge-Related Mechanical Properties of Fluorographene Nanoribbons. *Journal of Applied Mechanics* **2015**, *82* (4), 041007-041007-7.
29. Yang, Y.; Lu, G.; Li, Y.; Liu, Z.; Huang, X., One-Step Preparation of

Fluorographene: A Highly Efficient, Low-Cost, and Large-Scale Approach of Exfoliating Fluorographite. *ACS Applied Materials & Interfaces* **2013**, *5* (24), 13478-13483.

30. Yufei, W.; Sheng, C.; Ling, Q.; Kun, W.; Huanting, W.; P., S. G.; Dan, L., Graphene-Directed Supramolecular Assembly of Multifunctional Polymer Hydrogel Membranes. *Advanced Functional Materials* **2015**, *25* (1), 126-133.

31. Yuxi, X.; Zhaoyang, L.; Xiaoqing, H.; Yang, W.; Yu, H.; Xiangfeng, D., Graphene Hydrogels: Functionalized Graphene Hydrogel-Based High-Performance Supercapacitors (Adv. Mater. 40/2013). *Advanced Materials* **2013**, *25* (40), 5828-5828.

32. Xiang, Z.; Zhang, L.; Yuan, T.; Li, Y.; Sun, J., Healability Demonstrates Enhanced Shape-Recovery of Graphene-Oxide-Reinforced Shape-Memory Polymeric Films. *ACS Applied Materials & Interfaces* **2018**, *10* (3), 2897-2906.

33. Xiyao, Z.; Zhou, L.; Kesong, L.; Lei, J., Bioinspired Multifunctional Foam with Self-Cleaning and Oil/Water Separation. *Advanced Functional Materials* **2013**, *23* (22), 2881-2886.

34. Yan, S.; Zhao, J.; Yuan, Y.; Liu, S.; Huang, Z.; Chen, Z.; Jiang, D.; Zhao, W., Preparation and liquid-phase exfoliation of graphite fluoroxide towards graphene fluoroxide. *RSC Advances* **2013**, *3* (44), 21869-21876.

35. Zhang, J.; Azam, M. S.; Shi, C.; Huang, J.; Yan, B.; Liu, Q.; Zeng, H., Poly(acrylic acid) functionalized magnetic graphene oxide nanocomposite for removal of methylene blue. *RSC Advances* **2015**, *5* (41), 32272-32282.

36. Gong, Y.; Wu, Y.; Xu, Y.; Li, L.; Li, C.; Liu, X.; Niu, L., All-solid-state Z-scheme

CdTe/TiO₂ heterostructure photocatalysts with enhanced visible-light photocatalytic degradation of antibiotic waste water. *Chemical Engineering Journal* **2018**, *350*, 257-267.

37. Wu, H.; Shen, J.; Jiang, X.; Liu, X.; Sun, X.; Li, J.; Han, W.; Wang, L., Bioaugmentation strategy for the treatment of fungicide wastewater by two triazole-degrading strains. *Chemical Engineering Journal* **2018**, *349*, 17-24.

38. Wu, J.; Tao, K.; Zhang, J.; Guo, Y.; Miao, J.; Norford, L. K., Chemically functionalized 3D graphene hydrogel for high performance gas sensing. *Journal of Materials Chemistry A* **2016**, *4* (21), 8130-8140.

39. Zhao, Y.; Zhang, Y.; Liu, A.; Wei, Z.; Liu, S., Construction of Three-Dimensional Hemin-Functionalized Graphene Hydrogel with High Mechanical Stability and Adsorption Capacity for Enhancing Photodegradation of Methylene Blue. *ACS Applied Materials & Interfaces* **2017**, *9* (4), 4006-4014.

40. Zhou, M.; Tian, Y.; Sameoto, D.; Zhang, X.; Meng, Y.; Wen, S., Controllable Interfacial Adhesion Applied to Transfer Light and Fragile Objects by Using Gecko Inspired Mushroom-Shaped Pillar Surface. *ACS Applied Materials & Interfaces* **2013**, *5* (20), 10137-10144.

41. Zhang, Z.; Xiao, F.; Guo, Y.; Wang, S.; Liu, Y., One-Pot Self-Assembled Three-Dimensional TiO₂-Graphene Hydrogel with Improved Adsorption Capacities and Photocatalytic and Electrochemical Activities. *ACS Applied Materials & Interfaces* **2013**, *5* (6), 2227-2233.

42. Zhongxin, X.; Shutao, W.; Ling, L.; Li, C.; Mingjie, L.; Lin, F.; Lei, J., A Novel

Superhydrophilic and Underwater Superoleophobic Hydrogel-Coated Mesh for Oil/Water Separation. *Advanced Materials* **2011**, *23* (37), 4270-4273.

43. Dubecký, M.; Otyepková, E.; Lazar, P.; Karlický, F.; Petr, M.; Čépe, K.; Banáš, P.; Zbořil, R.; Otyepka, M., Reactivity of Fluorographene: A Facile Way toward Graphene Derivatives. *The Journal of Physical Chemistry Letters* **2015**, *6* (8), 1430-1434.

44. Holten-Andersen, N.; Harrington, M. J.; Birkedal, H.; Lee, B. P.; Messersmith, P. B.; Lee, K. Y. C.; Waite, J. H., pH-induced metal-ligand cross-links inspired by mussel yield self-healing polymer networks with near-covalent elastic moduli. *Proceedings of the National Academy of Sciences* **2011**, *108* (7), 2651-2655.

45. Huiyuan, L.; Huanting, W.; Xiwang, Z., Facile Fabrication of Freestanding Ultrathin Reduced Graphene Oxide Membranes for Water Purification. *Advanced Materials* **2015**, *27* (2), 249-254.

46. Lyu, C.-Q.; Lu, J.-Y.; Cao, C.-H.; Luo, D.; Fu, Y.-X.; He, Y.-S.; Zou, D.-R., Induction of Osteogenic Differentiation of Human Adipose-Derived Stem Cells by a Novel Self-Supporting Graphene Hydrogel Film and the Possible Underlying Mechanism. *ACS Applied Materials & Interfaces* **2015**, *7* (36), 20245-20254.

47. Cheng, G.; Dong, L.; Kamboj, L.; Khosla, T.; Wang, X.; Zhang, Z.; Guo, L.; Pesika, N.; Ding, J., Hydrothermal Synthesis of Monodisperse Hard Carbon Spheres and Their Water-Based Lubrication. *Tribology Letters* **2017**, *65* (4), 141.

48. Jing, W.; Yaoxin, H.; Yan, L.; Biao, K.; Jin, Z.; Jingchao, S.; Qiaoliang, B.; P., S. G.; Ping, J. S.; Huanting, W., Nitrogen-Doped Nanoporous Carbon/Graphene Nano-Sandwiches: Synthesis and Application for Efficient Oxygen Reduction. *Advanced*

Functional Materials **2015**, *25* (36), 5768-5777.

49. Zhang, Z.; Sun, T.; Chen, C.; Xiao, F.; Gong, Z.; Wang, S., Bifunctional Nanocatalyst Based on Three-Dimensional Carbon Nanotube–Graphene Hydrogel Supported Pd Nanoparticles: One-Pot Synthesis and Its Catalytic Properties. *ACS Applied Materials & Interfaces* **2014**, *6* (23), 21035-21040.

50. Oh, H. M.; Jeong, H.; Han, G. H.; Kim, H.; Kim, J. H.; Lee, S. Y.; Jeong, S. Y.; Jeong, S.; Park, D. J.; Kim, K. K.; Lee, Y. H.; Jeong, M. S., Modulating Electronic Properties of Monolayer MoS₂ via Electron-Withdrawing Functional Groups of Graphene Oxide. *ACS Nano* **2016**, *10* (11), 10446-10453.

51. Kolleboyina, J.; Ramanatha, D. K. K.; Christoph, R.; Martin, P.; Michal, O.; Radek, Z.; A., F. R., Biomimetic Superhydrophobic/Superoleophilic Highly Fluorinated Graphene Oxide and ZIF-8 Composites for Oil–Water Separation. *Angewandte Chemie International Edition* **2016**, *55* (3), 1178-1182.

52. Zhang, L.; Ji, L.; Glans, P.-A.; Zhang, Y.; Zhu, J.; Guo, J., Electronic structure and chemical bonding of a graphene oxide–sulfur nanocomposite for use in superior performance lithium–sulfur cells. *Physical Chemistry Chemical Physics* **2012**, *14* (39), 13670-13675.

53. Xiang, Z.; Ying, H.; Panbo, L., Enhanced Electromagnetic Wave Absorption Properties of Poly(3, 4-ethylenedioxythiophene) Nanofibers Decorated Graphene Sheets by Non-covalent Interactions. *Nano-Micro Letters* **2015**, *7* (?).

Chapter 4 Tannic Acid Modified MoS₂ Nanosheet Membranes with Superior Water Flux and Ion/Dye Rejection

4.1 Introduction

Membranes made from the stacking of 2D materials including graphene oxide (GO) and transition metal dichalcogenides (TMDCs) laminar nanosheets have shown great potential in a variety of applications, including water desalination and purification as well as ion separation.¹⁻¹² In ion separation, GO membranes have demonstrated a high rejection rate of cations, > 90%, in aqueous solutions, rendered by the electrostatic interaction between the cations and the anionic oxidized groups on the surfaces of GO nanosheets as evidenced by many relevant works published recently: M. Shan et.al developed a GO/PA/OCNT membrane with high rejection rate towards NaCl through diffusion process processes 114 LMH of water permeation;¹³ J.Zhang et.al found that a similar porous structure of OMWCNT membrane could reach the same level of water flux.¹⁴⁻¹⁷ GO membranes also show a high rejection of organic dyes, such as ~80% for Rhodamine B, though many papers have been published on the high performance of adsorption process for the removal of dyes, for example: J. Lin et.al developed a NF2A membrane with high rejection rate 99.2% of Methylene blue;¹⁸ H.Kang et.al discovered GO/OCNT composite membrane could have the same rejection effect towards the rejection of Methylene blue,¹⁹ however, the

separation efficiency would not meet the practical requirement restricted by the adsorption technology limitations (e.g. time consuming, recyclability etc.).^{20, 21}

Membrane technology is a promising candidate for the replacement of adsorption technology as considered to be more reliable and efficient. However, the conventional GO-based membranes generally suffer from their low water flux (typically ~25-75 L/(m²h.bar) (LMHB), 100 nm thick) and swelling in water.^{1, 22-}

27

MoS₂ membranes, a typical TMDCs membrane made of MoS₂ laminates, on the other hand, have better non-swelling performance in water and the water flux of MoS₂-based membranes (~1 μm thick) can be improved to the level of ~300 L/(m²h.bar), over 5 times higher than that of the GO-based membranes with comparable thicknesses.²⁸⁻³⁶ Furthermore, the ion rejection has been reported to be as high as >75% because of the interaction between the cations and the highly active sulfur bond in MoS₂.³⁷⁻⁴² Therefore, MoS₂-based membranes are considered as better candidates for water treatment including dye removal as compared to conventional GO-based membranes.⁴³⁻⁴⁹ However, how to further improve the separation performance of MoS₂-based membranes such as water flux and rejection rate of cations/organic dyes are very challenging, which is highly desirable for practical applications as energy-efficient membranes in water desalination, purification, and ion/dye separation. Tannic acid, as an environmental-friendly molecule has been used as a polar solvent to exfoliate the

TMDCs nanosheets efficiently. In addition, the tannic acid could enhance the membrane water flux significantly.

In this work, we report a novel method for preparing tannic acid (TA)-modified MoS₂ (or MoSe₂) nanosheets with a high yield production and have demonstrated the superior performance of water flux and rejection of cations/organic dyes on the as-prepared membranes based on the TA-modified MoS₂ (TAMoS₂) nanosheets. The reported method in this work would be cheaper and more energy efficient than the previous methods using hours of high-power sonication process. Under static diffusion mode, a hybrid membrane is designed and shows a fast water flux and high rejection of cations including K⁺, Na⁺, Li⁺, Ca²⁺, and Mg²⁺. When tested under vacuum-driven filtration condition, this hybrid membrane demonstrates ultrafast water flux as well as high rejection towards multiple model organic dyes, e.g., Basic Blue, Toluidine Blue and Rhodamine 6G, showing superior performance as compared to conventional membranes based on other 2D materials (e.g., graphene oxide). This work demonstrates the great potential of using TA-modified MoS₂ membranes in water treatment applications.

4.2 Materials and Methods

4.2.1 Two-stage Exfoliation Method

In Stage I, 0.25 g bulk Molybdenum (IV) sulfide powder (particle size: $\sim 6 \mu\text{m}$ (max. $40 \mu\text{m}$), Sigma Aldrich, Canada) and 0.25 g Molybdenum (IV) selenide (~ 325 mesh, 99.9% trace metals basis, Sigma Aldrich, Canada) were treated by thermal condensation recycling process with the assistance of 0.1 g L-Ascorbic acid (99%, Sigma Aldrich, Canada). The reaction temperature was set to 190°C under oil bath and the duration was 12 h. Then, the supernatant of the mixtures were obtained after centrifugation (Eppendorf AG 22331 Hamburg centrifuge, 460W, 50-60Hz, 120V, 6A) at 4000 rpm for 5 min. The precipitate from Stage I was resolved in 200 ml DI water ($>18\text{M}\Omega \text{ cm}$) and collected back to the thermal condensation recycling process. In Stage II, the supernatant from Stage I was sonicated with 0.25 g tannic acid (Sigma Aldrich, Canada) slowly added in for 30 min using Bransonic ultrasonic cleaner (2510R-DTH at, 100 W, frequency of 42 kHz $\pm 6\%$) to create a homogeneous suspension. The suspensions from Stage II for both MoS_2 and MoSe_2 were centrifuged using an Eppendorf AG 22331 Hamburg centrifuge at 4000 rpm for 15 min. The upper solutions were then collected as water stabilized, TAMoS₂/TAMoSe₂ nanosheets.

4.2.2 Preparation of MoS₂-based Membranes

TAMoS₂ membranes, bare MoS₂ nanosheet membranes, and hybrid membranes were fabricated through vacuum filtration method supported on commercial Mixed Cellulose Ester (MCE) substrates (circle WME range, $0.45\mu\text{m}$ pore size, sterile,

individually packed, white, 47mm, 100 pieces). The water stabilized TAMoS₂ suspensions as prepared from Stage II shown above were diluted and used directly in the vacuum filtration process for the preparation of TAMoS₂ membranes. The bare MoS₂ nanosheets that were simply prepared by ultrasonication for 240 h as reported previously⁵⁰ were used for the preparation of bare MoS₂ nanosheet membranes. The hybrid membranes were fabricated on MCE substrates by vacuum filtration of mixed suspensions consisting of a certain weight percentage of TAMoS₂ with balanced bare MoS₂ nanosheets in DI water. The vacuum pressure was set to be -0.7 bar during the preparation of the membranes. The thickness of the membranes was controlled by the loading amount of TAMoS₂ and/or bare MoS₂ nanosheets in suspensions.

4.2.3 Membrane Testing Condition

NaCl, KCl, LiCl, MgCl₂, CaCl₂ were the ion solutions used for water flux and ion rejection tests under static diffusion (**Figure S4.10**). The diffusion setup is consisted of two equal-sized 25 ml reservoir. The duration time was set to be 300 min. The feed side was DI water, and 0.25M cation solution was used as draw side under room temperature and atmospheric condition. Inductive Coupled Plasma Emission Spectrometer was used to determine the cation concentrations in the solutions.

The water flux and rejection rate for the rejection tests of multiple dyes were measured under vacuum filtration. 150 ml 0.1 mg/ml dye solution was vacuum filtrated through the tested membranes at a constant vacuum pressure of -0.7 bar. The concentration before and after filtration for the target dyes were measured by UV-Vis

analysis. The concentration standard line was conducted by UV-Vis analysis as shown in Figure S4.13a, Figure S4.13b, and Figure S4.14.

4.2.4 Osmotic Pressure

The osmotic pressure is calculated by using Vant Hoff equation⁵¹

$$\Pi = CRT \quad 4.1$$

Π = osmotic pressure (in atm, 1 atm = 1.01325 bar); C = concentration gradient across the membrane in g/mole; R = universal constant 0.0821 atm*L/mole*K; T = temperature in K.

4.2.5 Water Transport

The rate of water permeation through the semipermeable membrane is defined as

44, 51

$$J_w = \frac{\Delta V}{S \times h} \quad 4.2$$

J_w is the water permeation rate in LMH; ΔV is the volume change for water after osmotic pressure static diffusion process at steady state; h is steady state diffusion time; S is the effective membrane area.

4.2.6 Ion Transport

The rate of cation permeation through the membrane is defined as^{44, 51}

$$J_s = \frac{C_i}{S \times h} \quad 4.3$$

J_s is the cation flow rate of cation through the membrane; C_i is the feed side concentration after osmotic pressure static diffusion process; h is steady state diffusion time; S is the effective membrane area.

4.2.7 Surface Force Measurement

The surface forces between water droplets and MoS₂ or TAMoS₂ substrate in toluene were directly measured using the drop probe atomic force microscope (AFM) technique using an MFP-3D-BIO AFM (Asylum Research, Santa Barbara, CA). The detailed experiment setup has been reported elsewhere.⁵² Briefly, the water droplets were generated in toluene using an ultra-sharp glass pipet. MoS₂ or TAMoS₂ substrate was carefully placed in toluene near the water droplets. A custom-made rectangular tip-less AFM cantilever (400×70×2 μm) was used to pick up one water droplet with a radius around 70 μm to prepare a water drop probe. Then, this probe was moved above the substrate for the force measurements. During a typical force measurement, the drop probe was driven by a piezo to approach the substrate at a velocity of 1 μm/s till a loading force of 4 nN was reached, followed by the retraction of the probe from the substrate. Meanwhile, the deflection of the cantilever was monitored by an optical laser system. The spring constant of the cantilever was measured using the thermal tune method. Thus, the force profiles were obtained from the AFM software. Multiple force measurements were conducted between the water drops and MoS₂ or TAMoS₂ substrate to validate the force profiles.

4.2.8 Yield Calculation

The yield was calculated from Equation 4.4,

$$Y = \frac{M_T}{M_m + M_{TA} + M_{LA}} \quad 4.4$$

where Y: TAMoS₂ nanosheets yield; M_T: total mass for TAMoS₂ nanosheet after freeze drying; M_m: Initial MoS₂ weight; M_{TA}: Initial tannic acid added into the system; M_{LA}: Initial L-ascorbic acid added into the system.

4.2.9 Sample Characterization

Transmission electron microscopy (TEM) imaging was conducted on a JEOL JEM-ARM200CF S/TEM microscope operated at 200 kV. AFM imaging was carried out in tapping mode using a Dimension Icon AFM (Bruker, Santa Barbara, CA). X-ray diffraction (XRD) patterns were obtained from Rigaku Ultima IV, multipurpose X-ray (Cu-source) diffraction system at 40 kV and 44 mA, using the powder mode and scanned from 3° to 60°. Scanning electron microscopy (SEM) imaging and energy dispersive X-ray spectroscopy (EDX) mapping were performed on Zeiss Sigma Field Emission SEM operated under high vacuum. The SEM instrument is equipped with a Bruker EDX system with dual silicon drift detectors each with an area of 60 mm² and a resolution of 123 eV. X-ray photoelectron spectroscopy (XPS) was carried out using a Kratos AXIS Ultra-x-ray photoelectron spectrometer. Fourier-transform infrared spectroscopy (FTIR) was performed using a Nicolet 50 FTIR spectrometer (Thermo Fisher Scientific) with attenuated total reflection (ATR) mode. UV-vis absorption spectra were measured using a UV-2000 spectrophotometer in quartz cuvettes with a

path length of 2 mm. Inductive Coupled Plasma (ICP) Emission Spectrometer was used to determine the cation concentrations in solutions.

4.3 Results and Discussion

4.3.1 Synthesis and Characterization of TAMoS₂ (TAMoSe₂) Nanosheets

The general synthesis procedure and experimental setup of TAMoS₂ (TAMoSe₂) nanosheets are illustrated in **Figure 4.1a** and **Figure S4.1**, respectively. The bulk MoS₂ (or MoSe₂) powders were first mixed with LA acid in DI water and stirred at a comparatively high speed of 500 rpm under 190 °C, to realize the insertion of LA molecules into bare TMDC layers. Insertion of single polar molecule,^{50, 53} including water, ethanol, acetone, etc., has been widely reported by other researchers. It was also reported that at a temperature higher than 100 °C, graphene would be strongly attached to TMDCs nanosheets, because of the interaction between highly active sulfur bonds in TMDCs and π bonds from the conjugated aromatic structure in graphene.⁵⁴⁻⁵⁶ Therefore, it is expected that after the pre-hydrothermal treatment at 190 °C, the hydroxyl functional groups on the LA acid (of molecular weight 176.13) have been interacted with highly active sulfur bonds,⁵⁷⁻⁵⁹ which weakens the van der Waals interactions between the adjacent TMDC layers. After Stage I, the mixture was cooled down to room temperature and an extensive ultrasonic process (Stage II) was conducted by adding a relatively large-size TA molecules (of molecular weight 1701.23) to the mixture. The abundant hydroxyl and aromatic functional groups on the TA molecules facilitate their attachment to the previously weakened TMDC layers. The hydroxyl

functional groups on TA molecules also carried highly negative charges in DI water (see the discussion later) during the ultrasonic process, so they would stabilize the exfoliated nanosheets in water, realizing the efficient exfoliation of the MoS₂ (MoSe₂) laminates to be TA-modified MoS₂ (MoSe₂) (TAMoS₂ (TAMoSe₂)) nanosheets. Compared to a typical yield of 5%-20% from conventional synthesis methods using single polar molecule in previous reports,⁵⁰ a significantly higher yield of 90% ± 5% was achieved through this novel, two-stage exfoliation process, projecting the scalable production of TAMoS₂ (or TAMoSe₂) nanosheets. It is also noted that the yield of the exfoliation by using either LA molecules alone or TA molecules alone was lower than 20%, revealing the importance of this small LA - large TA, two-stage exfoliation strategy in improving the exfoliation efficiency. This method significantly decreased the ultra-sonication time with the assistance of pre-thermal treatment as shown in **Table S4.4**, illustrating an environmental-friendly and sustainable method for mass production of exfoliated TAMoS₂ nanosheets.

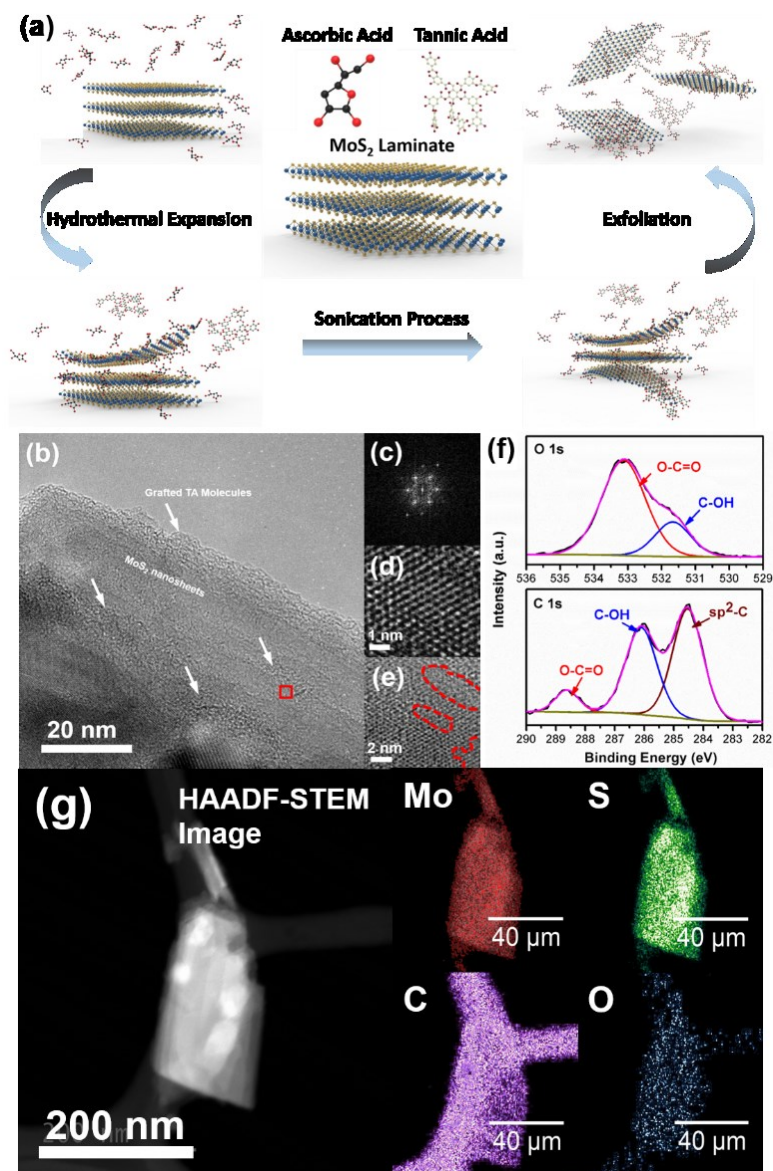


Figure 4.1. Schematic illustration of the exfoliation process for TAMoS₂ (TAMoSe₂) nanosheets (a); HRTEM image of TAMoS₂ nanosheets demonstrating the microstructure of TA-modified MoS₂ nanosheets (b); FFT pattern (c) obtained from the highlighted region in red in (b); reverse FFT-filtered atomic resolution image showing the atom arrangements in (002) plane of MoS₂ nanosheets (d); enlarged HRTEM image (e); high-resolution XPS patterns of C 1s and O1s (f), HAADF-STEM image and STEM-EDX mapping of TAMoS₂ nanosheets (elements C and O) illustrating the attachment of TA molecules onto the surface of MoS₂ nanosheets (g).

The microstructure and morphology of the exfoliated TAMoS₂ nanosheets are shown in high-resolution transmission electron microscopy (HRTEM) images (**Figure 4.1b-4.1e** and **Figure S4.2**). The nanosheet morphology is shown in **Figure 4.1b**, where the presence of the amorphous TA molecules can be clearly observed at the edge and on the surface of the exfoliated nanosheets, as labelled by the arrows in **Figure 4.1b**. The microstructure of the nanosheets is determined by performing fast Fourier transform (FFT) of the selected region in the red frame in **Figure 4.1b**. The FFT pattern in **Figure 4.1c** and its reverse FFT-filtered atomic resolution image in **Figure 4.1d** illustrate the hexagonally symmetric structure with the hexagon width of 3.7 Å, which confirms that the exfoliated nanosheets are MoS₂ nanosheets and the exposed zone is [002] zone axis of MoS₂. **Figure 4.1e** further demonstrates that amorphous TA molecules are deposited onto the surfaces of the exfoliated MoS₂ nanosheets, as indicated in the red region in **Figure 4.1e**, leaving some pristine MoS₂ zones uncovered. It was reported that 2D MoS₂ sheets generally do not have perfect lattices but present sulphur vacancies. These sulphur vacancies allow the strong covalent bonding between the organic and the inorganic molecules, rather than simply weak physisorption of organic molecules onto the MoS₂ sheets.^{50, 60-62} The presence of the defects on the surface of TAMoS₂ nanosheets is also shown in **Figure S4.2**. The small lateral size of the TAMoS₂ nanosheets is determined by TEM to be around 256 nm, as shown in **Figure S4.3**.

The chemical composition and chemical states of the nanosheets were investigated by X-ray photoelectron spectroscopy (XPS) (**Figure 4.1f** and **Figure S4.4**). Deconvolution of the C 1s and O 1s (**Figure 4.1f**) shows the presence of C-C sp² bond from aromatic functional groups, C-OH bond from hydroxyl functional groups, and O-

C=O bond from ester functional groups, indicating the successful deposition of TA molecules onto the exfoliated MoS₂ nanosheets, which is consistent with HRTEM results. The TAMoSe₂ nanosheets can also be successfully synthesized through the newly developed, two-stage exfoliation process (**Figure S4.4**). In addition, high-angle annular dark field-scanning TEM (HAADF-STEM) and STEM-EDX mapping images in **Figure 4.1g** show that TA molecules are homogeneously distributed on the exfoliated MoS₂ nanosheets, macroscopically. The thickness of the exfoliated nanosheets was further analyzed by AFM (**Figure S4.5a**). TAMoS₂ nanosheets were dispersed homogeneously in Milli-Q water and dropped onto the mica surface. The AFM height profiles of the TAMoS₂ nanosheets show a monolayer height of ~ 0.8 nm (red line 1 and red line 2 in **Figure S4.5a**) and a double-layer height of ~1.5 nm (green line 1 and green line 2 in **Figure S4.5a**), thicker than the height of unmodified MoS₂ nanosheets with a monolayer of ~0.65 nm and a double layer of ~1.3 nm from previous report.^{31, 63, 64} Thus, the above thickness difference is attributed to the deposition of TA molecules onto the outer surfaces of the exfoliated MoS₂ nanosheets, as also shown from the FTIR results in **Figure S4.6**. Thicker multilayer TAMoS₂ nanosheets may indicate thicker TA molecule deposition, as suggested in **Figure 4.1**. In order to further confirm the deposition of TA molecules, TAMoS₂, LAMoS₂ and MoS₂ were also characterized by XRD, as shown in **Figure 4.2**. It is clearly presented in the XRD patterns that, compared to the peaks in MoS₂ sample, most peaks are preserved in LAMoS₂ sample. However, there is only one broad amorphous bump besides (002) peak in the exfoliated TAMoS₂

sample, suggesting that the deposits are mainly TA molecules from the second exfoliation stage.

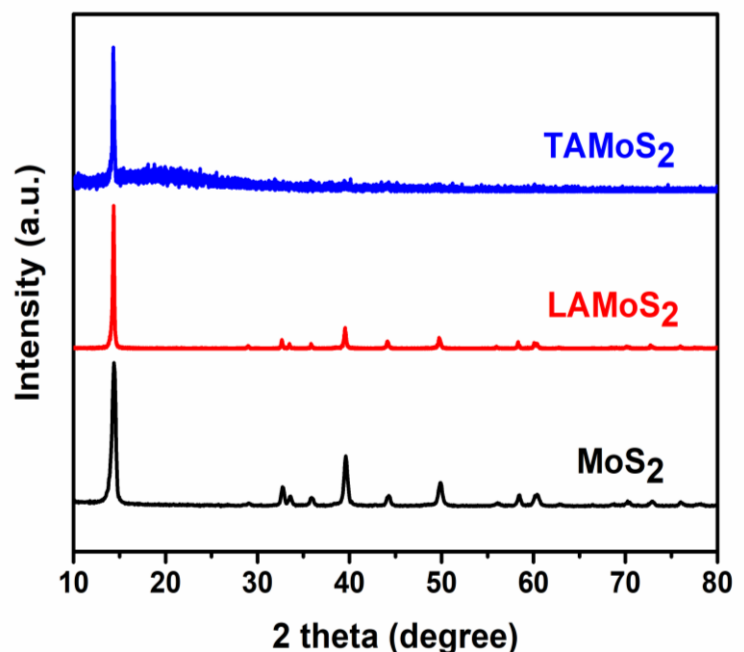


Figure 4.2. XRD spectra for TAMoS₂, LAMoS₂ and MoS₂.

Ultraviolet-visible (UV-vis) spectroscopy (**Figure S4.7**) was employed to evaluate the concentration gradient of TAMoS₂ (TAMoSe₂) nanosheets in aqueous solutions with gradually increased absorption peaks at wavelength 615 nm and 670 nm. The same phenomenon has also been observed for TAMoSe₂ nanosheets, as shown in **Figure S4.7b**. Furthermore, TAMoS₂ (TAMoSe₂) nanosheets demonstrate superior water stability to bulk MoS₂ (MoSe₂) powders and bare-MoS₂ (MoSe₂) sheets (**Figure S4.5b, c** and **Figure S4.8**). After 150 days of settling, the suspension of TAMoS₂ (TAMoSe₂) nanosheets still show excellent stability with more than 80% of the original TAMoS₂ (TAMoSe₂) nanosheets remaining well dispersed in water (**Figure S4.8**). In contrast, most of the bulk MoS₂ (MoSe₂) powders settled down with only 10% of the original MoS₂ (MoSe₂) powders remaining dispersed in water. To the best of our knowledge,

the stability of TAMoS₂ (TAMoSe₂) nanosheets in aqueous solutions reported here demonstrates a superior performance among other conventional surfactant-supported exfoliation methods. The significantly improved suspension stability can be attributed to the abundant hydroxyl functional groups from the deposited TA molecules on the exfoliated MoS₂ (MoSe₂) nanosheets (Figure S4.5c).

4.3.2 High water flux and high ion rejection rates for MoS₂ membranes with TA modification under osmosis pressure

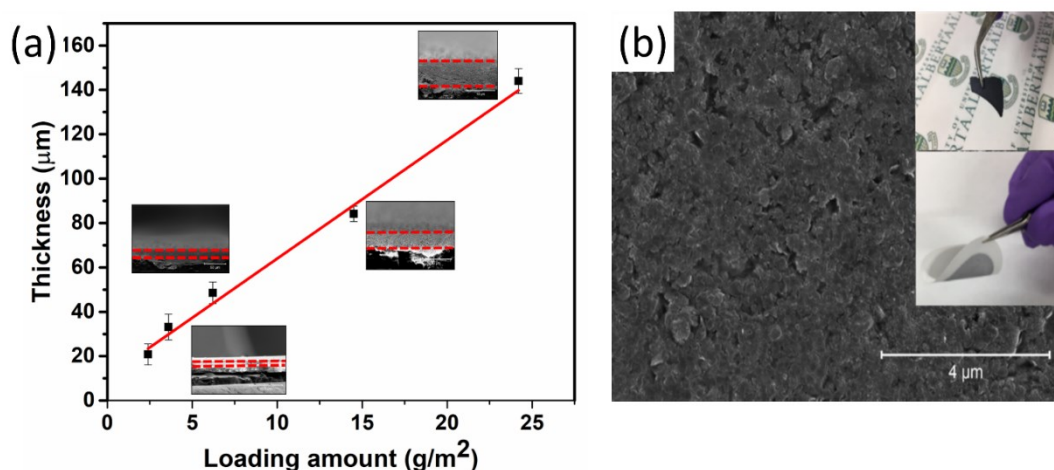


Figure 4.3. (a) Membrane thickness standard line versus loading amount for bare-MoS₂ membranes, TAMoS₂ membranes, and a hybrid membrane with 1 wt% TAMoS₂; (b) Top view SEM image of a 40-μm-thick TAMoS₂ membrane with an inset image of a freestanding 40-μm-thick TAMoS₂ membrane (upper) and an inset image of a flexible 5-μm-thick TAMoS₂ membrane on a support (lower).

Three types of MoS₂ (MoSe₂)-based membranes, i.e., bare-MoS₂ membranes, TAMoS₂ membranes, and a hybrid membrane with 1 wt% TAMoS₂ in MoS₂ membranes, were fabricated through vacuum filtration technique, where the thickness of the membranes was controlled by the loading of the nanosheets in the filtration water

(**Figure 4.3a**). **Figure 4.3a** shows that the thicknesses of all three types of membranes display the same linear relationship with the nanosheets loading in the filtration water. The top-view scanning electron microscope (SEM) image of a TAMoS₂ membrane is also shown in **Figure 4.3b**. The inserted photographs in **Figure 4.3b** show a 40- μ m-thick freestanding TAMoS₂ membrane (upper inserted image) and a 5- μ m-thick flexible TAMoS₂ membrane supported on a mixed cellulose ester substrate (lower inserted image). **Figure S4.9** demonstrates that the as-prepared TAMoS₂ membranes are very stable in water, demonstrating excellent non-swelling property of TAMoS₂ membranes as compared to GO membranes. This non-swelling property was also reported for bare-MoS₂ membranes,⁶⁵ which is essential for the membranes to be used in solution-phase applications.

The ion rejection rate and water flux tests were performed under static diffusion mode using the setup as shown in **Figure S4.10**. The feed side is DI water and the draw side is 0.25 M ionic solution under room temperature and atmospheric pressure. Two magnetic stir bars were used on both sides for stirring to avoid possible concentration gradient. The ion rejection performance of 5- μ m-thick bare-MoS₂ membranes show reasonable rejection rates higher than 75% for various cations including K⁺, Na⁺, Li⁺, Ca²⁺, and Mg²⁺ (**Table S4.1**), as displayed in **Figure 4.4a**. These values are comparable to those of MoS₂ membranes (~80%) made from unmodified MoS₂ nanosheets in previous reports.²⁴ The high rejection rates were attributed to the interaction between the cations and the highly active sulfur bond in MoS₂.^{60, 62} It is also demonstrated in **Figure 4.4a** that 5- μ m-thick TAMoS₂ membranes show higher ion rejection rates than

those from bare-MoS₂ membranes, revealing the advantages of using TA-modified MoS₂ nanosheets in the membranes. The deposited TA molecules, possessing abundant hydroxyl functional groups and aromatic ring structure, were suggested to capture the cations through the cation- π interaction and the interaction between the hydrated cations and the oxidized groups, in addition to the highly active sulfur bonds from uncovered the MoS₂ nanosheets (as shown in **Figure 4.1e**), and therefore, demonstrates the improved ion rejection performance. It is intriguing that the hybrid membrane with 1 wt% of TAMoS₂ nanosheets shows the best ion rejection rates (>97%) than the other two MoS₂-based membranes (**Figure 4.4a**). The corresponding ion permeation rates are the lowest for the hybrid membrane (**Figure 4b**). We hypothesize that the TA molecules in the added TAMoS₂ nanosheets may interact with the highly active sulfur bonds and defects in adjacent bare MoS₂ nanosheets, forming interconnected channels that may fully utilize the functional groups and sulfur bonds in the hybrid membranes when capturing cations. More importantly, **Figure 4.4c** also shows that the 5- μ m-thick hybrid membranes possess fast water flux at around 32 L m⁻² h⁻¹ (LMH), higher than TAMoS₂ membrane (~27.5 LMH) and MoS₂ membrane (~17 LMH). Previous work reported that conventional GO membranes (with the thickness of 5 μ m) had the water flux of ~0.007 LMH,^{22, 43, 66} while ~10% NaCl rejection rate was achieved; 5- μ m-thick MoS₂/Sunset Yellow (SY) membrane showed ~99% of NaCl rejection with the water flux of ~0.033 LMH.³² In addition, 6- μ m-thick MoS₂/Neutral Red (NR) membrane demonstrated 105 LMH of the water flux driven by osmosis pressure, however only ~37% of NaCl rejection rate was achieved³². The detailed comparison has been shown

in **Table S4.2**. Therefore, the 5- μm -thick hybrid membrane fabricated in this work demonstrates excellent performance in terms of a high-water flux at 32 LMH as well as a high ion rejection rate $>97\%$ over various cations.

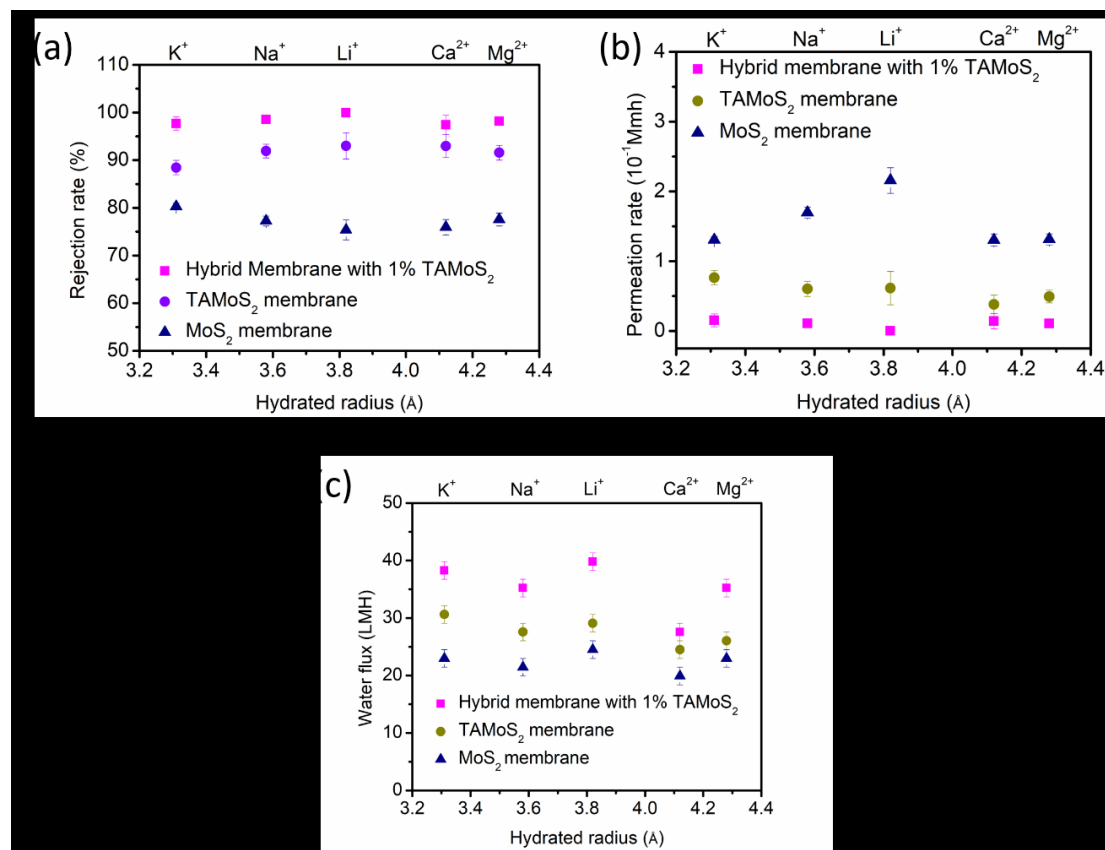


Figure 4.4. Comparison of 5- μm -thick hybrid membrane with 1% TAMoS₂, TAMoS₂ membrane and MoS₂ membrane in terms of rejection rate (a); cation permeation rate (b) and water flux (c). Feed side is DI water and 0.25M cationic solution as the draw side under room temperature and pressure, the stabilized time is set as 360 min. Inductive Coupled Plasma Emission Spectrometer was used to obtain the cation concentrations in solutions.

The stability test of the hybrid membrane is illustrated in **Figure S4.11**. Potassium and Calcium ions have been selected to conduct the stability test. The feed side is DI

water, and 0.25M cation solution is used as draw side under room temperature and atmospheric pressure. The result shown in **Figure S4.11** demonstrates a stable permeation performance.

4.3.3 Effect of TA Molecules on Water Flux

The effect of TA molecules on water flux was further investigated using AFM force measurements. In order to understand the trend of the effect of TA molecules, the vacuum pressure-driven nanofiltration method was used to obtain the water flux under vacuum pressure of -0.7 bar on hybrid membranes containing both TAMoS₂ nanosheets and bare-MoS₂ sheets, within which the weight percentage of TAMoS₂ nanosheets was carefully controlled. As expected, **Figure 4.5a** shows that, when only 1 wt% of TAMoS₂ nanosheets was added into the 5- μ m-thick hybrid membrane, the water flux reaches $15,000 \pm 100$ L/(m²h.bar). This value is even higher than as best-reported rGO-based membrane $\sim 10,000$ L/(m²h.bar)⁶⁷ under similar vacuum pressure-driven conditions. Further increasing the weight percentage of TAMoS₂ nanosheets in the hybrid membrane decreases the water flux. This trend is consistent with the results in **Figure S4.12** with two other thicknesses (40 μ m and 400 μ m) of the hybrid membranes.

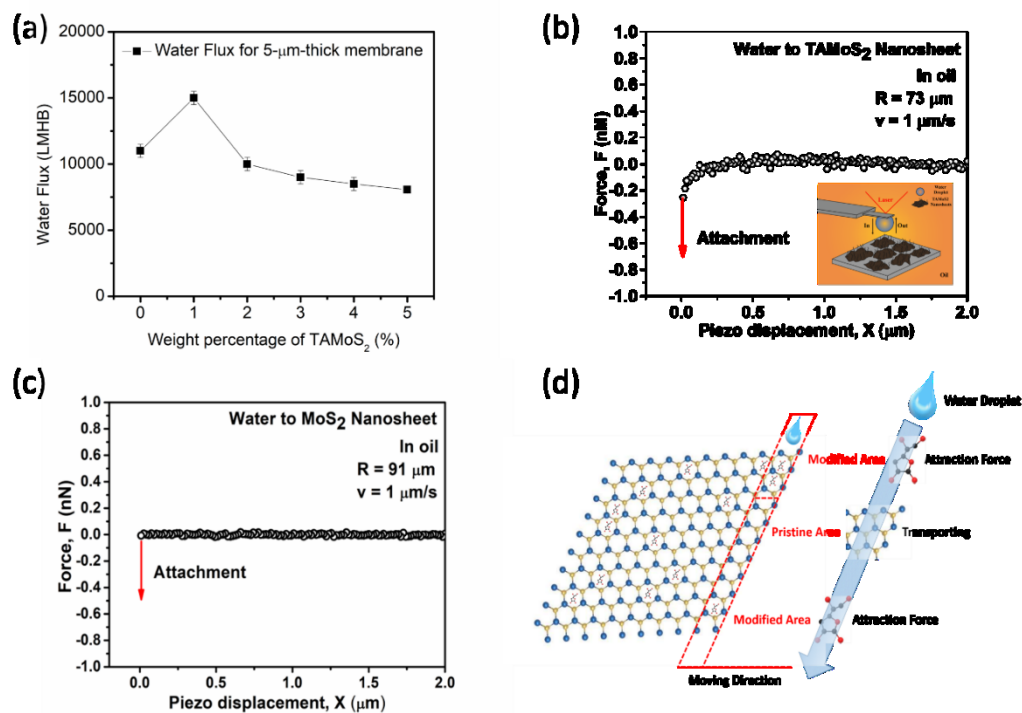


Figure 4.5. The synergistic effect to achieve the ultrafast water flux of $\sim 15,000$ L/(m²h.bar) at 1% weight percentage of TAMoS₂ nanosheets (a); AFM force measurement of a water droplet to TAMoS₂ membrane surface (b) (based on experimental setup shown in **Figure S4.10**); AFM force profile of a water droplet interacting with a bare MoS₂ membrane surface (c); schematic illustration showing the structure to achieve the synergistic effect (d).

In GO membranes, the oxidized zones act as spacer to provide relatively large interlayer distance as well as the hydrogen bonding to accommodate water molecules.^{68,}
⁶⁹ The pristine graphitic zones in rGO membranes facilitate rapid water permeability by nearly frictionless flow^{69, 70} and hence, rGO membranes have a higher water flux than that for GO membranes. It is therefore expected that the interaction between water and TAMoS₂ and that between water and MoS₂ are different. Thus, AFM force measurements were conducted between water droplets and TAMoS₂ or MoS₂ substrates

(**Figure 4.5b-4.5c**), during which a water droplet anchored on an AFM cantilever was driven to approach substrate surface in toluene. Long-range attraction was detected between water droplet and TAMoS₂ (**Figure 4.5b**). However, this long-range attraction phenomenon was not observed when the water droplet was approaching bare MoS₂ surface (**Figure 4.5c**). As compared to the MoS₂ case, the polyphenol groups of TA on the TAMoS₂ substrate could show stronger dipole-dipole interaction with water, thus contributing to the long-range attraction and strong affinity to water. It is also suggested that a small amount of TA molecules would facilitate the attraction of water molecules to the membrane and increase the water flux of the membrane; however, too many TA molecules on the surface would retard the water flux by impeding the water molecules leaving the membrane (**Figure 4.5a, Figure 4.5d**). The AFM force measurements explain the existence of the peak water flux in hybrid membranes, as shown in **Figure 4.5a**, which may provide useful information for designing functional membrane structure with tunable performance.

4.3.4 Ultrahigh water flux and dye rejection rate for MoS₂ membranes with TA modification in vacuum-driven conditions

To further demonstrate the practical significance of the hybrid membrane with the optimized TA composition, we measured its rejection rates of model organic dyes (i.e., basic blue, toluidine blue and rhodamine 6G) under vacuum pressure-driven filtration. The water flux and the rejection rate for model dyes were then tested at the same time on the three types of membranes through vacuum filtration. As shown in **Table S4.3**, most previous results demonstrated a high rejection rate toward the target organic dyes

but at low water flux in conventional membrane systems (e.g., GO/Psf membrane (~80% rejection rate toward methylene blue);^{20, 71} NF2A membrane (~99.2% methylene blue rejection rate, 19.5 L/(m²h.bar));²⁰ Desal 5DK membrane (~95% direct red rejection rate, 25-35 L/(m²h.bar)); polysulfone membrane (~97% acid red rejection rate, 0.23-0.28 L/(m²h.bar))²⁰), which limit the practical application of these membranes. Interestingly, **Figure 4.6a**, **Figure 4.6b** and **Figure 4.6c** show that the hybrid membrane with 1 wt% of TAMoS₂ developed in this work displays an outstanding combination of the performance, 15,000 ± 100 L/(m²h.bar) and nearly 99.87 ± 0.1% rejection of basic blue, toluidine blue and rhodamine 6g. To the best of our knowledge, this is the best performance reported for MoS₂-based membranes, demonstrating their great potential for energy-efficient membranes.

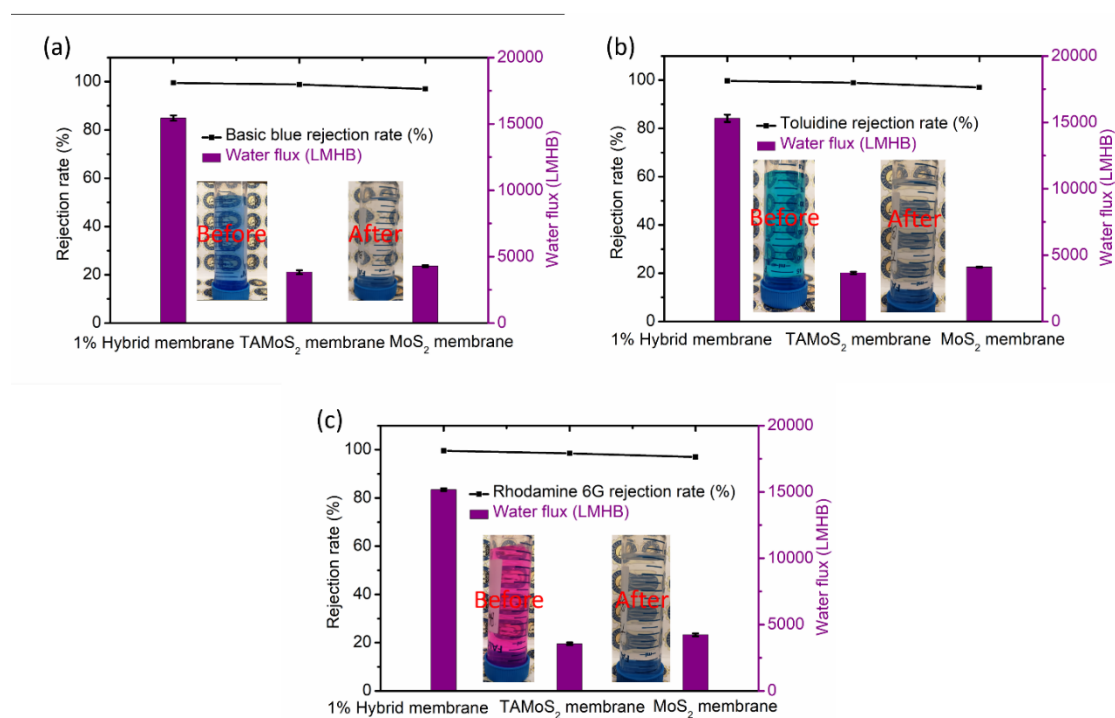


Figure 4.6. Water flux and rejection rates for 5 μm-thick 1% TAMoS₂ hybrid membrane, TAMoS₂ membrane and MoS₂ membrane on Basic Blue (a); Toluidine Blue

(b) and Rhodamine 6G (c) under vacuum filtration ~ 0.7 bar. The abbreviation LMHB represents $L/(m^2h.bar)$.

4.4 Conclusions

In summary, tannic acid-modified, water-stabilized MoS_2 ($MoSe_2$) nanosheets have been successfully synthesized through a two-stage, L-ascorbic acid (LA)-assisted exfoliation method with a high yield of $90\% \pm 5\%$. The as-prepared vacuum-filtered membranes from the resultant TAMoS₂ nanosheets show excellent non-swelling stability in water. The hybrid membrane with 1 wt% of TAMoS₂ in MoS_2 nanosheets at a thickness of 5 μm shows fast water flux around $32 L m^{-2} h^{-1}$ (LMH) and $>97\%$ rejection of various cations under osmosis pressure static diffusion mode, which are higher than the membranes with other compositions. Under vacuum-driven filtration conditions, such a hybrid membrane demonstrates ultrafast water flux of $15,000 \pm 100 L/(m^2h.bar)$ and $99.87 \pm 0.1\%$ rejection of various model organic dyes, e.g., basic blue, toluidine blue and rhodamine 6g, which shows the best performance reported for MoS_2 -based membranes. AFM force measurement reveals a long-range attraction between water droplet and TAMoS₂ surface, while this was not observed on bare MoS_2 surface, suggesting the important role of TA addition. The superior performance of TA-modified MoS_2 membranes demonstrate their significant potential for practical applications in water desalination, purification and ion/dye separation. Our results also provide new insights into the design and development of novel functionalized 2D material membranes with a wide range of engineering and environmental applications.

4.5 References

1. Hirunpinyopas, W.; Prestat, E.; Worrall, S. D.; Haigh, S. J.; Dryfe, R. A. W.; Bissett, M. A., Desalination and Nanofiltration through Functionalized Laminar MoS₂ Membranes. *ACS Nano* **2017**, *11* (11), 11082-11090.
2. Wang, P.; Chung, T.-S., Design and fabrication of lotus-root-like multi-bore hollow fiber membrane for direct contact membrane distillation. *Journal of Membrane Science* **2012**, *421-422*, 361-374.
3. Shim, J.; Banerjee, S.; Qiu, H.; Smithe, K. K. H.; Estrada, D.; Bello, J.; Pop, E.; Schulten, K.; Bashir, R., Detection of methylation on dsDNA using nanopores in a MoS₂ membrane. *Nanoscale* **2017**, *9* (39), 14836-14845.
4. Zong, X.; Yan, H.; Wu, G.; Ma, G.; Wen, F.; Wang, L.; Li, C., Enhancement of Photocatalytic H₂ Evolution on CdS by Loading MoS₂ as Cocatalyst under Visible Light Irradiation. *Journal of the American Chemical Society* **2008**, *130* (23), 7176-7177.
5. Yongjie, Z.; Zheng, L.; Sina, N.; M., A. P.; Jun, L., Large-Area Vapor-Phase Growth and Characterization of MoS₂ Atomic Layers on a SiO₂ Substrate. *Small* **2012**, *8* (7), 966-971.
6. Yi-Hsien, L.; Xin-Quan, Z.; Wenjing, Z.; Mu-Tung, C.; Cheng-Te, L.; Kai-Di, C.; Ya-Chu, Y.; Tse-Wei, W. J.; Chia-Seng, C.; Lain-Jong, L.; Tsung-Wu, L., Synthesis of Large-Area MoS₂ Atomic Layers with Chemical Vapor Deposition. *Advanced Materials* **2012**, *24* (17), 2320-2325.
7. Kaur, S.; Kempson, I.; Xu, H.; Nydén, M.; Larsson, M., Bio-template assisted synthesis of porous glutaraldehyde-polyethyleneimine particulate resin for selective

- copper ion binding and recovery. *RSC Advances* **2018**, *8* (22), 12043-12052.
8. Chen, M.; Shan, X.; Geske, T.; Li, J.; Yu, Z., Manipulating Ion Migration for Highly Stable Light-Emitting Diodes with Single-Crystalline Organometal Halide Perovskite Microplatelets. *ACS Nano* **2017**, *11* (6), 6312-6318.
 9. Adeli, E.; Thung, K.; An, L.; Wu, G.; Shi, F.; Wang, T.; Shen, D., Semi-Supervised Discriminative Classification Robust to Sample-Outliers and Feature-Noises. *IEEE Transactions on Pattern Analysis and Machine Intelligence* **2019**, *41* (2), 515-522.
 10. Bandara, N.; Esparza, Y.; Wu, J., Graphite Oxide Improves Adhesion and Water Resistance of Canola Protein–Graphite Oxide Hybrid Adhesive. *Scientific Reports* **2017**, *7* (1), 11538.
 11. Zhao, W.; Zhao, P.; Tian, Y.; Shen, C.; Li, Z.; Jin, C., Transport and retention of *Microcystis aeruginosa* in porous media: Impacts of ionic strength, flow rate, media size and pre-oxidization. *Water Research* **2019**, *162*, 277-287.
 12. Munz, M.; Oswald, S. E.; Schäfferling, R.; Lensing, H.-J., Temperature-dependent redox zonation, nitrate removal and attenuation of organic micropollutants during bank filtration. *Water Research* **2019**, *162*, 225-235.
 13. Shan, M.; Kang, H.; Xu, Z.; Li, N.; Jing, M.; Hu, Y.; Teng, K.; Qian, X.; Shi, J.; Liu, L., Decreased cross-linking in interfacial polymerization and heteromorphic support between nanoparticles: Towards high-water and low-solute flux of hybrid forward osmosis membrane. *Journal of Colloid and Interface Science* **2019**, *548*, 170-183.
 14. Waduge, P.; Bilgin, I.; Larkin, J.; Henley, R. Y.; Goodfellow, K.; Graham, A. C.;

- Bell, D. C.; Vamivakas, N.; Kar, S.; Wanunu, M., Direct and Scalable Deposition of Atomically Thin Low-Noise MoS₂ Membranes on Apertures. *ACS Nano* **2015**, *9* (7), 7352-7359.
15. Xu, Z.; Ye, H.; Li, H.; Xu, Y.; Wang, C.; Yin, J.; Zhu, H., Enhanced Lithium Ion Storage Performance of Tannic Acid in LiTFSI Electrolyte. *ACS Omega* **2017**, *2* (4), 1273-1278.
16. Bandara, N.; Wu, J., Chemically Modified Canola Protein–Nanomaterial Hybrid Adhesive Shows Improved Adhesion and Water Resistance. *ACS Sustainable Chemistry & Engineering* **2018**, *6* (1), 1152-1161.
17. Zhang, J.; Xu, Z.; Shan, M.; Zhou, B.; Li, Y.; Li, B.; Niu, J.; Qian, X., Synergetic effects of oxidized carbon nanotubes and graphene oxide on fouling control and anti-fouling mechanism of polyvinylidene fluoride ultrafiltration membranes. *Journal of Membrane Science* **2013**, *448*, 81-92.
18. Lin, J.; Ye, W.; Zeng, H.; Yang, H.; Shen, J.; Darvishmanesh, S.; Luis, P.; Sotto, A.; Van der Bruggen, B., Fractionation of direct dyes and salts in aqueous solution using loose nanofiltration membranes. *Journal of Membrane Science* **2015**, *477*, 183-193.
19. Kang, H.; Shi, J.; Liu, L.; Shan, M.; Xu, Z.; Li, N.; Li, J.; Lv, H.; Qian, X.; Zhao, L., Sandwich morphology and superior dye-removal performances for nanofiltration membranes self-assembled via graphene oxide and carbon nanotubes. *Applied Surface Science* **2018**, *428*, 990-999.
20. Morelos-Gomez, A.; Cruz-Silva, R.; Muramatsu, H.; Ortiz-Medina, J.; Araki, T.; Fukuyo, T.; Tejima, S.; Takeuchi, K.; Hayashi, T.; Terrones, M.; Endo, M., Effective

NaCl and dye rejection of hybrid graphene oxide/graphene layered membranes. *Nature Nanotechnology* **2017**, *12*, 1083.

21. Campbell, S.; Maitland, D.; Hoare, T., Enhanced Pulsatile Drug Release from Injectable Magnetic Hydrogels with Embedded Thermosensitive Microgels. *ACS Macro Letters* **2015**, *4* (3), 312-316.

22. Kang, H.; Gongping, L.; Yueyun, L.; Ziyue, D.; Jie, S.; Wanqin, J., A Graphene Oxide Membrane with Highly Selective Molecular Separation of Aqueous Organic Solution. *Angewandte Chemie International Edition* **2014**, *53* (27), 6929-6932.

23. Wojcik, M.; Hauser, M.; Li, W.; Moon, S.; Xu, K., Graphene-enabled electron microscopy and correlated super-resolution microscopy of wet cells. *Nature Communications* **2015**, *6*, 7384.

24. Heiranian, M.; Farimani, A. B.; Aluru, N. R., Water desalination with a single-layer MoS₂ nanopore. *Nature Communications* **2015**, *6*, 8616.

25. Yin, X.; Sun, C.; Zhang, B.; Song, Y.; Wang, N.; Zhu, L.; Zhu, B., A facile approach to fabricate superhydrophobic coatings on porous surfaces using cross-linkable fluorinated emulsions. *Chemical Engineering Journal* **2017**, *330*, 202-212.

26. Banerjee, P.; Mukhopadhyay, A.; Das, P., Graphene oxide–nanobentonite composite sieves for enhanced desalination and dye removal. *Desalination* **2019**, *451*, 231-240.

27. Chen, P.; Ma, X.; Zhong, Z.; Zhang, F.; Xing, W.; Fan, Y., Performance of ceramic nanofiltration membrane for desalination of dye solutions containing NaCl and Na₂SO₄. *Desalination* **2017**, *404*, 102-111.

28. Feldman, Y.; Wasserman, E.; Srolovitz, D. J.; Tenne, R., High-Rate, Gas-Phase Growth of MoS₂ Nested Inorganic Fullerenes and Nanotubes. *Science* **1995**, *267* (5195), 222-225.
29. Radisavljevic, B.; Whitwick, M. B.; Kis, A., Integrated Circuits and Logic Operations Based on Single-Layer MoS₂. *ACS Nano* **2011**, *5* (12), 9934-9938.
30. Jia, W.; Tang, B.; Wu, P., Nafion-assisted exfoliation of MoS₂ in water phase and the application in quick-response NIR light controllable multi-shape memory membrane. *Nano Research* **2018**, *11* (1), 542-553.
31. Yadong, Z.; Zhaoshun, M.; Qi, S.; Haiqi, G.; Yuzhen, L.; Yunhui, W.; Dewei, R.; Kaiming, D.; Ruifeng, L., Nanoporous MoS₂ monolayer as a promising membrane for purifying hydrogen and enriching methane. *Journal of Physics: Condensed Matter* **2017**, *29* (37), 375201.
32. Mi, B., Graphene Oxide Membranes for Ionic and Molecular Sieving. *Science* **2014**, *343* (6172), 740-742.
33. Yu, L.; Lee, Y.-H.; Ling, X.; Santos, E. J. G.; Shin, Y. C.; Lin, Y.; Dubey, M.; Kaxiras, E.; Kong, J.; Wang, H.; Palacios, T., Graphene/MoS₂ Hybrid Technology for Large-Scale Two-Dimensional Electronics. *Nano Letters* **2014**, *14* (6), 3055-3063.
34. Yan, Y. G.; Wang, W. S.; Li, W.; Loh, K. P.; Zhang, J., A graphene-like membrane with an ultrahigh water flux for desalination. *Nanoscale* **2017**, *9* (47), 18951-18958.
35. Zhou, Y.; Fan, R.; Short, M. D.; Li, J.; Schumann, R. C.; Xu, H.; Smart, R. S. C.; Gerson, A. R.; Qian, G., Formation of Aluminum Hydroxide-Doped Surface Passivating Layers on Pyrite for Acid Rock Drainage Control. *Environmental Science*

& Technology **2018**, *52* (20), 11786-11795.

36. Zembyla, M.; Murray, B. S.; Radford, S. J.; Sarkar, A., Water-in-oil Pickering emulsions stabilized by an interfacial complex of water-insoluble polyphenol crystals and protein. *Journal of Colloid and Interface Science* **2019**, *548*, 88-99.

37. Kou, J.; Yao, J.; Wu, L.; Zhou, X.; Lu, H.; Wu, F.; Fan, J., Nanoporous two-dimensional MoS₂ membranes for fast saline solution purification. *Physical Chemistry Chemical Physics* **2016**, *18* (32), 22210-22216.

38. Xiangdong, Y.; Yanbing, Y.; Linna, F.; Mingchu, Z.; Zhihao, L.; Anyuan, C.; Quan, Y., An Ultrathin Flexible 2D Membrane Based on Single-Walled Nanotube–MoS₂ Hybrid Film for High-Performance Solar Steam Generation. *Advanced Functional Materials* **2018**, *28* (3), 1704505.

39. Wang, Z.; Tu, Q.; Zheng, S.; Urban, J. J.; Li, S.; Mi, B., Understanding the Aqueous Stability and Filtration Capability of MoS₂ Membranes. *Nano Letters* **2017**, *17* (12), 7289-7298.

40. LaRue, R. J.; Cobble Dick, J.; Aubry, N.; Cranston, E. D.; Latulippe, D. R., The microscale flocculation test (MFT)—A high-throughput technique for optimizing separation performance. *Chemical Engineering Research and Design* **2016**, *105*, 85-93.

41. Hu, D.; Li, F.; Wang, B.; Lei, K.; Cao, A.; Wang, Z.; Yin-Hua, L., An effect analysis of changes in the composition of the water ecological footprint in Jiangyin City, China. *International Journal of Sustainable Development & World Ecology* **2008**, *15* (3), 211-221.

42. Berry, D.; Holder, D.; Xi, C.; Raskin, L., Comparative transcriptomics of the

response of *Escherichia coli* to the disinfectant monochloramine and to growth conditions inducing monochloramine resistance. *Water Research* **2010**, *44* (17), 4924-4931.

43. Hegab, H. M.; ElMekawy, A.; Barclay, T. G.; Michelmore, A.; Zou, L.; Losic, D.; Saint, C. P.; Ginic-Markovic, M., A Novel Fabrication Approach for Multifunctional Graphene-based Thin Film Nano-composite Membranes with Enhanced Desalination and Antibacterial Characteristics. *Scientific Reports* **2017**, *7* (1), 7490.

44. Joshi, R. K.; Carbone, P.; Wang, F. C.; Kravets, V. G.; Su, Y.; Grigorieva, I. V.; Wu, H. A.; Geim, A. K.; Nair, R. R., Precise and Ultrafast Molecular Sieving Through Graphene Oxide Membranes. *Science* **2014**, *343* (6172), 752-754.

45. Sun, P.; Zhu, M.; Wang, K.; Zhong, M.; Wei, J.; Wu, D.; Xu, Z.; Zhu, H., Selective Ion Penetration of Graphene Oxide Membranes. *ACS Nano* **2013**, *7* (1), 428-437.

46. Feng, L.; Li, L.; Zhang, Y.; Peng, H.; Zou, Y., Low temperature synthesis and ion conductivity of $\text{Li}_7\text{La}_3\text{Zr}_2\text{O}_{12}$ garnets for solid state Li ion batteries. *Solid State Ionics* **2017**, *310*, 129-133.

47. Haase, M. F.; Jeon, H.; Hough, N.; Kim, J. H.; Stebe, K. J.; Lee, D., Multifunctional nanocomposite hollow fiber membranes by solvent transfer induced phase separation. *Nature Communications* **2017**, *8* (1), 1234.

48. Liu, S.; Xie, L.; Liu, J.; Liu, G.; Zhong, H.; Wang, Y.; Zeng, H., Probing the interactions of hydroxamic acid and mineral surfaces: Molecular mechanism underlying the selective separation. *Chemical Engineering Journal* **2019**, *374*, 123-132.

49. Zhang, J.; Lu, X.; Shi, C.; Yan, B.; Gong, L.; Chen, J.; Xiang, L.; Xu, H.; Liu, Q.;

Zeng, H., Unraveling the molecular interaction mechanism between graphene oxide and aromatic organic compounds with implications on wastewater treatment. *Chemical Engineering Journal* **2019**, *358*, 842-849.

50. Hai, X.; Chang, K.; Pang, H.; Li, M.; Li, P.; Liu, H.; Shi, L.; Ye, J., Engineering the Edges of MoS₂ (WS₂) Crystals for Direct Exfoliation into Monolayers in Polar Micromolecular Solvents. *Journal of the American Chemical Society* **2016**, *138* (45), 14962-14969.

51. Lee, K. P.; Arnot, T. C.; Mattia, D., A review of reverse osmosis membrane materials for desalination—Development to date and future potential. *Journal of Membrane Science* **2011**, *370* (1), 1-22.

52. Shi, C.; Zhang, L.; Xie, L.; Lu, X.; Liu, Q.; He, J.; Mantilla, C. A.; Van den berg, F. G. A.; Zeng, H., Surface Interaction of Water-in-Oil Emulsion Droplets with Interfacially Active Asphaltenes. *Langmuir* **2017**, *33* (5), 1265-1274.

53. Ravula, S.; Essner, J. B.; Baker, G. A., Kitchen-Inspired Nanochemistry: Dispersion, Exfoliation, and Hybridization of Functional MoS₂ Nanosheets Using Culinary Hydrocolloids. *ChemNanoMat* **2015**, *1* (3), 167-177.

54. Feng, S.; Kin, T. M.; Zuopeng, L.; Matthias, B., Controlling Iron-Catalyzed Oxidation Reactions: From Non-Selective Radical to Selective Non-Radical Reactions. *Chemistry – A European Journal* **2008**, *14* (29), 8793-8797.

55. Feng, S.; Shuhua, L.; Haitao, G.; Ning, D.; Lijie, D.; Wolfgang, T.; Wolfgang, K., Magnetic-Field-Induced Locomotion of Glass Fibers on Water Surfaces: Towards the Understanding of How Much Force One Magnetic Nanoparticle Can Deliver. *Advanced*

Materials **2009**, *21* (19), 1927-1930.

56. Ganatra, R.; Zhang, Q., Few-Layer MoS₂: A Promising Layered Semiconductor. *ACS Nano* **2014**, *8* (5), 4074-4099.

57. Andersen, A.; Kathmann, S. M.; Lilga, M. A.; Albrecht, K. O.; Hallen, R. T.; Mei, D., Adsorption of Potassium on MoS₂(100) Surface: A First-Principles Investigation. *The Journal of Physical Chemistry C* **2011**, *115* (18), 9025-9040.

58. Presolski, S.; Pumera, M., Covalent functionalization of MoS₂. *Materials Today* **2016**, *19* (3), 140-145.

59. Chu, X. S.; Yousaf, A.; Li, D. O.; Tang, A. A.; Debnath, A.; Ma, D.; Green, A. A.; Santos, E. J. G.; Wang, Q. H., Direct Covalent Chemical Functionalization of Unmodified Two-Dimensional Molybdenum Disulfide. *Chemistry of Materials* **2018**, *30* (6), 2112-2128.

60. McNaughton, R. L.; Helton, M. E.; Cospers, M. M.; Enemark, J. H.; Kirk, M. L., Nature of the Oxomolybdenum–Thiolate π -Bond: Implications for Mo–S Bonding in Sulfite Oxidase and Xanthine Oxidase. *Inorganic Chemistry* **2004**, *43* (5), 1625-1637.

61. Deng, M.; Kwac, K.; Li, M.; Jung, Y.; Park, H. G., Stability, Molecular Sieving, and Ion Diffusion Selectivity of a Lamellar Membrane from Two-Dimensional Molybdenum Disulfide. *Nano Letters* **2017**, *17* (4), 2342-2348.

62. Ma, H.; Shen, Z.; Ben, S., Understanding the exfoliation and dispersion of MoS₂ nanosheets in pure water. *Journal of Colloid and Interface Science* **2018**, *517*, 204-212.

63. Li, Y.; Wang, H.; Xie, L.; Liang, Y.; Hong, G.; Dai, H., MoS₂ Nanoparticles Grown on Graphene: An Advanced Catalyst for the Hydrogen Evolution Reaction. *Journal of*

the American Chemical Society **2011**, 133 (19), 7296-7299.

64. Shen, Y.; Wang, H.; Zhang, X.; Zhang, Y., *MoS₂ nanosheets functionalized mixed matrix membrane for enhanced CO₂ capture via surface drop-coating method*. 2016; Vol. 8.

65. Xu, X.; Wu, J.; Meng, Z.; Li, Y.; Huang, Q.; Qi, Y.; Liu, Y.; Zhan, D.; Liu, X. Y., Enhanced Exfoliation of Biocompatible MoS₂ Nanosheets by Wool Keratin. *ACS Applied Nano Materials* **2018**.

66. Chu, K. H.; Huang, Y.; Yu, M.; Her, N.; Flora, J. R. V.; Park, C. M.; Kim, S.; Cho, J.; Yoon, Y., Evaluation of Humic Acid and Tannic Acid Fouling in Graphene Oxide-Coated Ultrafiltration Membranes. *ACS Applied Materials & Interfaces* **2016**, 8 (34), 22270-22279.

67. Thebo, K. H.; Qian, X.; Zhang, Q.; Chen, L.; Cheng, H.-M.; Ren, W., Highly stable graphene-oxide-based membranes with superior permeability. *Nature Communications* **2018**, 9 (1), 1486.

68. Han, Y.; Jiang, Y.; Gao, C., High-Flux Graphene Oxide Nanofiltration Membrane Intercalated by Carbon Nanotubes. *ACS Applied Materials & Interfaces* **2015**, 7 (15), 8147-8155.

69. Wang, S.; Wu, Y.; Zhang, N.; He, G.; Xin, Q.; Wu, X.; Wu, H.; Cao, X.; Guiver, M. D.; Jiang, Z., A highly permeable graphene oxide membrane with fast and selective transport nanochannels for efficient carbon capture. *Energy & Environmental Science* **2016**, 9 (10), 3107-3112.

70. Xiang, Z.; Zhang, L.; Yuan, T.; Li, Y.; Sun, J., Healability Demonstrates Enhanced

Shape-Recovery of Graphene-Oxide-Reinforced Shape-Memory Polymeric Films.

ACS Applied Materials & Interfaces **2018**, *10* (3), 2897-2906.

71. Badrinezhad, L.; Ghasemi, S.; Azizian-Kalandaragh, Y.; Nematollahzadeh, A., Preparation and characterization of polysulfone/graphene oxide nanocomposite membranes for the separation of methylene blue from water. *Polymer Bulletin* **2018**, *75* (2), 469-484.

Chapter 5 Novel Sodium Alginate-Assisted MXene Nanosheets for Ultrahigh Rejection of Multiple Cations and Dyes

5.1 Introduction

Energy-efficient membrane is urgently needed to access sufficient quantities of water for commercial and industrial uses with an explosive growth of population but limited availability of fresh water.¹ To overcome the global water shortage, seawater that is rich in minerals and abundantly stored on earth has attracted considerable interest from many researchers. Currently, the most advanced membrane techniques for desalination and purification include forward osmosis, reverse osmosis (RO), membrane distillation, pervaporation and nanofiltration (NF), which require a lot of extra costs including replacement of semipermeable membranes, pumps, initial investment, utility cost and operational cost.²⁻⁷ Application of forward osmosis as a typical pretreatment for reverse osmosis process is limited for its low water flux and membrane fouling.⁸⁻¹⁵ Therefore, it is of both fundamental and practical importance to develop suitable membrane materials to improve the separation efficiency (e.g., high rejection rate and water flux), which would be an effective solution to optimize water production costs and quality.^{3, 16-19}

Recently, two-dimensional (2D) materials including graphene oxide (GO) and transition metal dichalcogenides (TMDCs) laminar nanosheets have emerged as promising film/membrane materials in the field of water desalination and purification

as well as ion separation.²⁰⁻²⁵ In terms of ion separation, those 2D membranes have exhibited some rejection rates towards multiple cations during the osmosis process, which is attributed to the electrostatic attraction between cations and surface functional groups (e.g., hydroxyl and carboxyl) as controlled by the intercalation molecules (e.g., tannic acid, gallic acid, sodium alginate).²⁶⁻³¹ However, the membranes generally suffer from their low water flux (typically 25-75 L m⁻² h⁻¹ (LMH), 100 nm thick). In addition, the separation efficiency of the membranes is usually limited by the surface fouling and low rejection rates towards multiple small cations. Therefore, developing a suitable film or membrane material and fully understanding its permeation behavior for desalination process are urgently needed in order to significantly improve the rejection rate of those hydrated ions while maintaining high water flux.^{3, 18, 32-35}

The MXene films consisting of stacked MXene nanosheets have been widely investigated due to their unique electrical property and facile surface modification. Nb₂CT_x is a class of MXene nanosheets with very high surface area and hydrophilicity, which makes it a promising membrane material for water treatment as compared to other 2D MXene.^{27, 36-38} However, the separation efficiency for Nb₂CT_x nanosheet membrane is relatively low as compared to other 2D material membrane, which significantly limits its further advances towards energy-efficient membranes.^{20, 39, 40} It is known that the fabricated MXene nanosheets membrane with low rejection rate (~ 20%-50%) towards multiple ions could be enhanced through surface termination for better performance.^{1, 41-43} Hence, it is expected that the modification of Nb₂CT_x nanosheets membrane would promise a better separation performance for water treatment. Sodium alginate with

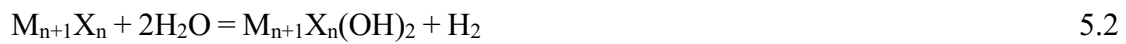
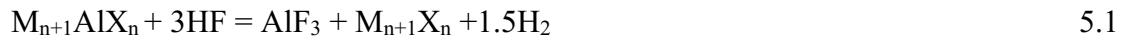
abundant carboxyl functional groups possesses outstanding ion rejection behavior, which has been widely used as a surface modifier. To the best of our knowledge, no previous work has been reported for Nb₂CT_x MXene nanosheets based membrane in the field of water treatment with ultrahigh rejection rates of multiple small cations/dyes while maintaining high water permeation rate through forward osmosis process and nanofiltration.^{44, 45}

In this work, we report a novel, facile and scalable method for preparing sodium alginate (SA)-modified Nb₂CT_x (NbSA) Mxene nanosheets membrane with high water flux and rejection rate towards multiple dyes and ions. The NbSA MXene nanosheets membrane exhibits enhanced ion rejection performance (>95%) towards multiple cations as compared to Nb₂CT_x MXene nanosheets membrane (~20%). In addition, the NbSA nanosheets membrane demonstrates an outstanding rejection performance (~100%, 100 ppm) towards multiple dyes including Basic blue, Rhodamine 6g and Toluidine blue through vacuum filtration (0.7 bar, ID = 36 mm, 100 mL solution per load run), while remaining high water flux (~2200 L m⁻² h⁻¹ bar⁻¹ (LMHB)) comparatively. This work demonstrates the potential application of NbSA membranes in wastewater treatment and provides new insights into the development and design of energy-efficient membranes based on functionalized 2D materials for various engineering and environmental applications.

5.2 Materials and Methods

5.2.1 Synthesis of Nb₂CT_x MXene nanosheets

Bulk Nb₂AlC (purity: 98%, particle size: 38 μm, - 400 mesh) was purchased from Weina Scientific (Shanghai) co. Ltd. 1.013 g Nb₂AlC powders were immersed in 50 mL Hydrofluoric Acid (49 wt%, Sigma Aldrich) with stirring at 200 rpm in a Teflon container at room temperature . After the reaction for 72 h, the bulk suspension was rinsed by ethanol (max 0.01% H₂O, Sigma Aldrich). The rinsed suspension was then taken out for centrifugation process (Eppendorf 5430) at 5000 rpm for 10 minutes. The sediments were washed by ethanol for at lease three times to completely remove hydrofluoric acid. The obtained multilayered Nb₂CT_x MXene nanosheets sediments were used for the next delamination process. The whole process undergoes the following reactions (5.1-5.3):^{33, 41, 46}



5.2.2 Delamination of Nb₂CT_x MXene nanosheets

The multilayered Nb₂CT_x MXene nanosheets sediments were mixed with dimethylsulfoxide (DMSO, >99.7 wt.%, Sigma Aldrich) under stirring for 18 h at room temperature, after which the suspension was centrifuged to separate the multilayered Nb₂CT_x MXene nanosheet sediments from the liquid DMSO. Deionized water (DI water) was then added to wash the sediments for several times for completely removal of the remaining DMSO. Thereafter, the residue was mixed with DI water at a weight ratio of 1:500 (Nb₂CT_x MXene nanosheets to water), and the suspension was then placed under ultrasonication process for 6 h. After ultrasonication, the suspension was centrifuged at 5000 rpm for 10 minutes, and the supernant was then filtrered by a porous polyvinylidene fluoride (PVDF) membrane substrate (47 mm diameter, 0.22 μm pore size, Fisher Scientific). The obtained sediments was dried in the oven at ~60 °C for 12 h. The dried powders were then redispersed in water at a weight ratio of 1:500 (Nb₂CT_x MXene nanosheets to water) and stored at room temperature.

5.2.3 Synthesis of NbSA nanosheets

The Nb₂CT_x MXene nanosheet suspension (2 mg/ml) was mixed with 1 mg/ml sodium alginate solution (Sigma Aldrich) at a weight ratio of 1:1. The mixture was then placed under ultrasonication process by Bransonic ultrasonic cleaner (2510R-DTH at 100 W, frequency of 42 kHz +/- 6%) for 24 h to create a homogeneous suspension. The resulted suspension was then dilluted and used as filtration precursor for membranes with varied thickness. In addition, the NbSA coated silica surface for AFM imaging characterization was prepared by spin coating (1000 rpm). The resulted pre-treated sample was dried in a desiccator at room temperature overnight before further

characterization.

5.2.4 Characterization

The Nb₂CT_x MXene nanosheets and NbSA nanosheets were characterized by Transmission electron microscopy (TEM), Atomic force microscopy (AFM), X-ray diffraction (XRD), Scanning electron microscopy (SEM) imaging and energy dispersive X-ray spectroscopy (EDX) mapping, X-ray photoelectron spectroscopy (XPS), UV-vis absorption spectra and Inductive Coupled Plasma (ICP) Emission Spectrometer. The TEM imaging was conducted on a JEOL JEM-ARM200CF S/TEM microscope operated at 200 kV. The AFM imaging was conducted in tapping mode (Icon, Bruker). Rigaku Ultima IV, multipurpose X-ray (Cu-source) diffraction system at 40 kV and 44 mA was used to obtain XRD powder mode patterns, and the scanning angle was from 5° to 80°. Zeiss Sigma Field Emission SEM was used for imaging and EDX mapping with a high resolution of ~10 nm. A Bruker EDX system was equipped with dual silicon drift detectors, each with an area of 60 mm² and a resolution of 123 eV. A Kratos AXIS type Ultra-x-ray photoelectron spectrometer was used for XPS.

5.2.5 Preparation of NbSA Membranes

NbSA membranes were fabricated through vacuum filtration method supported by commercialized Polyvinylidene fluoride (PVDF) membranes (0.22 μm, 47 mm in diameter, ~0.7 bar). The filtered NbSA membranes were dried under room

temperature for three days and stored in a petri dish sealed with parafilm for the water treatment.

5.2.6 NbSA Nanosheet Membrane testing condition

NaCl, KCl, LiCl, MgCl₂, and CaCl₂ were the salt solutions for the tests of water flux and cation rejection under osmotic static diffusion (**Figure S2**). The experimental setup consists of two equal-sized 200 ml reservoir. The duration time was set to be 360 min. The feed side was DI water and 0.25 M salt solution was used as draw side under room temperature and atmosphere. ICP Emission Spectrometer was used to obtain the cation concentrations in solutions after the above tests. For dye rejection test, 100 ppm of basic blue, rohdamine 6G and toluidine were used as feed solution through vacuum filtration (~0.7 bar). The filtered solution was taken out for further UV analysis based on the concentration standard line calibrated.

5.2.7 Osmotic pressure

The driving force for forward osmosis process is the osmotic pressure attributed to the concentration difference between feed side and draw side.

The osmotic pressure is calculated by using Vant Hoff equation^{47, 48}

$$\Pi = CRT \tag{5.4}$$

where Π is the osmotic pressure in atm (1 atm = 1.01325 bar), C is the concentration gradient across the membrane in g/mole, R is the universal constant 0.0821 atm*L/mole*K or 0.08314 L*bar*K⁻¹*mole⁻¹, and T is the temperature in K. The

osmotic pressure gradually decreases due to the water transport from feed side to draw side.

5.2.8 Water transport rate

The rate of water permeation through the semipermeable membrane is defined as:^{2, 47, 49}

$$J_w = \frac{\Delta V}{S \times h} \quad 5.5$$

where J_w is the water permeation rate in LMH, ΔV is the volume change for water after osmotic pressure static diffusion process at steady state, h is the steady state diffusion time, and S is the membrane effective area. During water transport process from feed side to draw side, a reverse transport for ions might occur.

5.2.9 Water transport rate (vacuum filtration)

$$J_w = \frac{\Delta V}{S \times h \times \Delta P} \quad 5.6$$

Where ΔP is the applied outer pressure.

5.2.10 Ion transport rate

The rate of cation permeation through the membrane is defined as:^{2, 47}

$$J_s = \frac{(C_t V_t - C_0 V_0)}{S \times h} \quad 5.7$$

where J_s is the flow rate of cation through the membrane, C_0, V_0 is the feed concentration and volume at time 0 and C_t, V_t indicate the final salt concentration and feed volume over time, h is the steady state diffusion time, and S is the membrane effective area.

5.2.11 Ion rejection rate

The ion rejection rate could be calculated as:^{2, 47}

$$\text{Ion rejection} = \left(1 - \frac{C_t V_t - C_0 V_0}{C_d V_d}\right) \times 100\% \quad 5.8$$

Where C_0 and V_0 are the initial feed concentration and volume, respectively; C_t and V_t indicate the salt concentration and feed volume at time t , respectively; C_d and V_d are the initial concentration and volume on the the draw side, respectively.

5.2.12 Dye rejection rate

The dye rejection rate could be calculated as:^{31, 50, 51}

$$\text{Dye rejection} = \left(1 - \frac{C_p V_p}{C_0 V_0}\right) \times 100\% \quad 5.9$$

Where, C_0 and V_0 are the initial feed concentration and volume, C_p and V_p are the permeate concentration and volume, respectively, at the final state.

5.3 Results and Discussion

5.3.1 Synthesis of Nb₂CT_x MXene and NbSA nanosheets

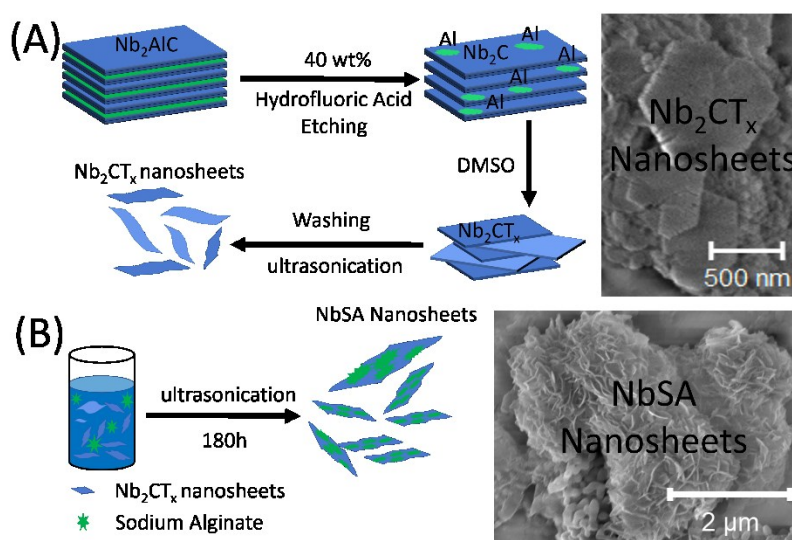


Figure 5.1. Schematic illustration for the synthesis process of Nb₂CT_x MXene nanosheets and NbSA nanosheets: (A) Hydrofluoric Acid (40 wt% concentration) etching process for the removal of Al from Nb₂AlC powders and the delamination process by using DMSO solution as polar solvent followed by washing and ultrasonication steps. (B) Ultrasonication process for the synthesis of NbSA nanosheets by using sodium alginate (1 mg/ml concentration).

The top-down method known as wet etching by hydrofluoric acid (HF) was used to synthesize Nb₂CT_x MXene nanosheets in this work (see the Experimental Section).^{27, 33, 52} The etchant (HF) can selectively etch Al atoms from the layered precursors Nb₂AlC (MAX phase),^{25, 53} and the schematic of the detailed process is shown in **Figure 5.1A**. In this process, the Al atoms are etched and occupied by O, OH or F atoms. As a result, the interactions between the MXene layers become weak since the Al-M metallic

bonds are replaced by hydrogen bonding and van der Waals interaction,^{28, 41, 52} thereby leading to the easy delamination under ultrasonication in the polar solvent (viz., DMSO in this work). The obtained Nb₂CT_x MXene nanosheets can be filtrated and stabilized in water, which enables further modification with eco-friendly and biodegradable water-soluble organic molecules.

It was reported that the binding energy of TMDCs nanosheets (~0.21 eV) was much lower than that between the nanosheets and small organic molecules (e.g., tannic acid ~75.95 eV).^{16, 26, 41} On the basis of binding energy consideration, the NbSA nanosheets could be readily synthesized by sonicating the mixture of sodium alginate solution and Nb₂CT_x MXene nanosheet solution as shown in **Figure 5.1B**, which could facilitate the two components to form strong hydrogen bonding interactions.^{54, 55} The Field Emission Scanning Electron Microscopy (FE-SEM) was used to investigate the morphology for both Nb₂CT_x MXene nanosheets and NbSA nanosheets as demonstrated in **Figure 5.1A** and **Figure 5.1B**, respectively. The lateral size of Nb₂CT_x MXene nanosheets is around 500-800 nm and the amorphous structure could be easily observed on the surface of NbSA nanosheets due to the adsorption of sodium alginate.

5.3.2 Characterization of NbSA nanosheets

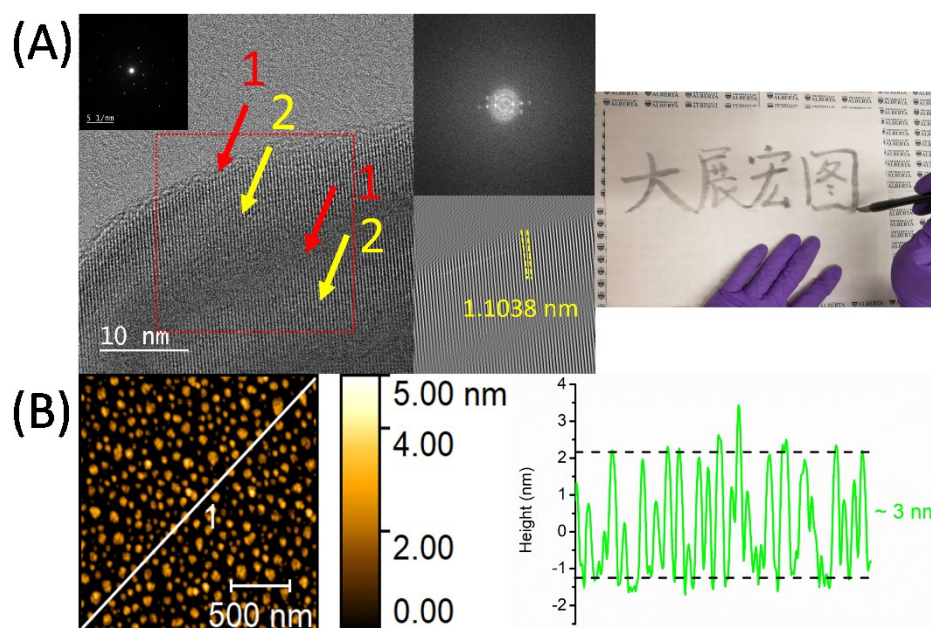


Figure 5.2. (A) High resolution TEM image of NbSA nanosheets (the inserted image on the right is written by a brush pen with MXene ink), (1) amorphous structure; (2) lattice structure with a lattice spacing of 1.1038 nm; (B) Atomic Force Microscopy (AFM) height profile of NbSA nanosheets coated on silica surface with the value of ~ 3 nm.

The NbSA nanosheets were further characterized by transmission electron microscopy (TEM) as shown in **Figure 5.2A**. Based on the high resolution TEM image, a homogeneous amorphous structure appeared in most regions of the nanosheets (**Figure 5.2A1**), while the crystalline structure could still be detected in some regions (**Figure 5.2A2**), illustrating the successful adsorption of sodium alginate molecules on Nb_2CT_x MXene nanosheets. The FFT and inverse FFT pattern in **Figure 5.2A** demonstrate the lattice spacing between Nb_2CT_x MXene nanosheets (crystalline region of NbSA nanosheets in TEM) are around 1.10 nm, which matches the lattice spacing

(0.9-1.2 nm) of Nb_2CT_x MXene nanosheets reported previously depending on the etching time period, etchant type, temperature and etchant concentration.^{38,46,56} Atomic force microscopy (AFM) was used to characterize the morphology of the NbSA nanosheets. As demonstrated in **Figure 5.2B**, the NbSA nanosheets are uniformly distributed on the silica wafer with the thickness of around 3 nm.

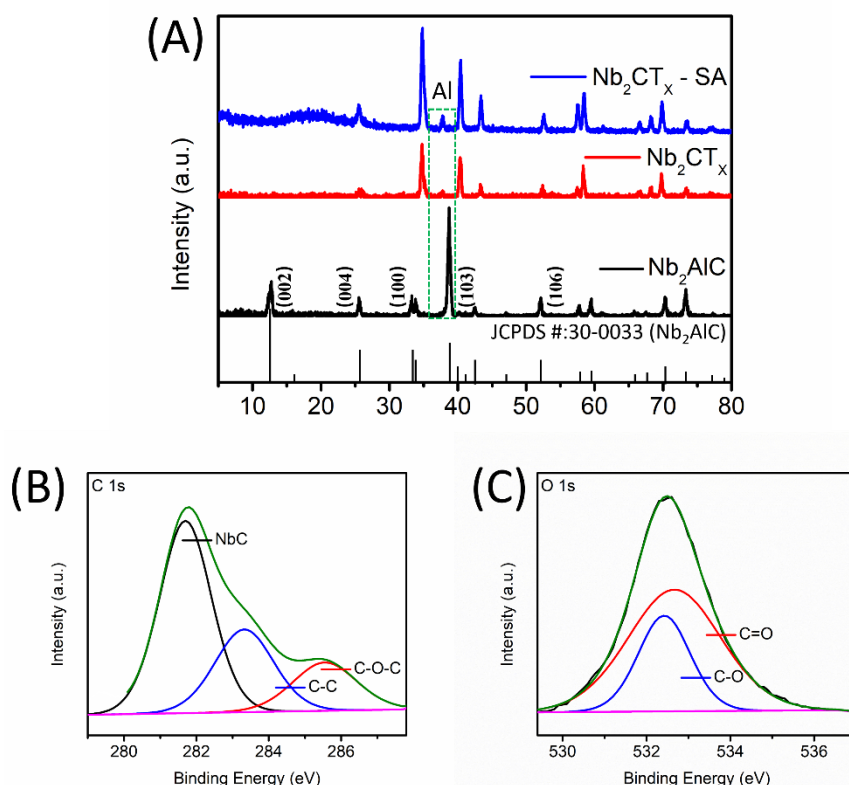


Figure 5.3. Characterization of NbSA nanosheets. (A) X-ray diffraction (XRD) analysis for Nb_2CT_x -SA (NbSA) nanosheets; Nb_2CT_x nanosheets and Nb_2AlC powders as compared to JCPDS #: 30-0033 (Nb_2AlC) card; (B and C) X-ray photoelectron spectroscopy (XPS) analysis for Nb_2CT_x – SA nanosheets (B) C1s and (C) O1s.

In addition, the NbSA nanosheets were further characterized by X-ray diffraction (XRD) and X-ray photoelectron spectroscopy (XPS) as shown in **Figure 5.3**. As compared to the XRD peak of Al at 39° for Nb_2AlC , an obviously shifted and

weakened peak was observed for Nb₂CT_x MXene and NbSA nanosheets as shown in **Figure 5.3A**, which demonstrates a successful delamination for Nb₂CT_x MXene nanosheets. The large amorphous peak between 15° and 25° detected for NbSA nanosheets corresponds to the sodium alginate molecules deposited on Nb₂CT_x MXene nanosheets. The XPS spectra for NbSA nanosheets in **Figure 5.3B** and **Figure 5.3C** show the peaks at binding energy of 281.5 eV, 283.5 eV and 285.5 eV for C1s corresponding to NbC, C-C and C-O-C bonds, respectively;⁵⁷⁻⁵⁹ while the binding energy peaks of 532.5 eV and 533.0 eV for O1s ascribe to C-O and C=O bonds, respectively.^{25, 60} The existence of C-C, C=O and C-O-C functional groups further demonstrate the successful modification of Nb₂CT_x MXene nanosheets with sodium alginate.

5.3.3 Synthesis and characterization of NbSA membrane

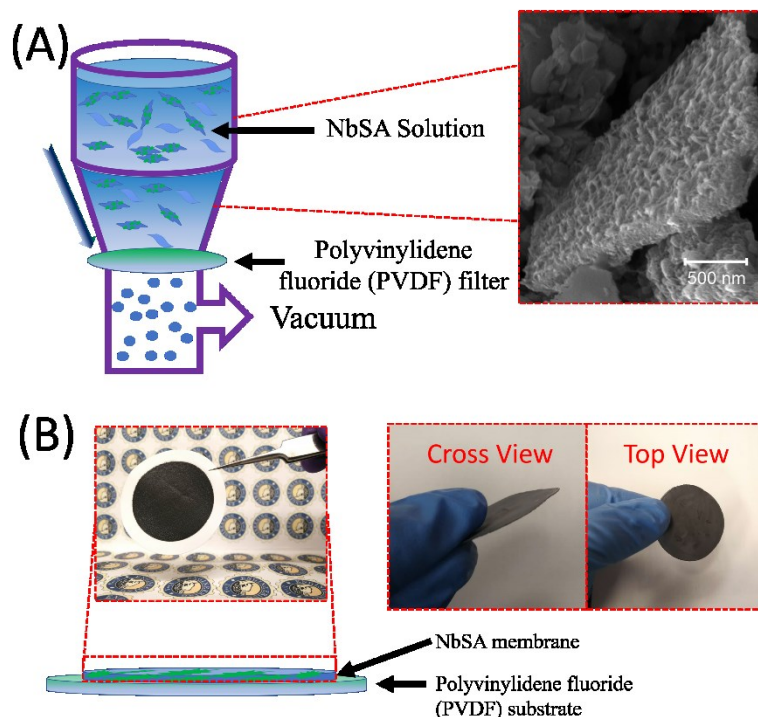


Figure 5.4. (A) Schematic illustration for synthesizing NbSA nanosheet (as shown on the right enlarged FE-SEM image) membrane through filtration method on polyvinylidene fluoride (PVDF) filter substrate (~ 0.7 bar) (B) Schematic image for the NbSA nanosheet membrane including cross view image and top view image.

Using the synthesized NbSA nanosheets (inserted image in **Figure 5.4A**), the NbSA membrane was fabricated through vacuum filtration as shown in **Figure 5.4A**. The photographs of the membrane in **Figure 5.4B** clearly show the cross view and top view of the free standing membrane. The membrane thickness could be controlled by altering the loading volume of NbSA solution (**Figure S5.1**). Nb₂CTx MXene nanosheets membrane, with an average pore size (~ 4 nm) (**Figure S5.5**) and porosity ($8\% \pm 3\%$) (calculated using **Eq. (S5.1)**), was also synthesized through the same filtration process for the comparison of water treatment.

5.3.4 Ion rejection performance through osmosis process

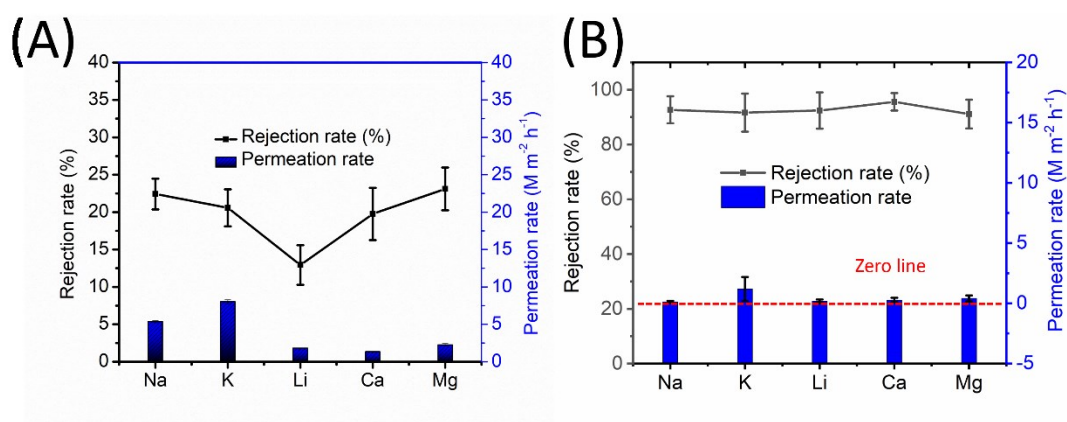


Figure 5.5. (A) Forward osmosis process results for Nb₂CT_x nanosheet membrane including the rejection rate/permeation rate for multiple cations; (B) Forward osmosis process results for NbSA nanosheet membrane. The feed side is DI water and the draw side is 0.25 M salt solution; both sides are under magnetic stirring at 100 rpm to avoid concentration gradient.

The 2D material type Nb₂CT_x MXene nanosheets membrane performs different rejection and permeation rates for various kinds of cations as shown in **Figure 5.5A**. The typical experimental setup for rejection and permeation for various kinds of cations under osmotic pressure static diffusion mode is shown in **Figure S5.2**. The osmotic pressure, water transport rate and ion transport rate could be calculated by using **Eq. 5.1** to **Eq. 5.3**, respectively. The feed side is 200 mL DI water and the draw side is 0.25 M salt solution. Therefore, the osmotic pressure is calculated to be 12 bar for monovalent salt solution (e.g., NaCl, KCl and LiCl) and 18 bar for divalent salt solution (e.g., MgCl₂ and CaCl₂). As shown in **Figure 5.5A**, the ionic permeation rates for different cations are determined as: K⁺ ($\sim 8.7 \pm 0.2\%$ mol m⁻² h⁻¹ (MMH)), Na⁺

($\sim 6.3 \pm 0.1\%$ MMH), Li^+ ($\sim 2.4 \pm 0.02\%$ MMH), Ca^{2+} ($\sim 2.3 \pm 0.02\%$ MMH), and Mg^{2+} ($\sim 1.7 \pm 0.02\%$ MMH). The different rates for cation permeation might be due to the combined influence of the water transport rates and the hydration numbers for each unique cations as shown in **Table S5.2**^{1, 25, 33}. The rejection rate for a 5- μm -thick Nb_2CT_x MXene nanosheets membrane (diffusion 10 h, salt concentration 0.25 M) is $21.2 \pm 2.1\%$ for K^+ , $22.5 \pm 2.2\%$ for Na^+ , $12.5 \pm 3.3\%$ for Li^+ , $20.4 \pm 4.2\%$ for Ca^{2+} , and $22.5 \pm 3.5\%$ for Mg^{2+} . The low cation rejection rates are mainly due to the presence of surface functional groups (e.g., -OH, -C-O-C-, -F and -COOH as detected by XPS analysis in **Figure 5.3**) on the Nb_2CT_x MXene nanosheets. The -OH and -COOH functional groups could have interactions with metal ions inside the Nb_2CT_x MXene nanosheets membrane layer channels. However, the pristine area for Nb_2CT_x nanosheet is not able to form chelates with metal ions, thereby resulting in the inefficient rejection of metal ions.

In terms of NbSA nanosheets membrane, the rejection rates for various kinds of cations could reach almost 100% as shown in **Figure 5.5B**. The rejection rate for a 5- μm -thick NbSA nanosheets membrane (diffusion 10 h, salt concentration 0.25 M) is $92.4 \pm 6.8\%$ for K^+ , $93.3 \pm 4.8\%$ for Na^+ , $95.2 \pm 4.1\%$ for Li^+ , $96.7 \pm 2.9\%$ for Ca^{2+} , and $92.5 \pm 5.2\%$ for Mg^{2+} . The corresponding ionic permeation rates for these cations are as follows: K^+ ($\sim 1.2 \pm 0.9\%$ MMH), Na^+ ($\sim 0.1 \pm 0.08\%$ MMH), Li^+ ($\sim 0.2 \pm 0.15\%$ MMH), Ca^{2+} ($\sim 0.3 \pm 0.2\%$ MMH), and Mg^{2+} ($\sim 0.4 \pm 0.2\%$ MMH). The obtained high cationic rejection rates are mainly because of the abundant hydroxyl and aromatic functional groups of sodium alginate molecules anchored on the nanosheets, which could easily

form chelates and cation- π interactions with the metal ions. Moreover, the deposited sodium alginate molecules could closely pack on the NbSA nanosheets, thus resulting in the formation of a dense membrane, which may block the cationic movement channel through the membrane. In addition, the NF process might have similar enhanced water permeation and cation rejection performance due to the negatively charged surface properties.

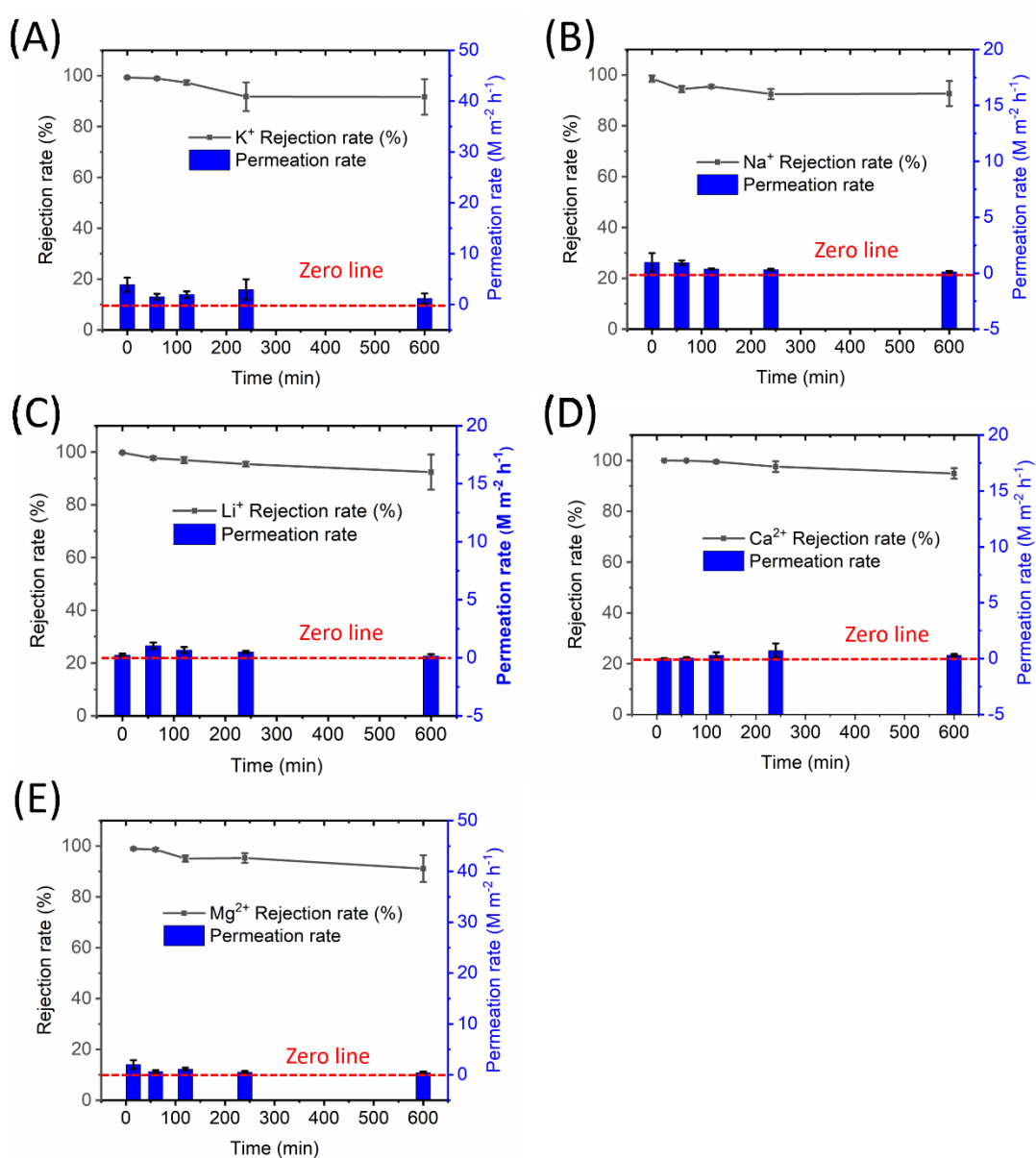


Figure 5.6. Stability test of the membrane for rejection rate versus permeation rate of multiple cations (A) K^+ ; (B) Na^+ ; (C) Li^+ ; (D) Ca^{2+} ; (E) Mg^{2+} . The process is forward osmosis with DI water as feed side and 0.25 M salt solution as draw side. The magnetic stir bars with 100 rpm speed are added at both sides to avoid concentration gradient.

In addition, the stability test for NbSA membrane is illustrated in **Figure 5.6A**, **Figure 5.6B**, **Figure 5.6C**, **Figure 5.6D** and **Figure 5.6E**, corresponding to K^+ , Na^+ , Li^+ , Ca^{2+} , and Mg^{2+} , respectively. The test time period is set as 600 minutes under room temperature and atmospheric pressure. Apparently, the NbSA nanosheets membrane is almost impermeable to all selected cation solutions and demonstrates the long-term rejection/permeation stability.

The osmosis static diffusion water fluxes of the 5- μ m Nb_2CT_x MXene nanosheets membrane and 5- μ m NbSA nanosheets membrane are displayed on **Figure S5.3**. Evidently, the 5- μ m NbSA nanosheets membranes fabricated in this work exhibited fast water flux at around 1.7-2.2 LMH, while maintaining ultrahigh rejection rates towards multiple cations (e.g. K^+ , Na^+ , Li^+ , Ca^{2+} and Mg^{2+}). The comparison results are listed in **Table S5.3**. At a comparable thickness (e.g. $\sim 5 \mu$ m), previous work reported that graphene oxide (GO) membrane exhibited the water flux of ~ 0.007 LMH, achieving a 97% NaCl rejection rate; MoS_2/SY (Solvent yellow) membrane showed $\sim 99\%$ NaCl rejection with the water flux of ~ 0.033 LMH.^{25, 61, 62} The conventional MoS_2 membrane shows a high-water flux of ~ 75 LMH, while only $\sim 27\%$ rejection rate is achieved.^{25, 61, 62} Similarly, the MoS_2/NR (Neutral red) membrane demonstrates a 105 LMH water flux but $\sim 37\%$ rejection rate, and commercialized PVDF membrane

performs ultrahigh water flux with the value of 2300 LMH but permeable to all solutes as well. Moreover, the $\text{Ti}_3\text{C}_2\text{T}_x$ MXene nanosheet membrane with a thickness of ~ 1.5 μm exhibits a water flux value of 37.4 LMH with only $\sim 20\%$ rejection rate towards NaCl ,^{46, 52, 57} which is far from practical application.

5.3.5 Vacuum filtration process towards multiple dyes

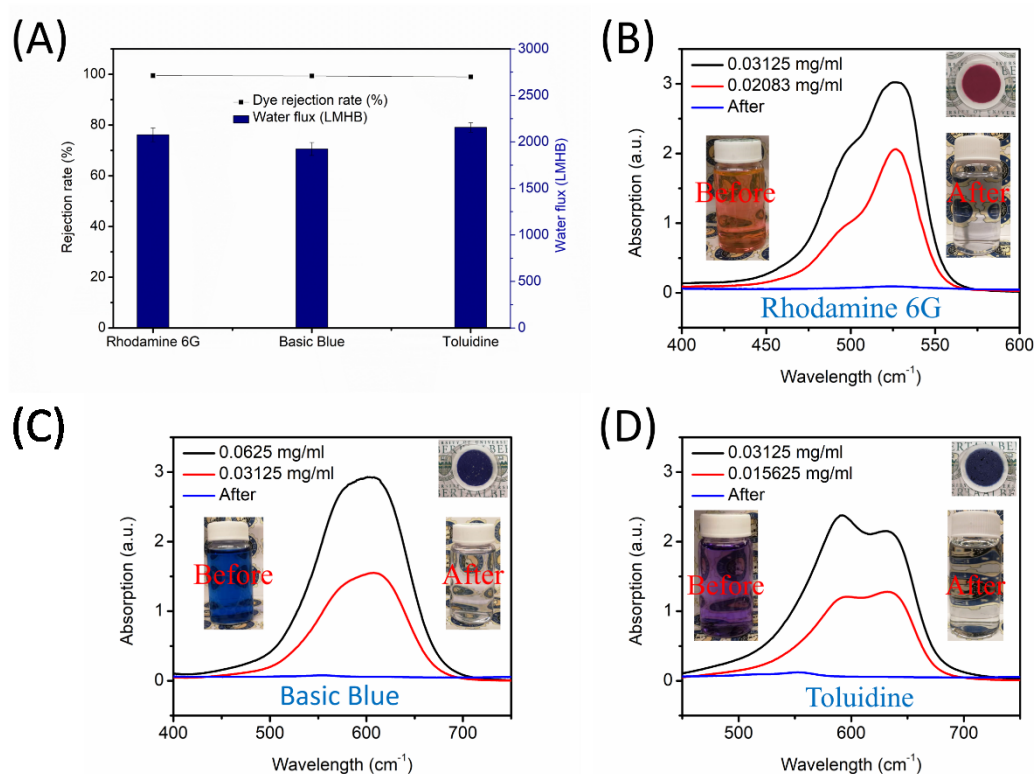


Figure 5.7. (A) Water flux and rejection rate toward target dyes (Rhodamine 6G, Basic Blue and Toluidine); (B) UV standard concentration line for Rhodamine 6G; (C) UV standard concentration line for Basic Blue; (D) UV standard concentration line for Toluidine Blue. The vacuum is ~ 0.7 bar and the dye concentration is 100 ppm.

The synthesized NbSA membrane possesses high water flux towards multiple dyes while remaining almost impermeable to all those selected dyes. As shown in **Figure 5.7**, the NbSA nanosheets membrane demonstrates an ultrahigh rejection rates

(~100%) toward multiple target dyes including Rhodamine 6G, Basic Blue and Toluidine Blue at a concentration of 100 ppm, while maintaining high water flux of ~2200 LMHB through vacuum filtration process. Previous works as shown in **Table S5.4** demonstrate some 2D type material membranes in the application of dye and salt rejection through vacuum filtration method display either low rejection rate or low water flux. For example, a 26-33 nm GO/FLG (Filaggrin) membrane shows only ~80% rejection rate towards Rhodamine B dye; NF2A type membrane with a thickness of 22-53 nm demonstrates a high rejection rate of 99.2% towards Methylene Blue dye with only 19.5 LMHB of the water flux; many other types such as Desal 5DK membrane possess 95% rejection rate for Direct red while only 25-35 LMHB water flux is achieved; Polysulfone membrane has a rejection rate of 97% with only 0.23-0.28 LMHB water flux value. In this work, the 5- μ m thick NbSA type membrane demonstrates ultrahigh rejection rate towards multiple dyes (~100%) – Rhodamine 6G, Basic Blue and Toluidine Blue as target dyes while maintaining high water flux comparatively (~2200 LMHB).

In addition, the membrane filtration process is relatively stable with only 13.55% loss in water flux after 2000 s filtration as shown in **Figure 5.8**. The outstanding separation performance listed above demonstrates the great potential application of the as-prepared 2D materials in terms of the wastewater treatment. The filtration process for high rejection rate and water flux toward multiple dyes is also shown in the two supporting videos for two independent tests in the Supplementary Information.

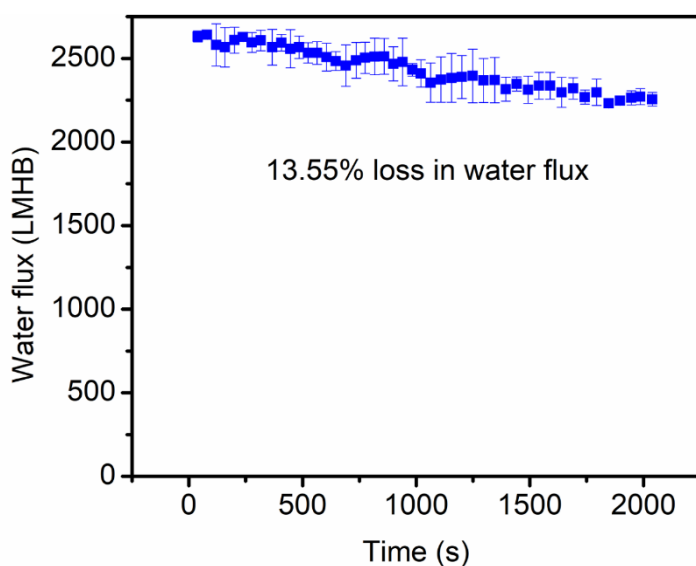


Figure 5.8. Declines in water flux with Basic blue dye solution (100 ppm) from filtration up to 2000 s.

5.3.6 $\text{Li}^+/\text{Mg}^{2+}$ selective separation after long-term stability

Lithium is a significant energy material and a strategic resource for the twenty-first century. The highly active lithium is naturally and abundantly occurring in compound form with water molecules or other ions (especially Mg^{2+}).^{63, 64} Therefore, it is urgently needed to separate lithium from those compounds to meet the increasing demand globally. In this work, it is surprisingly found that the NbSA nanosheet membrane after long-term stability for the forward osmosis process (~10 h) shows selective permeation performance for $\text{Li}^+/\text{Mg}^{2+}$ mixture solution at a ratio of 1:1 (0.25 M draw solution concentration) as shown in **Figure S5.4**. The selective permeation might be due to the combined influence of the water exchange rates and the hydration numbers for both Li^+ and Mg^{2+} as shown in **Table S5.2**.^{1, 25, 33} It was worth mentioning that within a nanoconfined channels, the water molecules could form clusters with

either Li^+ or Mg^{2+} ; meanwhile, due to the concentration gradient, the ion-water clusters would move through the nanoconfined channels by dynamic water-ion exchange process. From **Table S5.2**, the water-ion exchange rate for Li^+ has three magnitude times higher than Mg^{2+} , resulting in a selective separation performance.⁶⁵⁻⁶⁷

5.4 Conclusion

In this study, sodium alginate modified Nb_2CTx MXene nanosheets have been successfully synthesized through one-step ultrasonication method. The as-prepared NbSA nanosheet membrane from the vacuum filtration process shows excellent non-swelling stability in water and could be freely standable after the evaporation of moisture. The NbSA nanosheet membrane with a thickness of 5 μm shows ultrahigh rejection rates (>95%) towards multiple cations while maintaining high water flux of 1.7-2.2 LMH under forward osmosis process, which is competitive to benchmarking membranes reported previously. In terms of vacuum filtration, the NbSA nanosheet membrane demonstrates ultrahigh rejection rates (~100%) towards multiple target dyes including Rhodamine 6G, Basic Blue and Toluidine Blue while possesses high water flux of ~2200 LMHB, which is of superior level of separation performance and has never been reported for Nb_2CTx MXene nanosheets-based membranes.

Previously, the 2D material based membranes demonstrate either relatively low water permeation with high rejection rate or high water permeation with low rejection rate towards target contaminants.^{31, 35, 51, 54, 55} The performance of those membranes was limited by its surface properties and area, which could be investigated further. This study provides a one-step facile ultrasonication method for the fabrication of sodium alginate modified Nb_2CTx MXene nanosheets. The introduction of surface functional groups (e.g., -OH, -C-O-C- and -COOH) of the membrane could lead to a high water permeation and rejection rate towards multiple ions and dyes. This work has

demonstrated the building up of energy-efficient membranes in terms of desalination and wastewater treatment, holding great promise for the design and development of novel functionalized 2D material membranes in a wide range of engineering and environmental applications. For future study, the mechanism for underlying the transport phenomena of hydrated dyes or ions within nanoconfined lamellar channels could be investigated. Moreover, the selective separation performance and mechanism on $\text{Li}^+/\text{Mg}^{2+}$ mixture solution, which could be further investigated in details.

5.5 References

1. Osti, N. C.; Naguib, M.; Ostadhossein, A.; Xie, Y.; Kent, P. R. C.; Dyatkin, B.; Rother, G.; Heller, W. T.; van Duin, A. C. T.; Gogotsi, Y.; Mamontov, E., Effect of Metal Ion Intercalation on the Structure of MXene and Water Dynamics on its Internal Surfaces. *ACS Applied Materials & Interfaces* **2016**, *8* (14), 8859-8863.
2. Joshi, R. K.; Carbone, P.; Wang, F. C.; Kravets, V. G.; Su, Y.; Grigorieva, I. V.; Wu, H. A.; Geim, A. K.; Nair, R. R., Precise and Ultrafast Molecular Sieving Through Graphene Oxide Membranes. *Science* **2014**, *343* (6172), 752-754.
3. Ma, J.; Ping, D.; Dong, X., Recent Developments of Graphene Oxide-Based Membranes: A Review. *Membranes* **2017**, *7* (3), 52.
4. Kim, H. W.; Yoon, H. W.; Yoon, S.-M.; Yoo, B. M.; Ahn, B. K.; Cho, Y. H.; Shin, H. J.; Yang, H.; Paik, U.; Kwon, S.; Choi, J.-Y.; Park, H. B., Selective Gas Transport Through Few-Layered Graphene and Graphene Oxide Membranes. *Science* **2013**, *342* (6154), 91-95.
5. Chen, C.; Huang, Z.; Jiao, Y.; Shi, L.-A.; Zhang, Y.; Li, J.; Li, C.; Lv, X.; Wu, S.; Hu, Y.; Zhu, W.; Wu, D.; Chu, J.; Jiang, L., In Situ Reversible Control between Sliding and Pinning for Diverse Liquids under Ultra-Low Voltage. *ACS Nano* **2019**, *13* (5), 5742-5752.
6. Meng, J.; Li, P.; Cao, B., High-Flux Direct-Contact Pervaporation Membranes for Desalination. *ACS Applied Materials & Interfaces* **2019**, *11* (31), 28461-28468.
7. Chen, L.; Huang, Y.; Song, L.; Yin, W.; Hou, L.; Liu, X.; Chen, T., Biofriendly and Regenerable Emotional Monitor from Interfacial Ultrathin 2D PDA/AuNPs Cross-

- linking Films. *ACS Applied Materials & Interfaces* **2019**, *11* (39), 36259-36269.
8. Hirunpinyopas, W.; Prestat, E.; Worrall, S. D.; Haigh, S. J.; Dryfe, R. A. W.; Bissett, M. A., Desalination and Nanofiltration through Functionalized Laminar MoS₂ Membranes. *ACS Nano* **2017**, *11* (11), 11082-11090.
 9. Xu, Z.; Ye, H.; Li, H.; Xu, Y.; Wang, C.; Yin, J.; Zhu, H., Enhanced Lithium Ion Storage Performance of Tannic Acid in LiTFSI Electrolyte. *ACS Omega* **2017**, *2* (4), 1273-1278.
 10. Chu, K. H.; Huang, Y.; Yu, M.; Her, N.; Flora, J. R. V.; Park, C. M.; Kim, S.; Cho, J.; Yoon, Y., Evaluation of Humic Acid and Tannic Acid Fouling in Graphene Oxide-Coated Ultrafiltration Membranes. *ACS Applied Materials & Interfaces* **2016**, *8* (34), 22270-22279.
 11. Zhao, W.; Liu, H.; Liu, Y.; Jian, M.; Gao, L.; Wang, H.; Zhang, X., Thin-Film Nanocomposite Forward-Osmosis Membranes on Hydrophilic Microfiltration Support with an Intermediate Layer of Graphene Oxide and Multiwall Carbon Nanotube. *ACS Applied Materials & Interfaces* **2018**, *10* (40), 34464-34474.
 12. Jatukaran, A.; Zhong, J.; Persad, A. H.; Xu, Y.; Mostowfi, F.; Sinton, D., Direct Visualization of Evaporation in a Two-Dimensional Nanoporous Model for Unconventional Natural Gas. *ACS Applied Nano Materials* **2018**, *1* (3), 1332-1338.
 13. Li, Y.; Meng, H.; Liu, Y.; Narkar, A.; Lee, B. P., Gelatin Microgel Incorporated Poly(ethylene glycol)-Based Bioadhesive with Enhanced Adhesive Property and Bioactivity. *ACS Applied Materials & Interfaces* **2016**, *8* (19), 11980-11989.
 14. Wang, J.; Fang, R.; Hou, J.; Zhang, H.; Tian, Y.; Wang, H.; Jiang, L., Oscillatory

Reaction Induced Periodic C-Quadruplex DNA Gating of Artificial Ion Channels. *ACS Nano* **2017**, *11* (3), 3022-3029.

15. Wang, Y.; Liu, X.; Li, S.; Li, T.; Song, Y.; Li, Z.; Zhang, W.; Sun, J., Transparent, Healable Elastomers with High Mechanical Strength and Elasticity Derived from Hydrogen-Bonded Polymer Complexes. *ACS Applied Materials & Interfaces* **2017**, *9* (34), 29120-29129.

16. Guan, G.; Zhang, S.; Liu, S.; Cai, Y.; Low, M.; Teng, C. P.; Phang, I. Y.; Cheng, Y.; Duei, K. L.; Srinivasan, B. M.; Zheng, Y.; Zhang, Y.-W.; Han, M.-Y., Protein Induces Layer-by-Layer Exfoliation of Transition Metal Dichalcogenides. *Journal of the American Chemical Society* **2015**, *137* (19), 6152-6155.

17. Chen, X.; Qiu, M.; Ding, H.; Fu, K.; Fan, Y., A reduced graphene oxide nanofiltration membrane intercalated by well-dispersed carbon nanotubes for drinking water purification. *Nanoscale* **2016**, *8* (10), 5696-5705.

18. Deng, M.; Kwac, K.; Li, M.; Jung, Y.; Park, H. G., Stability, Molecular Sieving, and Ion Diffusion Selectivity of a Lamellar Membrane from Two-Dimensional Molybdenum Disulfide. *Nano Letters* **2017**, *17* (4), 2342-2348.

19. Hao, N.; Nie, Y.; Xu, Z.; Jin, C.; Fyda, T. J.; Zhang, J. X. J., Microfluidics-enabled acceleration of Fenton oxidation for degradation of organic dyes with rod-like zero-valent iron nanoassemblies. *Journal of Colloid and Interface Science* **2020**, *559*, 254-262.

20. Levita, G.; Restuccia, P.; Righi, M. C., Graphene and MoS₂ interacting with water: A comparison by ab initio calculations. *Carbon* **2016**, *107*, 878-884.

21. Mi, B., Graphene Oxide Membranes for Ionic and Molecular Sieving. *Science* **2014**, *343* (6172), 740-742.
22. Yu, L.; Lee, Y.-H.; Ling, X.; Santos, E. J. G.; Shin, Y. C.; Lin, Y.; Dubey, M.; Kaxiras, E.; Kong, J.; Wang, H.; Palacios, T., Graphene/MoS₂ Hybrid Technology for Large-Scale Two-Dimensional Electronics. *Nano Letters* **2014**, *14* (6), 3055-3063.
23. Yan, Y. G.; Wang, W. S.; Li, W.; Loh, K. P.; Zhang, J., A graphene-like membrane with an ultrahigh water flux for desalination. *Nanoscale* **2017**, *9* (47), 18951-18958.
24. Heiranian, M.; Farimani, A. B.; Aluru, N. R., Water desalination with a single-layer MoS₂ nanopore. *Nature Communications* **2015**, *6*, 8616.
25. Quain, E.; Mathis, T. S.; Kurra, N.; Maleski, K.; Van Aken, K. L.; Alhabeab, M.; Alshareef, H. N.; Gogotsi, Y., Direct Writing of Additive-Free MXene-in-Water Ink for Electronics and Energy Storage. *Advanced Materials Technologies* **2019**, *4* (1), 1800256.
26. Ghidui, M.; Kota, S.; Drozd, V.; Barsoum, M. W., Pressure-induced shear and interlayer expansion in Ti₃C₂ MXene in the presence of water. *Science Advances* **2018**, *4* (1), eaao6850.
27. Sarycheva, A.; Polemi, A.; Liu, Y.; Dandekar, K.; Anasori, B.; Gogotsi, Y., 2D titanium carbide (MXene) for wireless communication. *Science Advances* **2018**, *4* (9), eaau0920.
28. Huang, S.; Mochalin, V. N., Hydrolysis of 2D Transition-Metal Carbides (MXenes) in Colloidal Solutions. *Inorganic Chemistry* **2019**, *58* (3), 1958-1966.
29. Di Vitantonio, G.; Wang, T.; Haase, M. F.; Stebe, K. J.; Lee, D., Robust Bijels for

- Reactive Separation via Silica-Reinforced Nanoparticle Layers. *ACS Nano* **2019**, *13* (1), 26-31.
30. Gurera, D.; Bhushan, B., Designing bioinspired conical surfaces for water collection from condensation. *Journal of Colloid and Interface Science* **2020**, *560*, 138-148.
31. Guo, D.; Xiao, Y.; Li, T.; Zhou, Q.; Shen, L.; Li, R.; Xu, Y.; Lin, H., Fabrication of high-performance composite nanofiltration membranes for dye wastewater treatment: mussel-inspired layer-by-layer self-assembly. *Journal of Colloid and Interface Science* **2020**, *560*, 273-283.
32. Zhu, J.; Tian, M.; Hou, J.; Wang, J.; Lin, J.; Zhang, Y.; Liu, J.; Van der Bruggen, B., Surface zwitterionic functionalized graphene oxide for a novel loose nanofiltration membrane. *Journal of Materials Chemistry A* **2016**, *4* (5), 1980-1990.
33. Halim, J.; Kota, S.; Lukatskaya, M. R.; Naguib, M.; Zhao, M.-Q.; Moon, E. J.; Pitock, J.; Nanda, J.; May, S. J.; Gogotsi, Y.; Barsoum, M. W., Synthesis and Characterization of 2D Molybdenum Carbide (MXene). *Advanced Functional Materials* **2016**, *26* (18), 3118-3127.
34. Alhabeab, M.; Maleski, K.; Anasori, B.; Lelyukh, P.; Clark, L.; Sin, S.; Gogotsi, Y., Guidelines for Synthesis and Processing of Two-Dimensional Titanium Carbide (Ti₃C₂T_x MXene). *Chemistry of Materials* **2017**, *29* (18), 7633-7644.
35. Hu, W.; Cui, X.; Xiang, L.; Gong, L.; Zhang, L.; Gao, M.; Wang, W.; Zhang, J.; Liu, F.; Yan, B.; Zeng, H., Tannic acid modified MoS₂ nanosheet membranes with superior water flux and ion/dye rejection. *Journal of Colloid and Interface Science* **2020**,

560, 177-185.

36. Zhang, C.; McKeon, L.; Kremer, M. P.; Park, S.-H.; Ronan, O.; Seral-Ascaso, A.; Barwich, S.; Coileáin, C. Ó.; McEvoy, N.; Nerl, H. C.; Anasori, B.; Coleman, J. N.; Gogotsi, Y.; Nicolosi, V., Additive-free MXene inks and direct printing of micro-supercapacitors. *Nature Communications* **2019**, *10* (1), 1795.

37. Hart, J. L.; Hantanasirisakul, K.; Lang, A. C.; Anasori, B.; Pinto, D.; Pivak, Y.; van Omme, J. T.; May, S. J.; Gogotsi, Y.; Taheri, M. L., Control of MXenes' electronic properties through termination and intercalation. *Nature Communications* **2019**, *10* (1), 522.

38. Jiang, H.; Wang, Z.; Yang, Q.; Tan, L.; Dong, L.; Dong, M., Ultrathin Ti₃C₂T_x (MXene) Nanosheet-Wrapped NiSe₂ Octahedral Crystal for Enhanced Supercapacitor Performance and Synergetic Electrocatalytic Water Splitting. *Nano-Micro Letters* **2019**, *11* (1), 31.

39. Wang, L.-C.; Bao, S.-K.; Luo, J.; Wang, Y.-H.; Nie, Y.-C.; Zou, J.-P., Efficient exfoliation of bulk MoS₂ to nanosheets by mixed-solvent refluxing method. *International Journal of Hydrogen Energy* **2016**, *41* (25), 10737-10743.

40. Oener, S. Z.; Ardo, S.; Boettcher, S. W., Ionic Processes in Water Electrolysis: The Role of Ion-Selective Membranes. *ACS Energy Letters* **2017**, *2* (11), 2625-2634.

41. Zhang, J.; Zhao, Y.; Guo, X.; Chen, C.; Dong, C.-L.; Liu, R.-S.; Han, C.-P.; Li, Y.; Gogotsi, Y.; Wang, G., Single platinum atoms immobilized on an MXene as an efficient catalyst for the hydrogen evolution reaction. *Nature Catalysis* **2018**, *1* (12), 985-992.

42. Sugahara, A.; Ando, Y.; Kajiyama, S.; Yazawa, K.; Gotoh, K.; Otani, M.; Okubo,

- M.; Yamada, A., Negative dielectric constant of water confined in nanosheets. *Nature Communications* **2019**, *10* (1), 850.
43. Zhang, Y.; Zhang, N.; Ge, C., First-Principles Studies of Adsorptive Remediation of Water and Air Pollutants Using Two-Dimensional MXene Materials. *Materials* **2018**, *11* (11), 2281.
44. Sobolčiak, P.; Ali, A.; Hassan, M. K.; Helal, M. I.; Tanvir, A.; Popelka, A.; Al-Maadeed, M. A.; Krupa, I.; Mahmoud, K. A., 2D Ti₃C₂T_x (MXene)-reinforced polyvinyl alcohol (PVA) nanofibers with enhanced mechanical and electrical properties. *PLOS ONE* **2017**, *12* (8), e0183705.
45. Hu, W.; Zhang, P.; Liu, X.; Yan, B.; Xiang, L.; Zhang, J.; Gong, L.; Huang, J.; Cui, K.; Zhu, L.; Zeng, H., An amphiphobic graphene-based hydrogel as oil-water separator and oil fence material. *Chemical Engineering Journal* **2018**, *353*, 708-716.
46. Michael, J.; Qifeng, Z.; Danling, W., Titanium carbide MXene: Synthesis, electrical and optical properties and their applications in sensors and energy storage devices. *Nanomaterials and Nanotechnology* **2019**, *9*, 1847980418824470.
47. Lee, K. P.; Arnot, T. C.; Mattia, D., A review of reverse osmosis membrane materials for desalination—Development to date and future potential. *Journal of Membrane Science* **2011**, *370* (1), 1-22.
48. Shi, C.; Xie, L.; Zhang, L.; Lu, X.; Zeng, H., Probing the interaction mechanism between oil droplets with asphaltenes and solid surfaces using AFM. *Journal of Colloid and Interface Science* **2020**, *558*, 173-181.
49. Liu, J.; Cui, X.; Xie, L.; Huang, J.; Zhang, L.; Liu, J.; Wang, X.; Wang, J.; Zeng,

H., Probing effects of molecular-level heterogeneity of surface hydrophobicity on hydrophobic interactions in air/water/solid systems. *Journal of Colloid and Interface Science* **2019**, *557*, 438-449.

50. Yu, W.; Liu, Y.; Xu, Y.; Li, R.; Chen, J.; Liao, B.-Q.; Shen, L.; Lin, H., A conductive PVDF-Ni membrane with superior rejection, permeance and antifouling ability via electric assisted in-situ aeration for dye separation. *Journal of Membrane Science* **2019**, *581*, 401-412.

51. Chen, Y.; Teng, J.; Liao, B.-Q.; Li, R.; Lin, H., Molecular insights into the impacts of iron(III) ions on membrane fouling by alginate. *Chemosphere* **2020**, *242*, 125232.

52. Tang, H.; Hu, Q.; Zheng, M.; Chi, Y.; Qin, X.; Pang, H.; Xu, Q., MXene-2D layered electrode materials for energy storage. *Progress in Natural Science: Materials International* **2018**, *28* (2), 133-147.

53. Rasid, Z. A. M.; Omar, M. F.; Nazeri, M. F. M.; A'ziz, M. A. A.; Szota, M., Low Cost Synthesis Method of Two-Dimensional Titanium Carbide MXene. *IOP Conference Series: Materials Science and Engineering* **2017**, *209*, 012001.

54. Zhou, Z.; Liu, J.; Zhang, X.; Tian, D.; Zhan, Z.; Lu, C., Ultrathin MXene/Calcium Alginate Aerogel Film for High-Performance Electromagnetic Interference Shielding. **2019**, *6* (6), 1802040.

55. Xuan, D.; Zhou, Y.; Nie, W.; Chen, P., Sodium alginate-assisted exfoliation of MoS₂ and its reinforcement in polymer nanocomposites. *Carbohydrate Polymers* **2017**, *155*, 40-48.

56. Ma, H.; Shen, Z.; Ben, S., Understanding the exfoliation and dispersion of MoS₂

nanosheets in pure water. *Journal of Colloid and Interface Science* **2018**, *517*, 204-212.

57. Hyosung, A.; Touseef, H.; Smit, S.; Huili, G.; Anish, P.; Ian, E.; Xiaofei, Z.; Miladin, R.; Micah J., G.; Jodie L., L., *Water Sorption in MXene/Polyelectrolyte Multilayers for Ultrafast Humidity Sensing*. 2019.

58. Hanmei, J.; Zegao, W.; Qian, Y.; Luxi, T.; Lichun, D.; Mingdong, D., Ultrathin Ti₃C₂T_x (MXene) Nanosheets Wrapped NiSe₂ Octahedral Crystal for Enhanced Supercapacitor Performance and Synergetic Electrocatalytic Water Splitting. *Nano-Micro Letters* **2019**, *11*, 31.

59. Bao, W.; Tang, X.; Guo, X.; Choi, S.; Wang, C.; Gogotsi, Y.; Wang, G., Porous Cryo-Dried MXene for Efficient Capacitive Deionization. *Joule* **2018**, *2* (4), 778-787.

60. Zhu, J.; Li, G.; Feng, C.; Wang, L.; Zhang, W., Effect of Delaminated MXene (Ti₃C₂) on the Performance of Cement Paste. *Journal of Nanomaterials* **2019**, *2019*, 8.

61. Wang, S.; Wu, Y.; Zhang, N.; He, G.; Xin, Q.; Wu, X.; Wu, H.; Cao, X.; Guiver, M. D.; Jiang, Z., A highly permeable graphene oxide membrane with fast and selective transport nanochannels for efficient carbon capture. *Energy & Environmental Science* **2016**, *9* (10), 3107-3112.

62. Chu, X. S.; Yousaf, A.; Li, D. O.; Tang, A. A.; Debnath, A.; Ma, D.; Green, A. A.; Santos, E. J. G.; Wang, Q. H., Direct Covalent Chemical Functionalization of Unmodified Two-Dimensional Molybdenum Disulfide. *Chemistry of Materials* **2018**, *30* (6), 2112-2128.

63. Hu, S.; Sun, Y.; Pu, M.; Yun, R.; Xiang, X., Determination of Boundary Conditions for Highly Efficient Separation of Magnesium and Lithium from Salt Lake Brine by

Reaction-Coupled Separation Technology. *Separation and Purification Technology* **2019**, 115813.

64. Yang, G.; Shi, H.; Liu, W.; Xing, W.; Xu, N., Investigation of Mg²⁺/Li⁺ Separation by Nanofiltration. *Chinese Journal of Chemical Engineering* **2011**, 19 (4), 586-591.

65. Yeager, H. L., Cation and Water Diffusion in Nafion Ion Exchange Membranes: Influence of Polymer Structure. *Journal of The Electrochemical Society* **1981**, 128 (9), 1880.

66. Helm, L.; Merbach, A. E., Water exchange on metal ions: experiments and simulations. *Coordination Chemistry Reviews* **1999**, 187 (1), 151-181.

67. Neely, J.; Connick, R., Rate of water exchange from hydrated magnesium ion. *Journal of the American Chemical Society* **1970**, 92 (11), 3476-3478.

68. Xu, X.-L.; Lin, F.-W.; Du, Y.; Zhang, X.; Wu, J.; Xu, Z.-K., Graphene Oxide Nanofiltration Membranes Stabilized by Cationic Porphyrin for High Salt Rejection. *ACS Applied Materials & Interfaces* **2016**, 8 (20), 12588-12593.

69. Wang, J.; Zhang, P.; Liang, B.; Liu, Y.; Xu, T.; Wang, L.; Cao, B.; Pan, K., Graphene Oxide as an Effective Barrier on a Porous Nanofibrous Membrane for Water Treatment. *ACS Applied Materials & Interfaces* **2016**, 8 (9), 6211-6218.

70. Yadong, Z.; Zhaoshun, M.; Qi, S.; Haiqi, G.; Yuzhen, L.; Yunhui, W.; Dewei, R.; Kaiming, D.; Ruifeng, L., Nanoporous MoS₂ monolayer as a promising membrane for purifying hydrogen and enriching methane. *Journal of Physics: Condensed Matter* **2017**, 29 (37), 375201.

71. Oh, S. J.; Kim, N.; Lee, Y. T., Preparation and characterization of PVDF/TiO₂

organic–inorganic composite membranes for fouling resistance improvement. *Journal of Membrane Science* **2009**, *345* (1), 13-20.

72. Ren, C. E.; Hatzell, K. B.; Alhabeab, M.; Ling, Z.; Mahmoud, K. A.; Gogotsi, Y., Charge- and Size-Selective Ion Sieving Through Ti₃C₂T_x MXene Membranes. *The Journal of Physical Chemistry Letters* **2015**, *6* (20), 4026-4031.

73. Hu, M.; Mi, B., Enabling Graphene Oxide Nanosheets as Water Separation Membranes. *Environmental Science & Technology* **2013**, *47* (8), 3715-3723.

74. Akbari, A.; Sheath, P.; Martin, S. T.; Shinde, D. B.; Shaibani, M.; Banerjee, P. C.; Tkacz, R.; Bhattacharyya, D.; Majumder, M., Large-area graphene-based nanofiltration membranes by shear alignment of discotic nematic liquid crystals of graphene oxide. *Nature Communications* **2016**, *7*, 10891.

75. Han, Y.; Jiang, Y.; Gao, C., High-Flux Graphene Oxide Nanofiltration Membrane Intercalated by Carbon Nanotubes. *ACS Applied Materials & Interfaces* **2015**, *7* (15), 8147-8155.

76. Abraham, J.; Vasu, K. S.; Williams, C. D.; Gopinadhan, K.; Su, Y.; Cherian, C. T.; Dix, J.; Prestat, E.; Haigh, S. J.; Grigorieva, I. V.; Carbone, P.; Geim, A. K.; Nair, R. R., Tunable sieving of ions using graphene oxide membranes. *Nature Nanotechnology* **2017**, *12*, 546.

77. Lin, J.; Ye, W.; Zeng, H.; Yang, H.; Shen, J.; Darvishmanesh, S.; Luis, P.; Sotto, A.; Van der Bruggen, B., Fractionation of direct dyes and salts in aqueous solution using loose nanofiltration membranes. *Journal of Membrane Science* **2015**, *477*, 183-193.

78. Akbari, A.; Remigy, J. C.; Aptel, P., Treatment of textile dye effluent using a

polyamide-based nanofiltration membrane. *Chemical Engineering and Processing:*

Process Intensification **2002**, *41* (7), 601-609.

79. Akbari, A.; Desclaux, S.; Remigy, J. C.; Aptel, P., Treatment of textile dye effluents using a new photografted nanofiltration membrane. *Desalination* **2002**, *149* (1), 101-

107.

Chapter 6 Conclusions and Future Work

6.1 Major conclusions

In this study, a series of functionalized 2D nanomaterials were investigated and characterized using multiple complementary experimental techniques for unravelling the selective separation performance of the 2D nanomaterials and the underlying mechanisms of interfacial phenomena during separation, such as heterogeneity on nanosheet surface, steric hinderance effects and transport phenomena/mechanism within the nanoconfined channels.

A facile, novel, environment-friendly and economical method was proposed for synthesizing the fluorographene nanosheets through Michael's Addition reaction and fabricating amphiphobic L-ascorbic acid fluorinated rGO (LA/F/rGO) hydrogel that owns a low density of ~19 mg/ml, good thermal stability and a considerable adsorption capacity (up to 20 times its original weight) towards various organic solvents. A bouncing activity of the as-prepared LA/F/rGO hydrogel was observed for intriguing spontaneous repellence to oil droplets underwater. Alternatively, the bouncing activity of oil or water was dependent on the pre-soaking media condition for the LA/F/rGO hydrogel.

Another commonly used 2D materials MoS₂ (MoSe₂) nanosheets modified with tannic acid have been successfully synthesized through a two-stage, LA-assisted exfoliation method with a high yield of 90% ± 5%. The vacuum-filtered TAMoS₂

nanosheets membranes showed excellent non-swelling stability in water and fast water flux around $32 \text{ L m}^{-2} \text{ h}^{-1}$ (LMH) with $>97\%$ rejection of various cations under osmosis pressure static diffusion mode with 1 wt% of TAMoS₂ in MoS₂ nanosheets at a thickness of 5 μm . Under vacuum-driven filtration, an ultrafast water flux of $15,000 \pm 100 \text{ L}/(\text{m}^2\text{h}\cdot\text{bar})$ and $99.87 \pm 0.1\%$ rejection of various model organic dyes, e.g., basic blue, toluidine blue and rhodamine 6G, have been reported. In addition, a long-range attraction between water droplet and TAMoS₂ surface has been observed from AFM force measurement, while such an attraction was not observed on bare MoS₂ surface.

The artificial TMDCs nanosheets membrane (NbSA nanosheet membrane) has been synthesized and modified by sodium alginate through one-step ultrasonication method followed by the vacuum filtration process. The 5 μm NbSA nanosheet membrane showed ultrahigh rejection rates ($>95\%$) towards multiple cations while maintaining high water flux of 1.7-2.2 LMH under forward osmosis process. Under vacuum filtration, the membrane exhibited ultrahigh rejection rates ($\sim 100\%$) towards multiple target dyes including rhodamine 6G, basic blue and toluidine blue while possessing high water flux of $\sim 2200 \text{ LMHB}$. In addition, the one-step ultrasonication method for the fabrication of sodium alginate modified Nb₂CT_x MXene nanosheets introduced a bunches of surface functional groups such as: -OH, -C-O-C- and -COOH to the membrane, which could lead to a high-water permeation and rejection rate towards multiple ions and dyes. The mechanism underlying the transport phenomena of hydrated dyes or ions within nanoconfined lamellar channels was investigated, and the synergistic effect mechanism between ion-water clusters and ion exchange rates was

proposed for the first time to demonstrate the selective separation performance for Li^+ and Mg^{2+} .

6.2 Original contributions

In this work, three different types of starting materials incorporated with multiple guest materials were synthesized for the first time, and the resultant composite materials were studied in terms of stability, performance and transport mechanisms. The starting materials included: graphene oxide (GO), molybdenum disulfide (MoS_2) and niobium MXene. The detailed original contributions for those materials are listed as:

1a. A new, facile and cost-effective method has been demonstrated for the first time to fabricate fluorinated rGO nanosheets and fluorographene hydrogel in the presence of L-ascorbic acid through Michael's Addition reaction.

1b. The partially fluorinated structure derived switchable oil/water separation performance has been demonstrated for the first time.

2a. The two-stage highly efficient exfoliation method with the assistance of LA for the production of high yield, tannic acid-modified, and water-stabilized TAMoS₂ (TAMoSe₂) nanosheets has been reported for the first time.

2b. The synergistic effect between polyphenol groups of TA molecules and MoS₂ (MoSe₂) nanosheets has been demonstrated for top-level separation performance with ultrafast water flux under vacuum-driven filtration conditions without sacrificing dye rejection rate.

3a. The sodium alginate modified Nb₂CTx MXene nanosheets-based membranes have been synthesized for the first time through a one-step ultrasonication method.

3b. The introduction of guest materials that contained mixed carboxyl or hydroxyl functional groups played significant roles in achieving fast and selective ion transport within surface modified 2D material-based nanosheets channels.

3c. The selective separation performance for similar property material (Li⁺ and Mg²⁺) through simple forward osmosis process was discovered. This phenomenon was possibly explained by the different interaction mechanisms for Li⁺ and Mg²⁺ with modified 2D material-based nanosheet surface.

6.3 Suggestions for future work

(1) The mechanism underlying the transport phenomena of multiple dyes or hydrated ions within nanoconfined lamellar channels could be investigated. More complicated environments with the combined effects of water chemistry (e.g., pH, ion type and concentration) should be further investigated.

(2) A comprehensive understanding of enhanced water permeation, ion rejection rate and selectivity for guest-material-functionalized 2D material-based membrane could be investigated in details.

(3) The stronger and more direct evidence could be explored to support the proposed mechanisms, e.g., revealing the relationship between membrane selectivity and surface modification of 2D nanosheets.

(4) More efforts should be focused on the fundamental principles behind the explored results for better understanding the transport phenomena of wanted or unwanted species within the confined nanochannels.

Bibliography

1. Salgot, M.; Priestley, G. K.; Folch, M., Golf Course Irrigation with Reclaimed Water in the Mediterranean: A Risk Management Matter. *Water* **2012**, *4* (2), 389-429.
2. Bick, A.; Gillerman, L.; Manor, Y.; Oron, G., Economic Assessment of an Integrated Membrane System for Secondary Effluent Polishing for Unrestricted Reuse. *Water* **2012**, *4* (1), 219-236.
3. Bertone, E.; Stewart, R. A., Framework for Enhancing the Supply-Demand Balance of a Tri-Supply Urban Water Scheme in Australia. *Water* **2011**, *3* (4), 976-987.
4. Lazarova, V.; Sturny, V.; Sang, G. T., Relevance and Benefits of Urban Water Reuse in Tourist Areas. *Water* **2012**, *4* (1), 107-122.
5. Kapellakis, I. E.; Paranychianakis, N. V.; Tsagarakis, K. P.; Angelakis, A. N., Treatment of Olive Mill Wastewater with Constructed Wetlands. *Water* **2012**, *4* (1), 260-271.
6. Liang, X.; Dijk, M. P. v., Optimal Level of Groundwater Charge to Promote Rainwater Usage for Irrigation in Rural Beijing. *Water* **2011**, *3* (4), 1077-1091.
7. Voudouris, K., Artificial Recharge via Boreholes Using Treated Wastewater: Possibilities and Prospects. *Water* **2011**, *3* (4), 964-975.
8. Kalavrouziotis, I. K.; Arambatzis, C.; Kalfountzos, D.; Varnavas, S. P., Wastewater Reuse Planning in Agriculture: The Case of Aitolokarnania, Western Greece. *Water* **2011**, *3* (4), 988-1004.
9. Schacht, K.; Gönster, S.; Jüschke, E.; Chen, Y.; Tarchitzky, J.; Al-Bakri, J.; Al-Karablieh, E.; Marschner, B., Evaluation of Soil Sensitivity towards the Irrigation with Treated Wastewater in the Jordan River Region. *Water* **2011**, *3* (4), 1092-1111.
10. Apostolidis, N.; Hertle, C.; Young, R., Water Recycling in Australia. *Water* **2011**, *3* (3),

869-881.

11. Rodda, S. a., Global Hydrology and Water Resources. *Water Resources* **2003**.
12. Hepbasli, A.; Biyik, E.; Ekren, O.; Gunerhan, H.; Araz, M., A key review of wastewater source heat pump (WWSHP) systems. *Energy Conversion and Management* **2014**, *88*, 700-722.
13. Repert, D. A.; Barber, L. B.; Hess, K. M.; Keefe, S. H.; Kent, D. B.; LeBlanc, D. R.; Smith, R. L., Long-Term Natural Attenuation of Carbon and Nitrogen within a Groundwater Plume after Removal of the Treated Wastewater Source. *Environmental Science & Technology* **2006**, *40* (4), 1154-1162.
14. Larsen*, T. A.; Alder, A. C.; Eggen, R. I. L.; Maurer, M.; Lienert, J., Source Separation: Will We See a Paradigm Shift in Wastewater Handling? *Environmental Science & Technology* **2009**, *43* (16), 6121-6125.
15. Murphy, F.; Ewins, C.; Carbonnier, F.; Quinn, B., Wastewater Treatment Works (WwTW) as a Source of Microplastics in the Aquatic Environment. *Environmental Science & Technology* **2016**, *50* (11), 5800-5808.
16. Culha, O.; Gunerhan, H.; Biyik, E.; Ekren, O.; Hepbasli, A., Heat exchanger applications in wastewater source heat pumps for buildings: A key review. *Energy and Buildings* **2015**, *104*, 215-232.
17. Almeida, M. C.; Butler, D.; Friedler, E., At-source domestic wastewater quality. *Urban Water* **1999**, *1* (1), 49-55.
18. Hartmann, A.; Alder, A. C.; Koller, T.; Widmer, R. M., Identification of fluoroquinolone antibiotics as the main source of umuC genotoxicity in native hospital wastewater. **1998**, *17* (3), 377-382.
19. Chao, S.; Yiqiang, J.; Yang, Y.; Shiming, D., Experimental performance evaluation of a

novel dry-expansion evaporator with defouling function in a wastewater source heat pump. *Applied Energy* **2012**, *95*, 202-209.

20. Rodman, K. E.; Cervania, A. A.; Budig-Markin, V.; Schermesser, C. F.; Rogers, O. W.; Martinez, J. M.; King, J.; Hassett, P.; Burns, J.; Gonzales, M. S.; Folkerts, A.; Duin, P.; Virgil, A. S.; Aldrete, M.; Lagasca, A.; Infanzon-Marin, A.; Aitchison, J. R.; White, D.; Boutros, B. C.; Ortega, S.; Davis, B.; Tran, V. N.; Achilli, A., Coastal California Wastewater Effluent as a Resource for Seawater Desalination Brine Commingling. **2018**, *10* (3), 322.

21. Gatta, G.; Gagliardi, A.; Disciglio, G.; Lonigro, A.; Francavilla, M.; Tarantino, E.; Giuliani, M. M., Irrigation with Treated Municipal Wastewater on Artichoke Crop: Assessment of Soil and Yield Heavy Metal Content and Human Risk. **2018**, *10* (3), 255.

22. Schmid, S.; Bogner, F. X., What Germany's University Beginners Think about Water Reuse. **2018**, *10* (6), 731.

23. Colla, V.; Matino, I.; Branca, T. A.; Fornai, B.; Romaniello, L.; Rosito, F., Efficient Use of Water Resources in the Steel Industry. **2017**, *9* (11), 874.

24. Park, H.-G.; Kwon, Y.-N., Long-Term Stability of Low-Pressure Reverse Osmosis (RO) Membrane Operation—A Pilot Scale Study. **2018**, *10* (2), 93.

25. Hong, P.-Y.; Julian, T. R.; Pype, M.-L.; Jiang, S. C.; Nelson, K. L.; Graham, D.; Pruden, A.; Manaia, C. M., Reusing Treated Wastewater: Consideration of the Safety Aspects Associated with Antibiotic-Resistant Bacteria and Antibiotic Resistance Genes. **2018**, *10* (3), 244.

26. Manheim, D. C.; Jiang, S. C., Investigation of Algal Biotxin Removal during SWRO Desalination through a Materials Flow Analysis. **2017**, *9* (10), 730.

27. Jumat, M. R.; Hasan, N. A.; Subramanian, P.; Heberling, C.; Colwell, R. R.; Hong, P.-Y., Membrane Bioreactor-Based Wastewater Treatment Plant in Saudi Arabia: Reduction of Viral

Diversity, Load, and Infectious Capacity. **2017**, *9* (7), 534.

28. Kurihara, M.; Takeuchi, H., SWRO-PRO System in “Mega-ton Water System” for Energy Reduction and Low Environmental Impact. **2018**, *10* (1), 48.

29. Caldera, U.; Bogdanov, D.; Afanasyeva, S.; Breyer, C., Role of Seawater Desalination in the Management of an Integrated Water and 100% Renewable Energy Based Power Sector in Saudi Arabia. **2018**, *10* (1), 3.

30. Fletcher, T. D.; Deletic, A.; Mitchell, V. G.; Hatt, B. E., Reuse of Urban Runoff in Australia: A Review of Recent Advances and Remaining Challenges. **2008**, *37* (5_Supplement), S-116-S-127.

31. Gao, H.; Scherson, Y. D.; Wells, G. F., Towards energy neutral wastewater treatment: methodology and state of the art. *Environmental Science: Processes & Impacts* **2014**, *16* (6), 1223-1246.

32. Dinar, A.; Hogarth, M., Game Theory and Water Resources: Critical Review of its Contributions, Progress and Remaining Challenges. *Foundations and Trends® in Microeconomics* **2015**, *11* (1–2), 1-139.

33. Li, W.-W.; Yu, H.-Q., From wastewater to bioenergy and biochemicals via two-stage bioconversion processes: A future paradigm. *Biotechnology Advances* **2011**, *29* (6), 972-982.

34. Ali, M.; Okabe, S., Anammox-based technologies for nitrogen removal: Advances in process start-up and remaining issues. *Chemosphere* **2015**, *141*, 144-153.

35. Zhang, C.; Jiang, Y.; Li, Y.; Hu, Z.; Zhou, L.; Zhou, M., Three-dimensional electrochemical process for wastewater treatment: A general review. *Chemical Engineering Journal* **2013**, *228*, 455-467.

36. Huang, X.; Wang, R.; Jiao, T.; Zou, G.; Zhan, F.; Yin, J.; Zhang, L.; Zhou, J.; Peng, Q.,

Facile Preparation of Hierarchical AgNP-Loaded MXene/Fe₃O₄/Polymer Nanocomposites by Electrospinning with Enhanced Catalytic Performance for Wastewater Treatment. *ACS Omega* **2019**, *4* (1), 1897-1906.

37. Chandra, D.; Das, S. K.; Bhaumik, A., A fluorophore grafted 2D-hexagonal mesoporous organosilica: Excellent ion-exchanger for the removal of heavy metal ions from wastewater. *Microporous and Mesoporous Materials* **2010**, *128* (1), 34-40.

38. Dervin, S.; Dionysiou, D. D.; Pillai, S. C., 2D nanostructures for water purification: graphene and beyond. *Nanoscale* **2016**, *8* (33), 15115-15131.

39. Zhang, S.; Lian, G.; Si, H.; Wang, J.; Zhang, X.; Wang, Q.; Cui, D., Ultrathin BN nanosheets with zigzag edge: one-step chemical synthesis, applications in wastewater treatment and preparation of highly thermal-conductive BN-polymer composites. *Journal of Materials Chemistry A* **2013**, *1* (16), 5105-5112.

40. Li, R.; Zhang, L.; Shi, L.; Wang, P., MXene Ti₃C₂: An Effective 2D Light-to-Heat Conversion Material. *ACS Nano* **2017**, *11* (4), 3752-3759.

41. He, P.; Tang, X.; Chen, L.; Xie, P.; He, L.; Zhou, H.; Zhang, D.; Fan, T., Patterned Carbon Nitride-Based Hybrid Aerogel Membranes via 3D Printing for Broadband Solar Wastewater Remediation. **2018**, *28* (29), 1801121.

42. Kyzas, G. Z.; Deliyanni, E. A.; Matis, K. A., Graphene oxide and its application as an adsorbent for wastewater treatment. **2014**, *89* (2), 196-205.

43. Mousset, E.; Wang, Z.; Hammaker, J.; Lefebvre, O., Physico-chemical properties of pristine graphene and its performance as electrode material for electro-Fenton treatment of wastewater. *Electrochimica Acta* **2016**, *214*, 217-230.

44. Tatarova, E.; Bundaleska, N.; Sarrette, J. P.; Ferreira, C. M., Plasmas for environmental

issues: from hydrogen production to 2D materials assembly. *Plasma Sources Science and Technology* **2014**, *23* (6), 063002.

45. Coleman, J. N.; Lotya, M.; O'Neill, A.; Bergin, S. D.; King, P. J.; Khan, U.; Young, K.; Gaucher, A.; De, S.; Smith, R. J.; Shvets, I. V.; Arora, S. K.; Stanton, G.; Kim, H.-Y.; Lee, K.; Kim, G. T.; Duesberg, G. S.; Hallam, T.; Boland, J. J.; Wang, J. J.; Donegan, J. F.; Grunlan, J. C.; Moriarty, G.; Shmeliov, A.; Nicholls, R. J.; Perkins, J. M.; Grievson, E. M.; Theuwissen, K.; McComb, D. W.; Nellist, P. D.; Nicolosi, V., Two-Dimensional Nanosheets Produced by Liquid Exfoliation of Layered Materials. **2011**, *331* (6017), 568-571.

46. Grayfer, E. D.; Kozlova, M. N.; Fedorov, V. E., Colloidal 2D nanosheets of MoS₂ and other transition metal dichalcogenides through liquid-phase exfoliation. *Advances in Colloid and Interface Science* **2017**, *245*, 40-61.

47. Osada, M.; Sasaki, T., Exfoliated oxide nanosheets: new solution to nanoelectronics. *Journal of Materials Chemistry* **2009**, *19* (17), 2503-2511.

48. Kim, I. Y.; Jo, Y. K.; Lee, J. M.; Wang, L.; Hwang, S.-J., Unique Advantages of Exfoliated 2D Nanosheets for Tailoring the Functionalities of Nanocomposites. *The Journal of Physical Chemistry Letters* **2014**, *5* (23), 4149-4161.

49. Lin, Q.; Li, L.; Liang, S.; Liu, M.; Bi, J.; Wu, L., Efficient synthesis of monolayer carbon nitride 2D nanosheet with tunable concentration and enhanced visible-light photocatalytic activities. *Applied Catalysis B: Environmental* **2015**, *163*, 135-142.

50. Fukuda, K.; Akatsuka, K.; Ebina, Y.; Ma, R.; Takada, K.; Nakai, I.; Sasaki, T., Exfoliated Nanosheet Crystallite of Cesium Tungstate with 2D Pyrochlore Structure: Synthesis, Characterization, and Photochromic Properties. *ACS Nano* **2008**, *2* (8), 1689-1695.

51. Nicolosi, V.; Chhowalla, M.; Kanatzidis, M. G.; Strano, M. S.; Coleman, J. N., Liquid

Exfoliation of Layered Materials. **2013**, *340* (6139), 1226419.

52. Druce, J.; Téllez, H.; Burriel, M.; Sharp, M. D.; Fawcett, L. J.; Cook, S. N.; McPhail, D. S.; Ishihara, T.; Brongersma, H. H.; Kilner, J. A., Surface termination and subsurface restructuring of perovskite-based solid oxide electrode materials. *Energy & Environmental Science* **2014**, *7* (11), 3593-3599.

53. Pietsch, G. J.; Higashi, G. S.; Chabal, Y. J., Chemomechanical polishing of silicon: Surface termination and mechanism of removal. **1994**, *64* (23), 3115-3117.

54. Chambers, S. A.; Joyce, S. A., Surface termination, composition and reconstruction of Fe₃O₄(001) and γ -Fe₂O₃(001). *Surface Science* **1999**, *420* (2), 111-122.

55. Sun, S.; Sun, Y.; Liu, Z.; Lee, D.-I.; Peterson, S.; Pianetta, P., Surface termination and roughness of Ge(100) cleaned by HF and HCl solutions. **2006**, *88* (2), 021903.

56. Tryk, D. A.; Tsunozaki, K.; Rao, T. N.; Fujishima, A., Relationships between surface character and electrochemical processes on diamond electrodes: dual roles of surface termination and near-surface hydrogen. *Diamond and Related Materials* **2001**, *10* (9), 1804-1809.

57. Yagi, I.; Tsukagoshi, K.; Aoyagi, Y., Modification of the electric conduction at the pentacene/SiO₂ interface by surface termination of SiO₂. **2005**, *86* (10), 103502.

58. Song, H. S.; Kwon, O. S.; Kim, J.-H.; Conde, J.; Artzi, N., 3D hydrogel scaffold doped with 2D graphene materials for biosensors and bioelectronics. *Biosensors and Bioelectronics* **2017**, *89*, 187-200.

59. Xu, Y.; Lin, Z.; Huang, X.; Liu, Y.; Huang, Y.; Duan, X., Flexible Solid-State Supercapacitors Based on Three-Dimensional Graphene Hydrogel Films. *ACS Nano* **2013**, *7* (5), 4042-4049.

60. Xu, Y.; Lin, Z.; Huang, X.; Wang, Y.; Huang, Y.; Duan, X., Functionalized Graphene

Hydrogel-Based High-Performance Supercapacitors. **2013**, 25 (40), 5779-5784.

61. Lutolf, M. P.; Gilbert, P. M.; Blau, H. M., Designing materials to direct stem-cell fate. *Nature* **2009**, 462 (7272), 433-441.

62. Han, D.; Yan, L., Supramolecular Hydrogel of Chitosan in the Presence of Graphene Oxide Nanosheets as 2D Cross-Linkers. *ACS Sustainable Chemistry & Engineering* **2014**, 2 (2), 296-300.

63. Benoit, D. S. W.; Schwartz, M. P.; Durney, A. R.; Anseth, K. S., Small functional groups for controlled differentiation of hydrogel-encapsulated human mesenchymal stem cells. *Nature Materials* **2008**, 7 (10), 816-823.

64. Servant, A.; Leon, V.; Jasim, D.; Methven, L.; Limousin, P.; Fernandez-Pacheco, E. V.; Prato, M.; Kostarelos, K., Graphene-Based Electroresponsive Scaffolds as Polymeric Implants for On-Demand Drug Delivery. **2014**, 3 (8), 1334-1343.

65. Guo, W.; Cheng, C.; Wu, Y.; Jiang, Y.; Gao, J.; Li, D.; Jiang, L., Bio-Inspired Two-Dimensional Nanofluidic Generators Based on a Layered Graphene Hydrogel Membrane. **2013**, 25 (42), 6064-6068.

66. Ke, Q.; Wang, J., Graphene-based materials for supercapacitor electrodes – A review. *Journal of Materiomics* **2016**, 2 (1), 37-54.

67. Liu, G.; Jin, W.; Xu, N., Two-Dimensional-Material Membranes: A New Family of High-Performance Separation Membranes. **2016**, 55 (43), 13384-13397.

68. Ji, J.; Kang, Q.; Zhou, Y.; Feng, Y.; Chen, X.; Yuan, J.; Guo, W.; Wei, Y.; Jiang, L., Osmotic Power Generation with Positively and Negatively Charged 2D Nanofluidic Membrane Pairs. **2017**, 27 (2), 1603623.

69. Dong, Y.; Wu, Z.-S.; Ren, W.; Cheng, H.-M.; Bao, X., Graphene: a promising 2D material for electrochemical energy storage. *Science Bulletin* **2017**, 62 (10), 724-740.

70. Fathizadeh, M.; Xu, W. L.; Zhou, F.; Yoon, Y.; Yu, M., Graphene Oxide: A Novel 2-Dimensional Material in Membrane Separation for Water Purification. **2017**, *4* (5), 1600918.
71. Wang, Z.; Mi, B., Environmental Applications of 2D Molybdenum Disulfide (MoS₂) Nanosheets. *Environmental Science & Technology* **2017**, *51* (15), 8229-8244.
72. Kim, W.-g.; Nair, S., Membranes from nanoporous 1D and 2D materials: A review of opportunities, developments, and challenges. *Chemical Engineering Science* **2013**, *104*, 908-924.
73. Shao, J.; Xie, H.; Wang, H.; Zhou, W.; Luo, Q.; Yu, X.-F.; Chu, P. K., 2D Material-Based Nanofibrous Membrane for Photothermal Cancer Therapy. *ACS Applied Materials & Interfaces* **2018**, *10* (1), 1155-1163.
74. Zhu, X.; Tian, C.; Do-Thanh, C.-L.; Dai, S., Two-Dimensional Materials as Prospective Scaffolds for Mixed-Matrix Membrane-Based CO₂ Separation. **2017**, *10* (17), 3304-3316.
75. Liu, G.; Jin, W.; Xu, N., Graphene-based membranes. *Chemical Society Reviews* **2015**, *44* (15), 5016-5030.
76. Zhao, Y.; Xie, Y.; Liu, Z.; Wang, X.; Chai, Y.; Yan, F., Two-Dimensional Material Membranes: An Emerging Platform for Controllable Mass Transport Applications. **2014**, *10* (22), 4521-4542.
77. Inkson, B. J., 2 - Scanning electron microscopy (SEM) and transmission electron microscopy (TEM) for materials characterization. In *Materials Characterization Using Nondestructive Evaluation (NDE) Methods*, Hübschen, G.; Altpeter, I.; Tschuncky, R.; Herrmann, H.-G., Eds. Woodhead Publishing: 2016; pp 17-43.
78. Denk, W.; Horstmann, H., Serial Block-Face Scanning Electron Microscopy to Reconstruct Three-Dimensional Tissue Nanostructure. *PLOS Biology* **2004**, *2* (11), e329.
79. Venables, J. A.; Harland, C. J., Electron back-scattering patterns—A new technique for

- obtaining crystallographic information in the scanning electron microscope. *The Philosophical Magazine: A Journal of Theoretical Experimental and Applied Physics* **1973**, 27 (5), 1193-1200.
80. Nation, J. L., A New Method Using Hexamethyldisilazane for Preparation of Soft Insect Tissues for Scanning Electron Microscopy. *Stain Technology* **1983**, 58 (6), 347-351.
81. Cleveland, J. P.; Anczykowski, B.; Schmid, A. E.; Elings, V. B., Energy dissipation in tapping-mode atomic force microscopy. *Applied Physics Letters* **1998**, 72 (20), 2613-2615.
82. Fang, H. H. P.; Chan, K.-Y.; Xu, L.-C., Quantification of bacterial adhesion forces using atomic force microscopy (AFM). *Journal of Microbiological Methods* **2000**, 40 (1), 89-97.
83. Meyer, G.; Amer, N. M., Novel optical approach to atomic force microscopy. *Applied Physics Letters* **1988**, 53 (12), 1045-1047.
84. Lou, S.-T.; Ouyang, Z.-Q.; Zhang, Y.; Li, X.-J.; Hu, J.; Li, M.-Q.; Yang, F.-J., Nanobubbles on solid surface imaged by atomic force microscopy. *Journal of Vacuum Science & Technology B: Microelectronics and Nanometer Structures Processing, Measurement, and Phenomena* **2000**, 18 (5), 2573-2575.
85. Zhong, Q.; Inniss, D.; Kjoller, K.; Elings, V. B., Fractured polymer/silica fiber surface studied by tapping mode atomic force microscopy. *Surface Science Letters* **1993**, 290 (1), L688-L692.
86. Stipp, S. L. S.; Eggleston, C. M.; Nielsen, B. S., Calcite surface structure observed at microtopographic and molecular scales with atomic force microscopy (AFM). *Geochimica et Cosmochimica Acta* **1994**, 58 (14), 3023-3033.
87. Brooke, B. D.; Kloke, G.; Hunt, R. H.; Koekemoer, L. L.; Tem, E. A.; Taylor, M. E.; Small, G.; Hemingway, J.; Coetzee, M., Bioassay and biochemical analyses of insecticide resistance in southern African *Anopheles funestus* (Diptera: Culicidae). *Bulletin of Entomological Research*

2007, *91* (4), 265-272.

88. Sun, K.-t.; Lin, Y.-c.; Yu, C.-j., A study on learning effect among different learning styles in a Web-based lab of science for elementary school students. *Computers & Education* **2008**, *50* (4), 1411-1422.

89. Torpo, L.; Marlo, M.; Staab, T. E. M.; Nieminen, R. M., Comprehensiveab initiostudy of properties of monovacancies and antisites in 4H-SiC. *Journal of Physics: Condensed Matter* **2001**, *13* (28), 6203-6231.

90. Verhagen, T. E. M.; Hendriks, D. J.; Bancsi, L. F. J. M. M.; Mol, B. W. J.; Broekmans, F. J. M., The accuracy of multivariate models predicting ovarian reserve and pregnancy after in vitro fertilization: a meta-analysis. *Human Reproduction Update* **2008**, *14* (2), 95-100.

91. Steenweg, M. E.; Ghezzi, D.; Haack, T.; Abbink, T. E. M.; Martinelli, D.; van Berkel, C. G. M.; Bley, A.; Diogo, L.; Grillo, E.; Te Water Naudé, J.; Strom, T. M.; Bertini, E.; Prokisch, H.; van der Knaap, M. S.; Zeviani, M., Leukoencephalopathy with thalamus and brainstem involvement and high lactate 'LTBL' caused by EARS2 mutations. *Brain* **2012**, *135* (5), 1387-1394.

92. Hatchard, T. D.; Dahn, J. R., In Situ XRD and Electrochemical Study of the Reaction of Lithium with Amorphous Silicon. *Journal of The Electrochemical Society* **2004**, *151* (6), A838-A842.

93. Drits, V.; Środoń, J.; Eberl, D. D., XRD Measurement of Mean Crystallite Thickness of Illite and Illite/Smectite: Reappraisal of the Kubler Index and the Scherrer Equation. *Clays and Clay Minerals* **1997**, *45* (3), 461-475.

94. Kontoyannis, C. G.; Vagenas, N. V., Calcium carbonate phase analysis using XRD and FT-Raman spectroscopy. *Analyst* **2000**, *125* (2), 251-255.

95. Borchert, H.; Shevchenko, E. V.; Robert, A.; Mekis, I.; Kornowski, A.; Grübel, G.; Weller, H., Determination of Nanocrystal Sizes: A Comparison of TEM, SAXS, and XRD Studies of Highly Monodisperse CoPt₃ Particles. *Langmuir* **2005**, *21* (5), 1931-1936.
96. Haiss, W.; Thanh, N. T. K.; Aveyard, J.; Fernig, D. G., Determination of Size and Concentration of Gold Nanoparticles from UV-Vis Spectra. *Analytical Chemistry* **2007**, *79* (11), 4215-4221.
97. Lichtenthaler, H. K.; Buschmann, C., Chlorophylls and Carotenoids: Measurement and Characterization by UV-VIS Spectroscopy. *Current Protocols in Food Analytical Chemistry* **2001**, *1* (1), F4.3.1-F4.3.8.
98. Meier, H.; Stalmach, U.; Kolshorn, H., Effective conjugation length and UV/vis spectra of oligomers. *Acta Polymerica* **1997**, *48* (9), 379-384.
99. REHMAN, I.; BONFIELD, W., Characterization of hydroxyapatite and carbonated apatite by photo acoustic FTIR spectroscopy. *Journal of Materials Science: Materials in Medicine* **1997**, *8* (1), 1-4.
100. Byler, D. M.; Susi, H., Examination of the secondary structure of proteins by deconvolved FTIR spectra. *Biopolymers* **1986**, *25* (3), 469-487.
101. Chen, G.; Liu, S.; Chen, S.; Qi, Z., FTIR Spectra, Thermal Properties, and Dispersibility of a Polystyrene/Montmorillonite Nanocomposite. *Macromolecular Chemistry and Physics* **2001**, *202* (7), 1189-1193.
102. Fujii, T.; de Groot, F. M. F.; Sawatzky, G. A.; Voogt, F. C.; Hibma, T.; Okada, K., In situ XPS analysis of various iron oxide films grown by $\{\mathrm{NO}\}_2$ -assisted molecular-beam epitaxy. *Physical Review B* **1999**, *59* (4), 3195-3202.
103. Okpalugo, T. I. T.; Papakonstantinou, P.; Murphy, H.; McLaughlin, J.; Brown, N. M. D.,

High resolution XPS characterization of chemical functionalised MWCNTs and SWCNTs. *Carbon* **2005**, *43* (1), 153-161.

104. Grosvenor, A. P.; Biesinger, M. C.; Smart, R. S. C.; McIntyre, N. S., New interpretations of XPS spectra of nickel metal and oxides. *Surface Science* **2006**, *600* (9), 1771-1779.

105. Grosvenor, A. P.; Kobe, B. A.; Biesinger, M. C.; McIntyre, N. S., Investigation of multiplet splitting of Fe 2p XPS spectra and bonding in iron compounds. *Surface and Interface Analysis* **2004**, *36* (12), 1564-1574.

106. Dupin, J.-C.; Gonbeau, D.; Vinatier, P.; Levasseur, A., Systematic XPS studies of metal oxides, hydroxides and peroxides. *Physical Chemistry Chemical Physics* **2000**, *2* (6), 1319-1324.

107. Bhattacharjee, S., DLS and zeta potential – What they are and what they are not? *Journal of Controlled Release* **2016**, *235*, 337-351.

108. Kirby, B. J.; Hasselbrink Jr., E. F., Zeta potential of microfluidic substrates: 1. Theory, experimental techniques, and effects on separations. *ELECTROPHORESIS* **2004**, *25* (2), 187-202.

109. Clogston, J. D.; Patri, A. K., Zeta Potential Measurement. In *Characterization of Nanoparticles Intended for Drug Delivery*, McNeil, S. E., Ed. Humana Press: Totowa, NJ, 2011; pp 63-70.

110. Zisman, W. A., Relation of the Equilibrium Contact Angle to Liquid and Solid Constitution. In *Contact Angle, Wettability, and Adhesion*, AMERICAN CHEMICAL SOCIETY: 1964; Vol. 43, pp 1-51.

111. Yuan, Y.; Lee, T. R., Contact Angle and Wetting Properties. In *Surface Science Techniques*, Bracco, G.; Holst, B., Eds. Springer Berlin Heidelberg: Berlin, Heidelberg, 2013; pp 3-34.

112. Wenzel, R. N., Surface Roughness and Contact Angle. *The Journal of Physical and Colloid Chemistry* **1949**, *53* (9), 1466-1467.

113. Liu, Y.; Hu, Z.; Zong, K.; Gao, C.; Gao, S.; Xu, J.; Chen, H., Reappraisal and refinement of zircon U-Pb isotope and trace element analyses by LA-ICP-MS. *Chinese Science Bulletin* **2010**, *55* (15), 1535-1546.
114. Lee, S.; Boo, C.; Elimelech, M.; Hong, S., Comparison of fouling behavior in forward osmosis (FO) and reverse osmosis (RO). *Journal of Membrane Science* **2010**, *365* (1), 34-39.
115. Chung, T.-S.; Zhang, S.; Wang, K. Y.; Su, J.; Ling, M. M., Forward osmosis processes: Yesterday, today and tomorrow. *Desalination* **2012**, *287*, 78-81.
116. Cath, T. Y.; Childress, A. E.; Elimelech, M., Forward osmosis: Principles, applications, and recent developments. *Journal of Membrane Science* **2006**, *281* (1), 70-87.
117. Shaffer, D. L.; Werber, J. R.; Jaramillo, H.; Lin, S.; Elimelech, M., Forward osmosis: Where are we now? *Desalination* **2015**, *356*, 271-284.
118. Zhao, S.; Zou, L.; Tang, C. Y.; Mulcahy, D., Recent developments in forward osmosis: Opportunities and challenges. *Journal of Membrane Science* **2012**, *396*, 1-21.
119. Zhang, S.; Li, Y.; Pan, N., Graphene based supercapacitor fabricated by vacuum filtration deposition. *Journal of Power Sources* **2012**, *206*, 476-482.
120. Yoshimura, M.; Suda, H.; Okamoto, K.; Ioku, K. J. J. o. M. S., Hydrothermal synthesis of biocompatible whiskers. **1994**, *29* (13), 3399-3402.
121. Komarneni, S.; Roy, R.; Li, Q. H., Microwave-hydrothermal synthesis of ceramic powders. *Materials Research Bulletin* **1992**, *27* (12), 1393-1405.
122. Feng, S.; Xu, R., New Materials in Hydrothermal Synthesis. *Accounts of Chemical Research* **2001**, *34* (3), 239-247.
123. SIBSON, R. H.; MOORE, J. M. M.; RANKIN, A. H., Seismic pumping—a hydrothermal fluid transport mechanism. **1975**, *131* (6), 653-659.

124. Israelachvili, J.; Min, Y.; Akbulut, M.; Alig, A.; Carver, G.; Greene, W.; Kristiansen, K.; Meyer, E.; Pesika, N.; Rosenberg, K.; Zeng, H., Recent advances in the surface forces apparatus (SFA) technique. *Reports on Progress in Physics* **2010**, *73* (3), 036601.
125. Sridhar, I.; Johnson, K. L.; Fleck, N. A., Adhesion mechanics of the surface force apparatus. *Journal of Physics D: Applied Physics* **1997**, *30* (12), 1710-1719.
126. Crassous, J.; Charlaix, E.; Loubet, J. L., Capillary Condensation between High-Energy Surfaces. An Experimental Study with a Surface Force Apparatus. *Europhysics Letters (EPL)* **1994**, *28* (1), 37-42.
127. Shubin, V. E.; Kékicheff, P., Electrical Double Layer Structure Revisited via a Surface Force Apparatus: Mica Interfaces in Lithium Nitrate Solutions. *Journal of Colloid and Interface Science* **1993**, *155* (1), 108-123.
128. Bec, S.; Tonck, A.; Georges, J. M.; Georges, E.; Loubet, J. L., Improvements in the indentation method with a surface force apparatus. *Philosophical Magazine A* **1996**, *74* (5), 1061-1072.
129. Loubet, J. L.; Bauer, M.; Tonck, A.; Bec, S.; Gauthier-Manuel, B., Nanoindentation with a Surface Force Apparatus. In *Mechanical Properties and Deformation Behavior of Materials Having Ultra-Fine Microstructures*, Nastasi, M.; Parkin, D. M.; Gleiter, H., Eds. Springer Netherlands: Dordrecht, 1993; pp 429-447.
130. Stewart, A. M.; Christenson, H. K., Use of magnetic forces to control distance in a surface force apparatus. *Measurement Science and Technology* **1990**, *1* (12), 1301-1303.
131. Kumacheva, E., Interfacial friction measurement in surface force apparatus. *Progress in Surface Science* **1998**, *58* (2), 75-120.
132. Timonen, T.; Saksela, E., Isolation of human NK cells by density gradient centrifugation.

Journal of Immunological Methods **1980**, 36 (3), 285-291.

133. Murphy, J. R., Influence of temperature and method of centrifugation on the separation of erythrocytes. *The Journal of Laboratory and Clinical Medicine* **1973**, 82 (2), 334-341.

134. Brakke, M. K., Zonal separations by density-gradient centrifugation. *Archives of Biochemistry and Biophysics* **1953**, 45 (2), 275-290.

135. Chen, W.; Yu, H.; Liu, Y.; Chen, P.; Zhang, M.; Hai, Y., Individualization of cellulose nanofibers from wood using high-intensity ultrasonication combined with chemical pretreatments. *Carbohydrate Polymers* **2011**, 83 (4), 1804-1811.

136. Zhang, D.; Fu, H.; Shi, L.; Pan, C.; Li, Q.; Chu, Y.; Yu, W., Synthesis of CeO₂ Nanorods via Ultrasonication Assisted by Polyethylene Glycol. *Inorganic Chemistry* **2007**, 46 (7), 2446-2451.

137. Singh, A. K.; Fernando, S. D.; Hernandez, R., Base-Catalyzed Fast Transesterification of Soybean Oil Using Ultrasonication. *Energy & Fuels* **2007**, 21 (2), 1161-1164.

138. Zhang, L.-J.; Cheng, L.-M.; Xu, N.; Zhao, N.-M.; Li, C.-G.; Yuan, J.; Jia, S.-R., Efficient Transformation of Tobacco by Ultrasonication. *Bio/Technology* **1991**, 9 (10), 996-997.

139. Landfester, K.; Eisenblätter, J.; Rothe, R. J. J. R., Preparation of polymerizable miniemulsions by ultrasonication. **2004**, 1 (1), 65-68.

140. Imai, M.; Ikari, K.; Suzuki, I., High-performance hydrolysis of cellulose using mixed cellulase species and ultrasonication pretreatment. *Biochemical Engineering Journal* **2004**, 17 (2), 79-83.

141. Scriven, L. E., Physics and Applications of DIP Coating and Spin Coating. *MRS Proceedings* **1988**, 121, 717.

142. Flack, W. W.; Soong, D. S.; Bell, A. T.; Hess, D. W., A mathematical model for spin coating

of polymer resists. **1984**, *56* (4), 1199-1206.

143. Lawrence, C. J., The mechanics of spin coating of polymer films. **1988**, *31* (10), 2786-2795.

144. Bornside, D. E.; Macosko, C. W.; Scriven, L. E., Spin coating: One-dimensional model. **1989**, *66* (11), 5185-5193.

145. Chi, K.; Zhang, Z.; Xi, J.; Huang, Y.; Xiao, F.; Wang, S.; Liu, Y., Freestanding Graphene Paper Supported Three-Dimensional Porous Graphene–Polyaniline Nanocomposite Synthesized by Inkjet Printing and in Flexible All-Solid-State Supercapacitor. *ACS Applied Materials & Interfaces* **2014**, *6* (18), 16312-16319.

146. Chronopoulos, D. D.; Bakandritsos, A.; Lazar, P.; Pykal, M.; Čépe, K.; Zbořil, R.; Otyepka, M., High-Yield Alkylation and Arylation of Graphene via Grignard Reaction with Fluorographene. *Chemistry of Materials* **2017**, *29* (3), 926-930.

147. Das, S.; Irin, F.; Ma, L.; Bhattacharia, S. K.; Hedden, R. C.; Green, M. J., Rheology and Morphology of Pristine Graphene/Polyacrylamide Gels. *ACS Applied Materials & Interfaces* **2013**, *5* (17), 8633-8640.

148. Díaz-Blancas, V.; Ocampo-Pérez, R.; Leyva-Ramos, R.; Alonso-Dávila, P. A.; Moral-Rodríguez, A. I., 3D modeling of the overall adsorption rate of metronidazole on granular activated carbon at low and high concentrations in aqueous solution. *Chemical Engineering Journal* **2018**, *349*, 82-91.

149. Fu, Y.; Wang, J.; Liu, Q.; Zeng, H., Water-dispersible magnetic nanoparticle–graphene oxide composites for selenium removal. *Carbon* **2014**, *77*, 710-721.

150. Geim, A. K.; Novoselov, K. S., The rise of graphene. *Nature Materials* **2007**, *6*, 183.

151. González-Domínguez, J. M.; Martín, C.; Durá, Ó. J.; Merino, S.; Vázquez, E., Smart

Hybrid Graphene Hydrogels: A Study of the Different Responses to Mechanical Stretching Stimulus. *ACS Applied Materials & Interfaces* **2018**, *10* (2), 1987-1995.

152. Haibin, S.; Can, F.; Yanli, G.; Pengfei, G.; Chunlei, W.; Wenchao, Y.; Qishang, W.; Chongwu, Z.; Junya, W.; Junqi, X., Electrical property of macroscopic graphene composite fibers prepared by chemical vapor deposition. *Nanotechnology* **2018**, *29* (30), 305601.

153. Han, H.; Zongbin, Z.; Wubo, W.; Yury, G.; Jieshan, Q., Ultralight and Highly Compressible Graphene Aerogels. *Advanced Materials* **2013**, *25* (15), 2219-2223.

154. Lee, H.; Lee, B. P.; Messersmith, P. B., A reversible wet/dry adhesive inspired by mussels and geckos. *Nature* **2007**, *448*, 338.

155. Li, J.; Xie, J.; Gao, L.; Li, C. M., Au Nanoparticles–3D Graphene Hydrogel Nanocomposite To Boost Synergistically in Situ Detection Sensitivity toward Cell-Released Nitric Oxide. *ACS Applied Materials & Interfaces* **2015**, *7* (4), 2726-2734.

156. Liang, P.; Wang, F.; Hu, Z.-A., Controlled synthesis of ordered sandwich CuCo₂O₄/reduced graphene oxide composites via layer-by-layer heteroassembly for high-performance supercapacitors. *Chemical Engineering Journal* **2018**, *350*, 627-636.

157. Liu, X.; Miller, A. L.; Park, S.; Waletzki, B. E.; Zhou, Z.; Terzic, A.; Lu, L., Functionalized Carbon Nanotube and Graphene Oxide Embedded Electrically Conductive Hydrogel Synergistically Stimulates Nerve Cell Differentiation. *ACS Applied Materials & Interfaces* **2017**, *9* (17), 14677-14690.

158. Meng, X.; Lu, L.; Sun, C., Green Synthesis of Three-Dimensional MnO₂/Graphene Hydrogel Composites as a High-Performance Electrode Material for Supercapacitors. *ACS Applied Materials & Interfaces* **2018**, *10* (19), 16474-16481.

159. Mingyang, J.; Nan, J.; Jian, C.; Junqi, S., Near-Infrared Light-Driven, Highly Efficient

Bilayer Actuators Based on Polydopamine-Modified Reduced Graphene Oxide. *Advanced Functional Materials* **2014**, *24* (34), 5412-5419.

160. Wang, Q.; Zhang, X.; Huang, L.; Zhang, Z.; Dong, S., One-Pot Synthesis of Fe₃O₄ Nanoparticle Loaded 3D Porous Graphene Nanocomposites with Enhanced Nanozyme Activity for Glucose Detection. *ACS Applied Materials & Interfaces* **2017**, *9* (8), 7465-7471.

161. Xu, Y.; Sheng, K.; Li, C.; Shi, G., Self-Assembled Graphene Hydrogel via a One-Step Hydrothermal Process. *ACS Nano* **2010**, *4* (7), 4324-4330.

162. Ho, K.-I.; Huang, C.-H.; Liao, J.-H.; Zhang, W.; Li, L.-J.; Lai, C.-S.; Su, C.-Y., Fluorinated Graphene as High Performance Dielectric Materials and the Applications for Graphene Nanoelectronics. *Scientific Reports* **2014**, *4*, 5893.

163. Jeon, K.-J.; Lee, Z.; Pollak, E.; Moreschini, L.; Bostwick, A.; Park, C.-M.; Mendelsberg, R.; Radmilovic, V.; Kosteki, R.; Richardson, T. J.; Rotenberg, E., Fluorographene: A Wide Bandgap Semiconductor with Ultraviolet Luminescence. *ACS Nano* **2011**, *5* (2), 1042-1046.

164. R., N. R.; Wencai, R.; Rashid, J.; Ibtisam, R.; G., K. V.; Liam, B.; Peter, B.; Fredrik, S.; S., M. A.; Shengjun, Y.; I., K. M.; Hui-Ming, C.; Wlodek, S.; G., B. L.; V., O. A.; V., G. I.; N., G. A.; S., N. K.; K., G. A., Fluorographene: A Two-Dimensional Counterpart of Teflon. *Small* **2010**, *6* (24), 2877-2884.

165. Im, K.; Nguyen, D. N.; Kim, S.; Kong, H. J.; Kim, Y.; Park, C. S.; Kwon, O. S.; Yoon, H., Graphene-Embedded Hydrogel Nanofibers for Detection and Removal of Aqueous-Phase Dyes. *ACS Applied Materials & Interfaces* **2017**, *9* (12), 10768-10776.

166. Wang, X.; Dai, Y.; Gao, J.; Huang, J.; Li, B.; Fan, C.; Yang, J.; Liu, X., High-Yield Production of Highly Fluorinated Graphene by Direct Heating Fluorination of Graphene-oxide. *ACS Applied Materials & Interfaces* **2013**, *5* (17), 8294-8299.

167. Chronopoulos, D. D.; Bakandritsos, A.; Pykal, M.; Zbořil, R.; Otyepka, M., Chemistry, properties, and applications of fluorographene. *Applied Materials Today* **2017**, *9*, 60-70.
168. Ajao, V.; Bruning, H.; Rijnaarts, H.; Temmink, H., Natural flocculants from fresh and saline wastewater: Comparative properties and flocculation performances. *Chemical Engineering Journal* **2018**, *349*, 622-632.
169. Chen, C.; Li, F.; Zhang, Y.; Wang, B.; Fan, Y.; Wang, X.; Sun, R., Compressive, ultralight and fire-resistant lignin-modified graphene aerogels as recyclable absorbents for oil and organic solvents. *Chemical Engineering Journal* **2018**, *350*, 173-180.
170. Konwar, A.; Kalita, S.; Kotoky, J.; Chowdhury, D., Chitosan–Iron Oxide Coated Graphene Oxide Nanocomposite Hydrogel: A Robust and Soft Antimicrobial Biofilm. *ACS Applied Materials & Interfaces* **2016**, *8* (32), 20625-20634.
171. Lu, Z.; Yu, J.; Zeng, H.; Liu, Q., Polyamine-modified magnetic graphene oxide nanocomposite for enhanced selenium removal. *Separation and Purification Technology* **2017**, *183*, 249-257.
172. Shi, M.; Kan, Q.; Sha, Z.; Kang, G., The Edge-Related Mechanical Properties of Fluorographene Nanoribbons. *Journal of Applied Mechanics* **2015**, *82* (4), 041007-041007-7.
173. Yang, Y.; Lu, G.; Li, Y.; Liu, Z.; Huang, X., One-Step Preparation of Fluorographene: A Highly Efficient, Low-Cost, and Large-Scale Approach of Exfoliating Fluorographite. *ACS Applied Materials & Interfaces* **2013**, *5* (24), 13478-13483.
174. Yufei, W.; Sheng, C.; Ling, Q.; Kun, W.; Huanting, W.; P., S. G.; Dan, L., Graphene-Directed Supramolecular Assembly of Multifunctional Polymer Hydrogel Membranes. *Advanced Functional Materials* **2015**, *25* (1), 126-133.
175. Yuxi, X.; Zhaoyang, L.; Xiaoqing, H.; Yang, W.; Yu, H.; Xiangfeng, D., Graphene

Hydrogels: Functionalized Graphene Hydrogel-Based High-Performance Supercapacitors (Adv. Mater. 40/2013). *Advanced Materials* **2013**, 25 (40), 5828-5828.

176. Xiang, Z.; Zhang, L.; Yuan, T.; Li, Y.; Sun, J., Healability Demonstrates Enhanced Shape-Recovery of Graphene-Oxide-Reinforced Shape-Memory Polymeric Films. *ACS Applied Materials & Interfaces* **2018**, 10 (3), 2897-2906.

177. Xiyao, Z.; Zhou, L.; Kesong, L.; Lei, J., Bioinspired Multifunctional Foam with Self-Cleaning and Oil/Water Separation. *Advanced Functional Materials* **2013**, 23 (22), 2881-2886.

178. Yan, S.; Zhao, J.; Yuan, Y.; Liu, S.; Huang, Z.; Chen, Z.; Jiang, D.; Zhao, W., Preparation and liquid-phase exfoliation of graphite fluoroxide towards graphene fluoroxide. *RSC Advances* **2013**, 3 (44), 21869-21876.

179. Zhang, J.; Azam, M. S.; Shi, C.; Huang, J.; Yan, B.; Liu, Q.; Zeng, H., Poly(acrylic acid) functionalized magnetic graphene oxide nanocomposite for removal of methylene blue. *RSC Advances* **2015**, 5 (41), 32272-32282.

180. Gong, Y.; Wu, Y.; Xu, Y.; Li, L.; Li, C.; Liu, X.; Niu, L., All-solid-state Z-scheme CdTe/TiO₂ heterostructure photocatalysts with enhanced visible-light photocatalytic degradation of antibiotic waste water. *Chemical Engineering Journal* **2018**, 350, 257-267.

181. Wu, H.; Shen, J.; Jiang, X.; Liu, X.; Sun, X.; Li, J.; Han, W.; Wang, L., Bioaugmentation strategy for the treatment of fungicide wastewater by two triazole-degrading strains. *Chemical Engineering Journal* **2018**, 349, 17-24.

182. Wu, J.; Tao, K.; Zhang, J.; Guo, Y.; Miao, J.; Norford, L. K., Chemically functionalized 3D graphene hydrogel for high performance gas sensing. *Journal of Materials Chemistry A* **2016**, 4 (21), 8130-8140.

183. Zhao, Y.; Zhang, Y.; Liu, A.; Wei, Z.; Liu, S., Construction of Three-Dimensional Hemin-

Functionalized Graphene Hydrogel with High Mechanical Stability and Adsorption Capacity for Enhancing Photodegradation of Methylene Blue. *ACS Applied Materials & Interfaces* **2017**, *9* (4), 4006-4014.

184. Zhou, M.; Tian, Y.; Sameoto, D.; Zhang, X.; Meng, Y.; Wen, S., Controllable Interfacial Adhesion Applied to Transfer Light and Fragile Objects by Using Gecko Inspired Mushroom-Shaped Pillar Surface. *ACS Applied Materials & Interfaces* **2013**, *5* (20), 10137-10144.

185. Zhang, Z.; Xiao, F.; Guo, Y.; Wang, S.; Liu, Y., One-Pot Self-Assembled Three-Dimensional TiO₂-Graphene Hydrogel with Improved Adsorption Capacities and Photocatalytic and Electrochemical Activities. *ACS Applied Materials & Interfaces* **2013**, *5* (6), 2227-2233.

186. Zhongxin, X.; Shutao, W.; Ling, L.; Li, C.; Mingjie, L.; Lin, F.; Lei, J., A Novel Superhydrophilic and Underwater Superoleophobic Hydrogel-Coated Mesh for Oil/Water Separation. *Advanced Materials* **2011**, *23* (37), 4270-4273.

187. Dubecký, M.; Otyepková, E.; Lazar, P.; Karlický, F.; Petr, M.; Čépe, K.; Banáš, P.; Zbořil, R.; Otyepka, M., Reactivity of Fluorographene: A Facile Way toward Graphene Derivatives. *The Journal of Physical Chemistry Letters* **2015**, *6* (8), 1430-1434.

188. Holten-Andersen, N.; Harrington, M. J.; Birkedal, H.; Lee, B. P.; Messersmith, P. B.; Lee, K. Y. C.; Waite, J. H., pH-induced metal-ligand cross-links inspired by mussel yield self-healing polymer networks with near-covalent elastic moduli. *Proceedings of the National Academy of Sciences* **2011**, *108* (7), 2651-2655.

189. Huiyuan, L.; Huanting, W.; Xiwang, Z., Facile Fabrication of Freestanding Ultrathin Reduced Graphene Oxide Membranes for Water Purification. *Advanced Materials* **2015**, *27* (2), 249-254.

190. Lyu, C.-Q.; Lu, J.-Y.; Cao, C.-H.; Luo, D.; Fu, Y.-X.; He, Y.-S.; Zou, D.-R., Induction of

Osteogenic Differentiation of Human Adipose-Derived Stem Cells by a Novel Self-Supporting Graphene Hydrogel Film and the Possible Underlying Mechanism. *ACS Applied Materials & Interfaces* **2015**, *7* (36), 20245-20254.

191. Cheng, G.; Dong, L.; Kamboj, L.; Khosla, T.; Wang, X.; Zhang, Z.; Guo, L.; Pesika, N.; Ding, J., Hydrothermal Synthesis of Monodisperse Hard Carbon Spheres and Their Water-Based Lubrication. *Tribology Letters* **2017**, *65* (4), 141.

192. Jing, W.; Yaoxin, H.; Yan, L.; Biao, K.; Jin, Z.; Jingchao, S.; Qiaoliang, B.; P., S. G.; Ping, J. S.; Huanting, W., Nitrogen-Doped Nanoporous Carbon/Graphene Nano-Sandwiches: Synthesis and Application for Efficient Oxygen Reduction. *Advanced Functional Materials* **2015**, *25* (36), 5768-5777.

193. Zhang, Z.; Sun, T.; Chen, C.; Xiao, F.; Gong, Z.; Wang, S., Bifunctional Nanocatalyst Based on Three-Dimensional Carbon Nanotube–Graphene Hydrogel Supported Pd Nanoparticles: One-Pot Synthesis and Its Catalytic Properties. *ACS Applied Materials & Interfaces* **2014**, *6* (23), 21035-21040.

194. Oh, H. M.; Jeong, H.; Han, G. H.; Kim, H.; Kim, J. H.; Lee, S. Y.; Jeong, S. Y.; Jeong, S.; Park, D. J.; Kim, K. K.; Lee, Y. H.; Jeong, M. S., Modulating Electronic Properties of Monolayer MoS₂ via Electron-Withdrawing Functional Groups of Graphene Oxide. *ACS Nano* **2016**, *10* (11), 10446-10453.

195. Kollboyina, J.; Ramanatha, D. K. K.; Christoph, R.; Martin, P.; Michal, O.; Radek, Z.; A., F. R., Biomimetic Superhydrophobic/Superoleophilic Highly Fluorinated Graphene Oxide and ZIF-8 Composites for Oil–Water Separation. *Angewandte Chemie International Edition* **2016**, *55* (3), 1178-1182.

196. Zhang, L.; Ji, L.; Glans, P.-A.; Zhang, Y.; Zhu, J.; Guo, J., Electronic structure and chemical

bonding of a graphene oxide–sulfur nanocomposite for use in superior performance lithium–sulfur cells. *Physical Chemistry Chemical Physics* **2012**, *14* (39), 13670-13675.

197. Xiang, Z.; Ying, H.; Panbo, L., Enhanced Electromagnetic Wave Absorption Properties of Poly(3, 4-ethylenedioxythiophene) Nanofibers Decorated Graphene Sheets by Non-covalent Interactions. *Nano-Micro Letters* **2015**, *7* (?).

198. Hirunpinyopas, W.; Prestat, E.; Worrall, S. D.; Haigh, S. J.; Dryfe, R. A. W.; Bissett, M. A., Desalination and Nanofiltration through Functionalized Laminar MoS₂ Membranes. *ACS Nano* **2017**, *11* (11), 11082-11090.

199. Wang, P.; Chung, T.-S., Design and fabrication of lotus-root-like multi-bore hollow fiber membrane for direct contact membrane distillation. *Journal of Membrane Science* **2012**, *421-422*, 361-374.

200. Shim, J.; Banerjee, S.; Qiu, H.; Smithe, K. K. H.; Estrada, D.; Bello, J.; Pop, E.; Schulten, K.; Bashir, R., Detection of methylation on dsDNA using nanopores in a MoS₂ membrane. *Nanoscale* **2017**, *9* (39), 14836-14845.

201. Zong, X.; Yan, H.; Wu, G.; Ma, G.; Wen, F.; Wang, L.; Li, C., Enhancement of Photocatalytic H₂ Evolution on CdS by Loading MoS₂ as Cocatalyst under Visible Light Irradiation. *Journal of the American Chemical Society* **2008**, *130* (23), 7176-7177.

202. Yongjie, Z.; Zheng, L.; Sina, N.; M., A. P.; Jun, L., Large-Area Vapor-Phase Growth and Characterization of MoS₂ Atomic Layers on a SiO₂ Substrate. *Small* **2012**, *8* (7), 966-971.

203. Yi-Hsien, L.; Xin-Quan, Z.; Wenjing, Z.; Mu-Tung, C.; Cheng-Te, L.; Kai-Di, C.; Ya-Chu, Y.; Tse-Wei, W. J.; Chia-Seng, C.; Lain-Jong, L.; Tsung-Wu, L., Synthesis of Large-Area MoS₂ Atomic Layers with Chemical Vapor Deposition. *Advanced Materials* **2012**, *24* (17), 2320-2325.

204. Kaur, S.; Kempson, I.; Xu, H.; Nydén, M.; Larsson, M., Bio-template assisted synthesis of

porous glutaraldehyde-polyethyleneimine particulate resin for selective copper ion binding and recovery. *RSC Advances* **2018**, 8 (22), 12043-12052.

205. Chen, M.; Shan, X.; Geske, T.; Li, J.; Yu, Z., Manipulating Ion Migration for Highly Stable Light-Emitting Diodes with Single-Crystalline Organometal Halide Perovskite Microplatelets. *ACS Nano* **2017**, 11 (6), 6312-6318.

206. Adeli, E.; Thung, K.; An, L.; Wu, G.; Shi, F.; Wang, T.; Shen, D., Semi-Supervised Discriminative Classification Robust to Sample-Outliers and Feature-Noises. *IEEE Transactions on Pattern Analysis and Machine Intelligence* **2019**, 41 (2), 515-522.

207. Bandara, N.; Esparza, Y.; Wu, J., Graphite Oxide Improves Adhesion and Water Resistance of Canola Protein–Graphite Oxide Hybrid Adhesive. *Scientific Reports* **2017**, 7 (1), 11538.

208. Zhao, W.; Zhao, P.; Tian, Y.; Shen, C.; Li, Z.; Jin, C., Transport and retention of *Microcystis aeruginosa* in porous media: Impacts of ionic strength, flow rate, media size and pre-oxidization. *Water Research* **2019**, 162, 277-287.

209. Munz, M.; Oswald, S. E.; Schäfferling, R.; Lensing, H.-J., Temperature-dependent redox zonation, nitrate removal and attenuation of organic micropollutants during bank filtration. *Water Research* **2019**, 162, 225-235.

210. Shan, M.; Kang, H.; Xu, Z.; Li, N.; Jing, M.; Hu, Y.; Teng, K.; Qian, X.; Shi, J.; Liu, L., Decreased cross-linking in interfacial polymerization and heteromorphic support between nanoparticles: Towards high-water and low-solute flux of hybrid forward osmosis membrane. *Journal of Colloid and Interface Science* **2019**, 548, 170-183.

211. Waduge, P.; Bilgin, I.; Larkin, J.; Henley, R. Y.; Goodfellow, K.; Graham, A. C.; Bell, D. C.; Vamivakas, N.; Kar, S.; Wanunu, M., Direct and Scalable Deposition of Atomically Thin Low-Noise MoS₂ Membranes on Apertures. *ACS Nano* **2015**, 9 (7), 7352-7359.

212. Xu, Z.; Ye, H.; Li, H.; Xu, Y.; Wang, C.; Yin, J.; Zhu, H., Enhanced Lithium Ion Storage Performance of Tannic Acid in LiTFSI Electrolyte. *ACS Omega* **2017**, *2* (4), 1273-1278.
213. Bandara, N.; Wu, J., Chemically Modified Canola Protein–Nanomaterial Hybrid Adhesive Shows Improved Adhesion and Water Resistance. *ACS Sustainable Chemistry & Engineering* **2018**, *6* (1), 1152-1161.
214. Zhang, J.; Xu, Z.; Shan, M.; Zhou, B.; Li, Y.; Li, B.; Niu, J.; Qian, X., Synergetic effects of oxidized carbon nanotubes and graphene oxide on fouling control and anti-fouling mechanism of polyvinylidene fluoride ultrafiltration membranes. *Journal of Membrane Science* **2013**, *448*, 81-92.
215. Lin, J.; Ye, W.; Zeng, H.; Yang, H.; Shen, J.; Darvishmanesh, S.; Luis, P.; Sotto, A.; Van der Bruggen, B., Fractionation of direct dyes and salts in aqueous solution using loose nanofiltration membranes. *Journal of Membrane Science* **2015**, *477*, 183-193.
216. Kang, H.; Shi, J.; Liu, L.; Shan, M.; Xu, Z.; Li, N.; Li, J.; Lv, H.; Qian, X.; Zhao, L., Sandwich morphology and superior dye-removal performances for nanofiltration membranes self-assembled via graphene oxide and carbon nanotubes. *Applied Surface Science* **2018**, *428*, 990-999.
217. Morelos-Gomez, A.; Cruz-Silva, R.; Muramatsu, H.; Ortiz-Medina, J.; Araki, T.; Fukuyo, T.; Tejima, S.; Takeuchi, K.; Hayashi, T.; Terrones, M.; Endo, M., Effective NaCl and dye rejection of hybrid graphene oxide/graphene layered membranes. *Nature Nanotechnology* **2017**, *12*, 1083.
218. Campbell, S.; Maitland, D.; Hoare, T., Enhanced Pulsatile Drug Release from Injectable Magnetic Hydrogels with Embedded Thermosensitive Microgels. *ACS Macro Letters* **2015**, *4* (3), 312-316.
219. Kang, H.; Gongping, L.; Yueyun, L.; Ziyue, D.; Jie, S.; Wanqin, J., A Graphene Oxide

Membrane with Highly Selective Molecular Separation of Aqueous Organic Solution. *Angewandte Chemie International Edition* **2014**, *53* (27), 6929-6932.

220. Wojcik, M.; Hauser, M.; Li, W.; Moon, S.; Xu, K., Graphene-enabled electron microscopy and correlated super-resolution microscopy of wet cells. *Nature Communications* **2015**, *6*, 7384.

221. Heiranian, M.; Farimani, A. B.; Aluru, N. R., Water desalination with a single-layer MoS₂ nanopore. *Nature Communications* **2015**, *6*, 8616.

222. Yin, X.; Sun, C.; Zhang, B.; Song, Y.; Wang, N.; Zhu, L.; Zhu, B., A facile approach to fabricate superhydrophobic coatings on porous surfaces using cross-linkable fluorinated emulsions. *Chemical Engineering Journal* **2017**, *330*, 202-212.

223. Banerjee, P.; Mukhopadhyay, A.; Das, P., Graphene oxide–nanobentonite composite sieves for enhanced desalination and dye removal. *Desalination* **2019**, *451*, 231-240.

224. Chen, P.; Ma, X.; Zhong, Z.; Zhang, F.; Xing, W.; Fan, Y., Performance of ceramic nanofiltration membrane for desalination of dye solutions containing NaCl and Na₂SO₄. *Desalination* **2017**, *404*, 102-111.

225. Feldman, Y.; Wasserman, E.; Srolovitz, D. J.; Tenne, R., High-Rate, Gas-Phase Growth of MoS₂ Nested Inorganic Fullerenes and Nanotubes. *Science* **1995**, *267* (5195), 222-225.

226. Radisavljevic, B.; Whitwick, M. B.; Kis, A., Integrated Circuits and Logic Operations Based on Single-Layer MoS₂. *ACS Nano* **2011**, *5* (12), 9934-9938.

227. Jia, W.; Tang, B.; Wu, P., Nafion-assisted exfoliation of MoS₂ in water phase and the application in quick-response NIR light controllable multi-shape memory membrane. *Nano Research* **2018**, *11* (1), 542-553.

228. Yadong, Z.; Zhaoshun, M.; Qi, S.; Haiqi, G.; Yuzhen, L.; Yunhui, W.; Dewei, R.; Kaiming,

D.; Ruifeng, L., Nanoporous MoS₂ monolayer as a promising membrane for purifying hydrogen and enriching methane. *Journal of Physics: Condensed Matter* **2017**, *29* (37), 375201.

229. Mi, B., Graphene Oxide Membranes for Ionic and Molecular Sieving. *Science* **2014**, *343* (6172), 740-742.

230. Yu, L.; Lee, Y.-H.; Ling, X.; Santos, E. J. G.; Shin, Y. C.; Lin, Y.; Dubey, M.; Kaxiras, E.; Kong, J.; Wang, H.; Palacios, T., Graphene/MoS₂ Hybrid Technology for Large-Scale Two-Dimensional Electronics. *Nano Letters* **2014**, *14* (6), 3055-3063.

231. Yan, Y. G.; Wang, W. S.; Li, W.; Loh, K. P.; Zhang, J., A graphene-like membrane with an ultrahigh water flux for desalination. *Nanoscale* **2017**, *9* (47), 18951-18958.

232. Zhou, Y.; Fan, R.; Short, M. D.; Li, J.; Schumann, R. C.; Xu, H.; Smart, R. S. C.; Gerson, A. R.; Qian, G., Formation of Aluminum Hydroxide-Doped Surface Passivating Layers on Pyrite for Acid Rock Drainage Control. *Environmental Science & Technology* **2018**, *52* (20), 11786-11795.

233. Zembyla, M.; Murray, B. S.; Radford, S. J.; Sarkar, A., Water-in-oil Pickering emulsions stabilized by an interfacial complex of water-insoluble polyphenol crystals and protein. *Journal of Colloid and Interface Science* **2019**, *548*, 88-99.

234. Kou, J.; Yao, J.; Wu, L.; Zhou, X.; Lu, H.; Wu, F.; Fan, J., Nanoporous two-dimensional MoS₂ membranes for fast saline solution purification. *Physical Chemistry Chemical Physics* **2016**, *18* (32), 22210-22216.

235. Xiangdong, Y.; Yanbing, Y.; Linna, F.; Mingchu, Z.; Zhihao, L.; Anyuan, C.; Quan, Y., An Ultrathin Flexible 2D Membrane Based on Single-Walled Nanotube–MoS₂ Hybrid Film for High-Performance Solar Steam Generation. *Advanced Functional Materials* **2018**, *28* (3), 1704505.

236. Wang, Z.; Tu, Q.; Zheng, S.; Urban, J. J.; Li, S.; Mi, B., Understanding the Aqueous

- Stability and Filtration Capability of MoS₂ Membranes. *Nano Letters* **2017**, *17* (12), 7289-7298.
237. LaRue, R. J.; Cobble Dick, J.; Aubry, N.; Cranston, E. D.; Latulippe, D. R., The microscale flocculation test (MFT)—A high-throughput technique for optimizing separation performance. *Chemical Engineering Research and Design* **2016**, *105*, 85-93.
238. Hu, D.; Li, F.; Wang, B.; Lei, K.; Cao, A.; Wang, Z.; Yin-Hua, L., An effect analysis of changes in the composition of the water ecological footprint in Jiangyin City, China. *International Journal of Sustainable Development & World Ecology* **2008**, *15* (3), 211-221.
239. Berry, D.; Holder, D.; Xi, C.; Raskin, L., Comparative transcriptomics of the response of *Escherichia coli* to the disinfectant monochloramine and to growth conditions inducing monochloramine resistance. *Water Research* **2010**, *44* (17), 4924-4931.
240. Hegab, H. M.; ElMekawy, A.; Barclay, T. G.; Michelmores, A.; Zou, L.; Losic, D.; Saint, C. P.; Ginic-Markovic, M., A Novel Fabrication Approach for Multifunctional Graphene-based Thin Film Nano-composite Membranes with Enhanced Desalination and Antibacterial Characteristics. *Scientific Reports* **2017**, *7* (1), 7490.
241. Joshi, R. K.; Carbone, P.; Wang, F. C.; Kravets, V. G.; Su, Y.; Grigorieva, I. V.; Wu, H. A.; Geim, A. K.; Nair, R. R., Precise and Ultrafast Molecular Sieving Through Graphene Oxide Membranes. *Science* **2014**, *343* (6172), 752-754.
242. Sun, P.; Zhu, M.; Wang, K.; Zhong, M.; Wei, J.; Wu, D.; Xu, Z.; Zhu, H., Selective Ion Penetration of Graphene Oxide Membranes. *ACS Nano* **2013**, *7* (1), 428-437.
243. Feng, L.; Li, L.; Zhang, Y.; Peng, H.; Zou, Y., Low temperature synthesis and ion conductivity of Li₇La₃Zr₂O₁₂ garnets for solid state Li ion batteries. *Solid State Ionics* **2017**, *310*, 129-133.
244. Haase, M. F.; Jeon, H.; Hough, N.; Kim, J. H.; Stebe, K. J.; Lee, D., Multifunctional

nanocomposite hollow fiber membranes by solvent transfer induced phase separation. *Nature Communications* **2017**, *8* (1), 1234.

245. Liu, S.; Xie, L.; Liu, J.; Liu, G.; Zhong, H.; Wang, Y.; Zeng, H., Probing the interactions of hydroxamic acid and mineral surfaces: Molecular mechanism underlying the selective separation. *Chemical Engineering Journal* **2019**, *374*, 123-132.

246. Zhang, J.; Lu, X.; Shi, C.; Yan, B.; Gong, L.; Chen, J.; Xiang, L.; Xu, H.; Liu, Q.; Zeng, H., Unraveling the molecular interaction mechanism between graphene oxide and aromatic organic compounds with implications on wastewater treatment. *Chemical Engineering Journal* **2019**, *358*, 842-849.

247. Hai, X.; Chang, K.; Pang, H.; Li, M.; Li, P.; Liu, H.; Shi, L.; Ye, J., Engineering the Edges of MoS₂ (WS₂) Crystals for Direct Exfoliation into Monolayers in Polar Micromolecular Solvents. *Journal of the American Chemical Society* **2016**, *138* (45), 14962-14969.

248. Lee, K. P.; Arnot, T. C.; Mattia, D., A review of reverse osmosis membrane materials for desalination—Development to date and future potential. *Journal of Membrane Science* **2011**, *370* (1), 1-22.

249. Shi, C.; Zhang, L.; Xie, L.; Lu, X.; Liu, Q.; He, J.; Mantilla, C. A.; Van den berg, F. G. A.; Zeng, H., Surface Interaction of Water-in-Oil Emulsion Droplets with Interfacially Active Asphaltenes. *Langmuir* **2017**, *33* (5), 1265-1274.

250. Ravula, S.; Essner, J. B.; Baker, G. A., Kitchen-Inspired Nanochemistry: Dispersion, Exfoliation, and Hybridization of Functional MoS₂ Nanosheets Using Culinary Hydrocolloids. *ChemNanoMat* **2015**, *1* (3), 167-177.

251. Feng, S.; Kin, T. M.; Zuopeng, L.; Matthias, B., Controlling Iron-Catalyzed Oxidation Reactions: From Non-Selective Radical to Selective Non-Radical Reactions. *Chemistry – A*

European Journal **2008**, *14* (29), 8793-8797.

252. Feng, S.; Shuhua, L.; Haitao, G.; Ning, D.; Lijie, D.; Wolfgang, T.; Wolfgang, K., Magnetic-Field-Induced Locomotion of Glass Fibers on Water Surfaces: Towards the Understanding of How Much Force One Magnetic Nanoparticle Can Deliver. *Advanced Materials* **2009**, *21* (19), 1927-1930.

253. Ganatra, R.; Zhang, Q., Few-Layer MoS₂: A Promising Layered Semiconductor. *ACS Nano* **2014**, *8* (5), 4074-4099.

254. Andersen, A.; Kathmann, S. M.; Lilga, M. A.; Albrecht, K. O.; Hallen, R. T.; Mei, D., Adsorption of Potassium on MoS₂(100) Surface: A First-Principles Investigation. *The Journal of Physical Chemistry C* **2011**, *115* (18), 9025-9040.

255. Presolski, S.; Pumera, M., Covalent functionalization of MoS₂. *Materials Today* **2016**, *19* (3), 140-145.

256. Chu, X. S.; Yousaf, A.; Li, D. O.; Tang, A. A.; Debnath, A.; Ma, D.; Green, A. A.; Santos, E. J. G.; Wang, Q. H., Direct Covalent Chemical Functionalization of Unmodified Two-Dimensional Molybdenum Disulfide. *Chemistry of Materials* **2018**, *30* (6), 2112-2128.

257. McNaughton, R. L.; Helton, M. E.; Cospers, M. M.; Enemark, J. H.; Kirk, M. L., Nature of the Oxomolybdenum–Thiolate π -Bond: Implications for Mo–S Bonding in Sulfite Oxidase and Xanthine Oxidase. *Inorganic Chemistry* **2004**, *43* (5), 1625-1637.

258. Deng, M.; Kwac, K.; Li, M.; Jung, Y.; Park, H. G., Stability, Molecular Sieving, and Ion Diffusion Selectivity of a Lamellar Membrane from Two-Dimensional Molybdenum Disulfide. *Nano Letters* **2017**, *17* (4), 2342-2348.

259. Ma, H.; Shen, Z.; Ben, S., Understanding the exfoliation and dispersion of MoS₂ nanosheets in pure water. *Journal of Colloid and Interface Science* **2018**, *517*, 204-212.

260. Li, Y.; Wang, H.; Xie, L.; Liang, Y.; Hong, G.; Dai, H., MoS₂ Nanoparticles Grown on Graphene: An Advanced Catalyst for the Hydrogen Evolution Reaction. *Journal of the American Chemical Society* **2011**, *133* (19), 7296-7299.
261. Shen, Y.; Wang, H.; Zhang, X.; Zhang, Y., *MoS₂ nanosheets functionalized mixed matrix membrane for enhanced CO₂ capture via surface drop-coating method*. 2016; Vol. 8.
262. Xu, X.; Wu, J.; Meng, Z.; Li, Y.; Huang, Q.; Qi, Y.; Liu, Y.; Zhan, D.; Liu, X. Y., Enhanced Exfoliation of Biocompatible MoS₂ Nanosheets by Wool Keratin. *ACS Applied Nano Materials* **2018**.
263. Chu, K. H.; Huang, Y.; Yu, M.; Her, N.; Flora, J. R. V.; Park, C. M.; Kim, S.; Cho, J.; Yoon, Y., Evaluation of Humic Acid and Tannic Acid Fouling in Graphene Oxide-Coated Ultrafiltration Membranes. *ACS Applied Materials & Interfaces* **2016**, *8* (34), 22270-22279.
264. Thebo, K. H.; Qian, X.; Zhang, Q.; Chen, L.; Cheng, H.-M.; Ren, W., Highly stable graphene-oxide-based membranes with superior permeability. *Nature Communications* **2018**, *9* (1), 1486.
265. Han, Y.; Jiang, Y.; Gao, C., High-Flux Graphene Oxide Nanofiltration Membrane Intercalated by Carbon Nanotubes. *ACS Applied Materials & Interfaces* **2015**, *7* (15), 8147-8155.
266. Wang, S.; Wu, Y.; Zhang, N.; He, G.; Xin, Q.; Wu, X.; Wu, H.; Cao, X.; Guiver, M. D.; Jiang, Z., A highly permeable graphene oxide membrane with fast and selective transport nanochannels for efficient carbon capture. *Energy & Environmental Science* **2016**, *9* (10), 3107-3112.
267. Xiang, Z.; Zhang, L.; Yuan, T.; Li, Y.; Sun, J., Healability Demonstrates Enhanced Shape-Recovery of Graphene-Oxide-Reinforced Shape-Memory Polymeric Films. *ACS Applied Materials & Interfaces* **2018**, *10* (3), 2897-2906.

268. Badrinezhad, L.; Ghasemi, S.; Azizian-Kalandaragh, Y.; Nematollahzadeh, A., Preparation and characterization of polysulfone/graphene oxide nanocomposite membranes for the separation of methylene blue from water. *Polymer Bulletin* **2018**, *75* (2), 469-484.
269. Osti, N. C.; Naguib, M.; Ostadhossein, A.; Xie, Y.; Kent, P. R. C.; Dyatkin, B.; Rother, G.; Heller, W. T.; van Duin, A. C. T.; Gogotsi, Y.; Mamontov, E., Effect of Metal Ion Intercalation on the Structure of MXene and Water Dynamics on its Internal Surfaces. *ACS Applied Materials & Interfaces* **2016**, *8* (14), 8859-8863.
270. Joshi, R. K.; Carbone, P.; Wang, F. C.; Kravets, V. G.; Su, Y.; Grigorieva, I. V.; Wu, H. A.; Geim, A. K.; Nair, R. R., Precise and Ultrafast Molecular Sieving Through Graphene Oxide Membranes. *Science* **2014**, *343* (6172), 752-754.
271. Ma, J.; Ping, D.; Dong, X., Recent Developments of Graphene Oxide-Based Membranes: A Review. *Membranes* **2017**, *7* (3), 52.
272. Kim, H. W.; Yoon, H. W.; Yoon, S.-M.; Yoo, B. M.; Ahn, B. K.; Cho, Y. H.; Shin, H. J.; Yang, H.; Paik, U.; Kwon, S.; Choi, J.-Y.; Park, H. B., Selective Gas Transport Through Few-Layered Graphene and Graphene Oxide Membranes. *Science* **2013**, *342* (6154), 91-95.
273. Chen, C.; Huang, Z.; Jiao, Y.; Shi, L.-A.; Zhang, Y.; Li, J.; Li, C.; Lv, X.; Wu, S.; Hu, Y.; Zhu, W.; Wu, D.; Chu, J.; Jiang, L., In Situ Reversible Control between Sliding and Pinning for Diverse Liquids under Ultra-Low Voltage. *ACS Nano* **2019**, *13* (5), 5742-5752.
274. Meng, J.; Li, P.; Cao, B., High-Flux Direct-Contact Pervaporation Membranes for Desalination. *ACS Applied Materials & Interfaces* **2019**, *11* (31), 28461-28468.
275. Chen, L.; Huang, Y.; Song, L.; Yin, W.; Hou, L.; Liu, X.; Chen, T., Biofriendly and Regenerable Emotional Monitor from Interfacial Ultrathin 2D PDA/AuNPs Cross-linking Films. *ACS Applied Materials & Interfaces* **2019**, *11* (39), 36259-36269.

276. Hirunpinyopas, W.; Prestat, E.; Worrall, S. D.; Haigh, S. J.; Dryfe, R. A. W.; Bissett, M. A., Desalination and Nanofiltration through Functionalized Laminar MoS₂ Membranes. *ACS Nano* **2017**, *11* (11), 11082-11090.
277. Xu, Z.; Ye, H.; Li, H.; Xu, Y.; Wang, C.; Yin, J.; Zhu, H., Enhanced Lithium Ion Storage Performance of Tannic Acid in LiTFSI Electrolyte. *ACS Omega* **2017**, *2* (4), 1273-1278.
278. Chu, K. H.; Huang, Y.; Yu, M.; Her, N.; Flora, J. R. V.; Park, C. M.; Kim, S.; Cho, J.; Yoon, Y., Evaluation of Humic Acid and Tannic Acid Fouling in Graphene Oxide-Coated Ultrafiltration Membranes. *ACS Applied Materials & Interfaces* **2016**, *8* (34), 22270-22279.
279. Zhao, W.; Liu, H.; Liu, Y.; Jian, M.; Gao, L.; Wang, H.; Zhang, X., Thin-Film Nanocomposite Forward-Osmosis Membranes on Hydrophilic Microfiltration Support with an Intermediate Layer of Graphene Oxide and Multiwall Carbon Nanotube. *ACS Applied Materials & Interfaces* **2018**, *10* (40), 34464-34474.
280. Jatukaran, A.; Zhong, J.; Persad, A. H.; Xu, Y.; Mostowfi, F.; Sinton, D., Direct Visualization of Evaporation in a Two-Dimensional Nanoporous Model for Unconventional Natural Gas. *ACS Applied Nano Materials* **2018**, *1* (3), 1332-1338.
281. Li, Y.; Meng, H.; Liu, Y.; Narkar, A.; Lee, B. P., Gelatin Microgel Incorporated Poly(ethylene glycol)-Based Bioadhesive with Enhanced Adhesive Property and Bioactivity. *ACS Applied Materials & Interfaces* **2016**, *8* (19), 11980-11989.
282. Wang, J.; Fang, R.; Hou, J.; Zhang, H.; Tian, Y.; Wang, H.; Jiang, L., Oscillatory Reaction Induced Periodic C-Quadruplex DNA Gating of Artificial Ion Channels. *ACS Nano* **2017**, *11* (3), 3022-3029.
283. Wang, Y.; Liu, X.; Li, S.; Li, T.; Song, Y.; Li, Z.; Zhang, W.; Sun, J., Transparent, Healable Elastomers with High Mechanical Strength and Elasticity Derived from Hydrogen-Bonded

- Polymer Complexes. *ACS Applied Materials & Interfaces* **2017**, *9* (34), 29120-29129.
284. Guan, G.; Zhang, S.; Liu, S.; Cai, Y.; Low, M.; Teng, C. P.; Phang, I. Y.; Cheng, Y.; Duei, K. L.; Srinivasan, B. M.; Zheng, Y.; Zhang, Y.-W.; Han, M.-Y., Protein Induces Layer-by-Layer Exfoliation of Transition Metal Dichalcogenides. *Journal of the American Chemical Society* **2015**, *137* (19), 6152-6155.
285. Chen, X.; Qiu, M.; Ding, H.; Fu, K.; Fan, Y., A reduced graphene oxide nanofiltration membrane intercalated by well-dispersed carbon nanotubes for drinking water purification. *Nanoscale* **2016**, *8* (10), 5696-5705.
286. Deng, M.; Kwac, K.; Li, M.; Jung, Y.; Park, H. G., Stability, Molecular Sieving, and Ion Diffusion Selectivity of a Lamellar Membrane from Two-Dimensional Molybdenum Disulfide. *Nano Letters* **2017**, *17* (4), 2342-2348.
287. Hao, N.; Nie, Y.; Xu, Z.; Jin, C.; Fyda, T. J.; Zhang, J. X. J., Microfluidics-enabled acceleration of Fenton oxidation for degradation of organic dyes with rod-like zero-valent iron nanoassemblies. *Journal of Colloid and Interface Science* **2020**, *559*, 254-262.
288. Levita, G.; Restuccia, P.; Righi, M. C., Graphene and MoS₂ interacting with water: A comparison by ab initio calculations. *Carbon* **2016**, *107*, 878-884.
289. Mi, B., Graphene Oxide Membranes for Ionic and Molecular Sieving. *Science* **2014**, *343* (6172), 740-742.
290. Yu, L.; Lee, Y.-H.; Ling, X.; Santos, E. J. G.; Shin, Y. C.; Lin, Y.; Dubey, M.; Kaxiras, E.; Kong, J.; Wang, H.; Palacios, T., Graphene/MoS₂ Hybrid Technology for Large-Scale Two-Dimensional Electronics. *Nano Letters* **2014**, *14* (6), 3055-3063.
291. Yan, Y. G.; Wang, W. S.; Li, W.; Loh, K. P.; Zhang, J., A graphene-like membrane with an ultrahigh water flux for desalination. *Nanoscale* **2017**, *9* (47), 18951-18958.

292. Heiranian, M.; Farimani, A. B.; Aluru, N. R., Water desalination with a single-layer MoS₂ nanopore. *Nature Communications* **2015**, *6*, 8616.
293. Quain, E.; Mathis, T. S.; Kurra, N.; Maleski, K.; Van Aken, K. L.; Alhabeab, M.; Alshareef, H. N.; Gogotsi, Y., Direct Writing of Additive-Free MXene-in-Water Ink for Electronics and Energy Storage. *Advanced Materials Technologies* **2019**, *4* (1), 1800256.
294. Ghidui, M.; Kota, S.; Drozd, V.; Barsoum, M. W., Pressure-induced shear and interlayer expansion in Ti₃C₂ MXene in the presence of water. *Science Advances* **2018**, *4* (1), eaao6850.
295. Sarycheva, A.; Polemi, A.; Liu, Y.; Dandekar, K.; Anasori, B.; Gogotsi, Y., 2D titanium carbide (MXene) for wireless communication. *Science Advances* **2018**, *4* (9), eaau0920.
296. Huang, S.; Mochalin, V. N., Hydrolysis of 2D Transition-Metal Carbides (MXenes) in Colloidal Solutions. *Inorganic Chemistry* **2019**, *58* (3), 1958-1966.
297. Di Vitantonio, G.; Wang, T.; Haase, M. F.; Stebe, K. J.; Lee, D., Robust Bijels for Reactive Separation via Silica-Reinforced Nanoparticle Layers. *ACS Nano* **2019**, *13* (1), 26-31.
298. Gurera, D.; Bhushan, B., Designing bioinspired conical surfaces for water collection from condensation. *Journal of Colloid and Interface Science* **2020**, *560*, 138-148.
299. Guo, D.; Xiao, Y.; Li, T.; Zhou, Q.; Shen, L.; Li, R.; Xu, Y.; Lin, H., Fabrication of high-performance composite nanofiltration membranes for dye wastewater treatment: mussel-inspired layer-by-layer self-assembly. *Journal of Colloid and Interface Science* **2020**, *560*, 273-283.
300. Zhu, J.; Tian, M.; Hou, J.; Wang, J.; Lin, J.; Zhang, Y.; Liu, J.; Van der Bruggen, B., Surface zwitterionic functionalized graphene oxide for a novel loose nanofiltration membrane. *Journal of Materials Chemistry A* **2016**, *4* (5), 1980-1990.
301. Halim, J.; Kota, S.; Lukatskaya, M. R.; Naguib, M.; Zhao, M.-Q.; Moon, E. J.; Pitoock, J.;

Nanda, J.; May, S. J.; Gogotsi, Y.; Barsoum, M. W., Synthesis and Characterization of 2D Molybdenum Carbide (MXene). *Advanced Functional Materials* **2016**, *26* (18), 3118-3127.

302. Alhabeab, M.; Maleski, K.; Anasori, B.; Lelyukh, P.; Clark, L.; Sin, S.; Gogotsi, Y., Guidelines for Synthesis and Processing of Two-Dimensional Titanium Carbide (Ti₃C₂T_x MXene). *Chemistry of Materials* **2017**, *29* (18), 7633-7644.

303. Hu, W.; Cui, X.; Xiang, L.; Gong, L.; Zhang, L.; Gao, M.; Wang, W.; Zhang, J.; Liu, F.; Yan, B.; Zeng, H., Tannic acid modified MoS₂ nanosheet membranes with superior water flux and ion/dye rejection. *Journal of Colloid and Interface Science* **2020**, *560*, 177-185.

304. Zhang, C.; McKeon, L.; Kremer, M. P.; Park, S.-H.; Ronan, O.; Seral-Ascaso, A.; Barwich, S.; Coileáin, C. Ó.; McEvoy, N.; Nerl, H. C.; Anasori, B.; Coleman, J. N.; Gogotsi, Y.; Nicolosi, V., Additive-free MXene inks and direct printing of micro-supercapacitors. *Nature Communications* **2019**, *10* (1), 1795.

305. Hart, J. L.; Hantanasirisakul, K.; Lang, A. C.; Anasori, B.; Pinto, D.; Pivak, Y.; van Omme, J. T.; May, S. J.; Gogotsi, Y.; Taheri, M. L., Control of MXenes' electronic properties through termination and intercalation. *Nature Communications* **2019**, *10* (1), 522.

306. Jiang, H.; Wang, Z.; Yang, Q.; Tan, L.; Dong, L.; Dong, M., Ultrathin Ti₃C₂T_x (MXene) Nanosheet-Wrapped NiSe₂ Octahedral Crystal for Enhanced Supercapacitor Performance and Synergetic Electrocatalytic Water Splitting. *Nano-Micro Letters* **2019**, *11* (1), 31.

307. Wang, L.-C.; Bao, S.-K.; Luo, J.; Wang, Y.-H.; Nie, Y.-C.; Zou, J.-P., Efficient exfoliation of bulk MoS₂ to nanosheets by mixed-solvent refluxing method. *International Journal of Hydrogen Energy* **2016**, *41* (25), 10737-10743.

308. Oener, S. Z.; Ardo, S.; Boettcher, S. W., Ionic Processes in Water Electrolysis: The Role of Ion-Selective Membranes. *ACS Energy Letters* **2017**, *2* (11), 2625-2634.

309. Zhang, J.; Zhao, Y.; Guo, X.; Chen, C.; Dong, C.-L.; Liu, R.-S.; Han, C.-P.; Li, Y.; Gogotsi, Y.; Wang, G., Single platinum atoms immobilized on an MXene as an efficient catalyst for the hydrogen evolution reaction. *Nature Catalysis* **2018**, *1* (12), 985-992.
310. Sugahara, A.; Ando, Y.; Kajiyama, S.; Yazawa, K.; Gotoh, K.; Otani, M.; Okubo, M.; Yamada, A., Negative dielectric constant of water confined in nanosheets. *Nature Communications* **2019**, *10* (1), 850.
311. Zhang, Y.; Zhang, N.; Ge, C., First-Principles Studies of Adsorptive Remediation of Water and Air Pollutants Using Two-Dimensional MXene Materials. *Materials* **2018**, *11* (11), 2281.
312. Sobolčiak, P.; Ali, A.; Hassan, M. K.; Helal, M. I.; Tanvir, A.; Popelka, A.; Al-Maadeed, M. A.; Krupa, I.; Mahmoud, K. A., 2D Ti₃C₂T_x (MXene)-reinforced polyvinyl alcohol (PVA) nanofibers with enhanced mechanical and electrical properties. *PLOS ONE* **2017**, *12* (8), e0183705.
313. Hu, W.; Zhang, P.; Liu, X.; Yan, B.; Xiang, L.; Zhang, J.; Gong, L.; Huang, J.; Cui, K.; Zhu, L.; Zeng, H., An amphiphobic graphene-based hydrogel as oil-water separator and oil fence material. *Chemical Engineering Journal* **2018**, *353*, 708-716.
314. Michael, J.; Qifeng, Z.; Danling, W., Titanium carbide MXene: Synthesis, electrical and optical properties and their applications in sensors and energy storage devices. *Nanomaterials and Nanotechnology* **2019**, *9*, 1847980418824470.
315. Lee, K. P.; Arnot, T. C.; Mattia, D., A review of reverse osmosis membrane materials for desalination—Development to date and future potential. *Journal of Membrane Science* **2011**, *370* (1), 1-22.
316. Shi, C.; Xie, L.; Zhang, L.; Lu, X.; Zeng, H., Probing the interaction mechanism between oil droplets with asphaltenes and solid surfaces using AFM. *Journal of Colloid and Interface Science* **2020**, *558*, 173-181.

317. Liu, J.; Cui, X.; Xie, L.; Huang, J.; Zhang, L.; Liu, J.; Wang, X.; Wang, J.; Zeng, H., Probing effects of molecular-level heterogeneity of surface hydrophobicity on hydrophobic interactions in air/water/solid systems. *Journal of Colloid and Interface Science* **2019**, *557*, 438-449.
318. Yu, W.; Liu, Y.; Xu, Y.; Li, R.; Chen, J.; Liao, B.-Q.; Shen, L.; Lin, H., A conductive PVDF-Ni membrane with superior rejection, permeance and antifouling ability via electric assisted in-situ aeration for dye separation. *Journal of Membrane Science* **2019**, *581*, 401-412.
319. Chen, Y.; Teng, J.; Liao, B.-Q.; Li, R.; Lin, H., Molecular insights into the impacts of iron(III) ions on membrane fouling by alginate. *Chemosphere* **2020**, *242*, 125232.
320. Tang, H.; Hu, Q.; Zheng, M.; Chi, Y.; Qin, X.; Pang, H.; Xu, Q., MXene-2D layered electrode materials for energy storage. *Progress in Natural Science: Materials International* **2018**, *28* (2), 133-147.
321. Rasid, Z. A. M.; Omar, M. F.; Nazeri, M. F. M.; A'ziz, M. A. A.; Szota, M., Low Cost Synthesis Method of Two-Dimensional Titanium Carbide MXene. *IOP Conference Series: Materials Science and Engineering* **2017**, *209*, 012001.
322. Zhou, Z.; Liu, J.; Zhang, X.; Tian, D.; Zhan, Z.; Lu, C., Ultrathin MXene/Calcium Alginate Aerogel Film for High-Performance Electromagnetic Interference Shielding. **2019**, *6* (6), 1802040.
323. Xuan, D.; Zhou, Y.; Nie, W.; Chen, P., Sodium alginate-assisted exfoliation of MoS₂ and its reinforcement in polymer nanocomposites. *Carbohydrate Polymers* **2017**, *155*, 40-48.
324. Ma, H.; Shen, Z.; Ben, S., Understanding the exfoliation and dispersion of MoS₂ nanosheets in pure water. *Journal of Colloid and Interface Science* **2018**, *517*, 204-212.
325. Hyosung, A.; Touseef, H.; Smit, S.; Huili, G.; Anish, P.; Ian, E.; Xiaofei, Z.; Miladin, R.; Micah J., G.; Jodie L., L., *Water Sorption in MXene/Polyelectrolyte Multilayers for Ultrafast Humidity Sensing*. 2019.

326. Hanmei, J.; Zegao, W.; Qian, Y.; Luxi, T.; Lichun, D.; Mingdong, D., Ultrathin Ti₃C₂Tx (MXene) Nanosheets Wrapped NiSe₂ Octahedral Crystal for Enhanced Supercapacitor Performance and Synergetic Electrocatalytic Water Splitting. *Nano-Micro Letters* **2019**, *11*, 31.
327. Bao, W.; Tang, X.; Guo, X.; Choi, S.; Wang, C.; Gogotsi, Y.; Wang, G., Porous Cryo-Dried MXene for Efficient Capacitive Deionization. *Joule* **2018**, *2* (4), 778-787.
328. Zhu, J.; Li, G.; Feng, C.; Wang, L.; Zhang, W., Effect of Delaminated MXene (Ti₃C₂) on the Performance of Cement Paste. *Journal of Nanomaterials* **2019**, *2019*, 8.
329. Wang, S.; Wu, Y.; Zhang, N.; He, G.; Xin, Q.; Wu, X.; Wu, H.; Cao, X.; Guiver, M. D.; Jiang, Z., A highly permeable graphene oxide membrane with fast and selective transport nanochannels for efficient carbon capture. *Energy & Environmental Science* **2016**, *9* (10), 3107-3112.
330. Chu, X. S.; Yousaf, A.; Li, D. O.; Tang, A. A.; Debnath, A.; Ma, D.; Green, A. A.; Santos, E. J. G.; Wang, Q. H., Direct Covalent Chemical Functionalization of Unmodified Two-Dimensional Molybdenum Disulfide. *Chemistry of Materials* **2018**, *30* (6), 2112-2128.
331. Hu, S.; Sun, Y.; Pu, M.; Yun, R.; Xiang, X., Determination of Boundary Conditions for Highly Efficient Separation of Magnesium and Lithium from Salt Lake Brine by Reaction-Coupled Separation Technology. *Separation and Purification Technology* **2019**, 115813.
332. Yang, G.; Shi, H.; Liu, W.; Xing, W.; Xu, N., Investigation of Mg²⁺/Li⁺ Separation by Nanofiltration. *Chinese Journal of Chemical Engineering* **2011**, *19* (4), 586-591.
333. Yeager, H. L., Cation and Water Diffusion in Nafion Ion Exchange Membranes: Influence of Polymer Structure. *Journal of The Electrochemical Society* **1981**, *128* (9), 1880.
334. Helm, L.; Merbach, A. E., Water exchange on metal ions: experiments and simulations. *Coordination Chemistry Reviews* **1999**, *187* (1), 151-181.

335. Neely, J.; Connick, R., Rate of water exchange from hydrated magnesium ion. *Journal of the American Chemical Society* **1970**, *92* (11), 3476-3478.
336. Xu, X.-L.; Lin, F.-W.; Du, Y.; Zhang, X.; Wu, J.; Xu, Z.-K., Graphene Oxide Nanofiltration Membranes Stabilized by Cationic Porphyrin for High Salt Rejection. *ACS Applied Materials & Interfaces* **2016**, *8* (20), 12588-12593.
337. Wang, J.; Zhang, P.; Liang, B.; Liu, Y.; Xu, T.; Wang, L.; Cao, B.; Pan, K., Graphene Oxide as an Effective Barrier on a Porous Nanofibrous Membrane for Water Treatment. *ACS Applied Materials & Interfaces* **2016**, *8* (9), 6211-6218.
338. Yadong, Z.; Zhaoshun, M.; Qi, S.; Haiqi, G.; Yuzhen, L.; Yunhui, W.; Dewei, R.; Kaiming, D.; Ruifeng, L., Nanoporous MoS₂ monolayer as a promising membrane for purifying hydrogen and enriching methane. *Journal of Physics: Condensed Matter* **2017**, *29* (37), 375201.
339. Oh, S. J.; Kim, N.; Lee, Y. T., Preparation and characterization of PVDF/TiO₂ organic–inorganic composite membranes for fouling resistance improvement. *Journal of Membrane Science* **2009**, *345* (1), 13-20.
340. Ren, C. E.; Hatzell, K. B.; Alhabeab, M.; Ling, Z.; Mahmoud, K. A.; Gogotsi, Y., Charge- and Size-Selective Ion Sieving Through Ti₃C₂T_x MXene Membranes. *The Journal of Physical Chemistry Letters* **2015**, *6* (20), 4026-4031.
341. Hu, M.; Mi, B., Enabling Graphene Oxide Nanosheets as Water Separation Membranes. *Environmental Science & Technology* **2013**, *47* (8), 3715-3723.
342. Akbari, A.; Sheath, P.; Martin, S. T.; Shinde, D. B.; Shaibani, M.; Banerjee, P. C.; Tkacz, R.; Bhattacharyya, D.; Majumder, M., Large-area graphene-based nanofiltration membranes by shear alignment of discotic nematic liquid crystals of graphene oxide. *Nature Communications* **2016**, *7*, 10891.

343. Han, Y.; Jiang, Y.; Gao, C., High-Flux Graphene Oxide Nanofiltration Membrane Intercalated by Carbon Nanotubes. *ACS Applied Materials & Interfaces* **2015**, *7* (15), 8147-8155.
344. Abraham, J.; Vasu, K. S.; Williams, C. D.; Gopinadhan, K.; Su, Y.; Cherian, C. T.; Dix, J.; Prestat, E.; Haigh, S. J.; Grigorieva, I. V.; Carbone, P.; Geim, A. K.; Nair, R. R., Tunable sieving of ions using graphene oxide membranes. *Nature Nanotechnology* **2017**, *12*, 546.
345. Lin, J.; Ye, W.; Zeng, H.; Yang, H.; Shen, J.; Darvishmanesh, S.; Luis, P.; Sotito, A.; Van der Bruggen, B., Fractionation of direct dyes and salts in aqueous solution using loose nanofiltration membranes. *Journal of Membrane Science* **2015**, *477*, 183-193.
346. Akbari, A.; Remigy, J. C.; Aptel, P., Treatment of textile dye effluent using a polyamide-based nanofiltration membrane. *Chemical Engineering and Processing: Process Intensification* **2002**, *41* (7), 601-609.
347. Akbari, A.; Desclaux, S.; Remigy, J. C.; Aptel, P., Treatment of textile dye effluents using a new photografted nanofiltration membrane. *Desalination* **2002**, *149* (1), 101-107.

Appendix

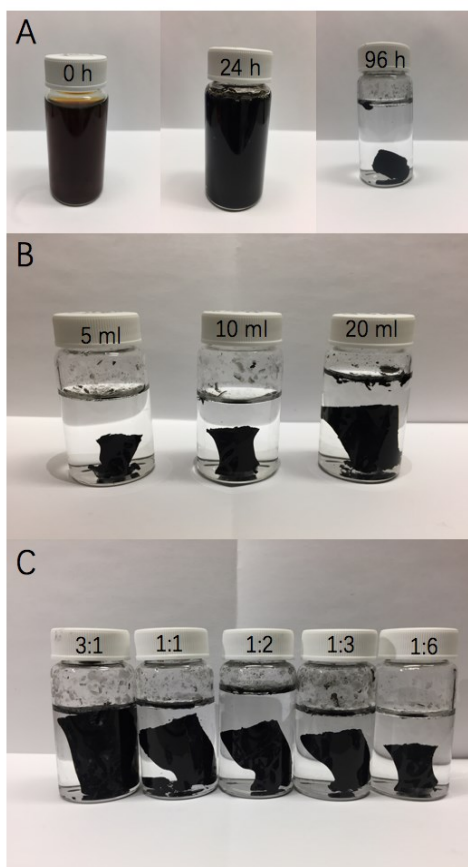


Figure S3.1. Photographs of LA/F/rGO hydrogel synthesized under different conditions: (A) different reaction time at 90 °C; (B) different loadings of GO dispersion (5mg/ml) at consistent 1H,1H,2H,2H-Perfluorodecanethiol concentration (0.1 g); (C) different GO (5mg/ml) dispersion to 1H,1H,2H,2H-Perfluorodecanethiol mass ratio. For B and C, the reaction temperature was set at 90 °C and the reaction time was set as 96 h.

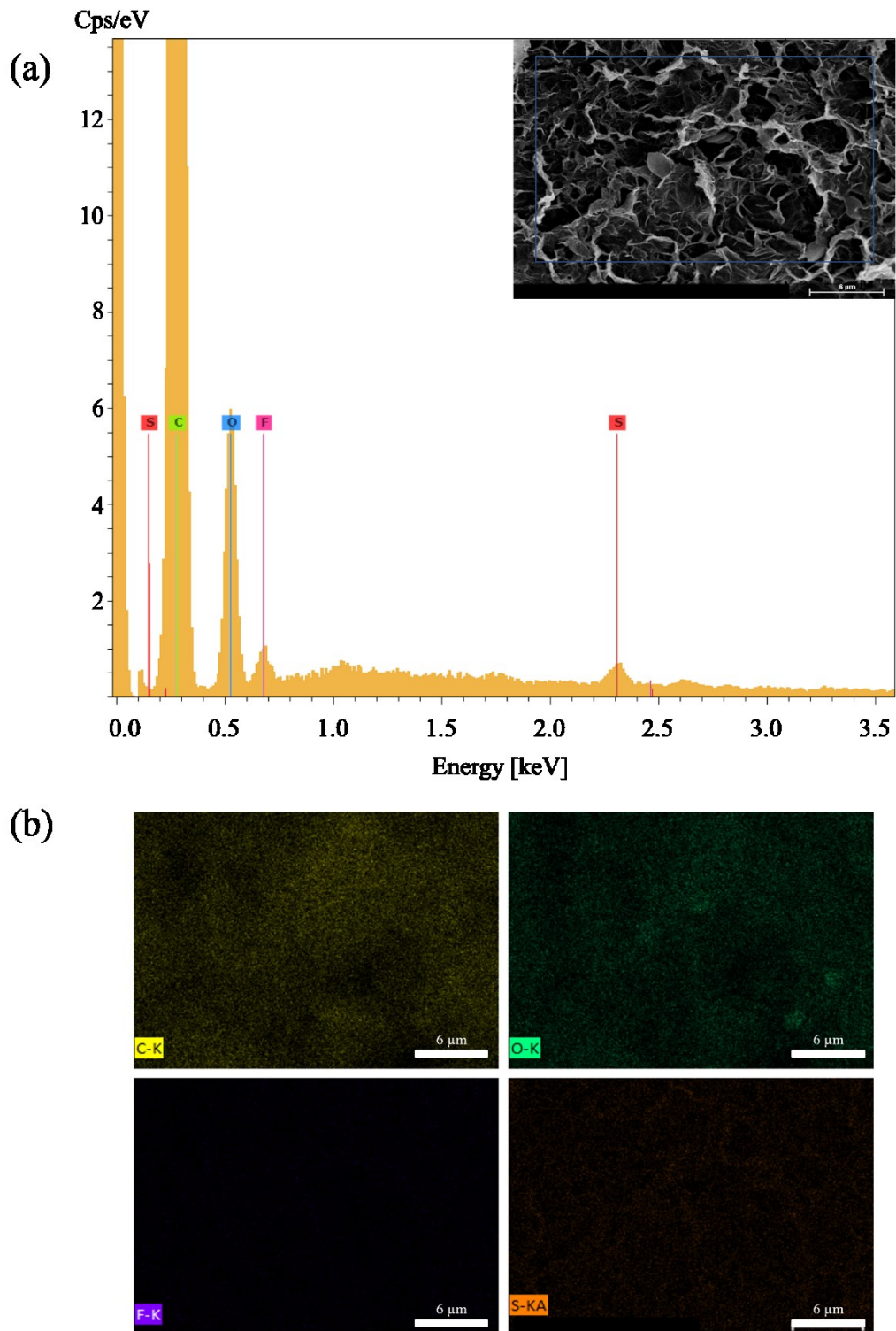


Figure S3.2. FESEM component image (a) and component mapping data for C, O, F, S (b).

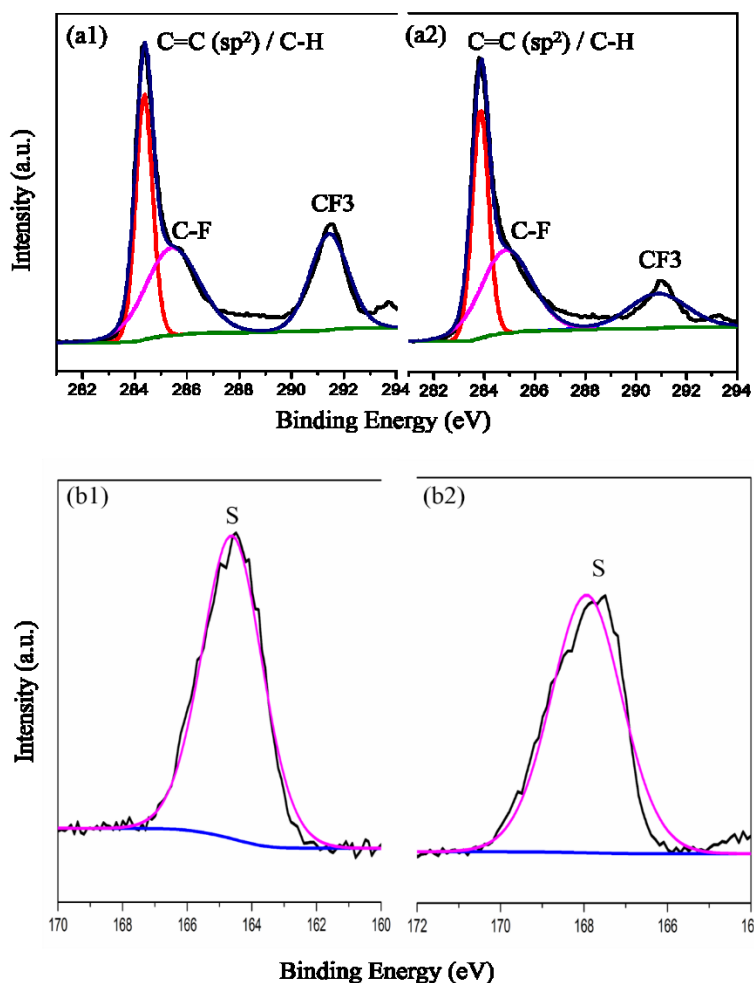


Figure S3.3. XPS spectra for C1s of the LA/F/rGO hydrogel (a1) before burning and (a2) after burning treatment on the flame of a fire lighter ($\sim 280^{\circ}\text{C}$), and core level S (b1) before burning and (b2) after burning treatment for 10 minutes.

The C, O, S, F elements in the LA/F/rGO hydrogel was evidenced by the XPS spectrum in **Figure S3.3** at 163.9, 285, 532, and 689 eV, attributed to S2p, C1s, O1s and CF₂, respectively. In high resolution C1s XPS spectrum in **Figure S3.3** (a1) and (a2), the nearly disappearing of oxygen containing carbon (epoxy C-O at 286.5 eV, carbonyl C=O at 287.9 eV, and carboxyl O=C-O at 289.0 eV), further confirmed the successful reduction of graphene nanosheets by the strong reduction reagent. The existence of high peak C=C (sp²)/C-H at 284.3 eV, C-F functional groups

at 285.7 eV and CF_3 at 291.8 eV indicated the successful Michael's Addition chemical reaction for the PF polymer onto the rGO nanosheets.^{52, 53} There is no obvious change for S element in **Figure S3.3** before (b1) and after (b2) burning treatment (discussed in Section 2.3), indicating that the thiol groups have been successfully grafted onto the graphene nanosheet surfaces.

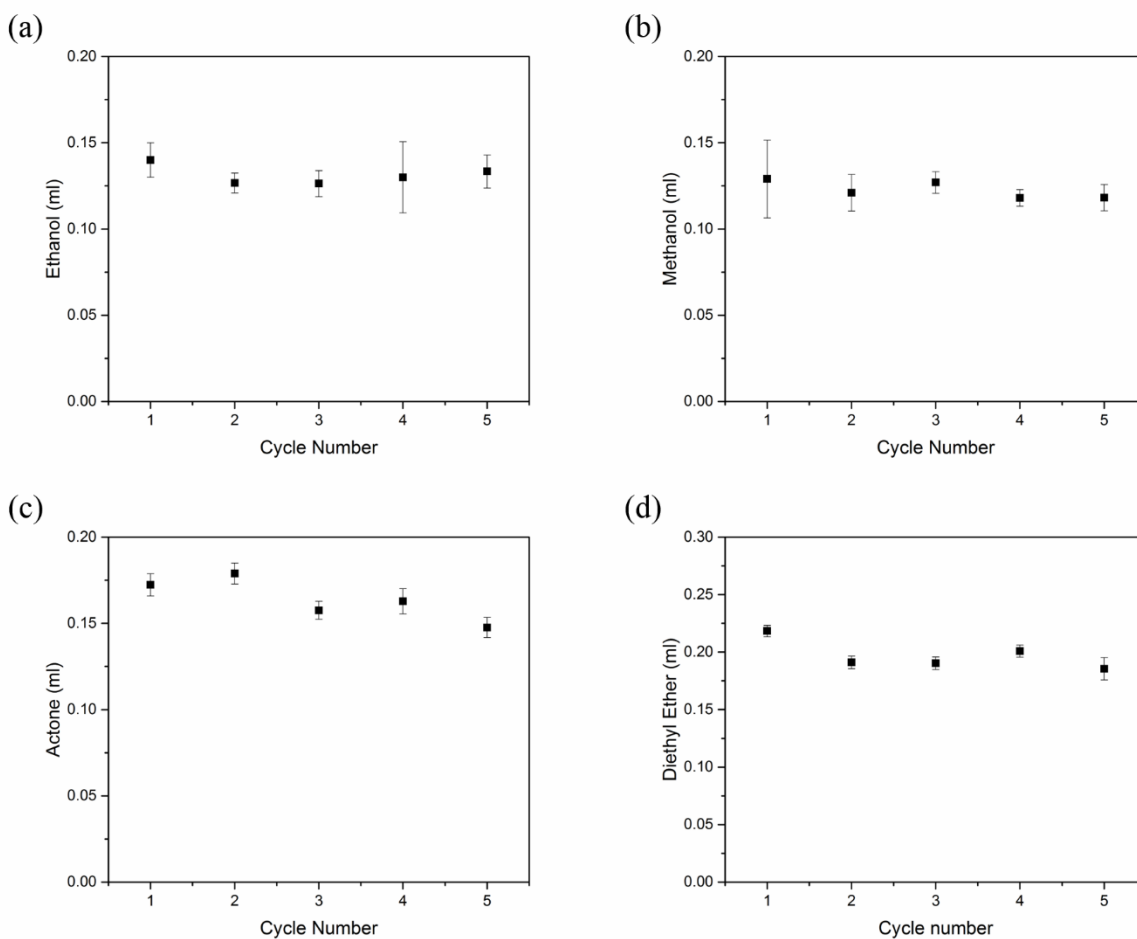


Figure S3.4. Adsorption cycle for various organic solvents: Ethanol (a), Acetone (b), Methanol (c), and Diethyl Ether (d).

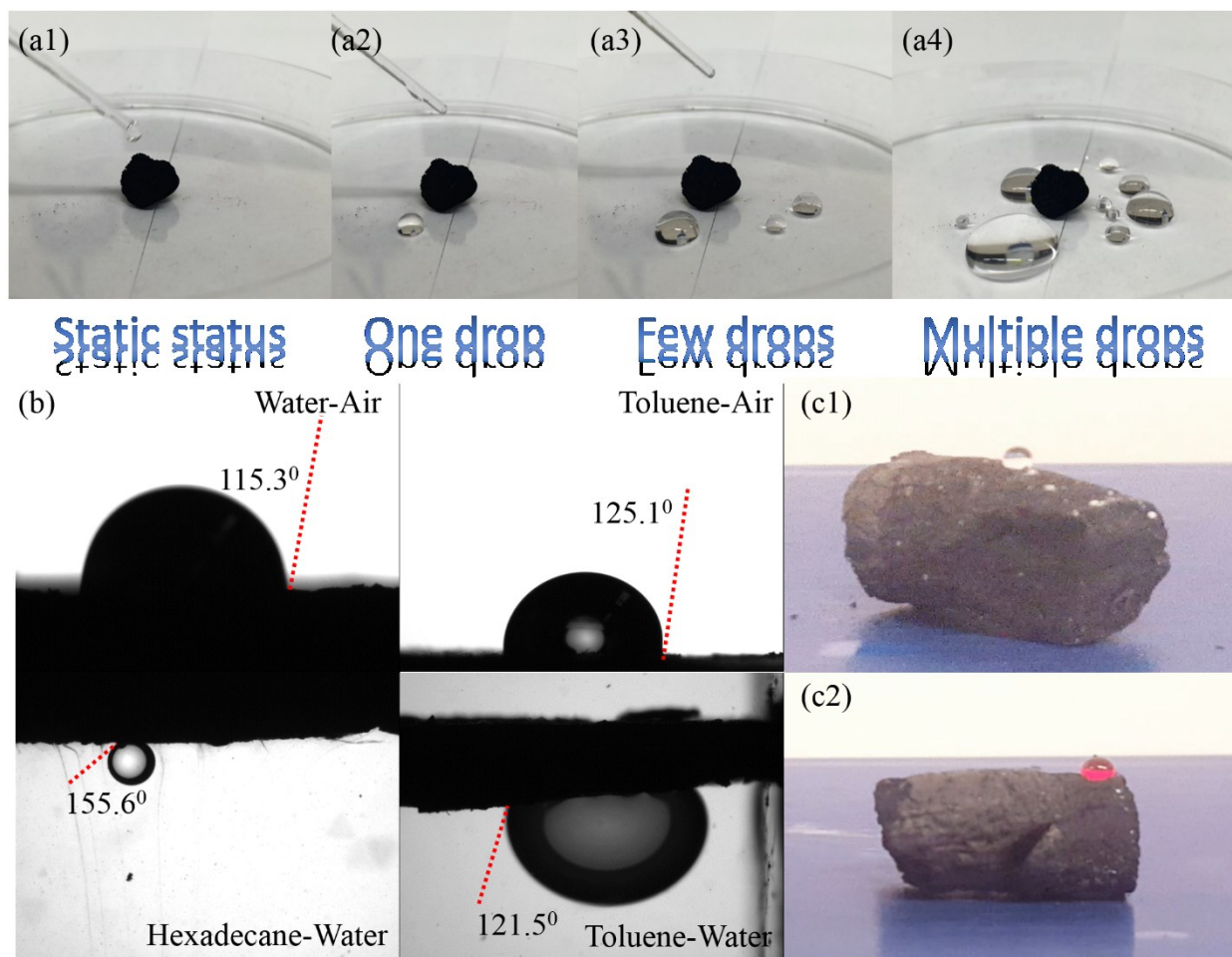


Figure S3.5. Hydrophobic performance for LA/F/rGO hydrogel (a1-a4); Images of contact angles for LA/F/rGO hydrogel in air and water (b); Images for Toluene (c1) and Chloroform (c1) drop on LA/F/rGO hydrogel.

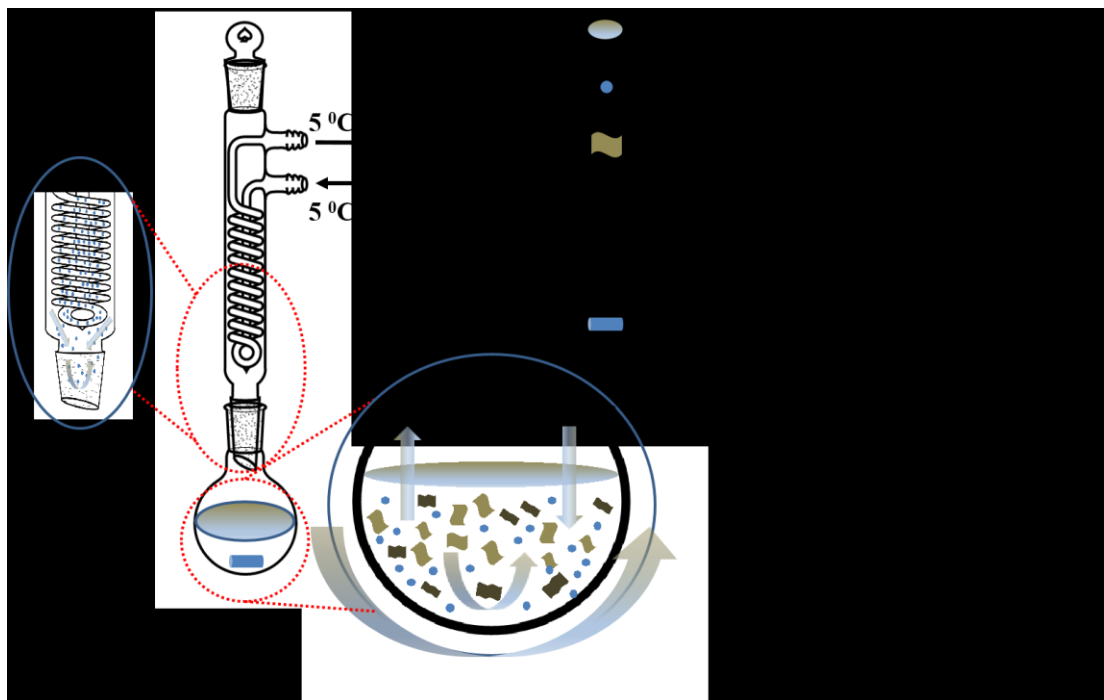


Figure S4.1. Pre-hydrothermal treatment process (Stage I) of MoS_2 (MoSe_2) suspension with the assistant of L-ascorbic acid.¹⁻³

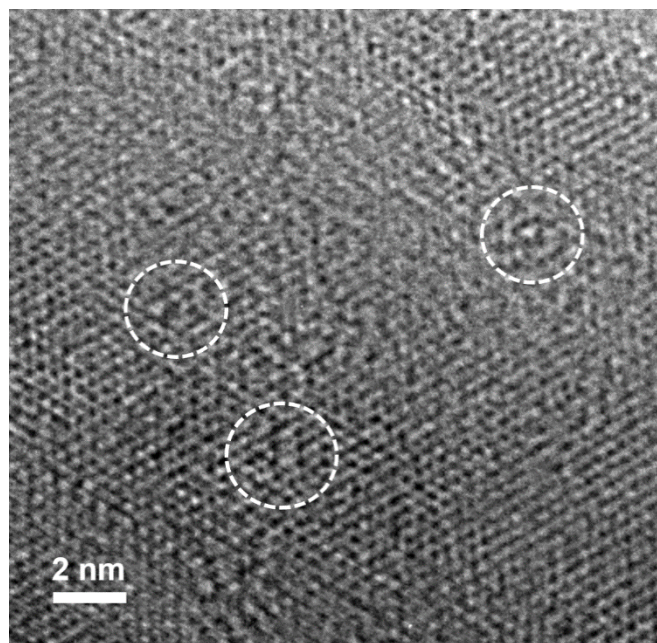
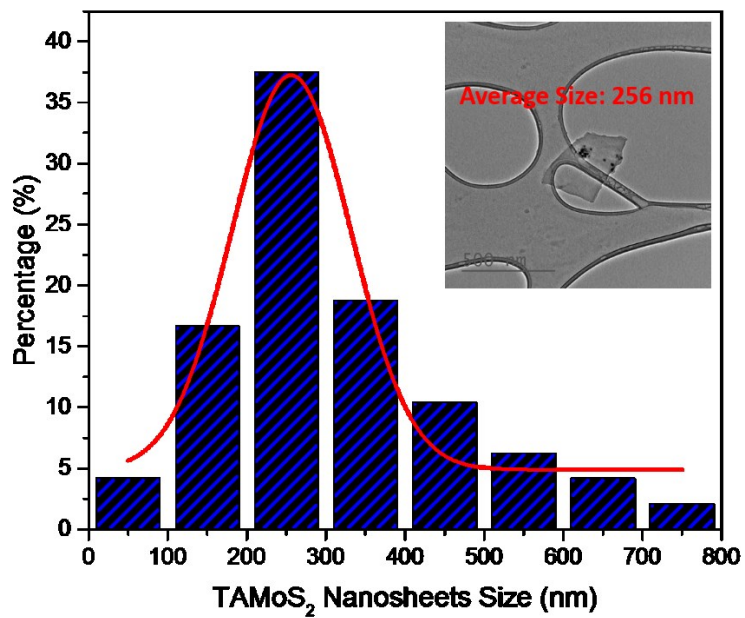


Figure S4.2. HRTEM image of exfoliated TAMoS₂ nanosheets with defects and the attachment of TA/LA molecules at those defects shown in the circles.



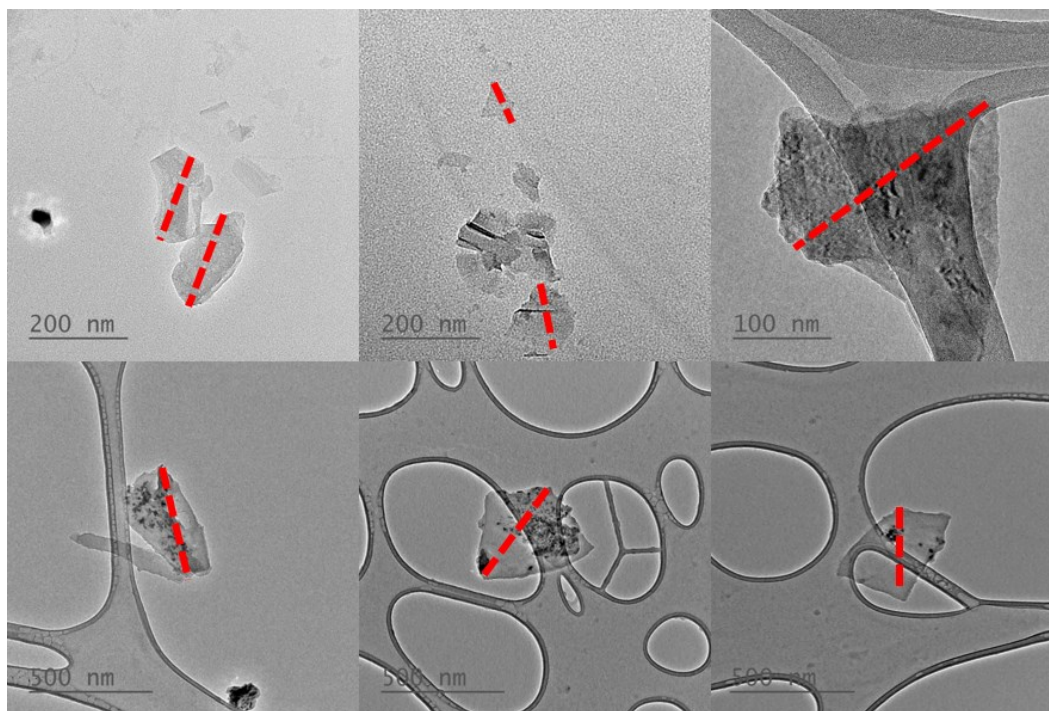


Figure S4.3. Lateral size distribution of TAMoS₂ nanosheets. The lateral size here is defined as the length for the diagonal line of each nanosheet. The size distribution curve is counted from 100 TEM images by measuring the diagonal line. Additional TEM images are listed below.

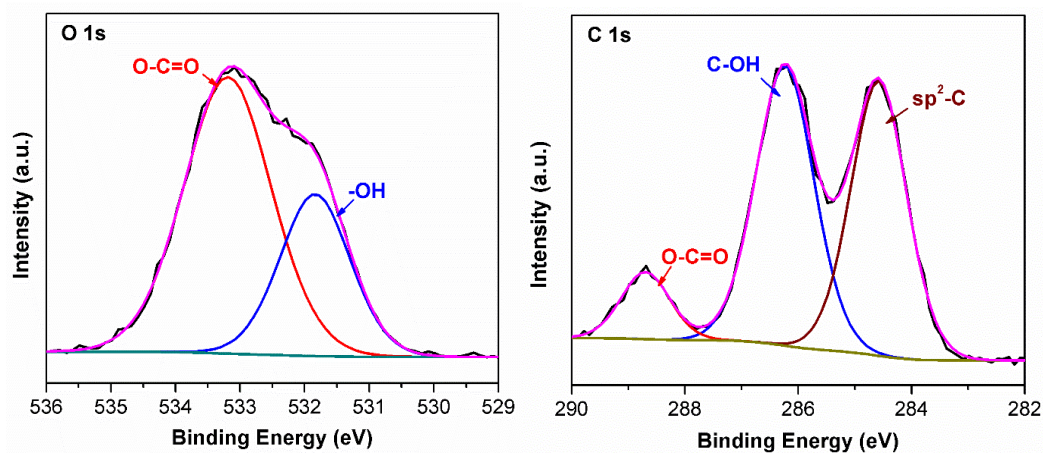


Figure S4.4. High-resolution XPS analysis of TAMoSe₂ nanosheets for O 1s and C 1s. The sp²-C, C-OH, and O-C=O functional groups represent the successful graft of TA molecules onto MoSe₂ nanosheets.

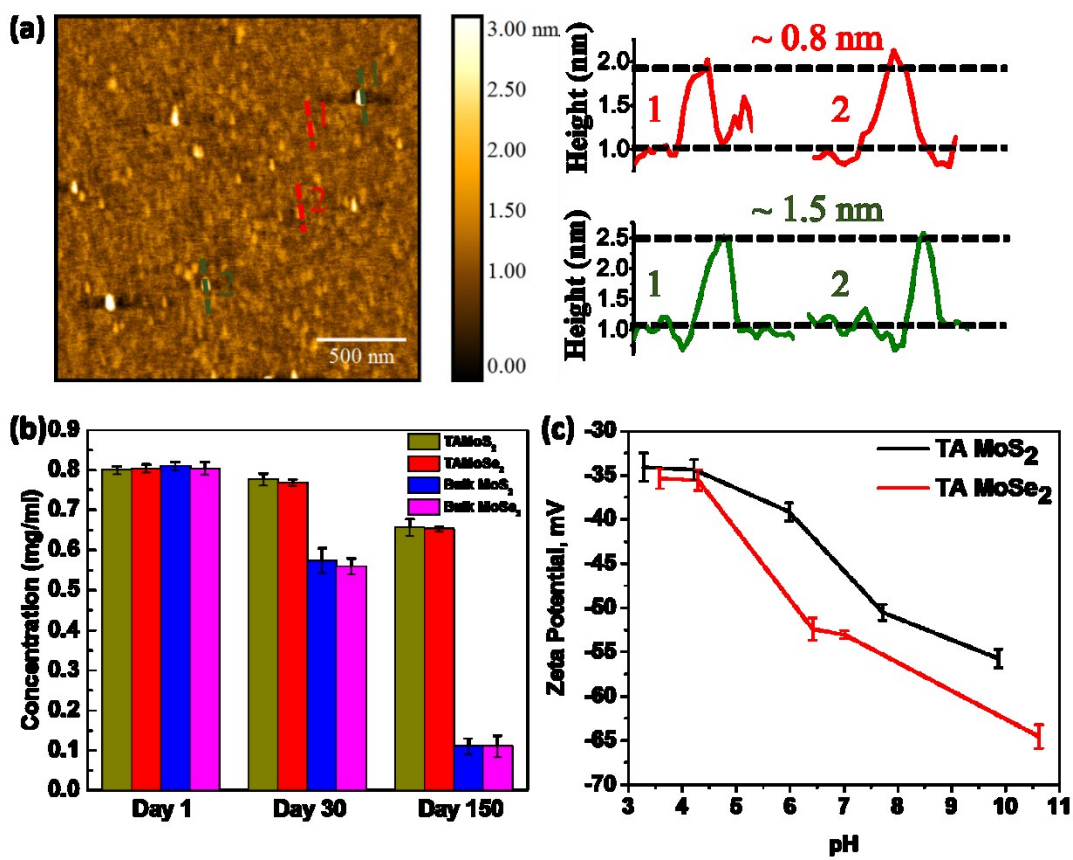


Figure S4.5. AFM height profiles and topographic image (a) of TAMoS₂ nanosheets; water stability performance of TAMoS₂ (TAMoSe₂) compared with bulk MoS₂ (MoSe₂) powders (b); Zeta Potential analysis of TAMoS₂ (TAMoSe₂) nanosheets dispersed in aqueous solutions with a wide range of pH values (c).

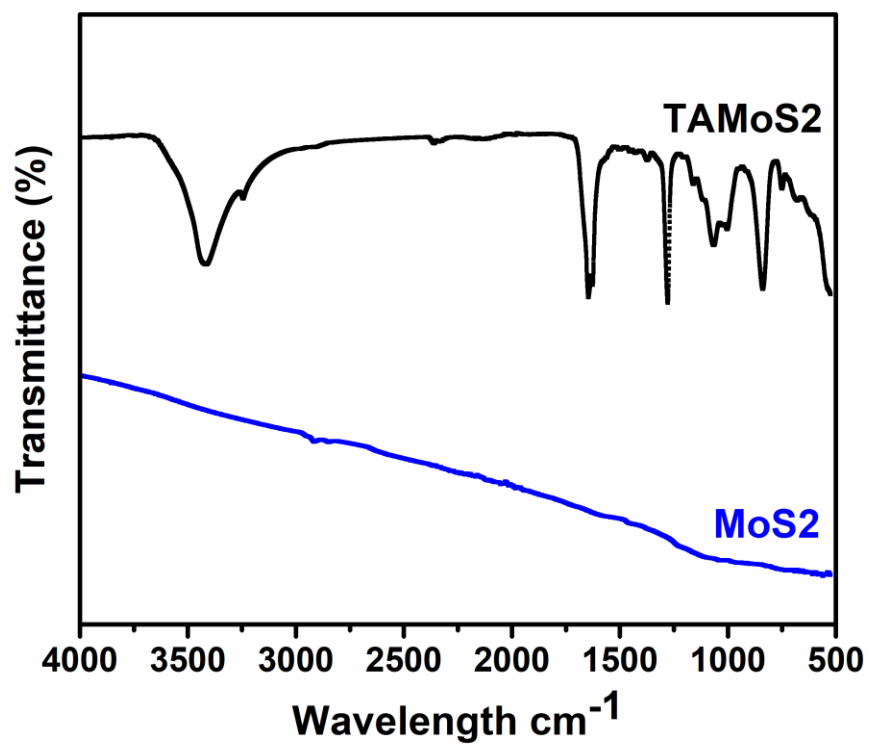


Figure S4.6. FT-IR spectra of TAMoS₂ and MoS₂ nanosheets.

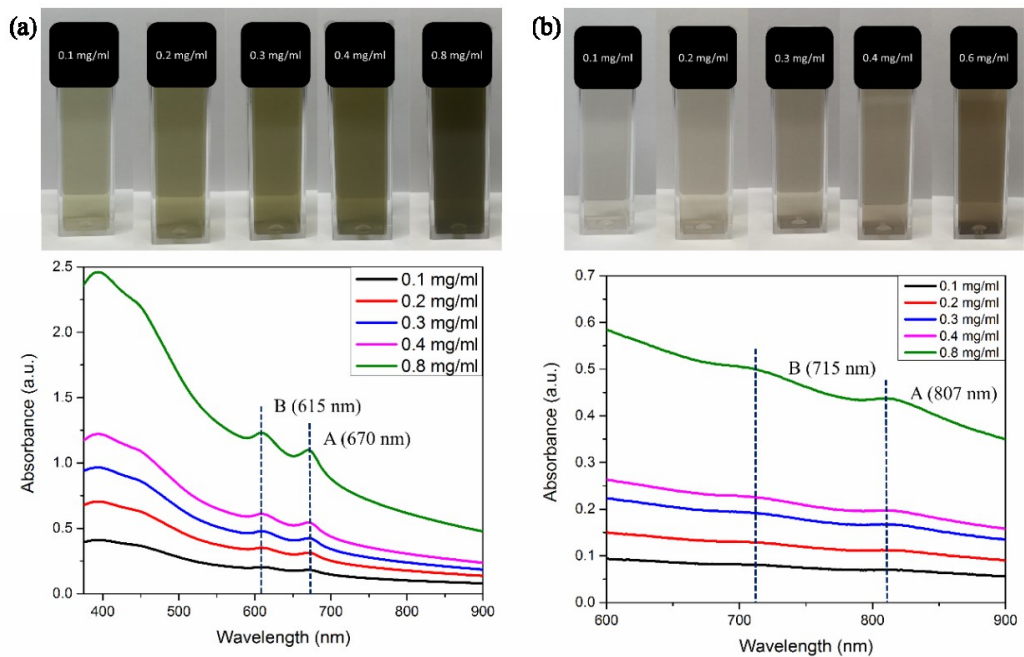


Figure S4.7. Ultraviolet light (UV) of (a) TAMoS₂ and (b) TAMoSe₂ nanosheets after exfoliation for multiple concentration range: 0.1 mg/ml, 0.2 mg/ml, 0.3 mg/ml, 0.4 mg/ml, 0.8 mg/ml.

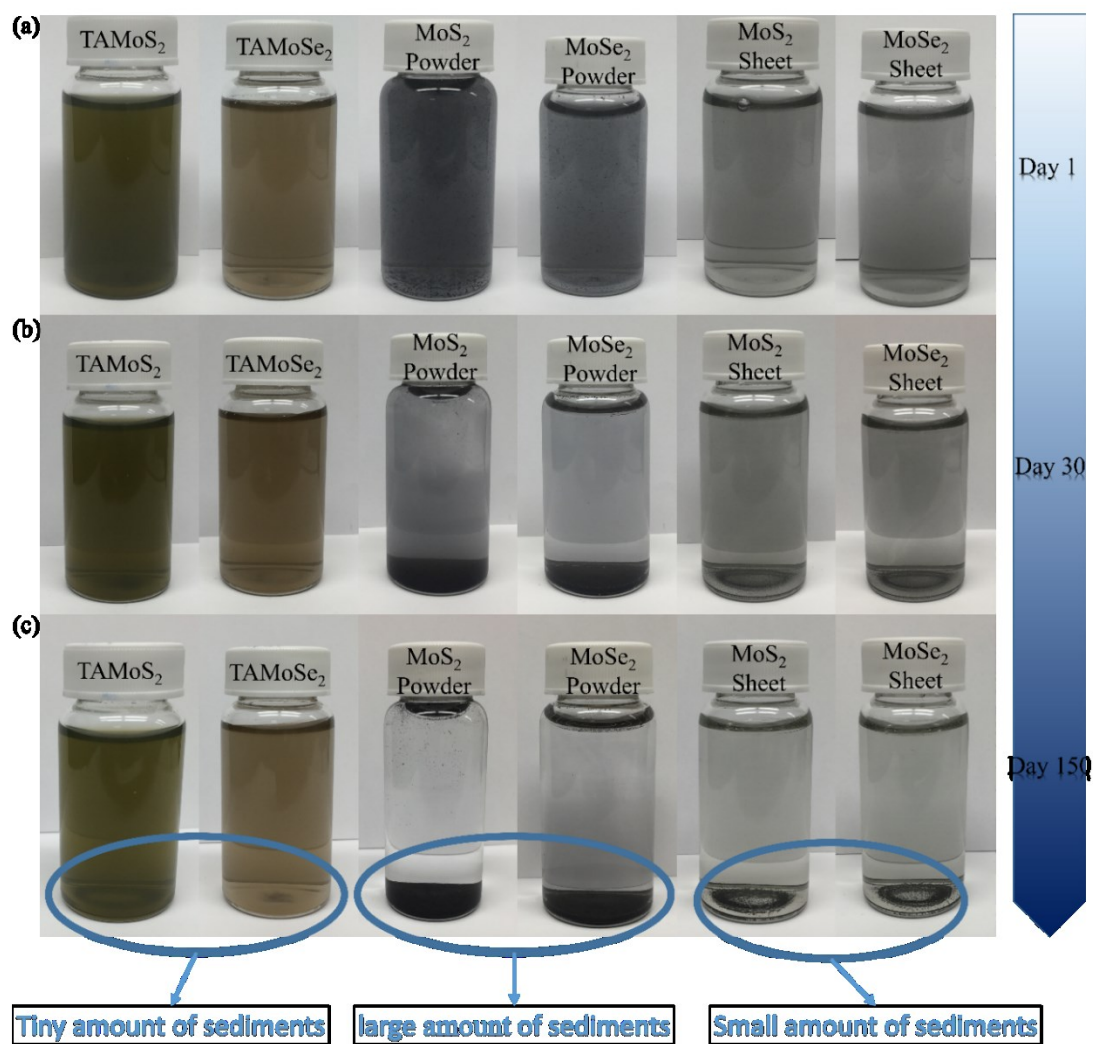


Figure S4.8. Photographs of the stability performance for TAMoS₂/TAMoSe₂ nanosheet (left), MoS₂/MoSe₂ sheet (right) and bulk MoS₂/MoSe₂ powder (middle) suspension recording from day 1 to day 150. The TAMoS₂/TAMoSe₂ nanosheets (left) show brilliant performance on its stabilities with very small amount of sediments after 150 days, while the MoS₂/MoSe₂ sheets (right) show

relatively good stabilities with a small amount of sediments present. Most of the bulk MoS₂/MoSe₂ powder (middle) suspension settled down demonstrating their poor stability in water.

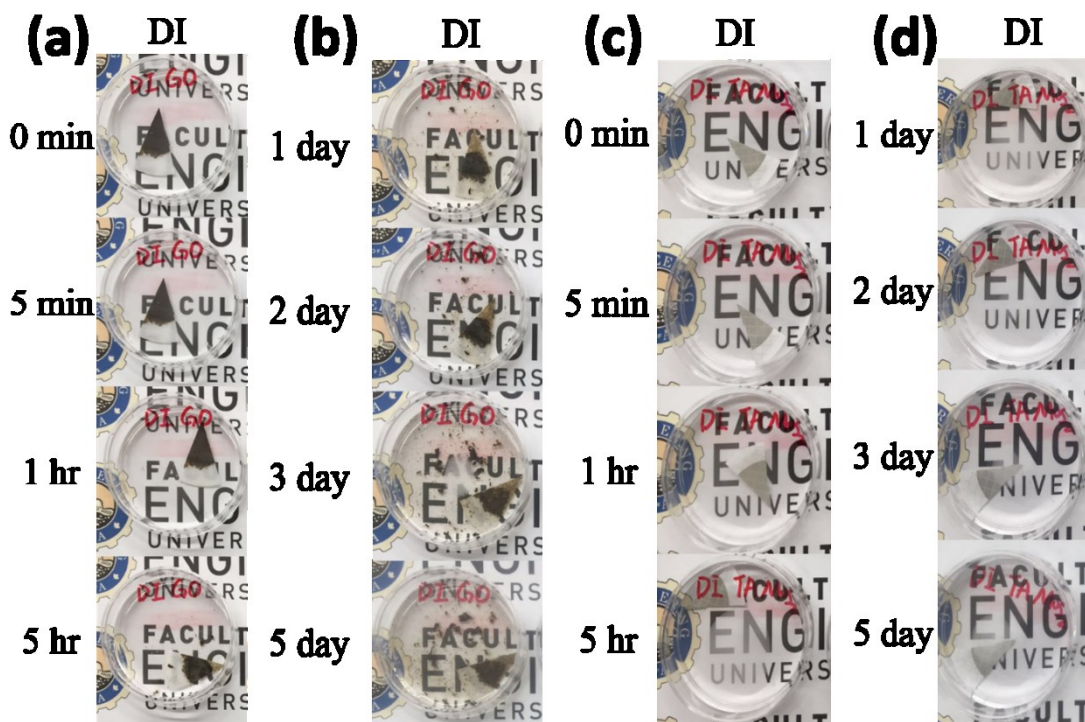


Figure S4.9. Photo image of stability of GO membrane (a), (b) and TAMoS₂ membrane (c), (d) soaking under DI water for 5 days.

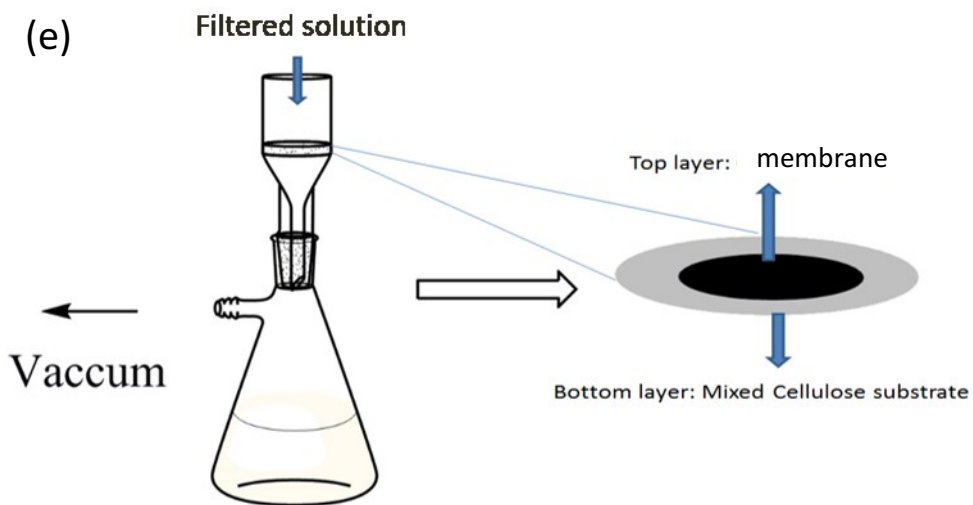
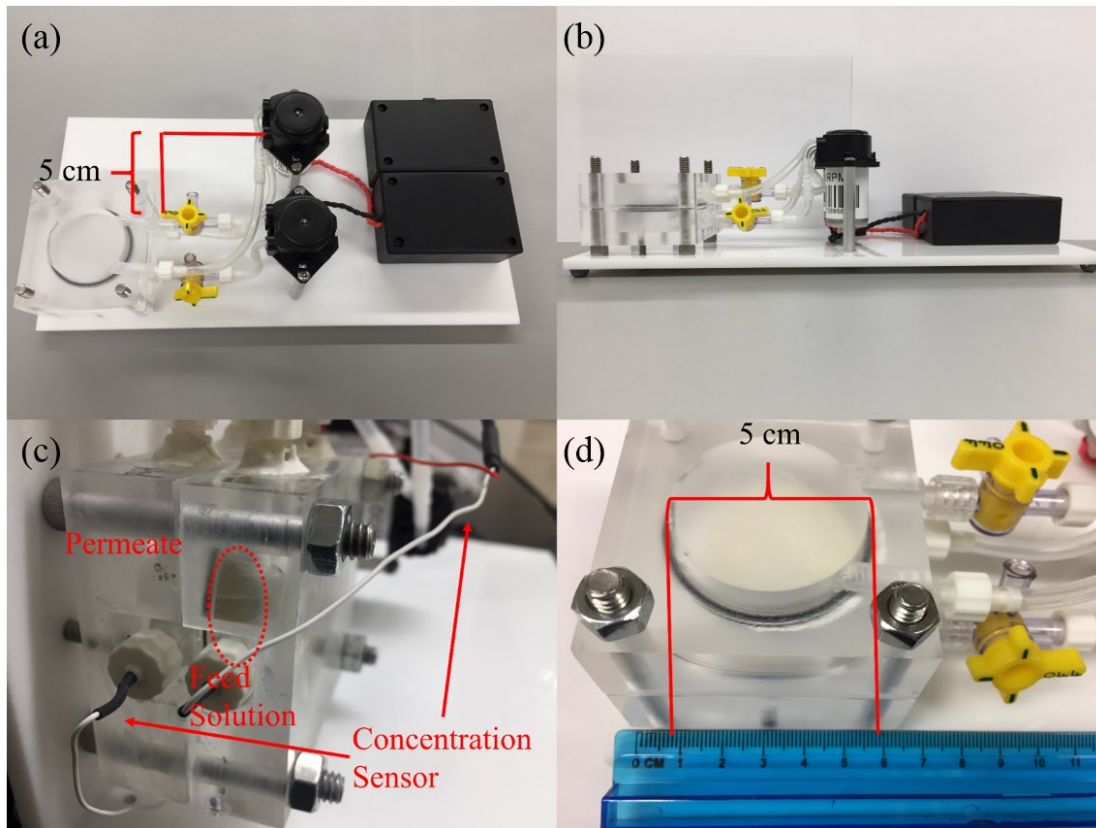


Figure S4.10. Photographs of osmosis set up with $D = 5$ cm dimension; the two peristaltic pumps could provide tiny turbulence (a-d) and vacuum filtration set up (e).

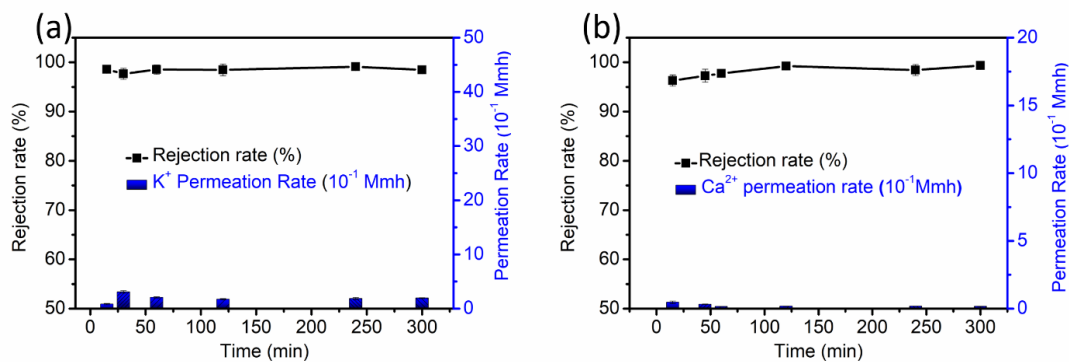


Figure S4.11. Stability test of K⁺ and Ca²⁺ through 40 μm hybrid membrane with 1% TAMoS₂. The duration time is set to be 300 min. The feed side is DI water and 0.25M cation solution as draw side under room temperature and pressure, the stabilized time is set as 360 min. Inductive Coupled Plasma Emission Spectrometer was used to obtain the cation concentrations in solutions.

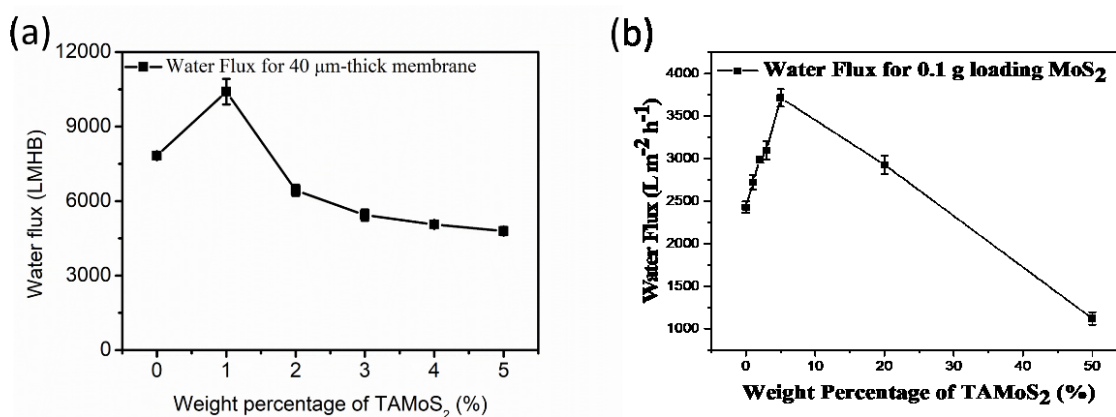


Figure S4.12. The synergistic effect to achieve the ultrafast water flux at 1% weight percentage of TAMoS₂ nanosheets in hybrid membranes with the thicknesses of 40 μm thick (a) and 400 μm thick (b).

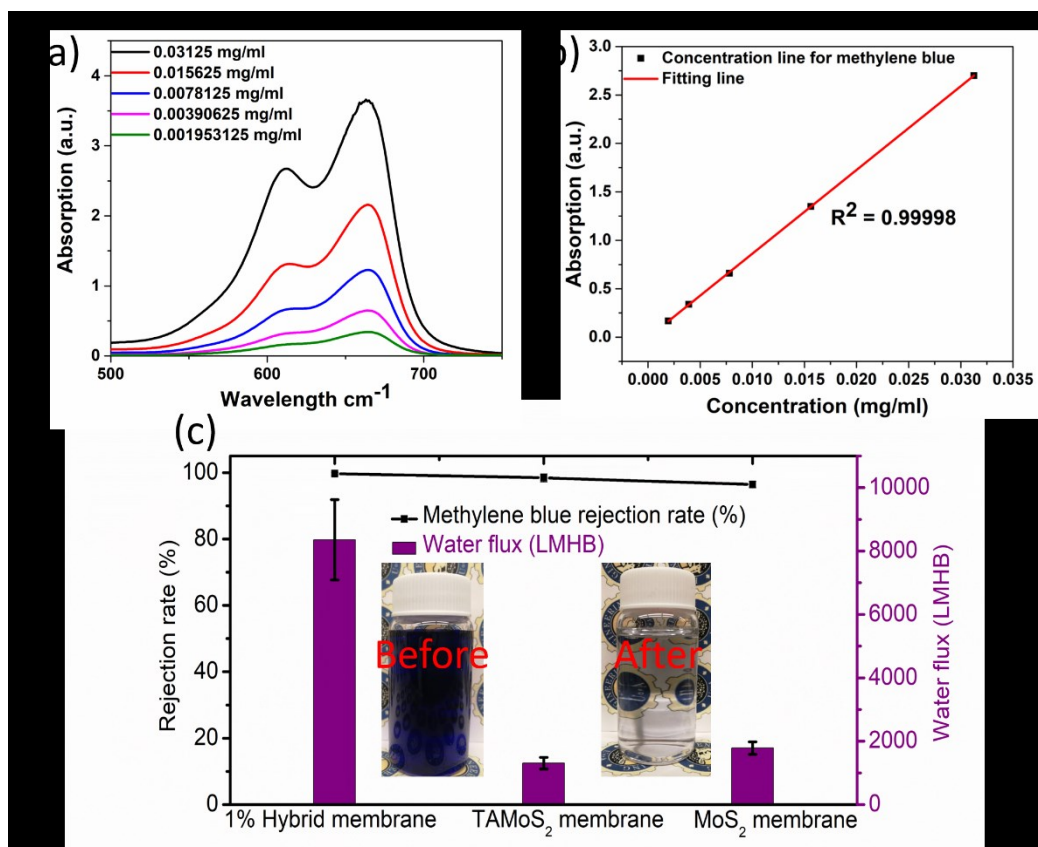


Figure S4.13. Methylene Blue concentration gradient standard line based on UV-vis spectra (a), (b); Water flux and rejection rate for 40 μm -thick 1% TAMoS₂ hybrid membrane, TAMoS₂ membrane and MoS₂ membrane under vacuum filtration ~ 0.7 bar (c).

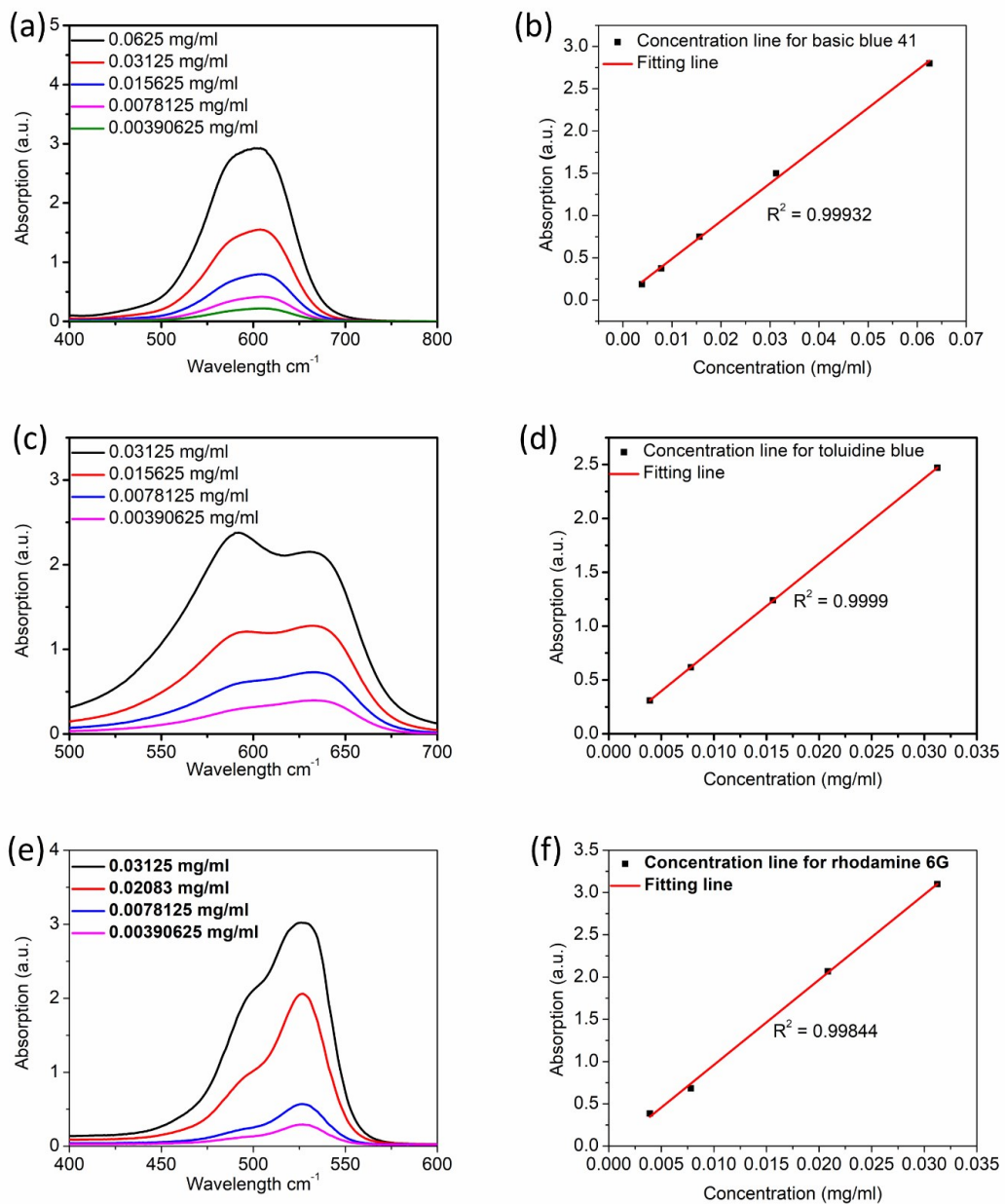


Figure S4.14. UV-vis spectrophotometer concentration gradient standard line for (a), (b) Basic Blue; (c), (d) Toluidine Blue and (e), (f) Rhodamine 6G.

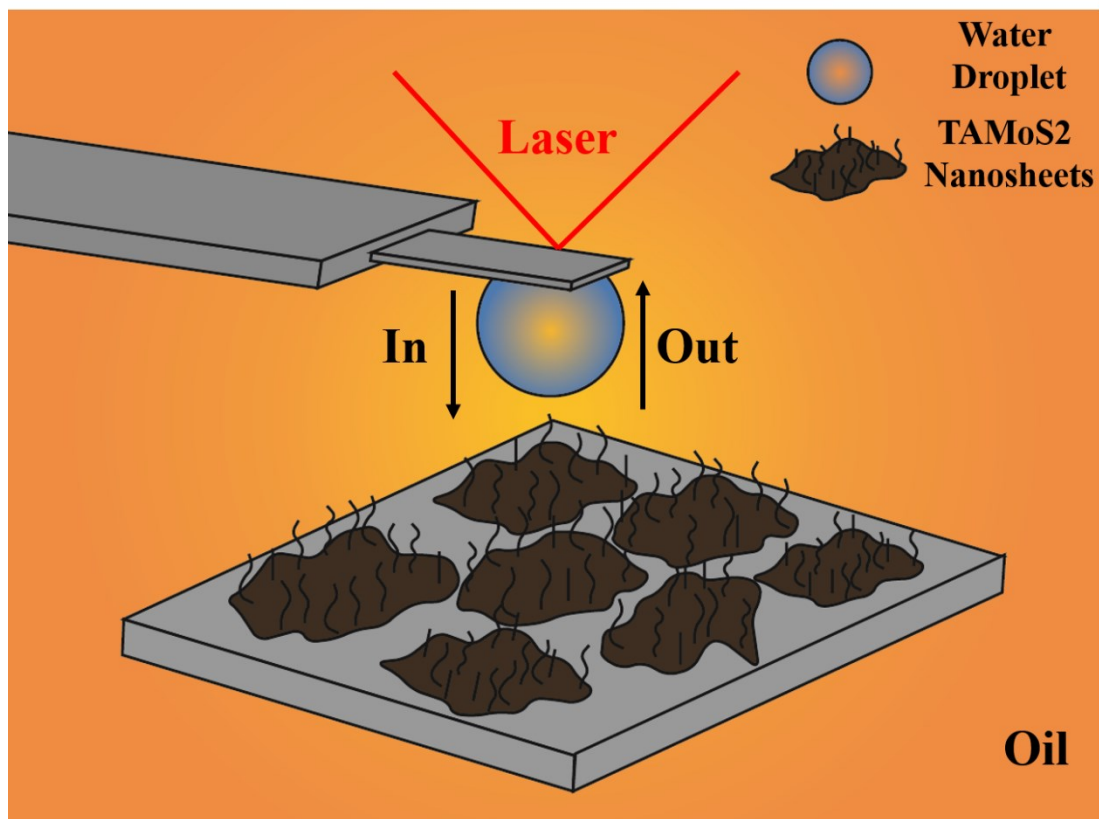


Figure S4.15. High resolution image for **Figure 4.5b** inserted picture.

The measured environment was in toluene with water droplet radius $R = 73 \mu\text{m}$ and the tip velocity was $1 \mu\text{m/s}$. It is interesting to detect an attraction force between the water droplet and the surface of the TAMoS₂ membrane (an attractive attachment value of 0.2 nN for water molecules to the TAMoS₂ membrane surface at a piezo displacement distance of $0.1 \mu\text{m}$).

Table S4.1. Effective and hydrated ionic radius in this work in literature⁷²

| UNIT (Å) | K ⁺ | Na ⁺ | Li ⁺ | Ca ²⁺ | Mg ²⁺ |
|-------------------------------|----------------|-----------------|-----------------|------------------|------------------|
| EFFECTIVE IONIC RADIUS | 1.38 | 1.02 | 0.76 | 1.00 | 0.72 |
| HYDRATED RADIUS | 3.31 | 3.58 | 3.82 | 4.12 | 4.28 |

Table S4.2. Comparison of literature values for target membranes under static diffusion mode.

| Membrane type | Water flux (LMH) | Membrane thickness | Feed & concentration (M) | Rejection | Reference |
|--|------------------|--------------------|--------------------------|----------------|------------------|
| Graphene Oxide | 0.007 | 5 μm | NaCl 0.1 | ~10% | 73 |
| MoS ₂ /SY | 0.033 | 5 μm | NaCl 0.1 | 99% | 1 |
| MoS ₂ | 75 | 6 μm | NaCl 0.1 | ~27% | 31 |
| MoS ₂ /NR | 105 | 6 μm | NaCl 0.1 | ~37% | 1 |
| PVDF | 2300 | 5 μm | NaCl 0.1 | ~0% | 74 |
| PA/GO/OCNT | 114 | N/A | NaCl 0.5 | N/A | 13 |
| OMWCNT | 116.5 | N/A | N/A | N/A | 17 |
| Hybrid membrane with 1% TAMoS₂ | 320 | 5 μm | NaCl 0.25 | ~97.93% | This work |
| TAMoS₂ | 275 | 5 μm | NaCl 0.25 | ~93.2% | This work |
| MoS₂ | 170 | 5 μm | NaCl 0.25 | ~74.3% | This work |

Table S4.3. Comparison of literature values for target membrane with Vacuum Filtration separation performance.

| Membrane type | Water flux (LMHB) | Membrane thickness | Feed & concentration (M) | Rejection | Reference |
|--|--------------------------|----------------------------|-------------------------------------|------------------|------------------|
| Graphene Oxide | 27.6 | ~18nm | NaCl 0.02 | 19% | 75 |
| Graphene Oxide | 71 \pm 5 | ~150nm | NaCl 0.034 | 25-40% | 76 |
| MoS ₂ /CV | ~270 | 5 μ m | NaCl 1 | ~ 20% | 1 |
| Graphene Oxide/CNTs | 11.3 | ~40 nm | NaCl 0.01 | 39.70% | 68 |
| GO/FLG | NA | 26-33 nm | Rhodamine B | ~80% | 77 |
| GO/Porphyrin | ~ 0.88 | N/A | NaCl 0.034 | ~25% | 78 |
| NF2A | 19.5 | 22-53 nm | Methylene blue N/A | 99.20% | 18 |
| GO/OCNT | 21.71 | N/A | Methylene blue | 99.3% | 19 |
| GO/OCNT-LbL | 6~10 | N/A | NaCl | N/A | 79 |
| Desal 5DK | 25-35 | N/A | Direct red | 95% | 80 |
| Polysulfone | 0.23-0.28 | N/A | Acid red 0.00025 | 97% | 81 |
| Hybrid membrane with 1% TAMoS₂ | ~10,000 | 5 μm | Methylene blue 0.1mg/ml | ~98.26% | This work |
| TAMoS₂ | ~1300 | 5 μm | Methylene blue 0.1mg/ml | ~95.43% | This work |
| MoS₂ | ~2000 | 5 μm | Methylene blue 0.1mg/ml | ~92.04% | This work |

Table S4.4. Comparison of literature values for the exfoliation time of MoS₂ with the assistance of polar solvent under sonication bath.

| Materials | Time | Reference |
|---|------------------|------------------|
| wool keratin (WK)-MoS₂ | 24 h | 82 |
| NMP-MoS₂ | 3 h | 83 |
| Multiple polar solvents exfoliation | 48 h | 50 |
| Lithium intercalation 1H- MoS₂ | 48 h | 84 |
| (H₃Mo₁₂O₄₀P/MoS₂)_n | 3 h | 85 |
| MoS₂-GG, MoS₂-XG, MoS₂- TA | 100 h | 53 |
| Two-stage exfoliation of preparing tannic acid (TA)- modified MoS₂ (or MoSe₂) nanosheets | 5 minutes | This work |

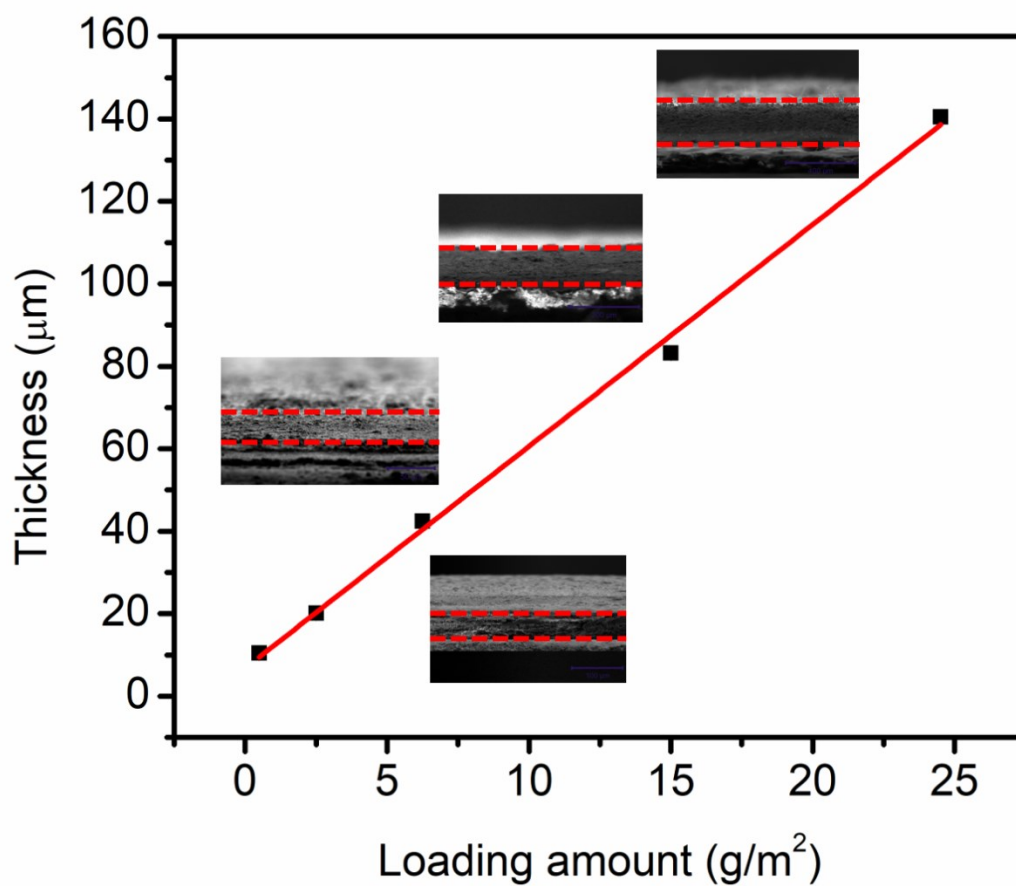
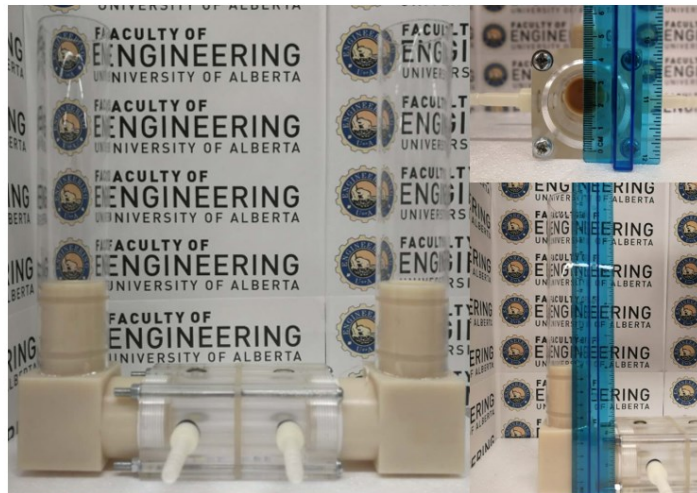


Figure S5.1. Thickness standard line for NbSA nanosheet membrane.

(A)



(B)

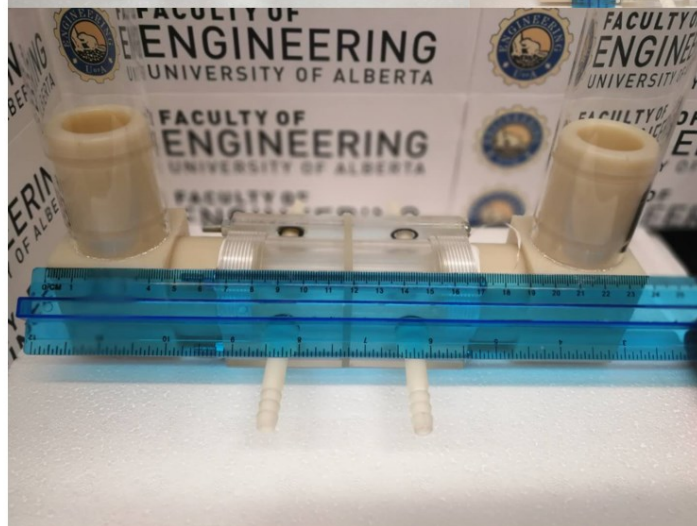


Figure S5.2. Experimental setup for forward osmosis process.

| | | | | | |
|-------------------------------|-------------|-------------|-------------|-------------|-------------|
| EFFECTIVE IONIC RADIUS | 1.38 | 1.02 | 0.76 | 1.00 | 0.72 |
|-------------------------------|-------------|-------------|-------------|-------------|-------------|

Table S5.1. Effective ionic radius and hydrated radius for multiple cations including K^+ ; Na^+ ; Li^+ ; Ca^{2+} and Mg^{2+} ,⁶⁸.

| | | |
|------------------------|----------|--------------------------|
| K⁺ | 3 | 10⁻⁹ |
| Li⁺ | 5 | 5*10⁻⁹ |
| Mg²⁺ | 6 | 10⁻⁶ |

Table S5.2. Hydration number and lifetime/exchange rate (s) for multiple cations including K^+ ; Na^+ ; Li^+ ; Ca^{2+} and Mg^{2+} ,⁶⁸.

| Membrane type | Water flux (LMH) | Membrane thickness | Feed & concentration (M) | Rejection | Reference |
|---|------------------|--------------------|--|-----------|------------------|
| Graphene Oxide | 0.007 | 5 μm | NaCl 0.1 | ~97% | ⁶⁹ |
| MoS ₂ /SY | 0.033 | 5 μm | NaCl 0.1 | 99% | ⁸ |
| MoS ₂ | 75 | 6 μm | NaCl 0.1 | ~27% | ⁷⁰ |
| MoS ₂ /NR | 105 | 6 μm | NaCl 0.1 | ~37% | ⁸ |
| PVDF | 2300 | 5 μm | NaCl 0.1 | ~0% | ⁷¹ |
| Ti ₃ C ₂ T _x MXene | 37.4 | 1.5 μm | NaCl 0.1 | ~20% | ⁷² |
| NbSA | | 5 μm | NaCl 0.25 KCl 0.25 LiCl 0.25 CaCl ₂ 0.25 MgCl ₂ 0.25 | 99% | This work |

Table S5.3. Comparison of literature values for target membrane with Forward Osmotic separation performance.

| Membrane type | Water flux (LMHB) | Membrane thickness | Feed & concentration (M) | Rejection | Reference |
|----------------------|-------------------|--------------------|---|-----------|-----------|
| Graphene Oxide | 71 ± 5 | ~150nm | NaCl 0.034 | 25-40% | 73 |
| MoS ₂ /CV | ~270 | 5 μm | NaCl 1 | ~ 20% | 74 |
| Graphene Oxide/CNTs | 11.3 | ~40 nm | NaCl 0.01 | 39.70% | 8 |
| GO/FLG | NA | 26-33 nm | Rhodamine B | ~80% | 75 |
| GO/Porphyrin | ~ 0.88 | N/A | NaCl 0.034 | ~25% | 76 |
| NF2A | 19.5 | 22-53 nm | Methylene blue N/A | 99.20% | 77 |
| Desal 5DK | 25-35 | N/A | Direct red | 95% | 78 |
| Polysulfone | 0.23-0.28 | N/A | Acid red 0.00025 | 97% | 79 |
| NbSA | ~2000 | 5 μm | Basic blue 100 ppm Rhodamine 6G 100ppm Toluidine 100 ppm | ~99% | This work |

Table S5.4. Comparison of literature values for target membrane with Vacuum Filtration separation performance.

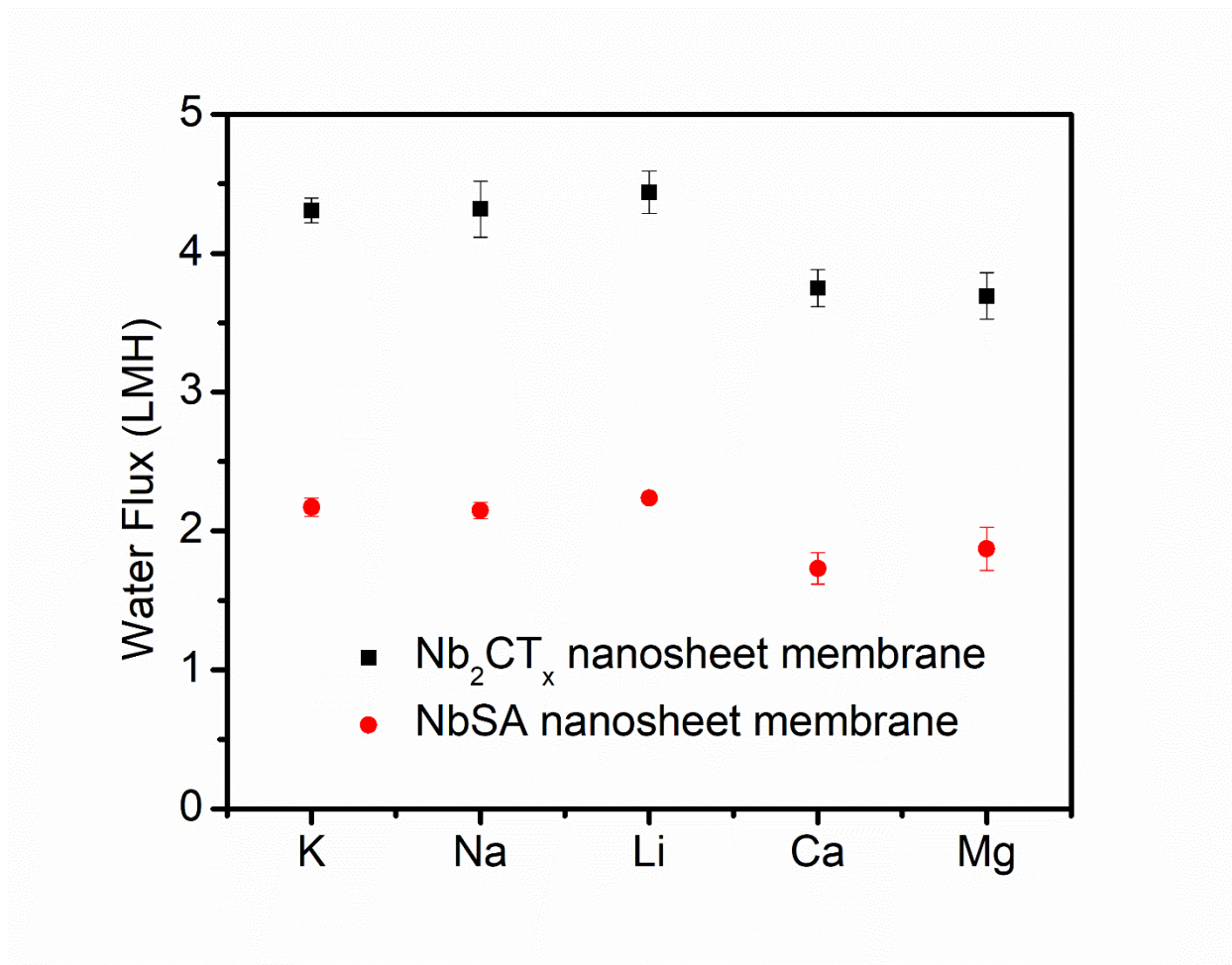


Figure S5.3. Water flux for Nb₂CT_x nanosheet membrane and NbSA nanosheet membrane through forward osmosis process. The Feed side is DI water and the draw side is 0.25 M cationic solution. Magnetic stirrers are added to both side to avoid concentration gradient²¹.

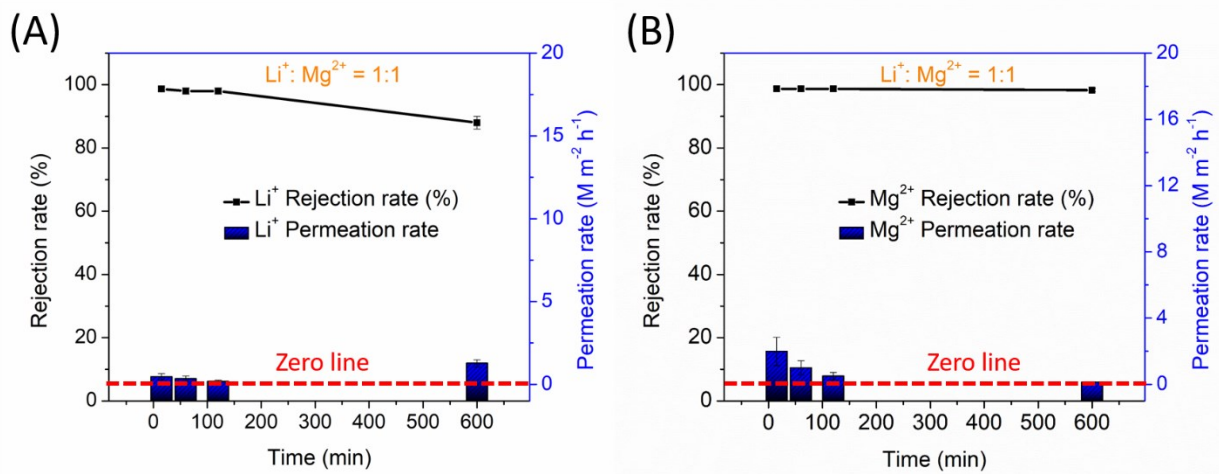


Figure S5.4. Lithium and Magnesium separation by NbSA nanosheet membrane through forward osmosis process after long term stability test. The Feed side is DI water and the draw side is 0.25 M mixture cationic solution ($\text{Li}^+/\text{Mg}^{2+} = 1:1$). Magnetic stirrers are added to both side to avoid concentration gradient²¹.

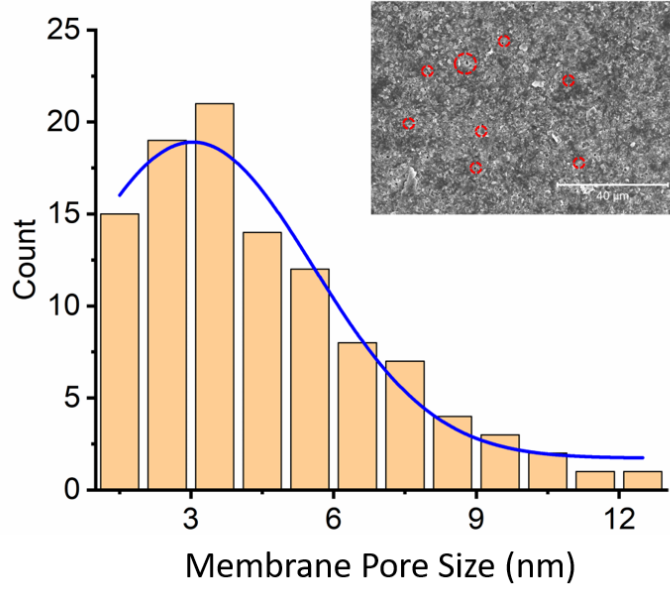


Figure S5.5. NbSA membrane pore size distribution as top view shown as inserted image.

Membrane porosity was measured by using the dry-wet weight method. The equation is listed as:

$$Porosity(\%) = \frac{W_w - W_d}{\rho_w A \delta} \quad S5.1$$

Where W_w is the wet sample weight (g), W_d is the dry sample weight (g), ρ_w is the density of pure water (g/cm^3), A is the area of membrane in the wet state (cm^2), and δ is the thickness of membrane in the wet state (cm).

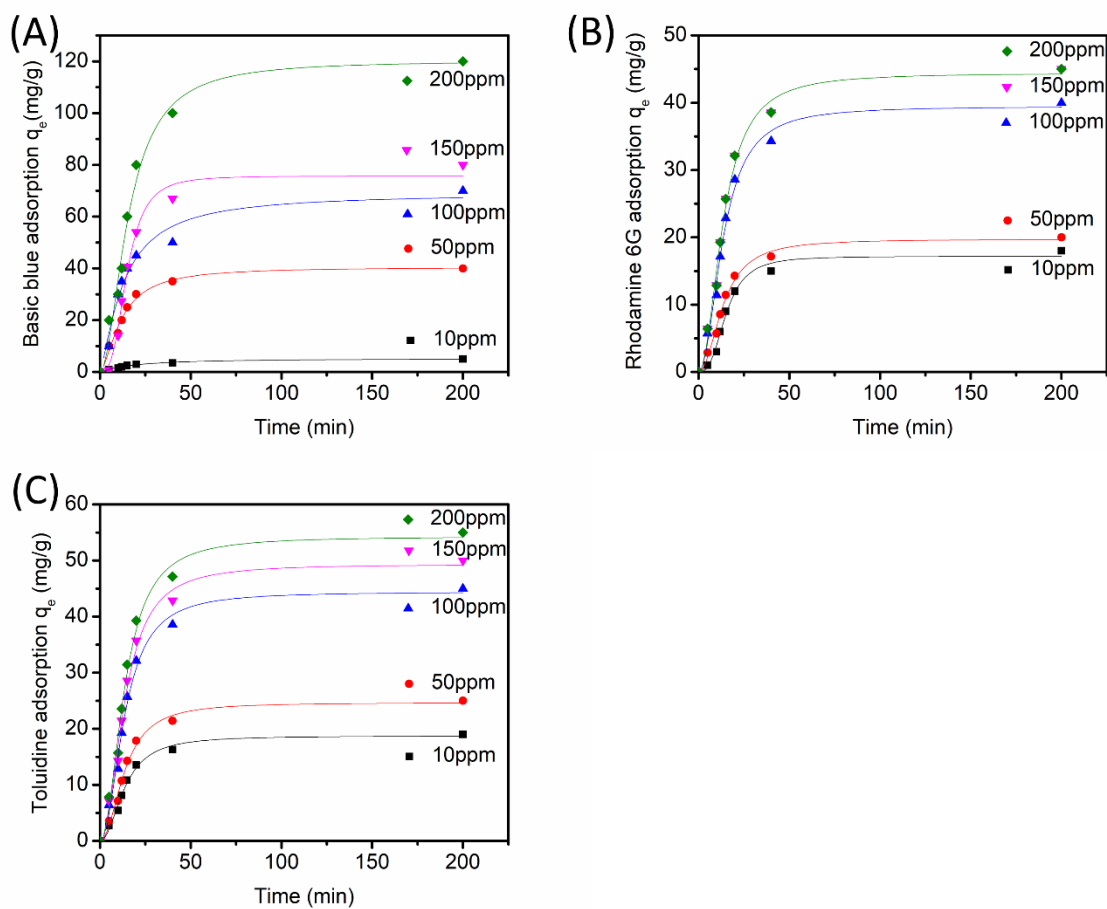


Figure S5.6. Adsorption kinetics at different concentrations (ppm) of (A) basic blue on NbSA nanosheet membrane, bottom to top, 10, 50, 100, 150 and 200; (B) Rhodamine 6G on NbSA nanosheet membrane, bottom to top: 10, 50, 100, 150 and 200; and (C) Toluidine on NbSA nanosheet membrane, bottom to top, 10, 50, 100, 150 and 200. The solid lines were obtained by fitting the data using the pseudo second-order kinetics.

Table S5.4. Pseudo-second order Adsorption Kinetics for Basic blue

Basic blue q_e mg/g

| <i>Parameter</i> | 10ppm | 50ppm | 100ppm | 150ppm | 200ppm |
|------------------|----------|----------|----------|--------|----------|
| K_2 | 0.00876 | 0.00161 | 8.50E-04 | 0.0379 | 3.22E-04 |
| q_e | 5.52007 | 44.8067 | 75.1169 | 82.466 | 140.174 |
| R^2 | 0.986495 | 0.967559 | 0.96869 | 0.9250 | 0.94727 |

Table S5.5. Pseudo-second order Adsorption Kinetics for Rhodamine 6G

Rhodamine 6G q_e mg/g

| <i>Parameter</i> | 10ppm | 50ppm | 100ppm | 150ppm | 200ppm |
|------------------|----------|----------|-------------|----------|----------|
| K_2 | 0.00182 | 0.00234 | 0.00117 | 0.00104 | 0.00104 |
| q_e | 21.57772 | 23.11408 | 46.22499 | 52.0069 | 52.00691 |
| R^2 | 0.906843 | 0.942412 | 0.942412286 | 0.942412 | 0.942412 |

Table S5.6. Pseudo-second order Adsorption Kinetics for Toluidine

Toluidine q_e mg/g

| <i>Parameter</i> | 10ppm | 50ppm | 100ppm | 150ppm | 200ppm |
|------------------|----------|----------|----------|----------|----------|
| K_2 | 0.00247 | 0.00187 | 0.00104 | 9.38E-04 | 8.52E-04 |
| q_e | 21.95858 | 28.89473 | 52.00696 | 57.78585 | 63.56416 |
| R^2 | 0.942412 | 0.942412 | 0.942412 | 0.942412 | 0.942412 |

Table S5.7. Desorption rate for NbSA membrane (shaking speed: ~ 100 rpm)

| | Desorption rate (mg/h) |
|--------------|---------------------------|
| Basic blue | 0.0625 |
| Toluidine | 0.0313 |
| Rhodamine 6G | 0.0167 |

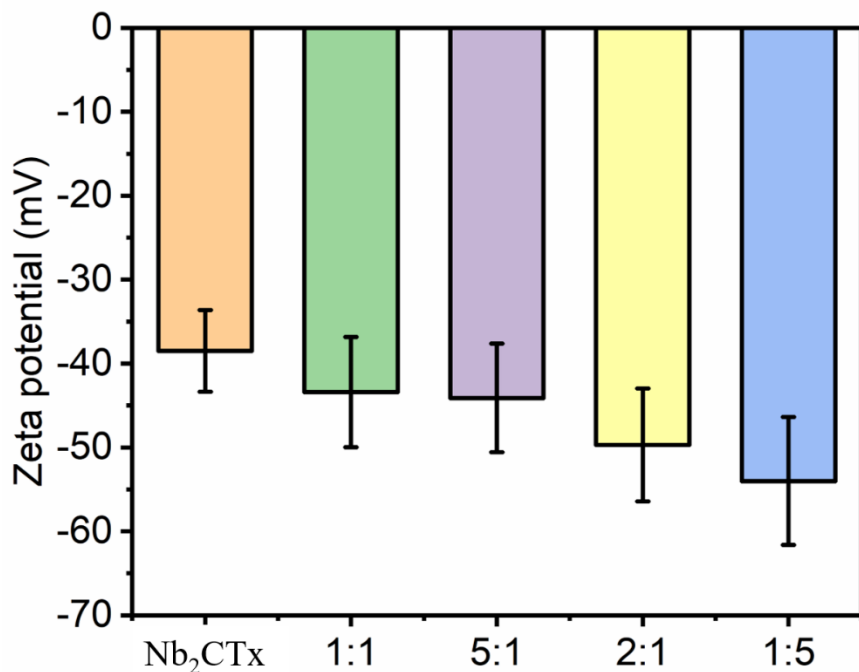


Figure S5.7. Zeta potential for sodium alginate (SA), Nb₂CTx nanosheet and their mixture under multiple concentration ratios (SA/Nb₂CTx).

In general, the surface charge properties (indicated by zeta potential values in **Figure S5.7**) would not significantly increase before and after modification of Nb₂CTx nanosheets at different concentration ratios (SA/Nb₂CTx) (e.g., 1:1, 5:1, 2:1, 1:5). After membrane modification, the flow rate decreases but the surface charge density remains almost unchanged, indicating the surface charge properties would not have significant influence on membrane performance.

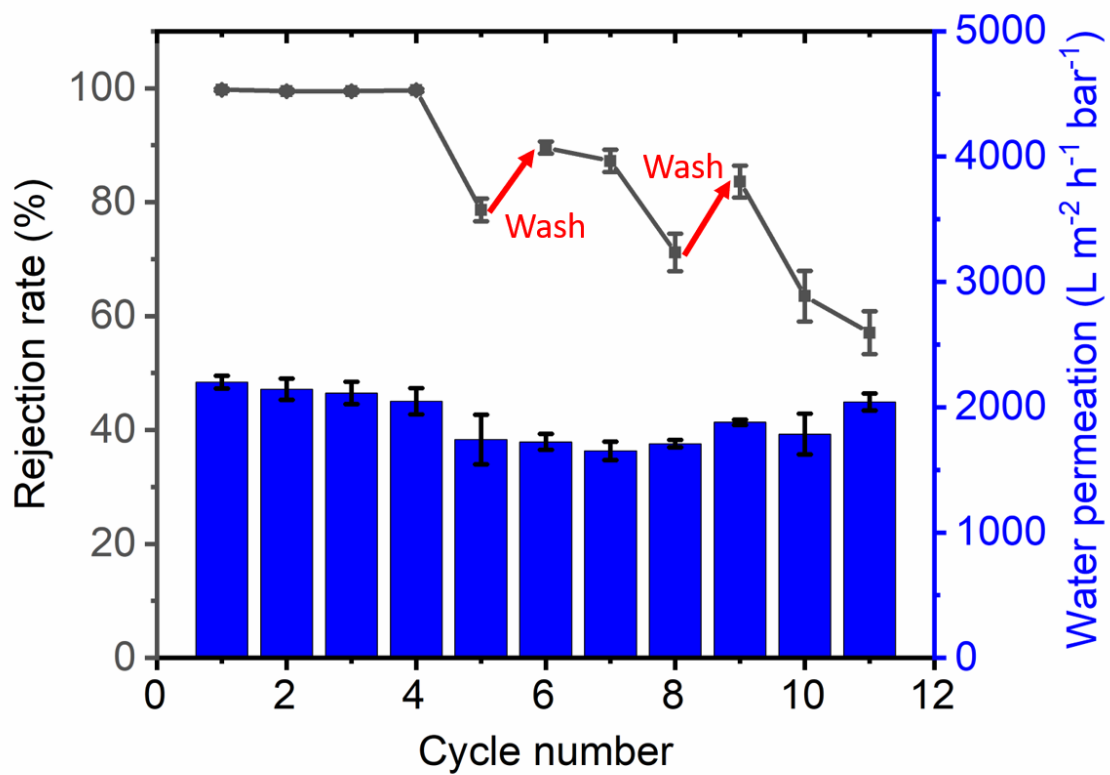


Figure S5.8. Cycle test for Basic blue dye (100 ppm).